ARCHIVES OF ACOUSTICS
16, 3–4 387–412 (1991)

TECHNOLOGY AND ACOUSTICAL PROPERTIES OF THE CERAMIC HIGH-TEMPERATURE SUPERCONDUCTORS

M. ALEKSIEJUK, J. RAABE*, J. RANACHOWSKI

Institute of Fundamental Technological Research Polish Academy of Sciences
(00-049 Warszawa, Świętokrzyska 21)

Technical University of Warsaw, Department of Chemistry
(00-604 Warszawa, Noakowskiego 3)

1. Introduction

The aim of the paper is to present the acoustic methods of investigating the phenomena taking place in the range of the conductor-superconductor transition in the selected ceramic superconducting materials.

The superconducting materials, used up till recently, which were limited mainly to metals, had the transition temperature of about several Kelvin. During seventy years, beginning from the first studies on superconductivity, the attempts to find materials with higher transition temperature failed, and it was only in 1973 that the Nb_3Ge alloy with the transition temperature of 23 K was discovered. This discovery caused a significant increase of interest in intermetallic alloys of the type Nb_3Ge or V_3X, where X is the metal from the intermediate group. These compounds have had the transition temperature between ten and twenty Kelvin. This allowed to utilize technically the superconductivity phenomenon in generating stable magnetic field. The next important step in this direction was the discovery of superconductivity in lithium titanate $LiTi_2O_4$ which is a typical oxide material. This discovery caused that into the investigation of superconductivity also the oxide materials have been included. The investigations resulted in the discovery, made by BEDNORZ and MULLER [1, 2], the Nobel prize winners, of the superconductivity phenomenon in the perovskites of the $La_{2-x}A_xCuO_y$ system (where A = Ca, Sr or Ba). The superconductivity in this perovskite ceramic has been later confirmed by CHU et al. [3]. That was the reason for directing the interests of theoretical physicists and technologists around the world towards the high-temperature superconductivity (HTS). The main interest of the superconductivity technology consists in the design of magnets generating strong magnetic fields in large volumes.

In all the superconducting devices the current density of about $I \geqslant 5 \cdot 10^4\ Acm^{-2}$ is demanded. As such values are already comparable with the values obtained for the

Y—Ba—Cu—O superconductors, the real possibility of practical application of HTS exists. The decisive factor for the victory of new materials will be economy, as it occures that the high-temperature superconductor can be competitive, with the respect of prize, with classical superconductors, in low as well as in high temperature. (Fig. 1).

The high-temperature superconductors can cause revolution in the superconductors technology. Their common use is widely planned in the new generation computers based on the switching elements using the Josephson phenomenon. It is possible that in the rearest future the HTS will replace the classical superconductors in the large scale plants.

The significant technological problem is to obtain the possibly dense and fine grained superconducting materials with reproducible microstructural parameters. The high apparent density is one of the basic conditions in this respect. The material should be free from large inter-grain as well as intra-grain pores. The distinct problem is to obtain the ceramic material with small grains, not larger than 10 μm. The exemplary microstructures are shown in Fig. 2.

At present it is generally agreed that the basis of superconductivity in ceramics is their crystallic structure. For the La—Cu—O and as well as for the Y—Ba—Cu—O materials the superconducting phase is orthorhombic in structure. The recent investigations of the La—Ba—Cu—O system demonstrate that two superconducting phases appear in it [5]. Those two phases are: the $La_3Ba_3Cu_6O_{14+x}$ phase and the well known composition "1,2,3", which, from a series of continuous solid solutions. The first ceramic superconductors had mainly the perovskite structure, that was common with such materials as $BaPb_{1-x}Bi_xO_3$ which is a regular perovskite. For the La—Cu—O materials the structure has been described as an intermediate one between a perovskite and NaCl [6], where layers of copper oxide sheets are the only bonding regions for the of Cu and O ions. (Fig. 3).

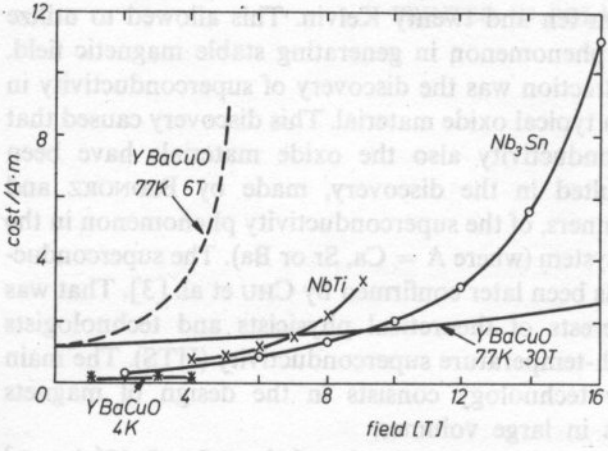

FIG. 1. Worth whileness coefficient of Y—Ba—Cu—O and conventional superconductors.

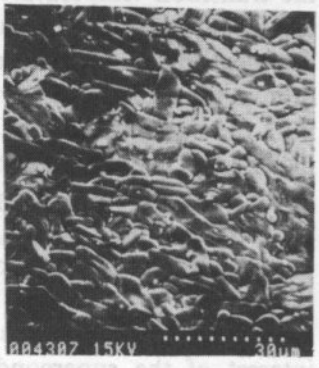

FIG. 2. Example of microstructure of Y—Ba—Cu—O superconductor. Electron scaning microscope. Opton.

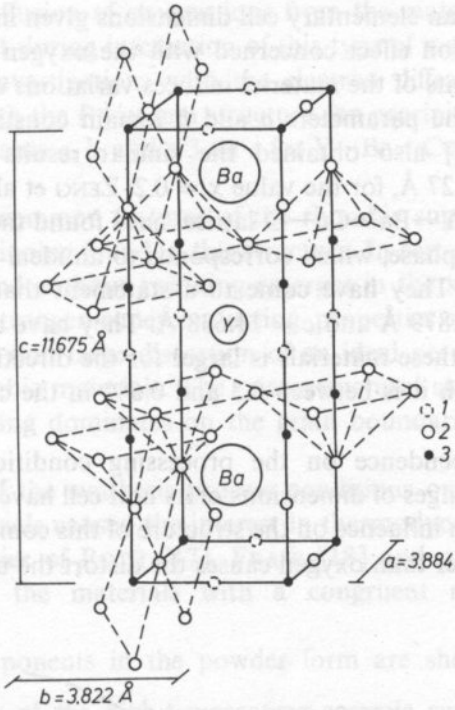

FIG. 3. The orthorhombic perovskite structure Y—Ba—Cu—O 1-vacancy, 2-oxygen, 3-copper.

The superconducting phase in the Y—Ba—Cu—O system deviates even more from the ideal perovskite structure. The oxygen consists in $YBa_2Cu_3O_x$ which could be ideal in respect of superconductivity was found to be $x = 6.95$–6.98 [7]. However the basic cation coordination in the structure corresponds to the structure of K_2NiF_4, structure despite the less than ideal oxygen content for the perovskite structure. In this case the rare earths ions exhibit the 8–fold coordination more frequently than the 12–fold one, barium ions have the 10–fold coordination instead of the 12–fold one, Cu^{2+} ions have the 5–fold coordination instead of the 6–fold one and Cu^{3+} ions have the 4–fold coordination instead of the 6–fold one. Description of the structure of these materials together with their superconducting properties indicates that in their structure the Cu_2O sheets are formed and numerous Cu—O—Cu—O chains are placed along the elementary cell axis [6]. Evidence of the laminar structure of the superconducting phase has been demonstrated by J. MELMED [8] by field image microscopy.

Structural analysis of the superconducting phase in the Y—Ba—Cu—O system ($YBa_2Cu_3O_{7-x}$) demonstrated that it can be classified as belonging to the Pmmm space spatial group with $a = 3.8185$, $b = 3.8856$ and $c = 11.6804$. It has been shown that the variations of the lattice constants are: $a = 3.8185$–3.839, $b = 3.883$–3.908 and $c = 11.64$–11.753 Å [9, 10, 11, 12, 13, 14].

The fluctuations of an elementary cell dimensions given in the literature are due mainly to the deformation effect concerned with the oxygen contents, Linang has stated that heat treatments of the material induces variations of all three dimensions of an unit cell, and if the parameters a and b remain constant, then the value of c increases. KHAN [15] also obtained the similar results $Sr_xLa_{2-x}CuO_y$ with $a = 3.775$ Å and $c = 13.27$ Å, for the value $x = 0.2$. ZENG et al. [16], in their studies on the distortion of the Y—Ba—Cu—O lattice, have found the critical phase, which corresponds the critical phase, which corresponds to an ideal orthorhombic layered perovskite $a = b = c/3$. They have come to a statement that the unit cell for the critical phase was $a = 3.879$ Å and $c = 11.638$ Å. They have also observed that the degree of distortion for these materials is larger for the direction $a(-1.3\%)$ than in the direction b, for which it is between 0.3 and 0.6% in the case of the least stable one-component system.

The structures dependence on the processing conditions used to produce $YBa_2Cu_3O_\delta$ and the changes of dimensions of its unit cell have been observed during the studies on the oxygen influence on the structure of this compound. Heating in the air or in atmosphere other than oxygen causes the distort the unit cell, what gives an

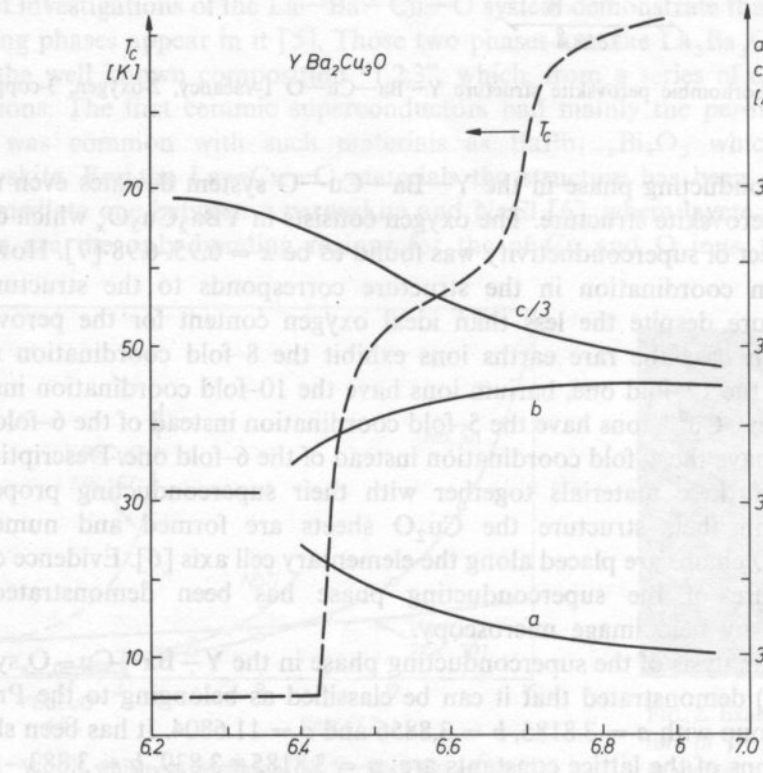

FIG. 4. The dependence T_c and lattice constants a, b and c/3 on δ for Y—Ba—Cu—O.

indication the rapid diffusion of oxygen ions from the material takes place. It has been also observed that during interaction of this type of material with an intensive electron flux, in the investigations with the electron diffraction method, a pseudo-tetragonal phase with the $P4/m\ mm$ structure can precipitate. The dependence of T_c and the lattice constants a, b, and $c/3$ on σ for Y—Ba—Cu—O has been shown in Fig. 4.

One of the basic common features of the rhombic superconducting phases of this system is heavy twinning found in this structure. In certain conditions, when the rhombic phase with and without twinning emerges in the specimen, in the greatly twinned regions the stronger superconducting properties are usually found. The twinning is concerned with large distortion of an ideal perovskite structure and is common in orthorhombic materials. The microstructural studies of these materials demonstrate that twining dominates on the grain boundaries during the sintering process.

Large influence of the synthesis process conditions on the final properties of superconducting materials caused the interest in thermodynamics of phase systems. According to the studies of ROTH [17], FRASE [18] and others, the $YBa_2Cu_3\ O_\delta$ "1,2,3" materials are the materials with a congruent melting point (melting temperature).

The starting components in the powder form are shown in Table 1.

2. Technology of the high-temperature ceramic superconductors

2.1. The solid phase reaction method

The investigations, carried out in the last years, on a new class of ceramic materials in the system: yttrium, barium and copper oxides, with the high transition temperature, demonstrated that this temperature depends on the relation $Cu^{3+}:Cu^{2+}$. This relation is strongly conditioned by the technological procedure used in producing this type of ceramic. In general, the ceramic superconductors can be manufactured in two ways: by the reaction in the solid phase or by the co-precipitation method. A typical technological procedure in the case of generation of the $YBa_2Cu_3O_{7-x}$ compound includes a number of following stages. The molar proportions of the yttrium oxide, Y_2O_3, barium carbonate $BaCO_3$ and cuprous oxide CuO are weighed and then mixed intensively in the ball or vibrating mill. The mixture of powders is then pilled with a small pressure about 100 bars and burned in the temperature 950°C for several hours in the atmosphere with higher oxygen content. The obtained sintered material is once again pulverized, pressed and burned. The optimal conditions are obtained for burning in 950°C for 24 hours in the oxygene flux. Also cooling the specimen after burning is an important factor. Slow cooling of the stove e.g. 1.5°C/min and keeping in the temperature of 650°C is applied. The influence of the subsequent stages of the synthesis of ceramic superconducting materials on their properties can be displayed in form of a diagram. (Fig. 5) Below, a detailed description of the method of obtaining $YBa_2Cu_3O_\sigma$ with the solid phase reactions method will be given [20].

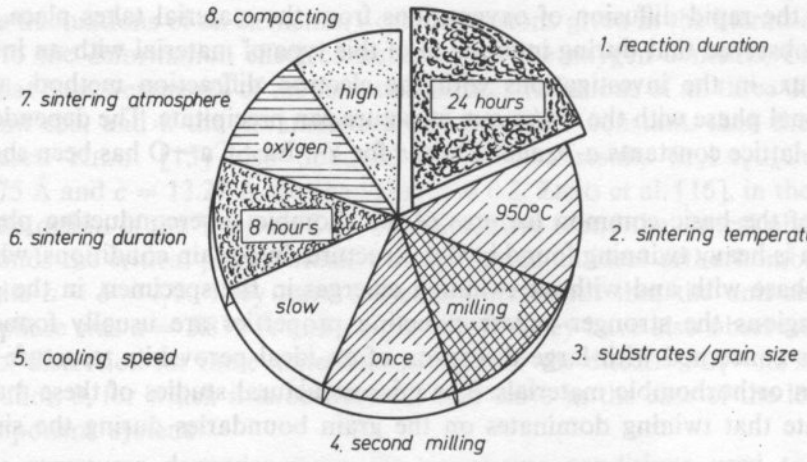

FIG 5. The influence subsequent stages of the synthesis of ceramic superconducting materials on their properties

To make a 30 g specimen of $Y_1Ba_2Cu_3O_\sigma$ the following substrates have been used:

$$Y_2O_3 - 6.11 \text{ g}; \quad BaCO_3 - 27.37 \text{ g}; \quad CuO - 12.92 \text{ g}.$$

The mixture of this quantity of substrates generatees to obtain as a final product the oxide mixture with the stechiometric relation 1–2–3. Attention must be paid to that the substrate should be weighed free from humidity.

Table 1

powder substrates		
material	molecular weight	producer
Y_2O_3	225.8	Aldrich Chemie Co.
BaCO	197.4	Aldrich Chemie Co.
CuO	79.5	Chem. Inc.

The basic technological operation is keeping the specimens in oxygen. The specimens are seasoned in oxygen in the temperature 500°C for 12 hours. The oxygen rotameter should indicate the flow 0.2 m^3/h. For the $Y_1Ba_2Cu_3O_{7-x}$ compound with the stechiometry "1–2–3" the maximum oxygen absorption occurs at about 500°C. This temperature for $Y_1Ba_2Cu_3O_{7-x}$ is below the temperature of transition of the tetragonal structure to the rhombic one, which equals 750°C. The high-temperature superconducting phase is, in principle, conform with the rhombic phase.

After having reasoned the specimens in 500° C for 12 h we switch off the stove and leave the specimens inside, while leaving the oxygen flux on until the temperature decreases down to the ambient temperature. The oxygen flux intensity should remain the same as during seasoning, i.e. 0.2 m^3/h.

After taking the specimens out from the store they should be kept in an oxygen exsiccator in the room temperature. Water causes decay and damage of the specimens.

Among the numerous factors which determine the specimen quality, attention should be paid to the five most important ones. These five quality factors are:

- stoichiometry
- mixture homogeneity
- sintering temperature
- oxygen contents and ordering
- cooling intensity

2.2. The method of co-precipitation

In the co-precipitation method the starting point are the substrates in the form of the solution of nitrates from which the mixture of appropriate carbonates is precipitated. The carbonate suspension is then filtered off and heated to remove water. The further procedure is the same as the one applied in the method with the solid phase reaction.

The advantage of the co-precipitation method over the solid phase reaction method is that if an additional, chemical stage of synthesis is included then the stoichiometry of the planned solid phase is known, because the components are mixed in the molecular scale in this case. In respect of this mixing homogeneity it is more probable that only the synthesized solid monophase will emerge and no other "contaminating" phases will be formed. The quick preparation method by the solid phase reaction gives the measurable composition inhomogeneity, despite the mixing and milling stages. This inhomogeneity can favour the forming of additional, contaminating phases.

The two other kinds of co-precipitation methods have also been worked out: the citrate and the oxalate methods. In each of these methods the process starts from the substrates in the form of nitrate powders solved in water. Then, in the citrate method, in primary co-precipitation the citrate acid and the ethylene glycol is applied in place of Na_2CO_3 used in the carbonate method. In the oxalate method as the precipitating agent the calium oxalate is used. In the application of both co-precipitation methods close attention should be paid to the process control, especially in the oxalate method in which the pH must be precisely regulated and it must be seen to that the double salt should not be formed.

A large problem, which appears in sintering the materials with smaller contents of rare soils [4], is the formation of a liquid phase in the temperature 950°C. It is known that despite the improvements of sintering conditions, the liquid phase worsens the properties of superconducting materials. HUANG et al. [4] stated that the liquid phase that covers the grains of the superconducting phase can really lower the superconducting properties. Similarly, Guba established recently that prolonging the

sintering in 950°C results in forming an eutectic liquid phase which tends not only to noisten the grains of the sintered ceramic, but also the crucible walls [19]. Huang observed also that the liquid phase caused the grain growth in these materials. In connection with the problems concerned with the liquid phase formation in 950°C and with poor sintering characteristics of there materials, i.e. the attained relative densities about 70–80% for pressure-free sintered compacts, their structural and chemical properties can not be considered separately. Indeed, the results of the applied sintering method as well as the gas atmosphere interaction strongly influence the superconducting properties. However, it should be underlined that the formation of the second phase is influenced by both thermal conditions and chemical constitution of the substrates.

In obtaining materials exhibiting the beginning of rapid resistance change by 53% in the temperature 260 K and the end about 240 K (Fig. 6). NARYEN et al. [21] identified the presence of a second phase in which $c = 13.55$ Å and which locates itself mainly the grain boundaries in the sinter. Conditions of synthesis of these materials include sintering in 960°C in oxygen for 12 hours what should gave the formation of an eutectic liquid phase in the regions where, in spite of mixing and

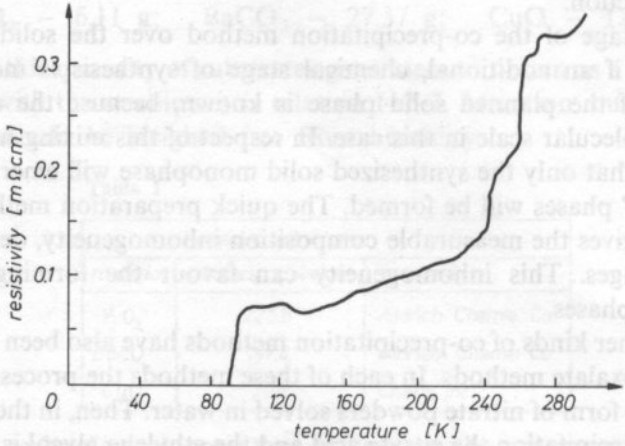

FIG. 6. Resistivity as a function of temperature for a material which exhibited unreproucable anomaly of resistivity at 260 K before reverting to the superconducting phase material

calcination in 900°C, the material is poor in Y and Ba. As the phase which emerges at the grain boundaries, which is responsible for the dramatic resistance decrease, was instable when subjected to heat cicles or to nucleation and transformed into a superconductor with $T_c = 90$ K, then also the influence of soaking in oxygen and cooling speed should be studied. The material which exhibited thee largest resistance decrease – by 50%, also shown the superconducting properties concerned with the phase at grain boundaries, with the volume contents of this phase equal to 0.3% [21].

The relation between superconductivity and oxygen contents and ordering in the considered materials was one of the earliest observations since their structure has been discovered. It has been found that the ordering of occupied positions in the plane Cu—O is strictly connected with the high-temperature superconductivity. Even if these positions are occupied only in one fourth, the $YBa_2Cu_3O_{7-x}$. ($x = 0.4$), can be a superconductor in 55 K as long as the occupied positions are ordered. In the opposite case, the material is tetragonal and is a superconductor. If the considered are occupied in half and ordered than the critical superconductivity temperature increases to 90 K [23], the rhombic structure is deformed and twinning takes place. Superconductivity in the materials La—Sr—Cu—O has been demonstrated by TARASCON [24] and its nature is very close to that of the Y—Ba—Cu—O materials. The loss of oxygen from the Cu—O planes destroys superconductivity in these materials. Discurring oxygen restoration in this plane, Tarascon describes oxygen reintercalation. The concept which assumes that the material is intercalated with O_2 is widely accepted because it explains the violent O_2 movement in the material and its influence on the physical phenomena. The proofs for the influence of the slow cooling on the oxygen contents and superconductivity have been presented by GOPALAKRISHNAN et al. [12]. If the sintered ceramics is slowly cooled with 0.1 K/min down to 850°C and 24 K/min down to 400°C then the transition temperature equal to 106 K is obtained. This temperature has been observed for a material which in normal process conditions has the transition temperature 95 K. Another her experiment with slow cooling, 1 K/min, has been carried out by NARAYAN et al. [21], but his specimens were probably overheated while sintering. The abnormalities observed in his material in the temperature 240–260 K were not due to the slow cooling of the specimens. Finally, oxygen in excees $\delta = 7$ influences the saturation of the CuO_2 plane, causes the electrostatic load breakdown through an expanded elementary cell and changes the Ba, Cu and Y coordination. The net effect is the transition into an isulator as it has been previously described.

In the first reports on the discovery of 90 K superconductors formed from the rare earths oxides, it has been said that these materials could be synthesized from ions of the majority of rare earths, irrespective of their magnetic moments. This seems to be in contradiction with the generally accepted theory of superconductivity. It has been established that three rare earths ions adversely affect the superconducting properties of these materials: Ce, Pr and Tb. The first two were not able to form a superconducting compound in the experiments carried out by MCKINNON et al. [25] and the compound containing Tb in place of Y can not exist. Replacing Y by other rare earths had the influence not only the crystallographic structure of the material, but also on its critical temperature. The relation of resistance to temperature for this group of compounds has been shown in Fig. 7 [41, 42]. McKinnon has demonstrated that the addition of rare earths to $La_{16}Sr_{02}CuO_{4-x}$ not larger than 0.2% at did not destroy superconductivity, in spite of the existence of magnetic moment. However, the synthesis temperature changed: it was the lower the larger was the lower the larger was the atomic number of the rare earth element.

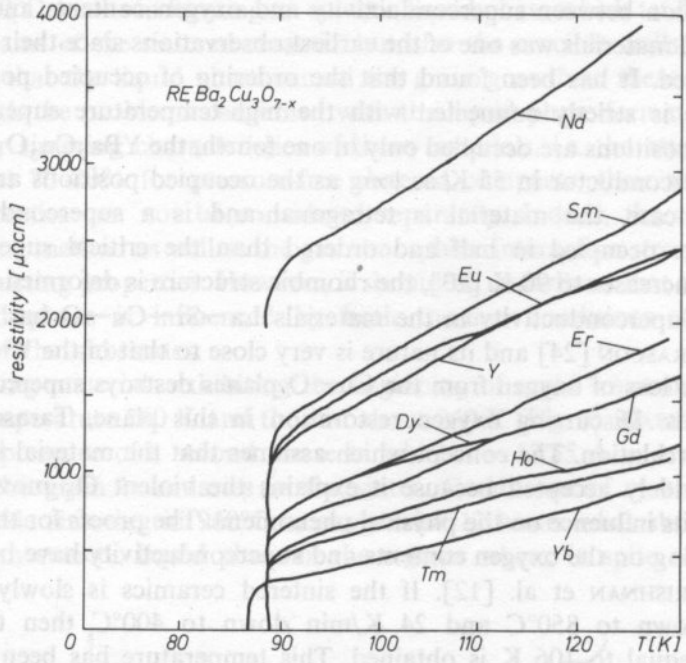

FIG. 7. Resistivity as a function of temperature for the $YBa_2Cu_3O_{7-x}$ perovskite, in which yttrium has been replaced by rare earths cations [42]

Another change which takes place as a result of replacement of the rare earths elements to the considered structures is the influence of the magnetic field on superconductivity. NEUMEIER et al. [26] have demonstrated that by replacing Y with Tm in the "1,2,3" compounds one obtains the materials which are less sensitive to external field.

Replacing copper by bivalent as well as trivalent cathions gains large interest. The primary aim of such investigations was better understanding of the role of Cu—O chains in the links of Cu—O planes, and estimation of the range inside which the dimension and elastic properties of the Ba atom have any influence on the semiconductor transition and the critical current in the new superconducting compounds. The studies carried out by TARASCON et al. [27] demonstrate that in $La_{2-x}SrCuO_4$ the replacement of 0.025 at % Cu by Ni results in the transition temperature decrease from 40 to 22 K. Further increase of Ni concentration leads to lower transition temperatures. The cause of these effects in the disorder introduced to the structure due to the changes of ion magnitude, changes of the oxidation degree of copper and even the possibility of destroying the magnetic couples by a magnetic Ni ion. The substitution by cobalt also reduces superconductivity. The replacement carried out by TARASCON et al. in the $YBa_2Cu_3O_\delta$ materials was limited to Ni. In this case the main difference was the substitution $x = 0.25$ and $x = 0.50$ for

$YBa_{3-x}Ni_xO_\sigma$. It gave the similar results, i.e. lowering the transition temperatures.

Other studies [28] in which Cu was substituted with Co and Fe in $YBa_2Cu_3O_\delta$ led to semiconducting materials. When Co was substituted, what led to Cu_3—Cu_2Co, the oxygen contents in this material correspond to $\delta = 7.25$. If Fe was substituted, what led to Cu_3—$Cu_{2.5}Fe_{0.5}$ oxygen contents in the obtained material corresponded to $\delta = 7.15$. Oxygen concentrations lower than $O_{6.7}$ for Co and $O_{6.4}$ for Fe gave disintegration of the respective materials. In the discussed works only the set containing $Cu_{2.963}O_{0.037}$ had the rhombic structure. The tests of single crystals of the "1,2,3" materials carried out by COLLIN et al. (not published) demonstrated the presence of rhombic highly twinned crystals with vacances in Cu positions. According to calculations, the Cu defficiency reached 8%, what has been confirmed by other authors. The reason of this deficiency in these single crystals could be the heating over 940–950°C, which is the temperature range corresponding to the thermal stability threshold of the "1,2,3" phase. Collin reports this as a reason why the green tetragonal phase is usually bound with a powder from which single crystals issue (Fig. 8). The Meissner magnetic effect for materials substituted with Ag

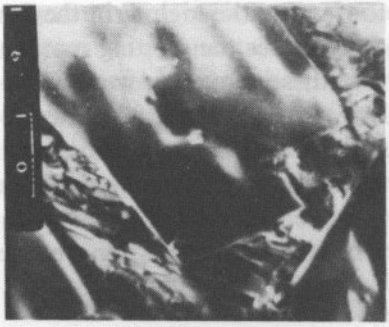

FIG. 8. $YBa_2Cu_3O_6$ crystals which emerged during cooling the alloy, usually crystalizing together with the so called "green" phase "211"

indicates that the 0.7% admixing leads to reducing the superconducting part in these materials [29]. Lack of influence on the transition temperature has been ascribed to nonhomogeneity of the materials, so that the superconductivity in mass was not changed even though some regions of a specimen were superconducting. Trials were also made to substitute Ba in the YBa_2CuO materials. In particular, the substitution of Ba with Sr in $YBa_{2-x}Sr_xCu_3O_4$, for $x = 0.2$; 0.5; 0.75; 1.0; 1.25; 1.5 and 2.0 has been studied. The effect has the continuous decrease of transition temperature in this material, together with the increase of Sr contents. Also the resistance over the critical temprature increased continuously. VEAL et al. [30] stated also that the lattice parameters b and c decreased together with the increase of Sr concentration.

M. F. YAN et al. [31] also worked upon the materials with variable Ba and Y contents. He concentrated mainly upon the materials with Ba as well as Y excess, or with only Ba excess. Because the applied substrates gave multiphase specimens after sintering, it has been stated that it was difficult to correlate the high transition temperatures with the material phases. The possibility of having superconducting

properties has been ascribed to the phase which emerged at the grain boundaries of four different phases in the specimens with the $Y_{4.1}Ba_{2.51}Cu_1O$ composition. The reason why it has been assumed that the phase at grain boundaries is probably a superconductor results from the measurement of diamagnetism which indicate that for 0.3% of the specimen the starting point of transition is in 550 K and that for long sintering time (113 h) in 950°C the "1, 2, 3" phase could pass to solution and precipitate at the grain boundaries of other phases formed during the cooling process. The superconducting phase at the grain boundary, observed also in other investigations, can give satisfactory explanation of the large resistance drop with the temperature decrease in such materials which should be classified as insulators.

The papers where the studies on introducing the F and Cl anions are described report that in partial substitution high T_c temperatures are obtained (more than 200 K). Investigations carried out in Energy Conversion Devices have indicated that the implementation of F to the material generates the oriented crystal growth, as it has been reported by Ovshinsky and Young. They have obtained the start of T_c in 265 K and zero resistance in 148 K for YBa_2Cu_3O treated with the ions of F with the parameters 180 keV and 1×10^{15} ions/cm^2 [4]. At the same time the attempts of confirming the high T_c in these materials reported by YAN [31] with the use of BaF_2 or $BaCl_2$ as the starting materials gave 91 K as a result. It has been also found out that these materials were multi-phase and contained the grains of CuO, $BaCl_2$ or BaF_2. In the "1, 2, 3" material Evibil studied also the use of BaF_2 as one of the substrate powders. In one, nonreproducible specimen he found a certain proof of transition to the superconducting state in the temperature 260 K. This transition remained in the specimen of the approximate contents $YBa_2Cu_3O_5F_2$ even after a couple of months of the specimen's life.

3. Microstructure of the high-temperature superconducting ceramic

The superconducting ceramic made from diverse compounds is the multi-phase material. One of the phases which should always be taken into consideration in the analysis of acoustic waves propagation is the gas phase contained in the open or closed pores. The acoustic properties of superconducting ceramic we influenced not only by the more value of porosity but also by its statistical parameters, such as pore diameters distribution, pores geometry, i.e. shape and mutual displacement, as well as volume shaves of different phases. The same remarks, although to smaller extents refer to the crystallic phases. In Fig. 9 the shapes of the pores in ceramic materials have been shematically shown.

The process of sintering and recrystallization leads to the decrease of porosity of the whole bath. In general, the increase of sintering temperature leads to deterioration of small pores with irregular shapes and to formation of spherical pores, mainly as a result of the tendency to minimize the free surface of the system. The histogram of pore dimension have the Poisson distribution. However, it should be taken into

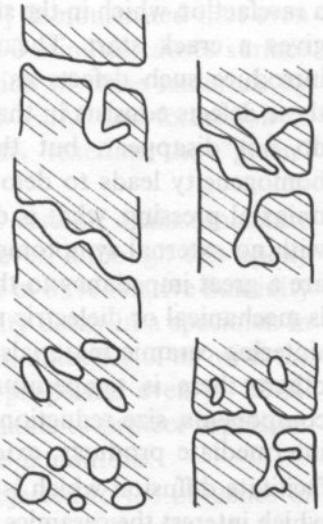

FIG. 9. Shape of pores found in ceramic materials

account that because of the complexity of pore shapes the microscopic studies not always give completely reliable results. In the microscopic measurement of absolute porosity the surface distribution of pore diameter does not correspond to the volume distribution, which is significant in calculation of mechanic stress fields, electric fields and acoustic wave propagation parameters. These problems have been solved in a number of papers and experimentally verified in a variety of ceramic materials and sintered metallic powders.

In general, the relation of elasticity modulus to absolute porosity is [40]:

$$E = E_0 e^{-kp}$$

where: E – porous materials elasticity modulus, E_0 non-porous material elasticity modulus, p – porosity, k – constant.

For the superconducting ceramic $YBa_2Cu_3O_{7-x}$ it has been found that the relation of the modulus to porosity has the form [40]:

$$E = E_0(1-p)^3$$

An equally important parameter for the acoustic properties of a specimen are the microstructural parameters of the solid phase, which include: dimension and shape of grains, type and shaves of different crystallic phases and glass, and the material texture. These parameters are dependent on all the technological operations. In the process of preparing powders an important operation is milling, which should lead to destroying the agglomerates of substrate materials and to precise mixing of the whole bath. If the process of preparation leaves the non-disintegrated grain agglomerates, the rigid configuration of these forms can be left uncharged in the process of pressing the powders. The non-disintegrated aglomerate can be

a rarefaction which in the sintering process, develops into a pore or a lamination that gives a crack start. The next technological operation, i.e. powder pressing can introduce such defects as density inhomogeneity or laminations. Noxiousness of these defects consists in that in the sintering process it is not only that those defects do not disappear, but they rather grow bigger. For example the density inhomogeneity leads to deformation of the specimen or to wide cracks especially in uniaxial pressing, what is due to different contractions in sintering. Invisible cracks with no external symptoms of deformation are much more dangerous. These cracks are a great impedancy to the specimens, for which the basic exploitational condition is mechanical or dielectric resistance. A number of factors influence the corectness of sintering ceramic materials and the concerned mass transport mechanisms. Among others there is temperature and time of sintering, crystal lattice defects in the components, size reduction and initial grain system geometry, formation of reactive intermediate products, external pressure and sintering atmosphere. Lattice defects facilitate diffusion which is the main mass transport mechanism. In the oxide links, which interest the ceramics researchers, a typical lattice disordering is an easy formed solid solution. Also the presence of a liquid phase interact with the sintering process. Depending on the amount of the liquid phase and its ability to moisten the grains one obtains different sinter structures. With a large volume shave of the liquid phase, which ensures filling the inter-grain spaces, there exists a possibility of completely eliminating porosity. Finally, the output sinter structure is formed by recrystallization. This process is concerned with the movement of grain boundaries which leads to minimization of the free surfaces of the system and is related to eliminating small grains in favour of the large ones. The basic technological problem at this stage of the process is not to allow the pores to detach from the grain boundaries and to remain behind the moving recrystallization front. This would lead to the intra-grain porosity, which is practically unremovable.

As it has been mentioned above, pores change the acoustical properties of the tested material. An equally unprofitable phenomenon engendered by recrystallization is a discontinuous grain growth. As its consequence in the microstructure the large grains emerge, the dimensions of which are larger than those of an average grain by one or to orders of magnitude. Grain boundaries of such large grains also cause the changes in velocity and damping of ultrasound waves, with respect to a medium without such boundaries.

4. Degradation of properties in ambient conditions

The greatest threat in application of the $YBa_2Cu_3O_\delta$ superconductors is their sensibility to moisture. This problem is particularly vital in all those measurements where it is necessary to cover the superconducting specimens with metallic films. The

introductory studies on this problem pursued by YAN [32] demonstrated that even air with 85% rh at 85°C interacting with a specimen for 90 minutes causes surface amorphization of the Y—Ba—Cu—O ceramic. Degradation of these materials by H_2O is caused by reduction of a trivalent cation Cu^{3+} to Cu^{2+} and formation of $Ba(OH)_2$ with the evolution of O_2. Further, after this reaction the "green" polycrystalline ceramic phase and CuO formed.

Barns and Landise tried to protect the Y—Ba—Cu—O ceramic against moisture influence by applying 0.5 mm thick epoxy coating. However, although this epoxy coating should protect against moisture, the influence of air of 85% relative humidity in the temperature 85°C for 70 min causes superconductivity decay in a specimen in 77 K, while a specimen not protected by a coating under an influence of air with the same parameters for 50 min looses its superconducting properties even in 22 K. Barns and Landise anticipated that their method would enable to protect superconductivity for 1000 h in room humidity and temperature conditions.

There were also tests in which the materials were subjected to the influence of air with relative humidity 100% and temperature 23°C. These tests demonstrated the formation of $Cu(OH)_2$ and $BaCO_3$, (probably as a result of noncomplete removal of CO in sintering) even after exposure for 3 h. The main effect of such interaction of air saturated with vapour was the formation of an amorphous layer. In this case the time of saturation was 120 h. The amorphic layer formed during this time inhibited further decay reaction in the material.

KARIOS and VANCE [4] found out that in the temperature 21°C the sulphuvic acid of pH = 1.2 completely dissolves the superconducting ceramic in 2–4 minutes.

TROLIER et al. [33] studied the influence of various solvents on the Y—Ba—Cu—O ceramic surface. They found that for short exposure times at 25°C in the solvents Cu can be found. Aromatic solvent have the tendency to form surfaces richer in Y while alcohols created Y–deficient surfaces in relation to Cu concentration. Isoamyl alcohol caused the complete decomposition of the superconductor, with CuO, $BaCO_3$ and a phase containing yttrium as products. Similarity, the decomposition of superconducting ceramic was caused by the acetic and formic acids. In the Fig. 10 the diffractograms of layers formed at the surface of $YBa_2Cu_3O_{7-x}$ ceramic under the influence of various solvents.

An alternative technology of protecting the superconducting materials has been described by MANKIEWICZ et al. [34]. He has stated that the layers of Y, Ca and BaF_2 formed with the vapour deposition technique before the oxidating heating are resistant to water. This suggests the possibility of manufacturing and storing the layers vapour deposited with fluoride and then doing the oxidating heating, i.e. before hermetization in the appropriate glass, metal or organic containers used in many practical applications.

The superconducting materials are also sensitive to electron or neutron bombardement. CLARK et al. [35] demonstrated that the inpingement with the by O ions doses of 1.1×10^{14} ions/cm^2 completely destroys superconductivity in these

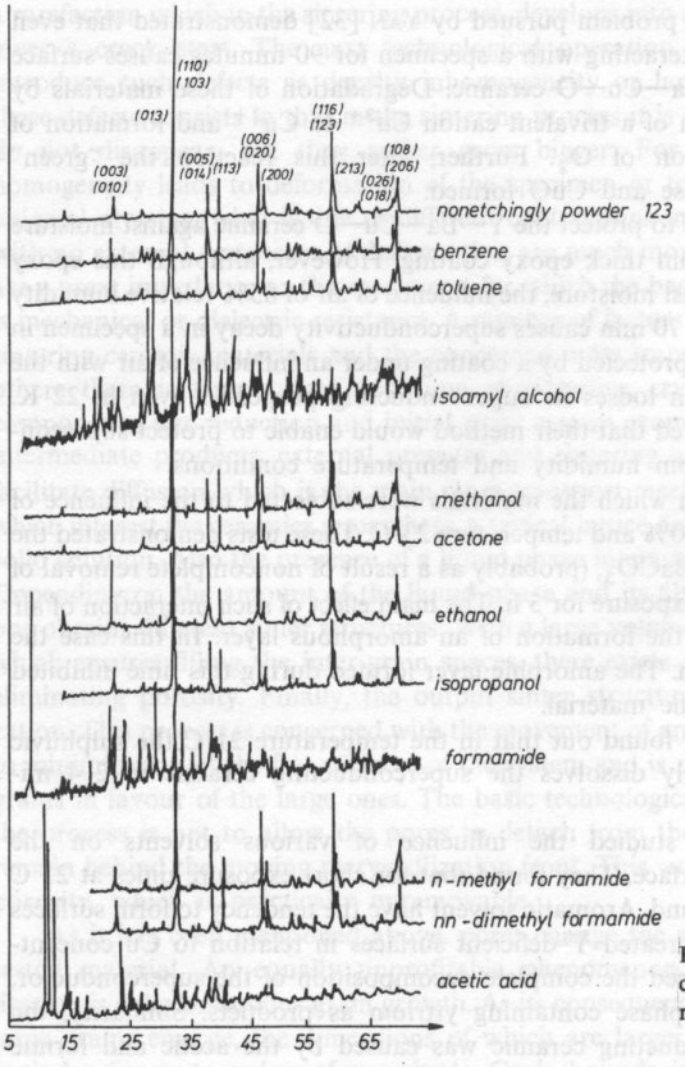

FIG. 10. Difractogrames of layers creating on surface $YBa_2Cu_3O_7$ as result interactions different solvents

materials. Also the ion flux with the intensity of 10^{13} ions/cm^2 initiates the loss of superconductivity.

The mechanism of superconductivity destruction resulting form the emergence of oxygen ions in the lattice consists in the reduction of vacancy ordering degree and in the transition from twinned orthorhombic structure to an amorphous material, after surpassing the threshold density of point defects [35, 36].

Irradiating the superconducting ceramic with a neutron beam has a relatively less destructive influence on the properties of these materials. Interaction of a neutron beam of the intensity 1.3×10^{18} n/cm^2 with a $La_{1.85}Sr_{0.15}CuO_y$ causes only the reduction of the critical temperature to 27 K [37].

KUPFER et al. [38] after having investigated the $YBa_2Cu_3O_7$ ceramic irradiation

with neutrons found out that the radiation intensity for these materials shouldn't exceed 5×10^{17} n/cm^2. A neutron flux with intensity equal to 6×10^{18} n/cm^2 lowers the critical temperature by a half. The results of studies of the influence of irradiation, which demonstrate loss of superconductivity of a superconducting ceramic, indicate that the perspectives of application of these materials in applications producing a high neutron flux as e.g. Tokamak, or with high-energy particles, as e.g. in the super-collider superconducting accelerators, can be problematic.

However the effective application of superconducting materials in the heavy particles environment can be improved by screening. In electronic applications the γ and X radiation can be more dangerous. BOHANDY et al. [39] found out, that the γ and X radiation, within the limits of experiment errors, does not interfere with the superconducting properties of the material for the intensities up to 1.3 Mrad. They have also found out that this radiation results in electron excitation and not the excitation of ion structure, so that the electrons return to the initial superconductivity state after the radiation emission stop.

From the above carried out review of problems concerned with manufacturing the ceramic oxide superconductors the sources of difficulties with the appropriate choice of the methods of measuring their properties clearly arise. These are connected with large sensitivity of the oxide superconductors to influences of typical organic investions and oxide solutions. The use of these reagents (in rinsing or submerging of metal coatings) can result in dissolving the measured layers. For these reasons, the acoustic methods, in particular those which do not necessitate for coating the durable contacts, can find wide application, especially in testing new superconducting materials of unknown properties.

5. Thin-layer superconductors technology

Most of the structural defects in ceramic superconductors of larger thicknesses, which have been described above, can be avoided by using thin HTS layers in acoustic measurements. There are several methods of coating: chemical, laser, and the most frequently used method of magneton spatering [43, 44]. The magneton spatering with the constant current method is done in the room temperature. As a target an element made at pressed superconductor powder is used; as a base the strontium titanate $SrTiO_3$ zirconium oxide ZrO_2, magnesium oxide MgO, galium lantanate $LaGaO_3$, aluminium lantanate $LaAlO_3$, and lithium niobate $NbLiO_3$ are applied. Coating is carried out at the pressure 0.01 Tr and with the coating speed 45 A/s. The layers can have high resistivity and then should be subjected to a heat treatment. They undergo quick heating up to 925°C in 5 minute time, in a helium atmosphere. Then, they are slowly cooled for 2–3 hours in the oxygen flow. The specimens obtained in this way are tested for surface homogeneity in a scanning microscope. The obtained 1, 2, 3 – compound microstructures in form of a thin layer coated on a ZrO_2 substrate are shown in Fig. 11.

The resistivity of the layers as a function of temperature has been measured. The current characteristic vs. temperature for a 1, 2, 3 layer coated on a base is displayed in Fig. 12. A sharp resistivity drop in 91 K, with the transition width below 3 K (10–90%) is observed.

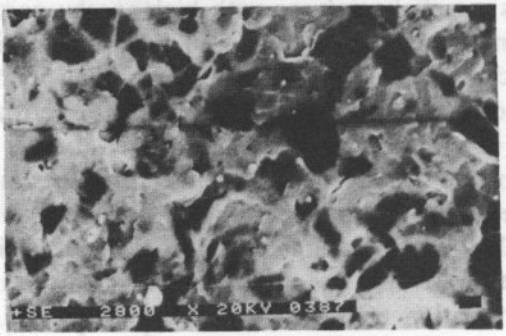

FIG. 11. Image of the 1, 2, 3 compound thin layer spreaded on the zirconium oxide

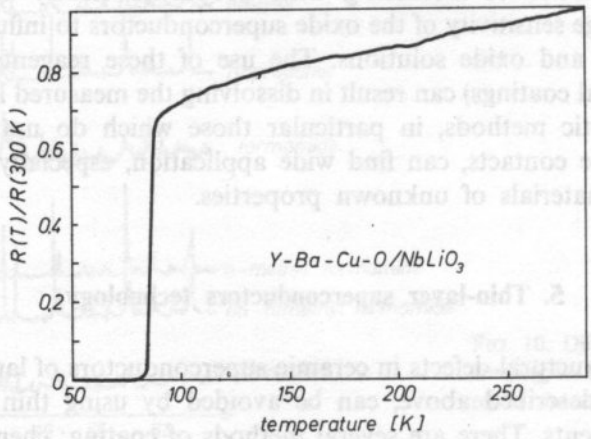

FIG. 12. Resistivity-temperature characteristic of the 1, 2, 3 – type compound spreaded on the $NbLiO_3$ substrate

6. Acoustic properties of superconductors

The measurements of macroscopic acoustic wave propagation parameters in conventional superconductors have played a significant role in confirming the BCS theory [45, 46]. The BCS theory satisfactorily explains the temperature relations of damping acoustic ways in superconductors. According to this theory in a superconductor for $T = 0$ two mechanisms of damping acoustic waves are possible: quasi-

-particles excitation or dispersion on them [45]. Excitation of quasi-particles can take place only with high frequencies, i.e. with $\hbar\omega > 2\Delta$, where $\hbar$ – Planck constant, ω – acoustic wave frequency, 2Δ – superconductor energetic gap width.

The fonon absorbtion probability in the superconducting state is expressed with the following realation [48]:

$$W_s = 2\int_{\Delta}^{\infty}\left(1-\frac{\Delta^2}{E_k E_{k'}}\right)\{f(E_k)[1-f(E_{k'})][1-f(E_k)\}\, N_s(E_k)\, dE$$

where: $f(E)$ – Fermi function, E_k, $E_{k'}$ – energy of the initial and final state of transition, $f(E_k)$, $f(E_{k'})$ – Fermi functions, N_s – density of states in a superconductor.

In the case of small frequencies of an acoustic wave ($\hbar\omega \ll 2\Delta$) we obtain

$$W_s = 2\int_{\Delta}^{\infty} N_N^2\{f(E_k)-f(E_k+\hbar\omega)\}\, dE = -2N_N^2\frac{df}{dE}\hbar\omega N_N^2 f(\Delta).$$

An analogous relation for absorbtion probability can be obtained for a metal in normal state:

$$W_N = 2\int_{0}^{x} N_N^2\{f(E_k)-f(E_k+\hbar\omega)\}\, dE = 2\hbar\omega N_N^2 f(0) = \hbar\omega N_N^2.$$

By comparing the two expressions we obtain:

$$\frac{W_s}{W_n} = \frac{\alpha_s}{\alpha_N} = 2f(\Delta)$$

where α_s – acoustic waves damping coefficient in superconducting state, α_N – acoustic waves damping coefficient above the critical temperature.

In the Fig. 13 an experimental relation $\frac{\alpha_s}{\alpha_N}$ for a lead crystal obtained for frequency 10 MHz has been shown.

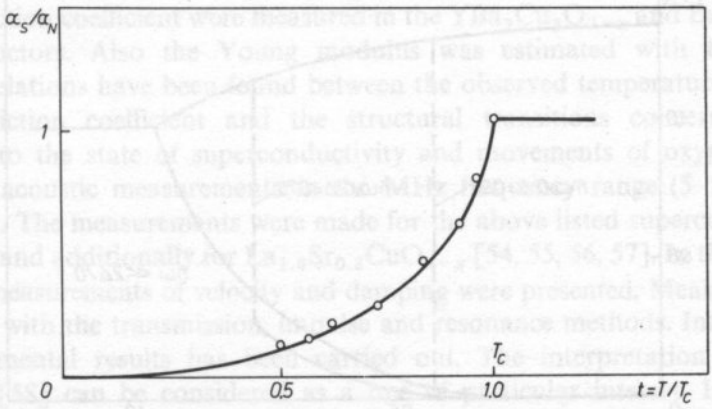

FIG. 13. Relation of the normalized atenuation to temperature for a Pb crystal. The same relation according to the BCS theory has been marked with the solid line

In the case of large frequencies $\hbar\omega > 2\Delta$ where the phenomenon of forming quasi-particles in the Cooper pairs fragmentation [18] the damping ratio is expressed with the following relation:

$$\frac{\alpha_s}{\alpha_n} = \frac{1}{\hbar\omega} \int_{-\infty}^{\infty} \left(1 - \frac{\Delta^2}{E_k E_{k'}}\right) [f(E_k) - f(E_{k'})]\, q_s(E_k)\, q_s(E_k)\, dE$$

where $q_s(E_k)$ – relative density of states $\frac{N_s}{N_N}$ equal to

$$q_s(E_k) = \begin{cases} 0 & \text{for } E_k \leqslant \Delta \\ \dfrac{|E_k|}{(E_k^2 - \Delta^2)^{1/2}} & \text{for } E_k > \Delta \end{cases}.$$

The integral in the above relation can be rewritten in the following form:

$$\frac{\alpha_s}{\alpha_n} = \frac{2}{\omega} \int_{\Delta}^{\infty} [f(E) - f(E+\hbar\omega)] \frac{[E(E+\hbar\omega) - \Delta^2]\, dE}{(E^2 - \Delta^2)[(E+\hbar\omega)^2 - \Delta^2]} - \frac{1}{\hbar\omega} \cdot \int_{s-\hbar\omega}^{s} (1 - 2f(E+\hbar\omega))$$

where the first component has been analyzed above, and the second component corresponds to formation of quasi-particles pairs and can not be calculated analytically. Numerical calculations give the results shown in Figs. 14 and 15. It can be seen on the graphs in Fig. 14 that when $\hbar\omega$ becomes larger than 2Δ by an arbitrarily small value there is a jump of damping value to a different curve.

In Fig. 15 the relation of α_s/α_N and for given values of T has been shown. For $\hbar\omega$ larger than 2Δ we obtain also the jump of damping. The above theoretical results have been confirmed in the analysis of working conditions of the supercon-

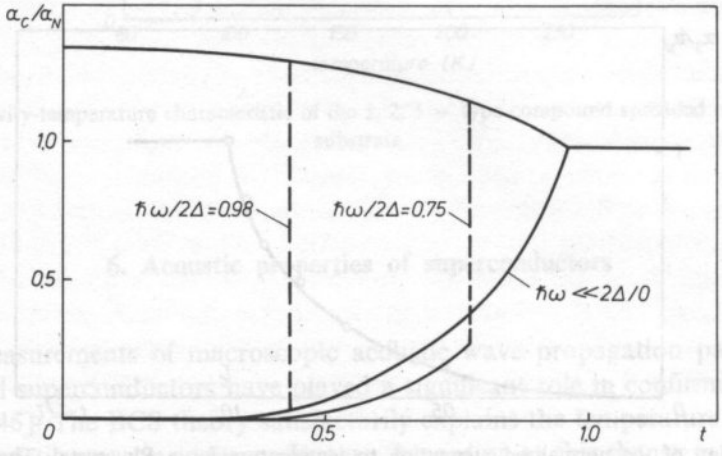

FIG. 14. Relation of α_s/α_N to temperature $t = T/T_c$

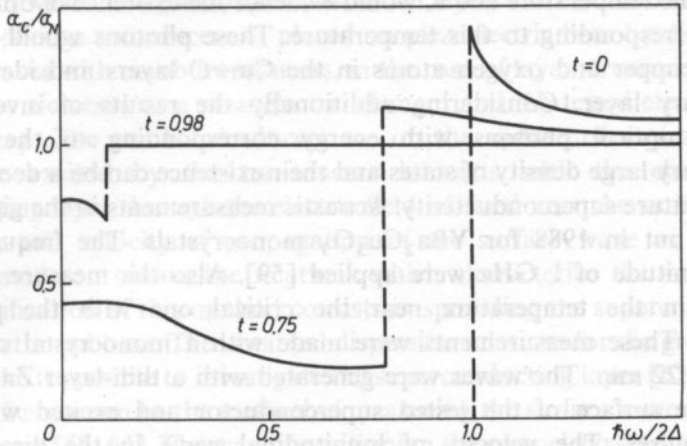

FIG. 15. Relation of α_s/α_N to $\hbar\omega/2\Delta$

ducting tunnel junctions applied as generators and detectors of hypersound tunnel vibrations [47].

Application of the hitherto discussed formulae to the description of damping acoustic waves in high-temperature superconductors is not justified, as up till now the coherent theory of high-temperature superconductivity is missing. Despite that, the experimental acoustic methods are already widely used. The reduction of damping with the decrease of temperature in the superconducting state is one of the more important proofs for that in normal metals large damping of acoustic waves is concerned with the existence of free electrons.

First acoustic measurements of superconductors were made with the frequencies of several kHz. The measurements were carried out with the resonance method for plates and disks [49, 50, 51]. With this method the resonance frequency and the internal friction coefficient were measured in the $YBa_2Cu_3O_{7-x}$ and $EuBa_2Cu_3O_{7-x}$ superconductors. Also the Young modulus was estimated with the resonance method. Relations have been found between the observed temperature peaks of the internal friction coefficient and the structural transitions concerned with the transition to the state of superconductivity and movements of oxygen vacancies. Then, the acoustic measurements in the MHz frequency range (5–15) have been carried out. The measurements were made for the above listed superconductors [52, 53, 54, 55] and additionally for $La_{1.8}Sr_{0.2}CuO_{4-x}$ [54, 55, 56, 57]. In these works the results of measurements of velocity and damping were presented. Measurements were performed with the transmission, impulse and resonance methods. Interpretation of the experimental results has been carried out. The interpretation presented by Y. HORIE [58] can be considered as a one of particular interest. He related the observed maxima of damping to the interaction of an electron and an optic photon of energy corresponding to the temperature 100 K. The similar maximum of

damping for the temperature 200 K would evidence the existence of optic photons of the energy corresponding to this temperature. These photons would be related to vibration of copper and oxygen atoms in the Cu—O layers and identical La—O atoms in every layer. Considering additionally the results of investigations in infrared, the optical photons with energy corresponding to the temperature 200 K have very large density of states and their existence can be a decisive factor of a high-temperature superconductivity. Acoustic measurements in the gigahertz range were carried out in 1988 for $YBa_2Cu_3O_7$ monocrystals. The frequencies of the order of magnitude of 1 GHz were applied [59]. Also the measurements of heat conductivity in the temperature near the critical one with the photothermal method [60]. These measurements were made with a monocrystal of dimensions $0.36 \times 0.27 \times 0.22$ mm. The waves were generated with a thin-layer ZnO transducer coated on the surface of the tested superconductor and excited with 10–20 ns electrical impulses. The velocity of longitudinal wave in the direction C was measured. In the Fig. 16 the measured changes $\Delta V/V$ near the critical temperature

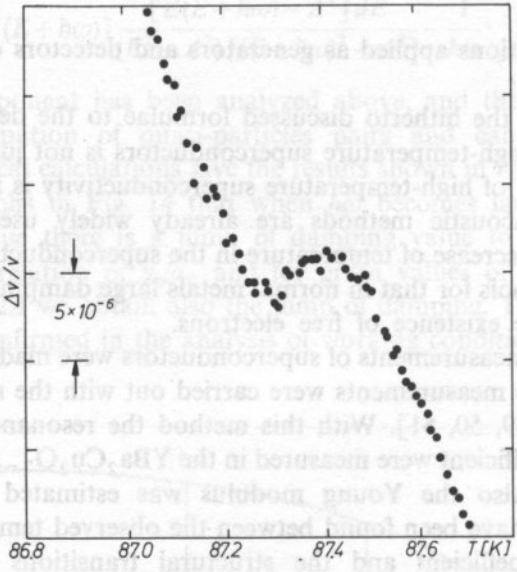

FIG. 16. Ultrasound waves travel velocity changes near the critical temperature for a 1, 2, 3-type superconductor 59

have been presented. In the work concerning the heat conductivity the conductivity increase in the temperature near to the critical temperature has been stated. The analysis made in this work relates these changes with the disturbancies of the copper atom position in the Cu—O layers [61].

It seems that more explicit measurement results can be obtained with thin superconducting layers dielectrically spreaded on the substrate. These measurements

are carried out with surface acoustic waves. Such layers can be tested in layer systems with the use of edge transducers or placed on piezoelectric base by direct excitation of acoustic waves with comb transducers, in the case of layer structures composed of two continous elements or a piezoelectric element and the tested element separated by a small gap. The comb transducers are on the surface of a piezoelectric. The surface wave excited by the transducers interacts with the electrons in the superconducting layer through the electric field induced near the surface. By testing the damping and velocity of propagation of the surface wave as a function of temperature one can obtain the relations which characterize the superconducting layer. A modification of this method consists in spreading the superconducting layer on a piezoelectric subbase. The obtained dispersion relations for the group and phase velocities make it possible to investigate the superconducting layer [62]. The method of great significance can be the method of measuring the surface wave with the use of edge transducers [63, 64]. The way of positioning the piezoelectric transducers in this method is shown in Fig. 17.

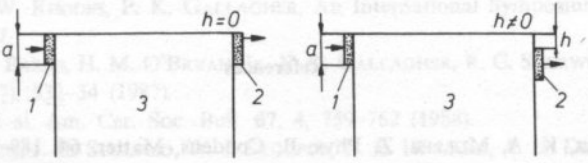

FIG. 17. Setup of transducers for the measurements of the relation between the surface wave amplitude and the distance h between a free surface and a transducer: *1* – sender, *2* – receiver, *3* – medium

Piezoelectric tile transducers are easy to manufacture and can be applied in the case of piezoelectric materials as well as the non-piezoelectric ones. The only limitation is frequency; this is concerned with the technological conditions and with the difficulty of manufacturing the adequately narrow and thin transducers (the upper bound is 100 MHz). The substantial novelty of the work is the theoretical analysis of surface waves generation in the case of title transducers, estimation of the optimal wave generation conditions and the original way of finding the coefficient of wave transmission from one surface to another. With this method the layers of the 1, 2, 3 superconductors spreaded on the strontium titanate and lithium niobate have been measured.

The measurements of damping for the above mentioned layer spreaded on the lithium niobate substrate with the use of edge transducers has been shown in Fig. 18. In the critical temperature a considerable increase of damping (by the order of magnitude of 10 dB) has been observed. Below the critical temperature the damping decreases. During passing through the critical point strong deformation of the sequence of acoustic echoes can be seen. This can evidence the increase of local mechanical stresses or the structural changes of the medium. In transition through the critical point the change of the acoustic wave velocity by the order of magnitude of $\Delta V/V = 10^{-3}$ is observed.

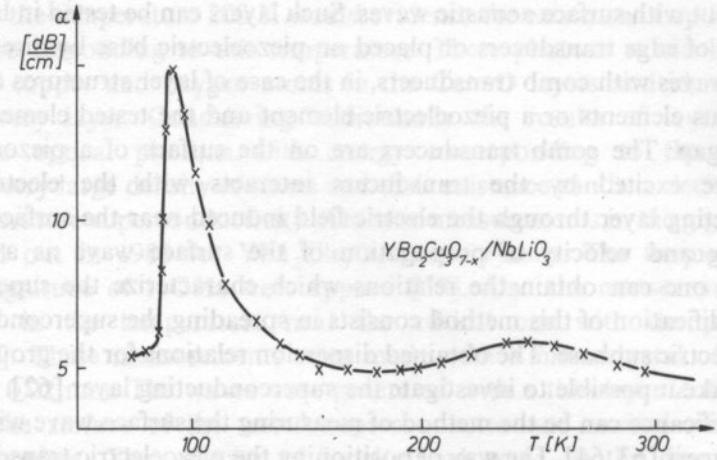

FIG. 18. Ultrasound waves attenuation in $YBa_2Cu_3O_{7-x}$ superconductors spreaded in a form of thin layer on $NbLiO_3$ substrate

References

[1] T. G. BEDNORZ, K. A. MULLER, Z. Phys. B: Condens. Matter. **64**, 189–193 (1986).

[2] G. BEDNORZ, N. TAKASHIGE, K. A. MULLER, Europhys Lett. **3**, 379 (1987).

[3] M. K. WU, J. R. ASHBURN, C. J. TORNG, P. H. HOR, R. L. MENG, L. GAO, Zl. HUANG, Q. WANG, C. W. CHU, Phys. Rev. Lett. **58**, 908 (1987).

[4] G. FISHER, Ceramic Bulletin, **67**, 4, 725–735 (1988).

[5] D. KLIBANOW, K. SUJATA, T. O. MASON, Appl. Phys. Lett., **53**, 125–127 (1988).

[6] A. W. SLEIGHT, 1–12 The Chemistry of High Temperature Superconductors, Ed. D. L. Nelson, M. S. Whittingham and T. F. George, American Chemical Society, Washington, DC 2–12 (1987).

[7] P. K. GALLAGHER, Adv. Ceram. Mater., **2** (3B), 632–39 (1987).

[8] A. J. MELMED, R. D. SHULL, C. K. CHIANG, H. A. FOWLER, Science Washington, DC **239**, 176–78 (1988).

[9] M. O. EATOUGH, D. S. GINLEY, B. MOROSIN, and E. L. VENTURINI, Appl. Phys. Lett., **51** (5), 367–8 (1987).

[10] J. K. LIANG, G. C. CHE, W. CHEN, K. Q. LU, Q. S. YANG, G. H. CHEN and Y. M. NI, J. Mater. Sci. Lett., **6**, 1321–22 (1987).

[11] R. S. ROTH, K. L. DAVIS and J. R. DENNIS, Adv. Ceram. Mater., **2** (**38**), 303–12 (1987).

[12] I. K. GOPALAKRISHNAN, J. V. YAKHAMI, M. A. VAIDYA and R. M. IYER, Appl. Phys. Lett., **51**, 17, 1367–69 (1987).

[13] R. BEYERS, G. LIM, E. M. ENGLER and R. J. SAVOY, Appl. Phys. Lett. **50** (26), 1918–20 (1987).

[14] H. HANEDA, M. ISOBE, S. HISHITA, Y. ISHIZAWA and S. SHIRASAKI, Appl. Phys. Lett. **51** (22), 1848–50 (1987).

[15] Y. KHAN, J. Mater. Scie. Lett., **6**, 1221–2 (1987).

[16] X. ZENG, X. JIANG, H. QI, D. PANG, N. ZHU and Z. ZHANG, Appl. Phys. Lett., **51** (9), 692–33 (1987).

[17] R. S. ROTH, K. L. DAVIS and J. R. DENNIS, Adv. Ceram. Mater., **2** (3B), 303–12 (1987).

[18] K. G. FRASE and D. R. CLARKE, Adv. Ceram. Mater., **2** (3B), 295–302 (1987).

[19] *Superconducting ceramics*, British Ceramic Procedings Nr 40. The Institut of Ceramics, Stoke-on-Trent, 1987.

[20] H. WANG et al. Inorg. Chem., **26**, 1474, (1987).
[21] J. NARAYAN, V. SHUKLA, S. J. ŁUKASIEWICZ, N. BIUNNO, R. SINGH, A. F. SCHREINER and S. J. PENNYCOOK, Appl. Phys. Lett. **51** (12), 940–42 (1987).
[22] K. N. TU, S. I. PARK and C. C. TSUEI, Appl. Phys. Lett., **51** (25), 2158–60 (1987).
[23] B. G. BAGLEY, L. H. GREENE, J. M. TARASCON and G. W. HULL, Appl. Phys, Lett., **51** (8), 622–624 (1987).
[24] J. M. TARASCON, L. H. GREENE, W. R. MCKINNON, Pergamon Journals Ltd., **63** (6), 499–505 (1987).
[25] W. R. MCKINNON, J. M. TARASCON, L. H. GREENE and G. W. HULL, *Extended abstracts of high temperature superconductors*, Mat. Res. Soc. 1987 Spring Meetinh Edition 185–87 (1987).
[26] J. J. NEUMEIER, Y. M. FERREIRA, R. R. HAKE, B. W. LEE, M. B. MAPLE, M. S. TOKORIKACHVILI, K. N. YANG and H. ZHOU, Appl. Phys. Lett. **51** (5), 371–73 (1987).
[27] J. M. TARASCON, L. H. GREENE, W. R. MCKINNON, G. W. HULL, T. P. ORLANDO, K. A. DELIN, S. FONER and E. J. MCNIFF Jr., Phys. Rev. B: Condens Matter, **36**, 16 (1987).
[28] Y. K. TAO, J. S. SWINNEA, A. M. MANTHIRAM, J. S. KIM, J. B. GOODENOUGH and H. STEINFINK, National Research Center of Canada, unpublished data.
[29] CAHEN et al., Mat. Res. Bull., **22**, 1581–1588 (1987).
[30] B. W. VEAL, W. K. KWOK, A. UMEZAWA, G. W. CRABTREE, J. D. JORGENSON, J. W. DOWNEY, L. J. NOWICKI, A. W. MITCHELL, A. P. PAULIKAS and C. H. SOWERS, Appl. Phys. Let., **51** (4), 279–81 (1987).
[31] M. F. YAN, W. W. RHODES, P. K. GALLAGHER, An International Symposium Denver, Colorado, October 19, 1987.
[32] M. F. YAN, R. L. BARNS, H. M. O'BRYAN, Jr., P. K. GALLAGHER, R. C. SHERWOOD and S. JIN, Appl. Phys. Lett., **51** (7), 532–34 (1987).
[33] S. E. TROLIER et al. Am. Cer. Soc. Bull. **67**, 4, 759–762 (1988).
[34] P. M. MANKEWICH, J. H. SCOLFIED, W. J. SKOCPOL, R. E. HOWARD, A. H. DAYEM, E. GOOD, Appl. Phys. Let., **51** (21), 1753–55 (1988).
[35] G. J. CLARK, A. D. MARWICK, R. H. KOCH and R. B. LAIBOWITZ, Appl. Phys. Let., **51** (2), 139–41 (1987).
[36] G. J. CLARK, F. K. LEGOUES, A. D. MARWICK and R. D. LAIBOWITZ, R. KOCH, Appl. Phys. Let., **51** (18), 1462–64 (1987).
[37] D. K. CHRISTEN, J. R. THOMPSON, S. T. SEKULA, L. A. BOATNER, B. C. SALES and S. J. PENNYCOCK, Jpn. J. Appl. Phys., **26**, 1057–58 (1987).
[38] H. KUPFER, I. APFELSTEDT, W. SCHAUER, R. FLUKIGER, R. MEIER-HIRMER, W. WUHL and H. SCHEURER, Z. Phys. B: Condens. Matter., **69**, 167–71 (1987).
[39] J. BOHANDY, J. SUTER, B. F. KIM, K. MOORJANI and F. J. ADRIAN, Appl. Phys. Let. **51** (25), 2161–63 (1987).
[40] J. RANACHOWSKI, F. REJMUND, Z. LIBRANT, *Acoustics in ceramic investigations* (in Polish), 28 IPPT Warsaw 1981.
[41] J. STANKOWSKI, *High-temperature superconductivity* (in Polish), Report for the Session of the General Meeting of PAS, Warsaw, May 1988.
[42] C. V. CHU, K. A. MÜLLER, Zeitschr. f. Phys., B64, 189 (1986).
[43] W. KULA, R. SOBOLEWSKI, P. GIERŁOWSKI, G. JUNG, A. KONOPKA, J. KONOPKA, S. LEWANDOWSKI, Thin Solid Films, **174**, 249–254 (1989).
[44] G. JUNG, A. DĄBKOWSKI, P. GIERŁOWSKI, W. KULA, Physica C 158, 419–423 (1989).
[45] J. BARDEEN, C. N. COOPER, J. R. SCHRIEFFER, Phys. Rev., **108**, 11, 75 (1957).
[46] G. RICKAYZEN, *Theory Superconductivity*, New York 1965.
[47] M. ALEKSIEJUK, M. DOBRZAŃSKI, W. LARECKI, Arch. of Acoustics, 1, 157–172 (1981).
[48] V. M. BOBETIC, Phys. Rev. 136A, 1535–1541 (1964).
[49] WANG YENING et al. Int. J. of Modern Phys., B. 1 273–276 (1987).
[50] C. CANNELLI, R. CANNELLI, F. CORDERO, G. A. COSTA, M. FERRETI, G. L. OLCESE, Phys. Rev. B. **36**, 8907–8910 (1987).

[51] C. DURAN, P. ESQUINAZI, C. FAINSTEIN, M. Nurvi Requiro, Sol. Stet. Comm., **65**, 957 (1988).
[52] D. P. ALMOND, E. F. LAMBSON, G. A. SANDERS, WANG HONG, J. Phys. F., Met. Phys., 457–460 (1987).
[53] S. BHATTACHARYA et al., Phys. Rev. Lett., **60**, 1181–83 (1988).
[54] M. LANG et al., Z. Phys. B69, 45–51 (1988).
[55] V. MULLER, K. DE GROOT, Jap. of Appl. Phys., **26**, 2139–2141 (1987).
[56] T. LEGREID, K. FOSSHIM, F. VASSENDEM, Proc. from HTS., Interloken 1988.
[57] B. LUHTI, B. WOLF, T. KIM, W. GRILL, Jap. of Appl. Phys., **26**, 26–3, 1127–1130 (1987).
[58] Y. HORIE, T. FUKAMI, S. MASC, Sol. Stet. Comm., **63**, 653–655 (1987).
[59] B. GOLDING, W. H. HAEMMERLE, C. F. SCHNEEMEYR, J. V. WASZCZUK, Ultrasonic Symposium, 1079–83 (1988).
[60] J. FANTON, G. S. KINO, B. T. KHURI-JAKUB, 1988 Ultrasonic Symposium, 1093–96 (1988).
[61] M. LEVY, M. F. XU, Bimal K. SARMA, Z. ZHCO, S. ADENWALLO, O. ROBINSON, J. B. KETTERSON, 1988 Ultrasonic Symposium, 1097–1103 (1988).
[62] Z. KUBIK, A. OPILSKI, Acta phys. slov., **37**, 359–362 (1987).
[63] W. PAJEWSKI, Arch. Akustyki, **12**, 3, 235–243 (1977).
[64] N. GYEN VIET KINK, W. PAJEWSKI, Arch. Akustyki **14**, 4, 367–376 (1979).
[65] Z. LIBRANT, A. GŁADKI, L. HOZER, M. PAWŁOWSKA, *Report of the Association of Polish Electricians* No. 07/16/89 (unpublished).

ARCHIVES OF ACOUSTICS
16, 3–4, 413–432 (1991)

EVALUATION OF THE EFFECTIVENESS OF PARAMETERS OF THE GLOBAL DESCRIPTION OF WORDS IN SIMPLE AUTOMATIC SPEECH RECOGNITION SYSTEMS

CZ. BASZTURA, W. MAJEWSKI, W. BARYCKI

Institute of Telecommunication and Acoustics Technical University of Wrocław
(50-370 Wrocław, Wybrzeże Wyspiańskiego 27

In this paper, oriented at the so-called simple systems of speech recognition, the effectiveness of 6 sets of parameters in the global description of words in a given vocabulary was analysed. The usability of simple parametrization methods and such parameters as: density of zero-crossings, distribution of intervals between zero-crossings, parameters of two so-called phase planes, spectral parameters in octave and tertiary bands, was investigated and analysed on the basis of sound material for one operator, mainly and a vocabulary from 5 to 40 words. It was proved that such parameters as the density of zero-crossings and the distribution of time intervals between zero-crossings can be applied in simple systems with a vocabulary preferably not exceeding 10 words, unless it would be possible to select certain words from the vocabulary. Parameters of the first phase plane and spectral parameters exhibited positively weak discrimination ability, especially in octave bands. Also the usability of the NN algorithm and the Camberra distance which standarizes parameters in such ASR systems was confirmed.

1. Introduction

As yet the problem of automatic recognition of continuous speech has not found a satisfactory solution [1, 12]. By far better results from the point of view of potential applications have been achieved in investigations concerning the recognition of a limited set of isolated words [5, 6, 7, 8, 9, 10, 11, 14, 15, 16]. DAXTER and ZWICKER, for example describe in paper [7] a simple on-line recognition system, which consists of an input analyser (12 filters in the range 170–10 000 Hz). A vocabulary of 38 words was used. Their duration was standarized to 500 ms, while the actual time ranged from 280 to 1000 ms. Every word was described by five groups of 12 spectral parameters each. It was proved that a 3–4 bit amplitude quantization is sufficient to

Research performed within program CPBP 02.03.9.3.

obtain satisfactory results. The mean recognition error was equal to 5.3% for a full frequency band.

Brown and Rabiner proved in another paper [5] that in definite experimental conditions the joint weighted functions of the energy distance and prediction coefficients reduce the recognition error by 6 to 25% at the average in comparison to the use of prediction coefficients only.

In SAMBURS and RABINER'S paper [16] 10 digits are recognized with the application of developed systems on acoustic level. In this case there was no need to tune the system to speakers voice. Every 10 ms the system measured the energy, zero-crossings, frequencies of poles determined with the use of linear prediction and prediction error. The recognition error, determined for 10 speakers, did not exceed 2.7%. These and other papers indicate that the recognition of isolated words remains in the range of interest of scientists. This is a result of a demand for simple automatic recognition (ASR) systems, which could recognize vocabularies consisting of tens, or even several words. Robotics should be mentioned as the main consumer of simple ASR systems. There are also trials of applying ASR instead of an alphanumeric keyboard, i.e. dat a input into a computer with the use of voice. Telephone inquiry systems are another example of ASR application.

Several approaches to the recognition of isolated words can be distinguished [1, 12, 18]. One of these are presented by KUBZDELA [11]. It consists in the global description of the whole word by a set of parameters. While another approach assumes that all segments, into which the word is divided, must have their references. The second method is much more complex, what also makes measuring systems and decision algorithms more complicated. Yet, the effectiveness of the segmentation method is better, what can lead to a larger recognized vocabulary, independence of the speaker's voice and smaller recognition error.

However, the mentioned above demand for simple ASR systems prefers global descriptions of words. This manifests itself in the form of e.g. one parameter vector for the whole word. Many factors influence the widely understood effectiveness of simple ASR systems [12]. Parametrization, aimed at the extraction of parameters used in the global description of words, is one of the most important factors. Some parametrization methods extract parameters which are time functions, such as the envelope curve; while other methods use parameters averaged over time. Parameters averaged over time have this advantage that they do not have to undergo time normalization e.g. paper by DAXTER and ZWICKER [7].

The aim of this paper was to study chosen parametrization methods from the point of view of their effectiveness of recognition of isolated words from a vocabulary consisting of 40 words. In consequence studies aimed at the determination of the best algorithm and similarity function were carried out also. The relationship between the effectiveness of parameters and size of the vocabulary was investigated. Such a complex approach made it possible to specify more fully the evaluation of the usability of studied parameters in simple ASR systems.

2. Methods

The fundamental acoustic material of these studies was based on a 40-word vocabulary recorded by two operators (first one – 5 times, second one – 2 times). The 40-word vocabulary can be considered among average size vocabularies, while the recognition of e.g. 10 digits refers to small vocabularies. The used vocabulary is presented below together with phonetic transcriptions. The same vocabulary was used at the same time in another paper concerned with automatic segmentation of a speech signal [4]:

JEDEN	(jeden) ("one")	PLUS	(plus) ("plus")
DWA	(dva) ("two")	MINUS	(minus) ("minus")
TRZY	(tʃɨ) ("three")	MNOŻ	(mnuʃ) ("multiply")
CZTERY	(t͡ʃteri) ("four")	DZIEL	(d͡zel) ("divide")
PIĘĆ	(pieɲt͡ɕ) ("five")	POTĘGA	(poteŋga) ("power")
SZEŚĆ	(ʃeɕt͡ɕ) ("six")	KROPKA	(kropka) ("dot")
SIEDEM	(ɕedem) ("seven")	WYNIK	(vɨnik) ("result")
OSIEM	(oɕem) ("eight")	TAK	(tak) ("yes")
DZIEWIĘĆ	(d͡zevjeɲt͡ɕ) ("nine")	NIE	(ɲe) ("no")
ZERO	(zero) ("zero")	NAWIAS	(navjas) ("bracket")
START	(start) ("start")	PROGRAM	(program) ("programme")
STOP	(stop) ("stop")	TEKST	(tekst) ("text")
GOTOWY	(gotovɨ) ("ready")	FUNKCJA	(fuŋk͡tsja ("function")
ZAJĘTY	(zajentɨ) ("occupied")	ARGUMENT	(argument) ("argument")
PISZ	(piʃ) ("write")	A	(a)
CZYTAJ	(t͡ʃɨtaj) ("read")	DO	(do) ("to")
ŁADUJ	(waduj) ("load")	LUB	(lup) ("or")
SKOCZ	(skot͡ʃ) ("jump")	NIECH	(ɲex) ("let")
POWTÓRZ	(poftuʃ) ("repeat")	I	(i) ("and")
ŁĄCZ	(wont͡ʃ) ("join")	APOSTROF	(apostrof) ("apostrophe")

The vocabulary was divided into groups of 10 word: the first group included digits, the second group – mathematical operations, the third group – certain commands, while the fourth group – certain names or elements in programming.

Possibly smallest dimensions of the observation space for individual parametrization methods were accepted, because simple ASR systems must have a compact vector description. For example, for parameters of the zero-crossings density, the space dimension is $P = 40$, for spectral parameters $P = 6$ (octaves) and $P = 16$ (tertiary).

Simple ASR systems should have possibly simplest classifiers which make it possible to realize a quick classifier "learning" process without a need of many repetitions of the same word. Two heuristic algorithms were applied, i.e. NN (nearest neighbour) and NM (nearest mean).

The experimental systems was provided for one operator, but the results of recognition were verified for a second operator.

3. Parameters

On the basis of the principle of system simplification, parameter which do not require time normalization were chosen mainly to globally represent words included in the vocabulary. The set of parameters of zero-crossings of the speech signal is an exception. Observation parameter spaces, x^P, with dimension P are as follows:

- discrete function of zero-crossings density $\varrho_0(p)$ with dimension $P = 40$ and linear normalization of function,
- parameters of the distribution of time intervals between zero-crossings of the speech signal $x(p)$, $P = 8$,
- parameters of the so-called first phase plane $Pf_1(r)$, $R = 8$,
- parameters of the so-called second phase plane $Pf_2(r)$, $R = 8$,
- spectral parameters in octave bands $F_{oct}(p)$, $P = 6$,
- spectral parameters in tertiary bands $F_{ter}(p)$, $P = 16$.

3.1. Parameters of the density function of zero-crossings

The density of zero-crossings is a parameter frequently used in the analysis and recognition of speech signals [1, 2, 8, 17]. The mean density of zero-crossings of a signal in a time interval T_p is expressed by

$$\varrho_0[u(t), T_P] = \frac{1}{T_P} \frac{\int_{-\infty}^{+\infty} f^2 P(f)\, df}{\int_{-\infty}^{+\infty} P(f)\, df} \tag{1}$$

where $P(f)$ – spectrum of signals power density in time interval T_p, f – frequency of signal.

If T_p values are sufficiently small and the signal with length T is divided into P segments, then the value from expression (1) will be a component of a vector

$$\varrho_0(P) = \mathrm{col}\{\varrho_0(1), \varrho_0(2), \varrho_0(3), \ldots, \varrho_0(P)\}. \tag{2}$$

The digital measurement of components of the density of zero-crossings is very simple in practice. It consists in the summation of moments in which samples change

sign in windows with length T_p. Therefore, the length of a vector depends on the number of windows. It is subject to time normalization in the recognition process. Non-linear time normalization would be most advantageous here [1, 18]. However, linear time normalization was applied, because of the simplicity of measurements [1]. Figure 1 presents discrete $\varrho_0(p)$ functions, with linear normalization on the length $P = 40$ for the first four words in the vocabulary, i.e. "jeden", "dwa", "trzy", "cztery".

Detailed parametrization data for $\varrho_0(p)$ is as follows: $f_{pr} = 10\,000$ samples/s, dynamics described with 10 bits, window length $T_p = 10$ ms. Dimension of parameter vector after normalization $P = 40$ for the whole vocabulary and all repetitions.

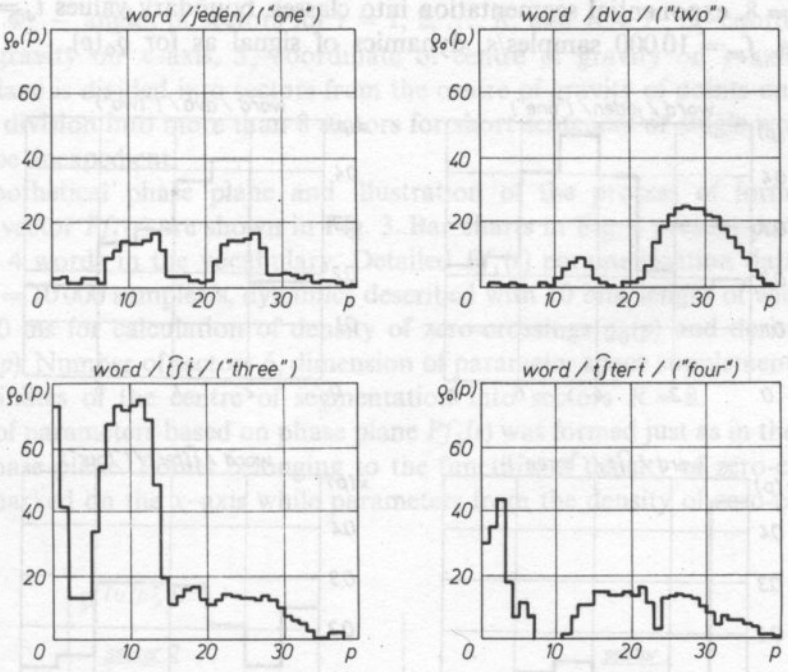

FIG. 1. Examples of parameter ϱ_0(p) values, P = 40, for first four words in the vocabulary

3.2. Parameters of distributions of time intervals between zero-crossings of a speech signal

In spite of its long name parameters of distributions of time intervals between zero-crossings of a speech signal $x(p)$ are a significant "reduction" of the parameter space dimension in relation to the zero-crossings density. The detailed analysis and description of this problem can be found in several papers — [1, 2], among others. It

should be mentioned that

$$x(p) = \mathrm{col}\{x(1), x(2), \ldots, x(P)\} \tag{3}$$

has components calculated according to

$$x(p) = x(t_{p-1}, t_p) = \begin{cases} x(t_{p-1}, t_p)+1 & \text{for } t_j \in (t_{p-1}, t_p\rangle \\ x(t_{p-1}, t_p) & \text{for } t_j \notin (t_{p-1}, t_p\rangle \end{cases} \tag{4}$$

where: $(t_{p-1}, t_p\rangle$ – range of hidden time, called the p-time channel 2, t_j – interval between the j–1 and j zero-crossing of a speech signal.

Figure 2 presents examples of distributions of time interval of the first four words in the vocabulary as in Fig. 1. Detailed $x(p)$ parametrization data are as follows: $P = 8$, exponential segmentation into classes, boundary values $t_d = 0.2$ ms, $t_g = 6.2$ ms, $f_{pr} = 10\,000$ samples/s, dynamics of signal as for $\varrho_0(p)$.

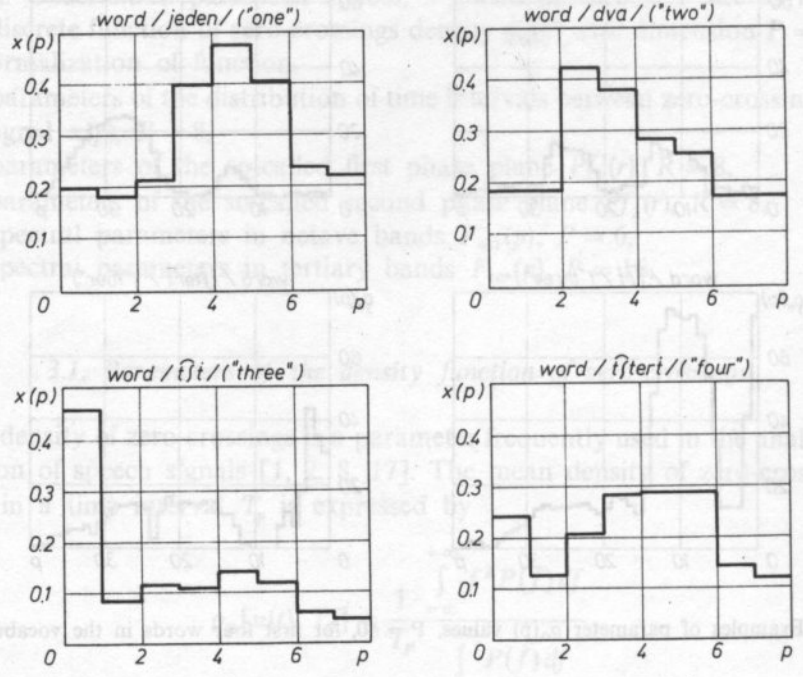

FIG. 2. Examples of parameter x(p) values, $P = 8$, for first four words in the vocabulary

3.3. *Parameters of phase planes Pf_1 and Pf_2*

Two short comings of the density function of zero-crossings of a speech signal, i.e.:

a) large dimension of the parameter vector, and
b) necessity of time normalization

have induced a search for such a modification of this parameter that it would be possible to avoid the shortcomings with possibly smallest effectiveness loss. The idea of new sets of parameters on so-called phase planes originated [1, 2].

It is possible to create a new set of parameters on the first phase plane Pf_1. The number of points in assigned R sectors will be their components. The x– axis of the plane forms the density of zero-crossings $\varrho_0(p)$, the y–axis-derivative of the density of zero-crossings $\varrho_0'(p)$. The principle of forming components of the parameter vectors is as follows

$$Pf_l(r) = Pf_l(r)+l \text{ if}$$

$$\Phi_{r-1} \leqslant \operatorname{Arg}\{\varrho_0[u_n(pT_p)]-S_x, \quad \varrho_0'[u_n(pT_p)]-S_y\} < \Phi_r \tag{5}$$

where Φ_r – angles of sectors for $r = 1, 2, \ldots, R$, and $R \ll P$, S_x–coordinate of centre of gravity on x–axis, S_y–coordinate of centre of gravity on y–axis.

The plane is divided into sectors from the centre of gravity of points on the Pf_1 plane. The division into more than 8 sectors for short sentences or single words was found to be inexpedient.

A hypothetical phase plane and illustration of the process of forming the parameter vector $Pf_1(r)$ are shown in Fig. 3. Bar charts in Fig. 4 present parameters of the first 4 words in the vocabulary. Detailed $Pf_1(r)$ parametrization data are as follows $f_{pr} = 10\,000$ samples/s, dynamics described with 10 bits, length of window T_p equal to 10 ms for calculation of density of zero-crossings $\varrho_0(p)$ and derivative of density $\varrho_0'(p)$. Number of sectors 6, dimension of parameter space supplemented with two coordinates of the centre of segmentation into sectors $R = 8$.

A set of parameters based on phase plane $Pf_2(r)$ was formed just as in the case of the first phase plane. Points belonging to the function of density of zero-crossings $\varrho_0(p)$ are marked on the x–axis while parameters from the density of zero-crossings

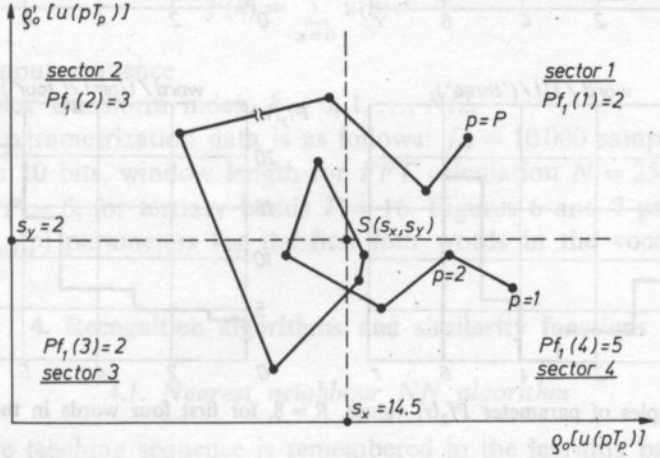

FIG. 3. Method of forming parameters of phase plane $Pf_1(r)$, $R = 4+2$

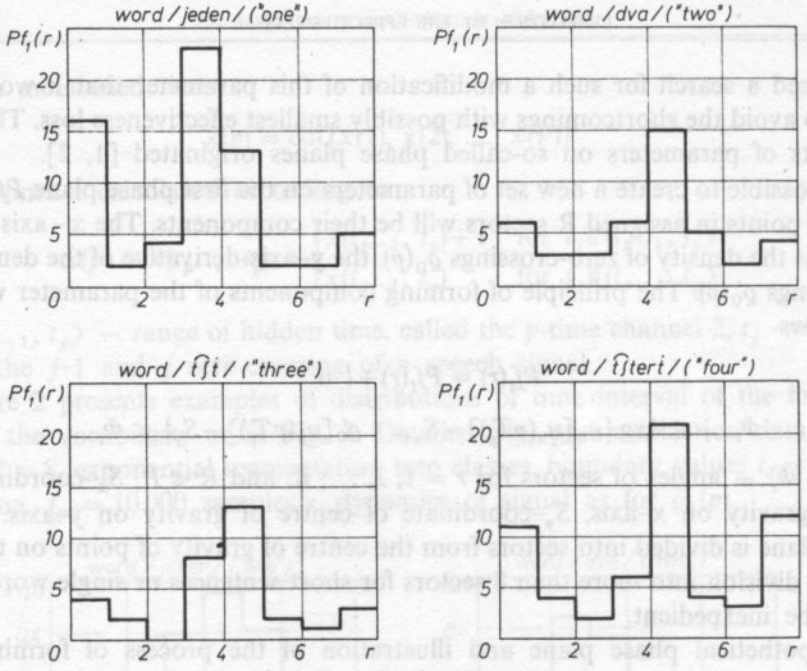

FIG. 4. Examples of parameter $Pf_1(r)$ values, $R = 8$, for first four words in the vocabulary

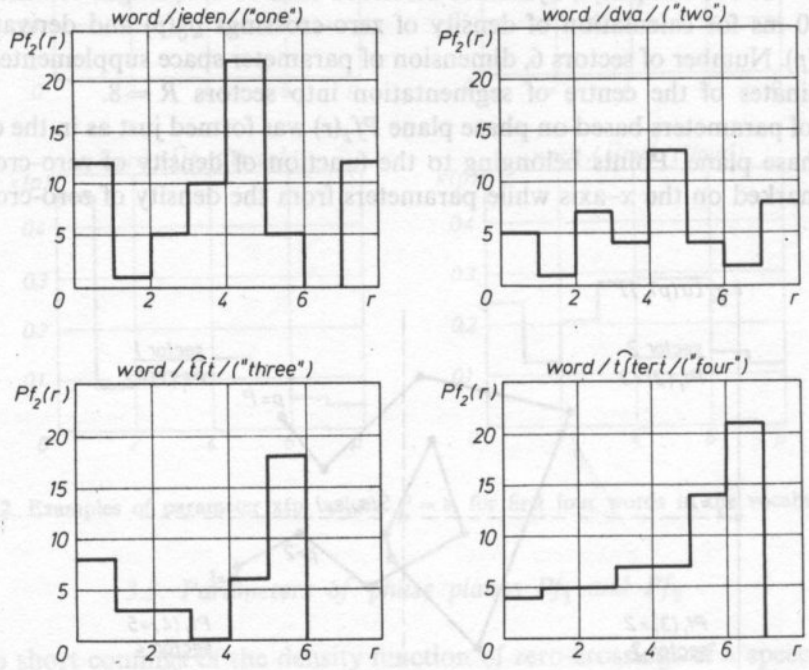

FIG. 5. Examples of parameter $Pf_2(r)$ values, $R = 8$, for first four words in the vocabulary

of the speech signals derivative are marked on the y–axis. The principle of forming components of the parameter vector $Pf_2(r)$ is as follows:

$$Pf_2(r) = Pf_2(r)+1 \quad \text{if}$$
$$\Phi_{r-1} \leqslant \operatorname{Arg}\{\varrho_0[u_n(pT_p)]-S_x, \quad \varrho_0[u'_n(u_n(pT_p)]-S_y\} < \phi_r \tag{6}$$

denotation as in (5).

Figure 5 presents the set of Pf_2 parameters for the 4 first words in the vocabulary. Detailed Pf_2 parametrization data is the same as for $Pf_1(r)$.

3.4. Spectral parameters F

Vectors with components that are signal energies in $P = 6$ and $P = 16$ frequency channels were used as spectral parameters. Components, corresponding with individual bands, were calculated according to expression

$$F(p) = \frac{1}{K_p - P_p + 1} \sum_{j=P_p}^{K_p} [ReF(j)]^2 + [\operatorname{Im} F(j)]^2 \tag{7}$$

where

$$P_p = f_p \frac{N}{f_{pr}}$$

$$K_p = f_{p+1} \frac{N}{f_{pr}}$$

f_p – boundary frequency between the $(p-1)$ and p frequency band, N – number of FFT samples, f_{pr} – signal sampling frequency,

$$F(k) = \sum_{n=0}^{N-1} u(n)\, e^{-j\frac{2\pi}{N}nk} \tag{8}$$

$u(n)$ – real input sequence
$F(k)$ – complex transform index, $k = 0, 1, \ldots, N/2$.
Detailed $F(p)$ parametrization data is as follows: $f_{pr} = 10\,000$ samples/s, dynamics described with 10 bits, window length for FFT calculation $N = 256$ samples. For octave bands $P = 6$, for tertiary bands $P = 16$. Figures 6 and 7 present values of $F_{ter}(p)$ and $P_{oct}(p)$ parameters for the first four words in the vocabulary.

4. Recognition algorithms and similarity functions

4.1. Nearest neighbour NN algorithm

The entire teaching sequence is remembered in the learning process. A set of pairs: vector (describing the word) – vocabulary indication word number is called

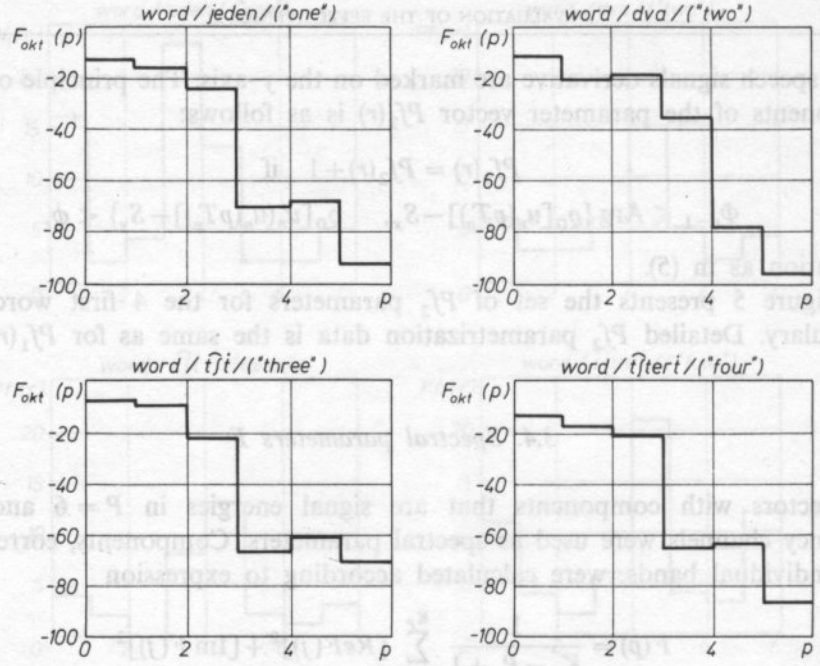

FIG. 6. Examples of parameter $F_{oct}(p)$ values, $P = 6$, for first four words in the vocabulary

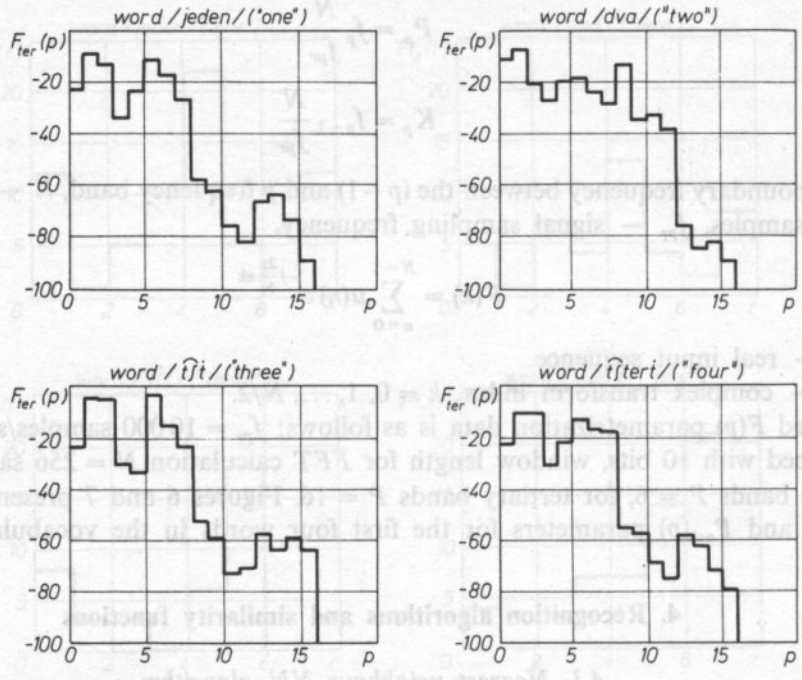

FIG. 7. Examples of parameter $F_{ter}(p)$ values, $P = 16$, for first four words in the vocabulary

the teaching sequence. The length of the sequence is a result of multiplication of the numbers M of words and number I_m of repetitions of the m–th word. In the process of actual recognition a sequence of unknown images (y) appears, described in the same parameter space as the teaching sequence (x). The NN procedure calculates a definite similarity function FP (e.g. distance) between all images in the teaching sequence and successive unknown image y:

$$FP(y, x_{m,i}) \tag{9}$$

while $\left.\begin{matrix} i = 1, 2, \ldots, I_m \\ m = 1, 2, \ldots, M \end{matrix}\right\}$ parameters of teaching sequence

$x_{m,i}$ – i–repetition of m-class word of teaching sequence.

When all FP are calculated, the smallest one is found (in the case of distance). The class (word) number, which includes the image of the teaching sequence and which is found to be closest to the recognized image (in the sense of similarity function) is given as the classifier decision.

$$\Phi(y) = k \text{ i.e. } y \rightarrow k \tag{10}$$

if

$$FP(y, x_{k,i}) < FP(y, x_{l,i})$$
$$m = 1, 2, \ldots, M$$
$$l = 1, 2, \ldots, k-1, k+1, \ldots, M$$

In this case FP is a distance function. The algorithm is very simple. It assures good recognition results. The necessity of storing a great number of reference images is its only shortcoming.

4.2. Nearest mean NM algorithm

The necessity of storing all images of the teaching sequence is eliminated in the case of the NM algorithm. And this is an advantage of this algorithm with respect to the previous one. These images are replaced with the storage of mean images, as most typical for a given class. The decision rule has the following form:

$$\Phi(y) = m \text{ i.e. } y \rightarrow m$$

if

$$FP(y, W_m) < FP(y, W_l) \tag{11}$$

where

W_m – mean image of class word

$l = 1, 2, \ldots, m-1, m+1, \ldots, M$.

The *NM* algorithm is not recommended in these situations in which distributions of probability density of images are multimodal distributions.

4.3. Similarity functions

Descriptions and interpretations of similarity functions can be found in papers [1, 12, 18], among others. Thus, we will limit ourselves to the formulation of the mathematical notation of two similarity functions, i.e. Euclidean and Camberra. The first one was chosen, because of its wide application in ASR systems. The second one, because of its form which has a standarizing effect on parameters [1, 3, 18].

a) Euclidean distance

$$D^{\mathrm{EU}}(x, y) = \Big[\sum_{p=1.}^{P} (x_p - y_p)^2\Big]^{1/2} \tag{12}$$

b) Camberra distance

$$D^{\mathrm{CAM}}(x, y) = \sum_{p=1}^{P} \frac{|x_p - y_p|}{|x_p + y_p|} \tag{13}$$

5. Experiments and results

The experiments were carried out in several stages, because of the complexity of accepted input data, i.e., various parametrization methods, classification algorithms and similarity functions. The structure of experiments is shown in Fig. 8. It contains four different combinations of the "source", i.e. vocabulary, and two types of test sequences (CT_w – individual test sequence, i.e. the same speaker recorded the teaching and test sequence and CT_0 what means that another speaker recorded the test sequence). 6 sets of parameters, two decision algorithms and two similarity functions were investigated. The number of possible combinations is tremendous. The needless variation was eliminated by accepting the following order of research:

stage I – the classification algorithm and similarity function were determined for the entire experimental material,

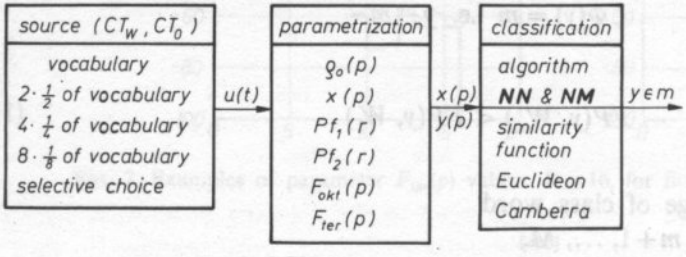

FIG. 8. Arrangement of experiments

stage II – the influence of the size of the vocabulary on the effectiveness of recognition was determined for all parameters,

stage III – evaluation of the system after eliminating from the vocabulary words, which in stage I were recognized worst of all. All these analysis and evaluations were performed for all 6 sets of parameters. At the same time their effectiveness and directions of changes due to investigated external factors were observed. It was accepted that the teaching sequence will consist of the first 3 repetitions of the first speaker, while the test sequence – of 2 succeeding repetitions from among the recordings of the first speaker and two repetitions of the second speaker.

5.1. Evaluation of algorithms and similarity functions

Within the first stage of experiments the whole vocabulary was recognized for both algorithms, both probability functions and all 6 sets of parameters. Cumulative results are presented in Table 1.

Table 1. Results of the first stage of recognition experiments [in %] for $M = 40$ words including all parameters of classifier and different sets of parameters

Parameters	Algorithm							
	NN				*NM*			
	Euclidean distance		Camberra distance		Euclidean distance		Camberra distance	
	CT_w	CT_0	CT_w	CT_0	CT_w	CT_0	CT_w	CT_0
$\varrho_0(p)$ $P = 40$	68.75	13.75	73.75	20.00	60.00	17.50	70.00	22.50
$x(p)$ $P = 8$	47.50	15.00	52.50	20.00	41.25	12.50	53.75	13.75
$Pf_1(r)$ $R = 8$	25.00	10.00	21.25	7.50	28.75	10.00	31.25	11.25
$Pf_2(r)$ $R = 8$	37.50	8.75	27.50	12.50	42.50	8.75	32.50	10.00
$F_{oct}(p)$ $P = 6$	16.25	1.25	23.75	6.25	21.25	6.25	35.00	10.00
$F_{ter}(p)$ $P = 16$	20.00	3.75	33.75	10.00	12.50	7.50	40.00	12.50

Results from Table 1 were considered from the point of view of further studies on the algorithm and similarity function. We can see that best results were achieved for most parameters for the Camberra distance. A small number of repetitions of the teaching and test sequence could not be decisive in the choice of algorithm. Yet, because of the fact that as a rule 3 repetitions of teaching sequence do not determine the reference as a mean exactly the *NN* algorithm was used in further research. The *NN* algorithm and the Camberra distance will be classified in further experiments. The results of experiments provided a rather clear explanation of the problem of using the system in the recognition of statements of another operator (CT_0). From results gathered in Table 1 we can see that for all cases of CT_0 effectiveness values are several times smaller than for CT_w. This means that global recognition parameters are strongly dependent on individual features of the voice. Therefore further analysis will refer to CT_w only.

5.2. The effect of word set size on recognition results

The second stage of recognition experiments was aimed at the determination of the relationship between recognition effectiveness and number of words in the vocabulary. Tables 2, 3 and 4 contain results for individual parameters. These tables indicate a monotone effectiveness increase accompanying the decrease of the number

Table 2. Recognition results [in %] for two parts of the vocabulary (2 × 20), separately, Algorithm *NN*, Camberra distance, test sequence CT_w

Parameters	Vocabulary words		Mean value
	1÷20	21÷40	
$\varrho_0(p)$ $P = 40$	82.50	80.00	81.25
$x(p)$ $P = 8$	65.00	65.00	65.00
$Pf_1(r)$ $R = 8$	22.50	42.50	32.50
$Pf_2(r)$ $R = 8$	52.50	22.50	37.50
$F_{oct}(p)$ $P = 6$	42.50	32.50	37.50
$F_{ter}(p)$ $P = 16$	47.50	35.00	41.25

Table 3. Recognition results [in %] for 4 parts of the vocabulary (4×10), separately. Algorithm *NN*, Camberra distance, test sequence CT_w

Parameters	Vocabulary words				Mean value
	1÷10	11÷20	21÷30	31÷40	
$\varrho_0(p)$ $P = 40$	85.00	90.00	100.00	75.00	87.50
$x(p)$ $P = 8$	55.00	90.00	90.00	70.00	76.25
$Pf_1(r)$ $R = 8$	45.00	40.00	50.00	55.00	47.50
$Pf_2(r)$ $R = 8$	55.00	75.00	40.00	45.00	53.75
$F_{okt}(p)$ $P = 6$	60.00	80.00	40.00	45.00	56.25
$F_{ter}(p)$ $P = 16$	65.00	80.00	40.00	60.00	61.25

Table 4. Recognition results [in %] for 8 parts of the vocabulary (8×5), separately. Algorithm NN, Camberra distance, test sequence CT_w

Parameters	Vocabulary words								Mean value
	1÷5	6÷10	11÷15	16÷20	21÷25	26÷30	31÷35	36÷40	
$\varrho_0(p)$ $P = 40$	90	100	100	90	100	100	80	80	92.50
$x(p)$ $P = 8$	100	70	100	100	90	90	80	80	88.75
$Pf_1(r)$ $R = 8$	70	60	50	60	90	80	60	60	66.25
$Pf_2(r)$ $R = 8$	80	50	60	90	80	60	70	70	70.00
$F_{oct}(P)$ $P = 6$	90	70	80	100	40	80	50	80	73.75
$F_{ter}(p)$ $P = 16$	90	70	90	90	40	70	60	80	73.75

of classes (words). The next observation results from Fig. 9.: when the number of classes is decreased then differences in effectiveness between individual parameters also decrease. A rather big differentiation of recognition effectiveness between individual groups of recognized words can be clearly noticed on the basis of all tables. These differences range from 25% for $\varrho_0(p)$ up to 20% for $Pf_1(r)$, for $M = 20$, and are equal to about 60% for a set of $M = 5$ words and parameter $F_{ter}(p)$.

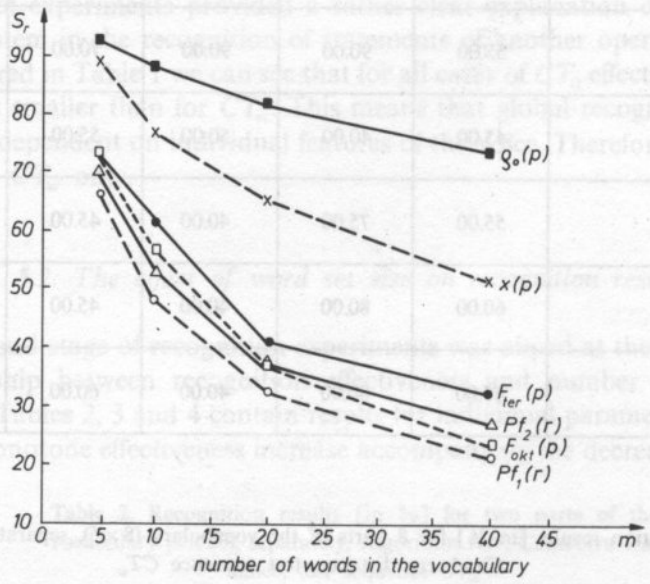

FIG. 9. Recognition effectiveness s_r [in %] in terms of the number of words in the vocabulary [m]

5.3. Selective choice of vocabulary

Differences in recognition results stated for various parts of the vocabulary clearly indicate that the choice of vocabulary influences the results of recognition. Hence, at this stage of research ten and twenty words which obtained worst recognition results for most parameters were eliminated from the vocabulary. The goal of the experiment was to determine quantitative effectiveness changes relative to control groups of words, i.e. average from successive sets of 30 and 20 words. Research results are presented in Table 5. A significant increase of correct recognition is visible, especially for the 20-word vocabulary. For example: for $\varrho_0(p)$ the effectiveness increased by 18.75%, for $x(p)$ by 20.00% and for $F_{ter}(p)$ by 26.25%. Next trials consisted in the arbitrary choice of the "best" with respect to achieved results, words from the whole vocabulary. Previously the effectiveness criterion with respect to most parameters was used, while now in two following trials the effectiveness of $x(p)$ selection a and $Pf_2(p)$ selection were applied as the criterions.

Table 5. Recognition results [in %] when words with worst recognition results achieved in the stage with reference to average results for sets of words taken in a fixed order are eliminated

Parameters	30-word vocabulary		20-word vocabulary	
	succesive words	Selected words	succesive words	selected words
$\varrho_0(p)$ $P = 40$	79.17	86.67	81.25	100.00
$x(p)$ $P = 8$	59.16	66.67	65.00	85.00
$Pf_1(r)$ $R = 8$	30.00	31.67	32.50	47.50
$Pf_2(r)$ $R = 8$	32.50	38.33	37.50	55.00
$F_{oct}(p)$ $P = 6$	31.67	46.67	37.50	57.50
$F_{ter}(p)$ $P = 16$	40.00	46.67	41.25	67.50

Table 6. Recognition results [in %], when 10 words with best recognition results in the I stage with reference to average results to sets of words taken in a fixed order are chosen. Selection a) — according to criterion $x(p)$, selection b) — according to criterion $Pf_2(r)$

Parameters	10-word vocabulary		
	mean for 10 words	selection a)	selection b)
$\varrho_0(p)$ $P = 40$	87.50	90.00	90.00
$x(p)$ $P = 8$	76.25	100.00	90.00
$Pf_1(r)$ $R = 8$	47.50	65.00	60.00
$Pf_2(r)$ $R = 8$	53.75	85.00	80.00
$F_{oct}(p)$ $P = 6$	56.25	50.00	70.00
$F_{ter}(p)$ $P = 16$	61.25	70.00	80.00

Results are presented in Table 6. The advantages of selecting words according to a definite set of parameters are clearly visible. For $x(p)$, for example, the recognition correctness improved from 76.25% to 100%. Similarly, the effectiveness for $Pf_2(r)$ increased from 53.75% to 80%.

5.4. *Usability analysis of individual sets of parameters*

Six sets of parameters were selected initially: $p_0(p)$, $x(p)$, $Pf_1(p)$, $Pf_2(p)$, $F_{oct}(p)$, $F_{ter}(p)$. The first parameter required time normalization – the others did not. Spectral parameters were derived from *FFT* calculations. This was the most complex analysis from among all applied parametrization methods. From the point of view of potential implementation the simplicity and speed of the parametrization procedure is very important. Spectral analysis in time close to real time requires an adequate signal processor or a bank of analogue or digital filters. Thus, it does not satisfy the requirement of system simplicity. Other parameters are based on the method of zero-crossings analysis. The simplicity of parameter extraction at high effectiveness is their fundamental advantage [2, 7, 16].

Ranges of effectiveness changes versus number of words are presented in graphical form in Fig. 9. It is characteristic that if for $M = 40$ the spread between sets of parameters is considerable, s_r values become more concentrated when the size of the vocabulary is decreased. This means that it is possible to apply $\varrho_0(p)$, $x(p)$, $Pf_2(p)$, $F_{oct}(p)$, $F_{ter}(p)$ to small vocabularies. The $x(p)$ set would be most preferred, because of its high effectiveness, small dimension of the parameter vector and calculation simplicity. $\varrho_0(p)$ was found to be most stable for all vocabularies, what can be explained by the time structure for this set of parameters. In spite of normalization significant differences in the current signal structure of words are retained. From a comparison of results for various equipotent subsets of vocabularies we can see (Table 2) that the smallest diversification is achieved from parameters $\varrho_0(p)$ and $x(p)$. The $Pf_1(r)$ set turned out to be positively the worst parameter. In its construction it took advantage of the same $\varrho_0(p)$ information twice on both axii of coordinates and acquiring a simple form it "lost" its force of discriminating parameters of zero-crossings density. The effectiveness of $Pf_2(r)$ parameters is somewhat better. It may be explained by the fact that the second axis of ordinates was calculated on the basis of the signals derivative. A division into two groups of parameters can be clearly noticed. $\varrho_0(p)$ and $x(p)$ belong to the first group, while the rest to the second one. The application of the traditional spectral analysis of octave bands ($P = 6$), as well as tertiary bands ($P = 16$), gave worse than expected results. Performed trials of reducing the parameter space resulted in the worsening of the results, while trials of vectors' concatenation resulted in a slight effectiveness improvement. For example, the concatenation of $\varrho_0(p)$ and $x(p)$ for $M = 40$ resulted in an effectiveness increase from 73.15% for $\varrho_0(p)$ to 76.25%. Similar results for voice identification were obtained by MAJEWSKI [13]. It results from Table 4 that most parameters could be

used as a parametrization method, especially for an adequately selected small vocabulary ($M \leqslant 5$). For slightly larger sets ($M \leqslant 10$), only $\varrho_0(p)$ and $x(p)$ could assure satisfactory discrimination force.

It is difficult to determine the typical effectiveness threshold of parameters, because it depends on the actual operating conditions of the ASR system. It seems that if it would be possible to provide a certain protection, e.g. two repetitions of the same word or a back confirmation, then ASR systems could fulfill a fundamental role in man-machine communication with effective recognition of isolated words beginning from 70%–80% [1, 11]. In a contrary case the required level of correct recognition for simple systems should exceed 90% [12]. It should be noted here that recognition does not exceed 95% in a case of listeners listening to so-called word lists, even when transmission and surrounding conditions are very favourable.

Many of the recognition systems of limited word vocabularies, described in literature, can collaborate with many operators speakers because of the segmental approach used to describe words. Thus, the simplicity of the global approach is connected with its smaller versatility.

6. Summary and conclusions

Most detailed analysis and comments can be found in paragraph 5.3. Thus, here we will only formulate general thesis and conclusions.

1. All three blocks of the system, i.e. "source", "measurement" and "classifier" are important when creating simple ASR systems.

2. Research has proved that in the "source" block the correct selection of the vocabulary is important – not only with respect to size, but also with respect to adequate phonetical diversification. This way the recognition effectiveness can be improved by over ten per cent.

3. The proper selection of parameters in the "measurement" block is traditionally the most important criterion affecting the systems effectiveness. The parameters of the time structure, i.e. $\varrho_0(p)$ and $x(p)$, satisfy the effectiveness and measurement simplicity criteria at the same time, best of all investigated sets of parameters.

4. A simple decision principle and adequate similarity function should be established in the classification block. Performed research and other authors papers [3, 18] indicate that the NN algorithm is the best classifier in simple systems. When parameters are normalized, it is convenient to use the Euclidean or Hamming distance function, while for not normalized parameters – the Camberra distance function is best.

5. In the global discription of words with single vectors in an observation space with dimension p, small vocabularies under 10 freely selected words (Table 3) or vocabularies containing 20 words adequately chosen on the basis of phonetical selection Table 5 have a chance of being implementated. The recognition effectiveness or the size of the vocabulary may probably be increased by introducing the global frequency-time description, for example [11, 18].

References

[1] Cz. BASZTURA, *Acoustic sources, signals and images* (in Polish) WKiŁ 1988.

[2] Cz. BASZTURA, *Automatic speaker recognition by zero-crossing analysis of the speech signal*, in: Speech Analysis and Synthesis, [Ed.] W. Jassem, 5, PWN, Warszawa 1980, pp. 5–40.

[3] Cz. BASZTURA, J. ZUK, *Similarity functions of images in non-parametric voice identification algorithms*, Archives of Acoustics, **16**, 2, (1991).

[4] Cz. BASZTURA, T. SAWCZYN, *Automatic segmentatation of a speech signal with the application of selected parametrization methods*, submitted for publication in Archives of Acoustics.

[5] M. K. BROWN, L. R. RABINER, *On the use of energy in LPC-based recognition of isolated words*, Bells System Techn. Journal, **61**, 10, 2971–2987 (1982).

[6] K. H. DAVIS, R. BIDDULPH, S. BALASHEK, *Automatic recognition of spoken digits*, J.A.S.A., **24**, 6, 637–642 (1952).

[7] W. DAXTER, E. ZWICKER, *On-line isolated word recognition using a microprocessor system*, Speech Communication **1**, 1, 21–27 (1982).

[8] R. GUBRYNOWICZ, *Application of zero-crossing method in speech signal analysis and automatic word recognition* (in Polish) Prace IPPT PAN 31, (1974).

[9] S. HUANG, R. GRAY, *Spellmode recognition based on vector quantization*, Speech Communication, **7**, 1, 41–53 (1988).

[10] A. ICHIKAWA, Y. NAKAO, K. NAKATA, *Evaluation of various parameter sets in spoken digits recognition*, IEEE Transactions on Audio and Electroacustics, AU–21, 3, 202–209 (1973).

[11] H. KUBZDELA et al., *Speech visualization* (in Polish) Ed. W. Jassem Prace IPPT PAN Warszawa 1987.

[12] W. A. LEA, *Trends in speech recognition*, Prentice-Hall Inc., Englewood Cliffs 1980.

[13] W. MAJEWSKI, *Speaker identification by means of averaged spectra of key words* (in Polish) Proc. XXXVI Open Seminar on Acoustics, Szczyrk-Biła September 1989, pp. 85–90.

[14] L. R. RABINER, J. G. WILPON, *Speaker-indpendent isolated word recognition for a moderate size 54 word vocabulary*, IEEE Trans. Acoust. Speech and Signal Processing, ASSP-27, 6, (1979) 583–587.

[15] L. R. RABINER, S. E. LEVINSON, M. M. SONDHI, *On the application of vector quantization and hidden Markov models to speaker-independent isolated word recognition*, Bell System Techn. Journal **62**, 4, 1075–1105 (1983).

[16] M. R. SAMBUR, L. R. RABINER, *A speaker-independent digit recognition system*, Bell System Techn. Journal, 54, 1, 81–102 (1975).

[17] R. W. SCHAFER, L. R. RABINER, *Digital representations of speech signals*, Proc. the IEEE, **64**, 4, 662–677 (1975).

[18] R. TADEUSIEWICZ, Speech signal (in Polish), WKiŁ Warszawa 1989.

Received November 28, 1989

ARCHIVES OF ACOUSTICS
16, 3–4, 433–439 (1991)

SOUND VELOCITY AND LOSS FACTOR OF POLYURETHANE COMPOSITES. PART I

W. BANDERA AND K. PAWLACZYK*

Laboratory of Applied Acoustics and Spectroscopy University of Gdańsk
(80-952 Gdańsk, ul. Wita Stwosza 57)
*Institute of Chemical Technology Technical University of Szczecin
(70-322 Szczecin, ul. Pułaskiego 10)

The paper reports development of elastic, unfoamed polyurethane compositions to be used as vibro-insulating materials. The examined compositions were prepared using poly(propylenoethers) of different molecular weights, toluylene diisocyanate and glass microspheres separated from fly-ashes. The effect of varied proportions of components on visco-elastic properties of the material, that is on sound velocity and loss factor was examined experimentally. The measurements were taken at room temperature within frequency range of 20 Hz to 1000 Hz. It was discovered that modification of the polyurethane binder content and alteration of the number of microspheres in a composition permit modification of properties of the material and especially its stiffness and internal damping.

1. Introduction

Production technology and methods of investigating the basic properties of syntactic foam were developed when searching for new thermoinsulating material to be employed in hyperbaric appliances operating at great depths under the water surface [5, 6, 7, 10]. Elasticity of the material was obtained through employment of soft unfoamed polyurethane as a binding agent, thermoinsulation and relatively low density being achieved by the introduction of spherical grains, empty or filled with neutral gas, as the filler of the microspheres. Such microbubbles are readily isolated while burning coal dust [3].

Apart from the initially demanded properties, the resulting material exhibits several other interesting features, such as, for example, insulating properties which have already been investigated [1, 2].

The task of the present paper is to determine experimentally the correlation between chemical composition of the polyurethane binder, the amount of the filter, and elasticity and damping capacity of the composite. Thus, we concentrated on

sound velocity and loss factor. Both the latter quantities enable calculation of the components of Young's complex modulus, which is of fundamental significance for the proper choice of vibroinsulating materials.

2. Characteristics of the material

The object of our investigation was unfoamed polyurethane (PU) composition where microspheres obtained with a simple method from fly-ashes produced during burning coal dust were used as the filling agent. The PU binder is composed of poly(oxypropylene) trioles and diisocyanates.

The microspheres are built of glasslike substance and a considerable part of them take the form of spheres filled with gas (N_2 and CO_2). The shape and the size of the microspheres are shown in Fig. 1. Introduction of microspheres into the polyurethane composition induces changes in the PU lattice structure. It decreases mobility of the lattice fragments and increases rigidity of the polymer chain.

The investigation was carried out on four series of samples. In the first series, the ratio of the number of —OH functional groups to that of —NCO groups in the isocyanate was constant, amounting to 1:1.3, whereas the amount of microspheres varied from 10% to 60% depending on the main component of the PU composition chosen. One of the PU components was Rokopol M–12 i.e. poly(oxypropylene-ethylene) triole with the molecular weight of 4800, the other was TDI isocyanate, a mixture of 2,4- and 2,6-diisocyanatotolylene.

In the second series, properties of the binding agent were altered by choosing new proportions of the reacting isocyanate (NCO) and hydroxyl (OH) functional groups (—NCO:—OH) from 1.1:1 to 1.9:1, with the microsphere content of 30% remaining constant.

In the third series, the PU binder properties were again changed by substituting TDI with MDI isocyanate (4,4-diisocyanatodiphenylmethane), while the number of microspheres amount to 30% of the contents, and the functional group ratio (—NCO:—OH = 1.1:1) were held constant.

In the last series, the properties of the PU binder were changed once more by replacing Rokopol M–12 with Rokopol 111, characterized by molecular weight of 6000. The number of microspheres was constant (30%), and functional group ratios remained fixed (—NCO:—OH = 1.3:1 and 1.9:1). The second component of the PU binder was TDI isocyanate. Compositions with Rokopol 111 as the basic component were examined earlier and the results were reported in [1, 2].

3. Measurement method

In order to determine sound velocity and loss factor of the PU composites seen as a function of frequency, the vibration transfer function method was used. The idea of the measurement procedure is shown in Fig. 2. The theoretical model of this

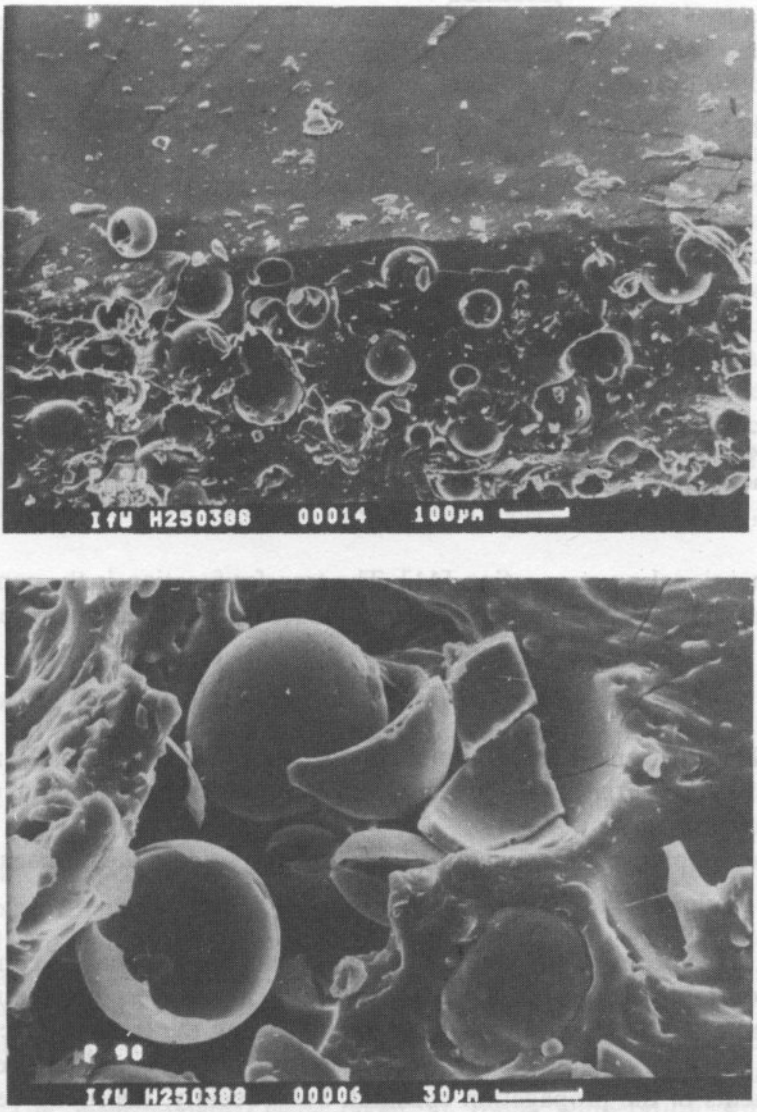

FIG. 1. Cross-section of syntactic polyurethane foam showing the shape and dimension of microspheres a–100-fold magnification, b–500-fold magnification

arrangement is, in the general case, a longitudinally vibrating rod with an end mass. For deriving the transfer function it is assumed that the cross-section of the rod is constant, the rod material is homogeneous and isotropic, the relation between stress and strain is linear, lateral motion is not prevented at the rod ends, and the width of the rod is much smaller than the mechanical wavelength [4, 8]. Under these assumptions, the longitudinal vibration of a rod is described by the well-known

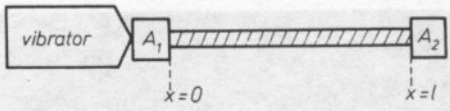

FIG. 2a. Rod-like specimen excited to longitudinal vibrations by means of a vibrator

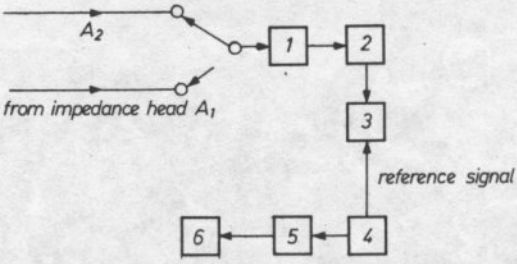

FIG. 2b. Arrangement for measuring the transfer function. 1-preamplifier, Brüel & Kjaer (B&K) type 2635; 2-measuring amplifier and filter, B&K type 2120; 3-digital phase meter, B&K type 2977; 4-sine generator, B&K type 1027; 5-power amplifier, B&K type 2706; 6-vibration exciter, B&K type 4809

one-dimensional wave equation [11]. The transfer function is the complex ratio of the vibration accelerations of the mass-loaded and excited ends, respectively:

$$T = \frac{A_2}{A_l} = |T| \cdot e^{i\varphi} = \left|\frac{A_2}{A_l}\right| e^{i\varphi} \tag{1}$$

where $|T|$ is the transfer function modulus, A_2 and A_l stand for vibration acceleration at the two ends of the specimen respectively, φ is the transfer function phase and i is the imaginary unit.

The complex transfer function, T, can be expressed by the propagation constant

$$T = [\operatorname{ch} \gamma l + (M/m)\gamma l \cdot \operatorname{sh} \gamma l]^{-1} \tag{2}$$

where γ is the propagation constant, $\gamma = \alpha + i\beta$, α is the attenuation constant, β is the phase constant, l is the rod length, M is the accelerometer, functioning as loading mass and m is the specimen mass. While measuring the transfer function modulus and the phase for each frequency, formula (2) served for establishing the values of the components of the propagation constant. Subsequently, the sound velocity, c, and the loss factor, η, were calculated from the well-known formulae

$$c = \frac{2\pi f}{\beta}, \qquad \eta = \frac{2d}{1-d^2} \tag{3, 4}$$

where f is the frequency and $d = \alpha/\beta$.

A block diagram of the measuring apparatus is presented in Figure 2b. Longitudinal vibrations were excited with an electrodynamic vibrator. A prism-shaped specimen of 1 cm^2 in cross-section and about 12 cm in length was bonded with a perfectly hardening adhesive to the impedance head A_1 (Brüel & Kjaer, type 8000) and the accelerometer A_2 (Brüel & Kjaer, type 4366) (see

Figure 2). The amplitude of vibration acceleration of the vibrator was kept constant and adjusted carefully not to exceed the dynamic strain limit of linear properties of the material investigated. In order to achieve the highest measuring accuracy, a one-channel technique was used for measuring the modulus and the phase of the transfer function. Due to the technique the error in measuring $|T|$ did not exceed 5% which, in turn, allowed us to estimate that the error in calculating sound velocity was also lower than 5%. The signal of an acoustic generator was used as reference for measuring the phase by the one-channel technique. The accuracy of the digital phase meter amounted to 0.1 deg. However, the error in the measured phase was larger due to phase shifts of the attenuators of the measuring amplifiers. It could be stated that the overall error in measuring the transfer function phase was not larger than 0.4 deg at all frequencies of investigation. Hence, we could estimate that the error in calculating loss factor did not exceed 10%. A detailed description of the measuring system and the method of identifying the values of the transfer function was published by Pritz in [8, 9].

4. Results and discussion

4.1. The effect of the Rokopol type on velocity and loss factor in PU compositions

Two PU compositions, one with Rokopol 111 as the basic component and the second with Rokopol M–12 were prepared to examine the effect of the type of Rokopol on the viscoelastic properties of the material under investigation. In both cases TDI isocyanate was added as the second component. The ratio of the number of functional groups —OH in macrotriole to that of the —NCO groups in isocyanate was raised to 1 : 1.3 and 1 : 1.9. Microspheres serving as the filling material constituted 30% of basic component. The modulus and the phase of the transfer function measured for the above compositions and the calculated values of sound velocity and loss factor have been shown in Figs. 3, 4 and 5, 6, for each type respectively. The measurements were taken at room temperature within the frequency range of 20 Hz–1000 Hz. Measurement of transfer function modulus for frequencies exceeding 1000 Hz was not possible because of significant damping of the signal in the investigated material. For the upper limit of the measurement range, the ratio of the length of the longitudinal wave to the width of the specimen was properly high which allowed for accepting insignificance of transverse vibrations when calculating sound velocity and loss factor.

As in Figs. 5 and 6, both sound velocity and loss factor greatly depend on the type of Rokopol. Substitution of Rokopol 111 with Rokopol M–12 results in an almost 2–fold increase in sound velocity at the frequency of 20 Hz, and a 1.5-fold increase at 1000 Hz. On the other hand we observed, marked suppression of the PU

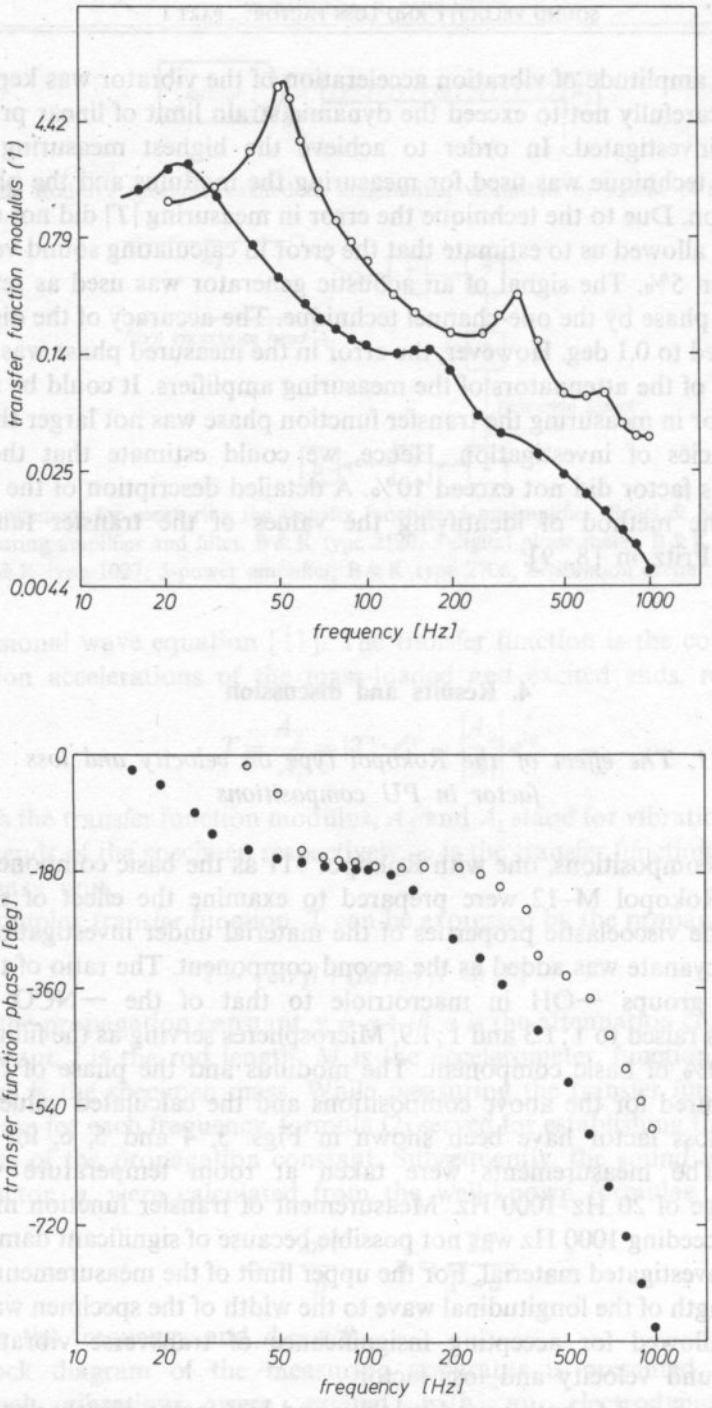

FIG. 3. Measured modulus (a) and phase (b) of the transfer function plotted against frequency for compositions with Rokopol M–12 —○—○— and Rokopol 111 —●—●— Molar ratio NCO/OH = 1.3

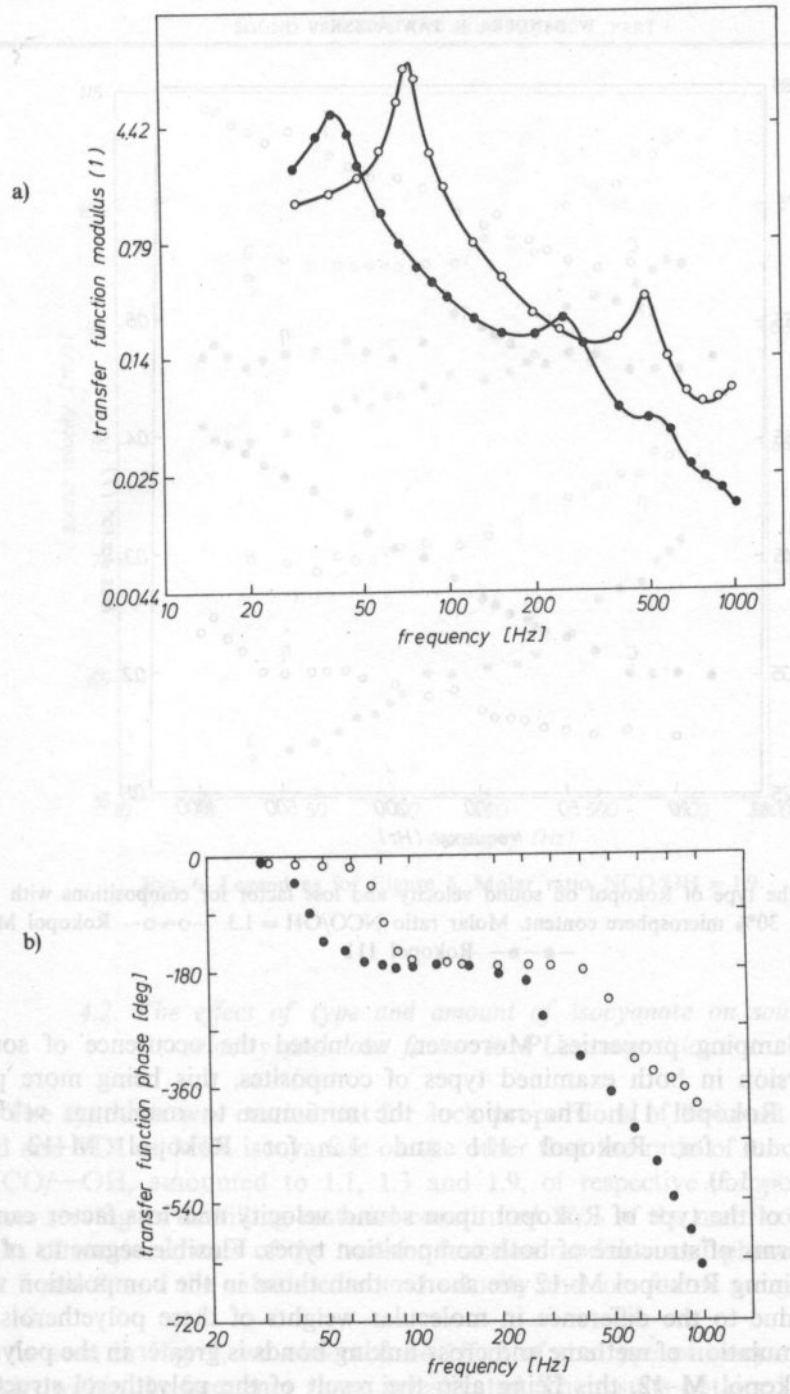

FIG. 4. Measured modulus (a) and phase (b) of the transfer function plotted against frequency for compositions with Rokopol M–12 –○–○– and Rokopol 111 –●–●– Molar ratio NCO/OH = 1.9

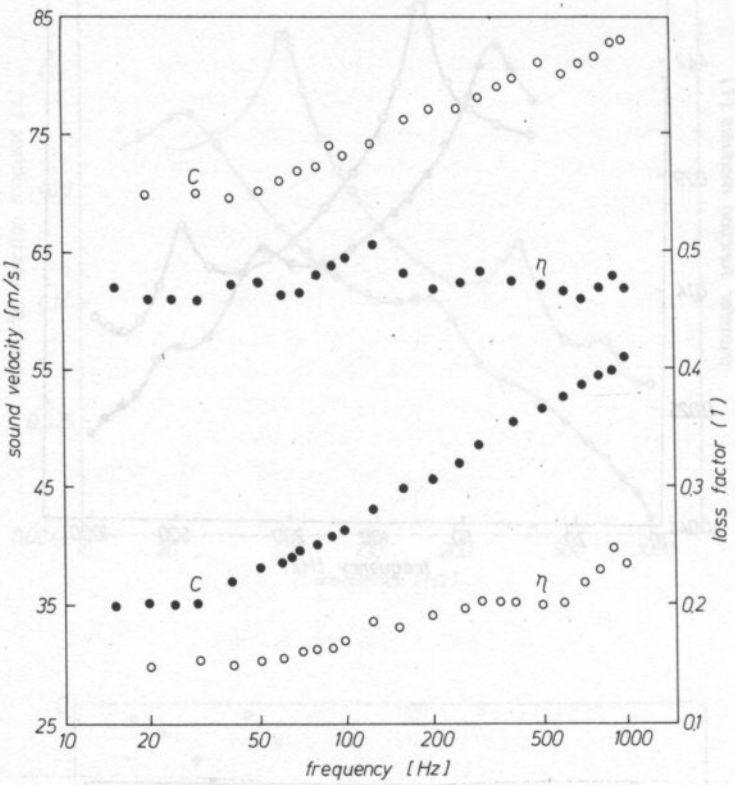

FIG. 5. Effect of the type of Rokopol on sound velocity and loss factor for compositions with TDI isocyanate, with a 30% microsphere content. Molar ratio NCO/OH = 1.3. —o—o— Rokopol M–12, —●—●— Rokopol 111

composition damping properties. Moreover, we noted the occurence of sound velocity dispersion in both examined types of composites, this being more pronounced with Rokopol 111. The ratio of the minimum to maximum velocity amounts to 1.6 for Rokopol 111 and 1.2 for Rokopol M–12 (for —NCO/—OH = 1.3).

The effect of the type of Rokopol upon sound velocity and loss factor can be explained in terms of structure of both composition types. Flexible segments of the material containing Rokopol M–12 are shorter than those in the composition with Rokopol 111 due to the difference in molecular weights of these polyetherols. In addition, accumulation of methane and cross-linking bonds is greater in the polymer containing Rokopol M–12, this being also the result of the polyetherol structure (shorter flexible segments). Materials containing Rokopol M–12 solidify faster and deaerate more readily compared to those with Rokopol 111, which is related to lower viscosity of Rokopol M–12, and in turn, affects damping properties of the composition.

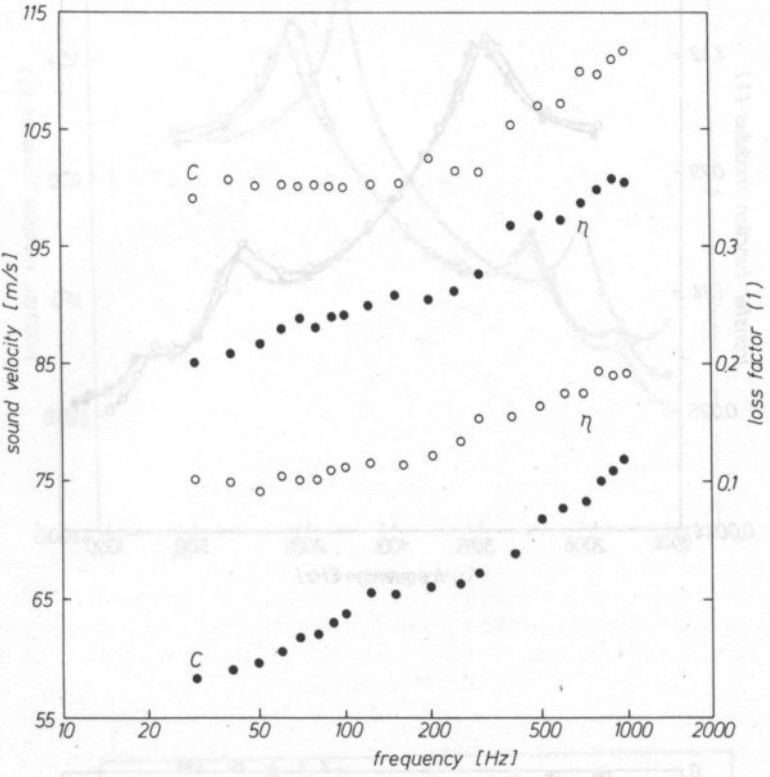

FIG. 6. Legend as for Figure 5. Molar ratio NCO/OH = 1.9

4.2. The effect of type and amount of isocyanate on sound velocity and loss factor in PU compositions

The synthesis was carried out for such proportions of Rokopol M–12 on one hand and TDI or MDI isocyanate on the other that the ratio of functional groups, —NCO/—OH, amounted to 1.1, 1.3 and 1.9, of respective components. Microspheres serving as the filling material constituted 30% of the main component. The results of measurements of the transfer function modulus and phase are shown in Figs. 7 and 8, and the calculated sound velocity and loss factor are given in Figs. 9 and 10.

As seen in Fig. 9, we observed no effect of the type of isocyanate on sound velocity within the frequency range investigated. The results obtained with TDI and MDI isocyanate are identical within experimental error. Nevertheless, with MDI isocyanate we noticed slight increase of the loss factor at frequencies up to 500 Hz.

Sound velocity is enhanced considerably upon the increase of the amount of isocyanate used in the synthesis (Fig. 10a), which is readily seen in the functional

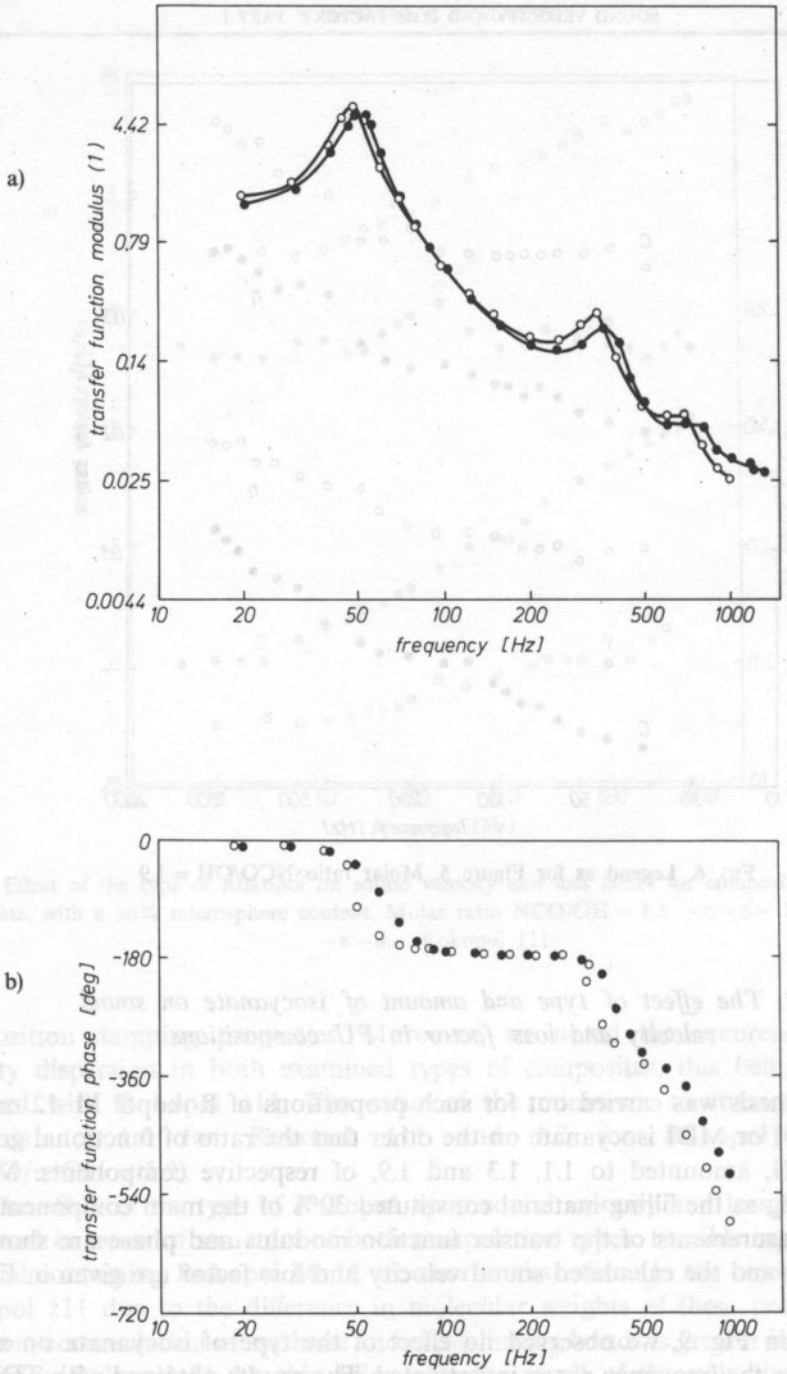

FIG. 7. Measured modulus (a) and phase (b) of the transfer function plotted against frequency for compositions with TDI isocyanate —○—○— and MDI isocyanate —●—●—. Molar ratio NCO/OH = 1.1

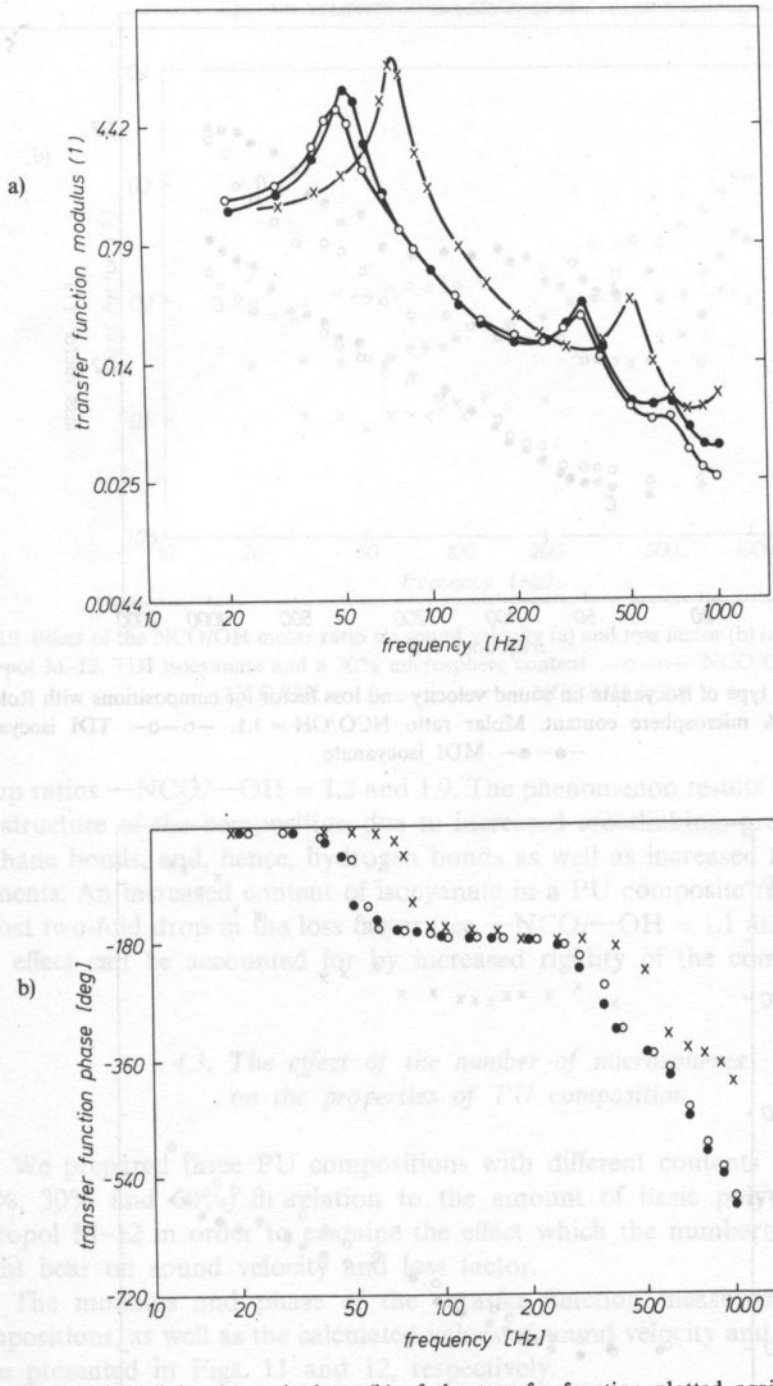

FIG. 8. Measured modulus (a) and phase (b) of the transfer function plotted against frequency for compositions with different ratio of NCO/OH. —○—○— NCO/OH = 1.1. —●—●— NCO/OH = 1.3. — × — × — NCO/OH = 1.9

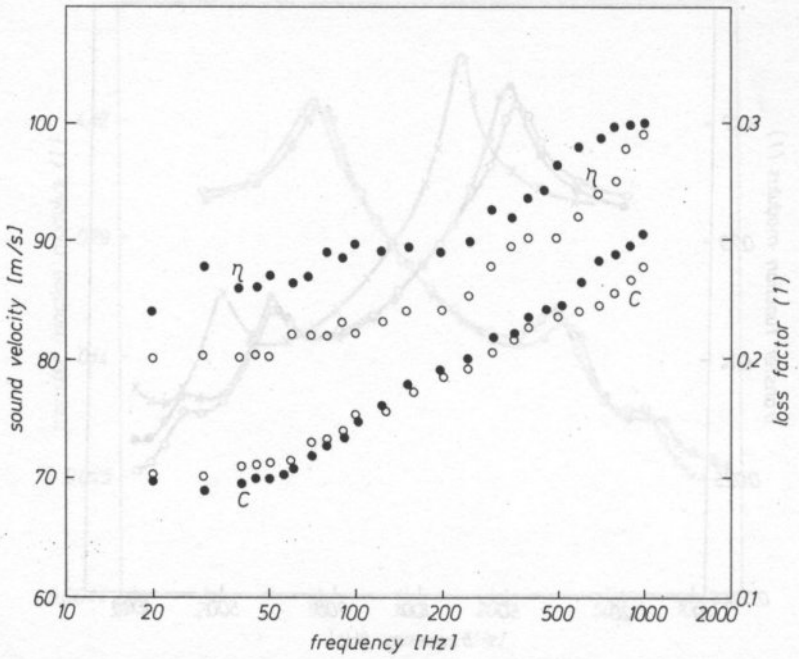

FIG. 9. Effect of the type of isocyanate on sound velocity and loss factor for compositions with Rokopol M–12, with a 30% microsphere content. Molar ratio NCO/OH = 1.1. —○—○— TDI isocyanate, —●—●— MDI isocyanate

a)

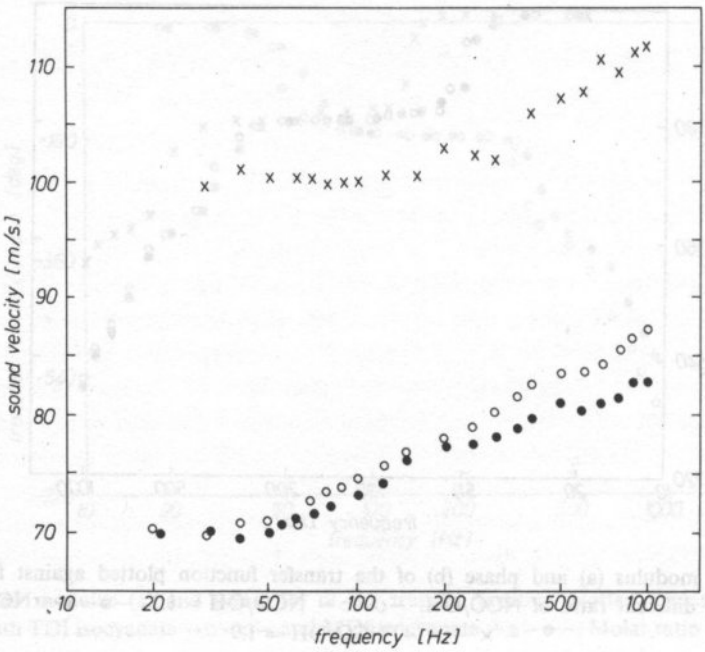

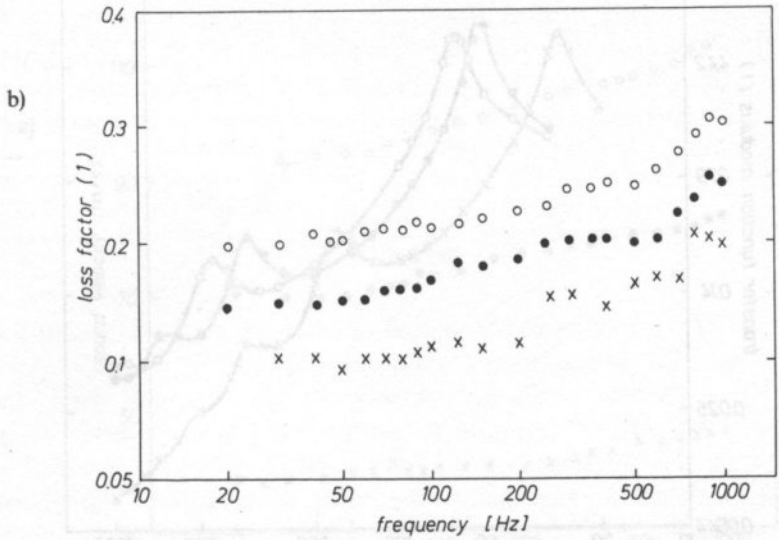

FIG. 10. Effect of the NCO/OH molar ratio on sound velocity (a) and loss factor (b) in compositions with Rokopol M–12. TDI isocyanate and a 30% microsphere content. —o—o— NCO/OH = 1.1, —●—●— NCO/OH = 1.3, — × — × — NCO/OH = 1.9

group ratios —NCO/—OH = 1.3 and 1.9. The phenomenon results from changes in the structure of the composition due to increased crosslinking, greater number of urethane bonds, and, hence, hydrogen bonds as well as increased number of rigid segments. An increased content of isocyanate in a PU composite results also in an almost two-fold drop in the loss factor (see —NCO/—OH = 1.1 and 1.9, Fig. 10b). The effect can be accounted for by increased rigidity of the composition.

4.3. The effect of the number of microspheres on the properties of PU composition

We prepared three PU compositions with different contents of microspheres (10%, 30% and 60%) in relation to the amount of basic polyurethane binder Rokopol M–12 in order to examine the effect which the number of microspheres might bear on sound velocity and loss factor.

The modulus and phase of the transfer function measured for the above compositions, as well as the calculated values of sound velocity and loss factor have been presented in Figs. 11 and 12, respectively.

As seen in Fig. 12a, sound velocity in the compositions investigated depended strongly on the amount of contained microspheres and enhanced when increasing their number. Simultaneously, we observed dispersion of sound, the dependence of the sound velocity on frequency being almost linear. The value of the loss factor was

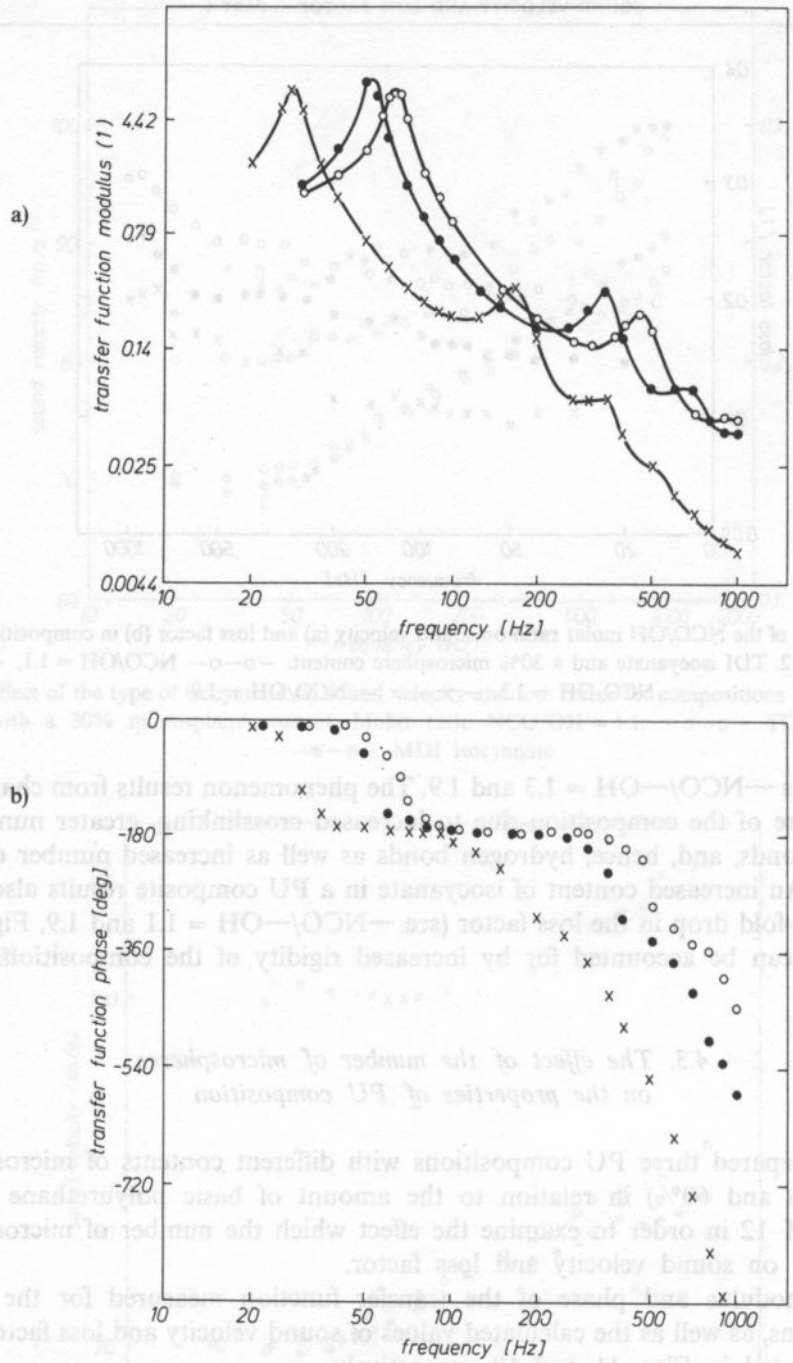

FIG. 11. Measured modulus (a) and phase (b) of the transfer function plotted against frequency for compositions with different contents of microspheres in relation to the basic PU binder. — × — × — 10%, —●—●— 30%, —○—○— 60%. Molar ratio NCO/OH = 1.3

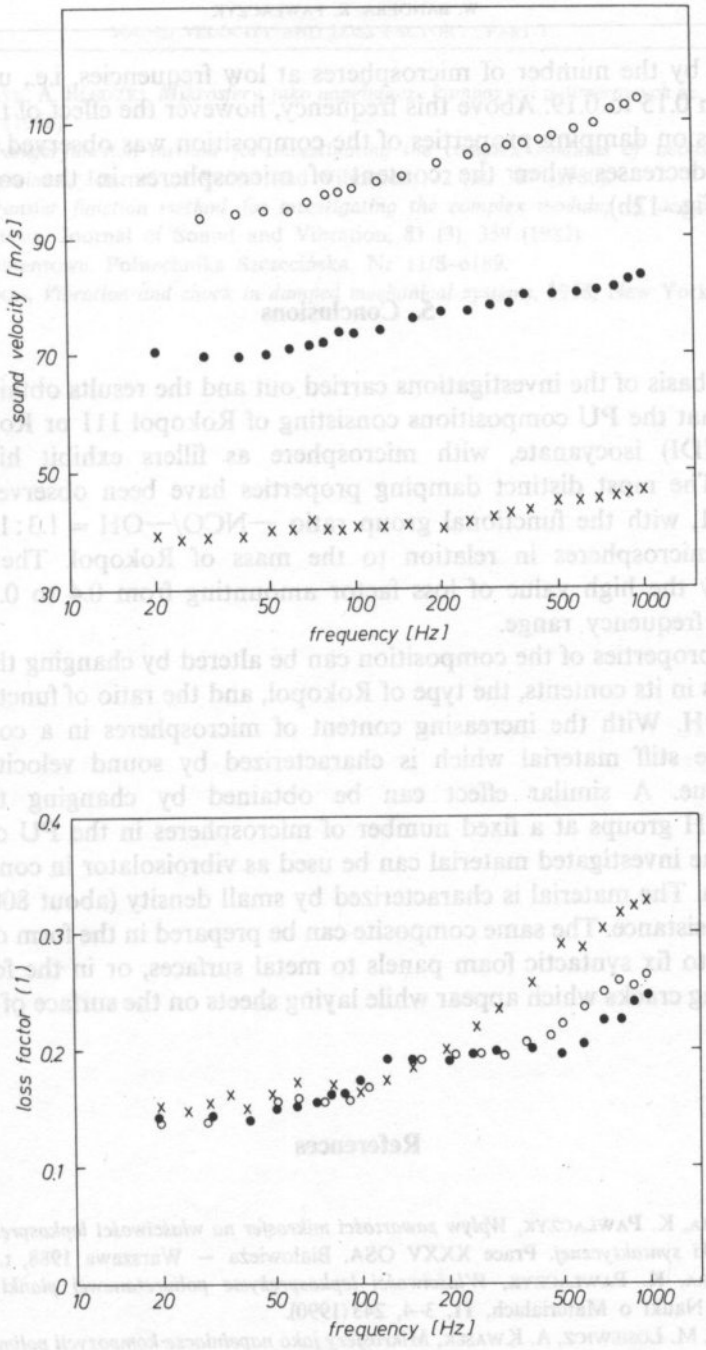

FIG. 12. Effect of microsphere contents on sound velocity (a) and loss factor (b) for compositions with Rokopol M–12 and TDI isocyanate. Molar ratio NCO/OH = 1.3. – × – × – 10%, –●–●– 30%, –○–○– 60% microsphere content

not affected by the number of microspheres at low frequencies, i.e., up to 200 Hz, varying from 0.15 to 0.19. Above this frequency, however the effect of the number of microspheres on damping properties of the composition was observed. The value of loss factor decreases when the content of microspheres in the composition is increased (Fig. 12b).

5. Conclusions

On the basis of the investigations carried out and the results obtained it can be concluded that the PU compositions consisting of Rokopol 111 or Rokopol M–12, TDI (or MDI) isocyanate, with microsphere as fillers exhibit high damping properties. The most distinct damping properties have been observed in case of Rokopol 111, with the functional group ratio —NCO/—OH = 1.3:1 and a 30% content of microspheres in relation to the mass of Rokopol. The property is evidenced by the high value of loss factor amounting from 0.4 to 0.5 within the investigated frequency range.

Elastic properties of the composition can be altered by changing the number of microspheres in its contents, the type of Rokopol, and the ratio of functional groups —NCO/—OH. With the increasing content of microspheres in a composite one obtains more stiff material which is characterized by sound velocity of almost doubled value. A similar effect can be obtained by changing the ratio of —NCO/—OH groups at a fixed number of microspheres in the PU composite. It seems that the investigated material can be used as vibroisolator in constructions of various types. The material is characterized by small density (about 800 kg/m^3 and high water resistance. The same composite can be prepared in the form of glue which can be used to fix syntactic foam panels to metal surfaces, or in the form of paste useful in filling cracks which appear while laying sheets on the surface of an insulated object.

References

[1] W. BANDERA, K. PAWLACZYK, *Wpływ zawartości mikrosfer na właściwości lepkosprężyste poliuretanowej pianki syntaktycznej*. Prace XXXV OSA, Białowieża – Warszawa 1988, t. 1, 102–107.

[2] W. BANDERA, K. PAWLACZYK, *Właściwości lepkosprężyste poliuretanowej pianki syntaktycznej*, Archiwum Nauki o Materiałach, **11**, 3–4, 243 (1990).

[3] A. BŁĘDZKI, M. ŁOSIEWICZ, A. KWASEK, *Mikrosfery jako napełniacze kompozycji polimerowych cz. II*, Polimery, **30** (4), 154 (1985).

[4] I. L. BUCHANAN, *Numerical solution for the dynamic moduli of a viscoelastic bar*, Journal of Acoustical Society of America, 81 (6), 1775 (1987).

[5] K. PAWLACZYK, A. BŁĘDZKI, Patent PRL Nr 129137 (1983).

[6] K. PAWLACZYK, A. BŁĘDZKI, *Mikrosfery jako napełniacze kompozycji polimerowych* cz. III, Polimery **31**, (7), 254 (1986).

[7] K. PAWLACZYK, A. BŁĘDZKI, *Mikrosfery jako napełniacze kompozycji polimerowych* cz. IV, Polimery, **31** (11), 425 (1986).
[8] T. PRITZ, *Transfer function method for investigating the complex modulus of acoustic materials: spring-like specimen*, Journal of Sound and Vibration, 72 (3), 317 (1980).
[9] T. PRITZ, *Transfer function method for investigating the complex modulus of acoustic materials: rod-like specimen*, Journal of Sound and Vibration, 81 (3), 359 (1982).
[10] Zgłoszenie patentowe, Politechnika Szczecińska, Nr 11/S–6189.
[11] J. C. SNOWDON, *Vibration and shock in damped mechanical systems*, 1968, New York, John Wiley & Sons.

ARCHIVES OF ACOUSTIC
16, 3–4, 451–460 (1991)

SOUND VELOCITY AND LOSS FACTOR OF POLYURETHANE COMPOSITES. PART II

W. BANDERA AND K. PAWLACZYK*

Laboratory of Applied Acoustics and Spectroscopy Gdańsk University
(80-952 Gdańsk, ul. Wita Stwosza 57)
* Institute of Chemical Technology Technical University of Szczecin
(70-322 Szczecin, ul. Pułaskiego 10)

Elastic, non-foamed polyurethane compositions to be used as vibro-insulating materials have been developed. The compositions were prepared using poly (propyleno-ethers) of different molecular weights, toluyene diisocyanate and aluminum hydrate as the filling agent. The effect of the composition contents on viscoelastic properties that is, on sound velocity and loss factor has been determined. It has been found that various types of the filler permit to modify properties of composite and especially its stiffness and internal damping.

1. Introduction

The production technology and the methods of investigating the basic viscoelastic properties of polyurethane composites were developed when searching for new acoustic materials to be employed for solving vibration isolation problems. Part one of these investigations has been devoted to polyurethane composites filled with microspheres [1].

In that paper the effect of the chemical compositions of the polyurethane binder and the amount of microspheres, acting as the filling agent, upon the elasticity and damping ability of the composition have been investigated, i.e., the sound velocity and loss factor were determined. The both quantities enable the components of Young's complex modulus to be calculated, thus being of fundamental significance for proper choice of vibroinsulating materials.

The aim of the present paper is to determine the correlation between the type and amount of the filler, and sound velocity and loss factor of the polyurethane PU composite. In order to investigate this correlation we prepared a new kind of PU composite filled with aluminium hydrate $Al_2O_3 \cdot 3H_2O$ instead of microspheres [1, 3].

2. Characteristics of the material

Unfoamed PU composition was the investigation object, where aluminum hydrate in the form of powder was used as the filling agent. The PU binder is composed of poly(oxypropylene)trioles and diisocyanates. The introduction of the filler into the polyurethane composition induces the changes in the PU lattice structure, the mobility of the lattice fragments and the increase in the rigidity of the polymer chain. The investigation was carried out on two series of specimens.

In the first series, one of the PU binder components was Rokopol M–12, i.e., poly(oxypropyleneethylene)triole with the molecular weight of 4800, the other was MDI isocyanate (4.4-diisocyanatodiphenylomethane). The ratio of the number of hydroxyl functional group —OH in macrotriole to that of the —NCO group in isocyanate was 1:1.3. The amount of aluminum hydrate serving as the filling agent was varied from 10% to 60% relative to the main component of PU binder, i.e., Rokopol M–12.

In the second series, the properties of the PU binder were changed by replacing Rokopol M–12 with Rokopol 111, characterized by molecular weight of 6000. The ratio of the functional groups —OH and —NCO was 1:1.5, and the amount of the filler varied from 20% to 60% relative to Rokopol 111. One more specimen with fixed filler content (30%) and functional group ratio —OH:—NCO = 1:1.3 was also prepared in order to compare viscoelastic properties of the composite with those ones obtained earlier for PU composite filled with microspheres [1, 2]. Density of the PU composition with aluminum hydrate as the filling agent is varied from 1200 kg/m^3 to 1300 kg/m^3 depending on the amount of the filler.

3. Measurement method

In order to find the sound velocity and loss factor of the PU composite in frequency function the measurement method of vibration transfer function has been used [4, 5]. Figure 1 presents the idea of the measurement.

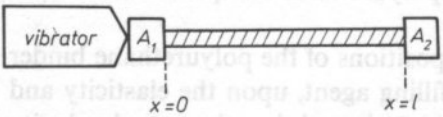

FIG. 1. Rod-like specimen excited to longitudinal vibrations by means of a vibrator

It is assumed that the cross-section of the rod is constant, the relation between stress and strain is linear, lateral motion is not prevented at the rod ends and the lateral dimension is much smaller than the elastic wavelength. The expression for the complex transfer function can be formulated as the ratio of magnitudes of vibration accelerations at both ends of the specimen

$$\mathbf{T} = \frac{A_2}{A_1} = |T| \cdot e^{i\varphi} = \left|\frac{A_2}{A_1}\right| e^{i\varphi} \tag{1}$$

where $|T|$ is the transfer function modulus, A_2 and A_1 are vibration accelerations at the end of the specimen, respectively, φ is the transfer function phase and i is the imaginary unit.

The complex transfer function **T** can be expressed by the propagation constant

$$\mathbf{T} = [\operatorname{ch}\gamma l + (M/m)\gamma l \cdot \operatorname{sh}\gamma l]^{-1} \tag{2}$$

where γ is the propagation constant, $\gamma = \alpha + i\beta$, α is the attenuation constant, β is the phase constant, l is the rod length, m is the specimen mass, M is the loaded mass including accelerometer mass.

While measuring the transfer function modulus and the phase for each frequency, the components of propagation constant were found from formula (2) and subsequently, sound velocity c and loss factor η were calculated from well-known formulae [5]

$$C = \frac{2\pi f}{\beta}, \quad \eta = \frac{2d}{1-d^2} \tag{3, 4}$$

where f is the frequency and $d = \alpha/\beta$.

The measurement error of transfer function modulus $|T|$ was not larger than $\pm 5\%$ and the phase was determined with the error not larger than ± 0.4 deg in the whole range of frequency i.e. from 20 Hz to 1000 Hz. It allowed to find the sound velocity with the error of $\pm 5\%$, and the loss factor with the error of $\pm 10\%$.

In investigations a prismatic shaped specimens of 1 cm^2 cross-section and about 12 cm length were used. The amplitude of the vibration acceleration was adjusted carefully not to exceed the dynamic strain limit of linearity of the investigated material. A detailed description of the measurement system and the method of carrying out the measurements of the transfer function modulus and phase have been presented in [1, 6].

4. Results and discussion

The measurements were made at room temperature in frequency range from 20 Hz to 1000 Hz. The measurement of transfer function modulus for frequencies above 1000 Hz was not possible because of the large damping of the signal in the material investigated. For the upper limit of the measurement range, the ratio of the length of the longitudinal wave to the lateral dimensions of the specimen was properly large which allowed to neglect the influence of transverse vibrations on the calculation of sound velocity and loss factor.

The modulus and phase of the transfer function measured for the first series of specimens and the calculated values of the sound velocity and loss factor have been shown in Figures 2, 3 and 4, respectively.

It is seen from the presented results that the change of the number of aluminum hydrate from 10% to 30% practically does not have any effect on the sound velocity in the composition investigated.

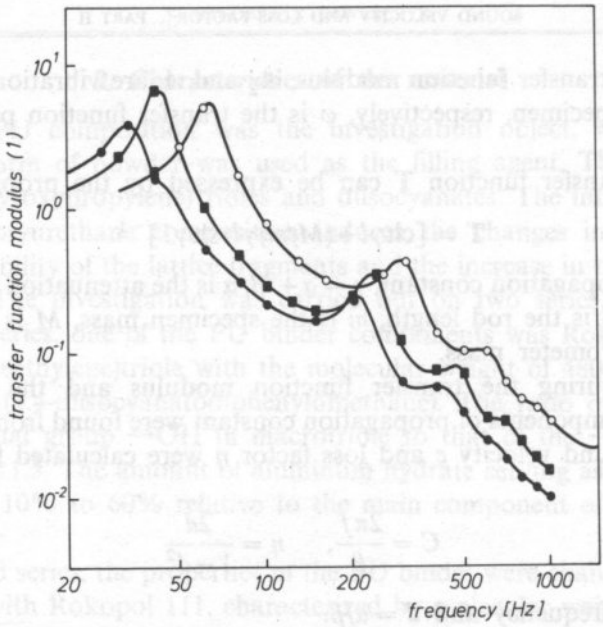

FIG. 2. Measured modulus of the transfer function plotted against frequency for the compositions with Rokopol M–12 and different contents of aluminum hydrate. ■■ 10%, ●● 30%, ○○ 60%. Molar ratio —OH/—NCO = 1:1.3

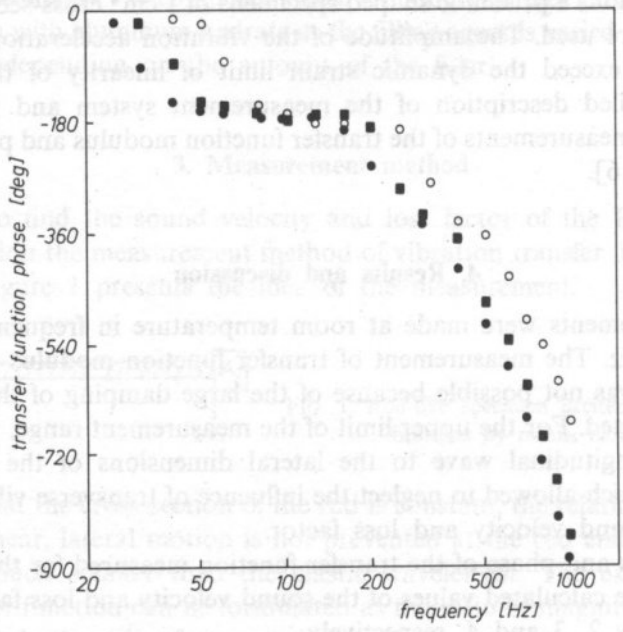

FIG. 3. Measured phase of the transfer function. Further legend as for Fig. 2

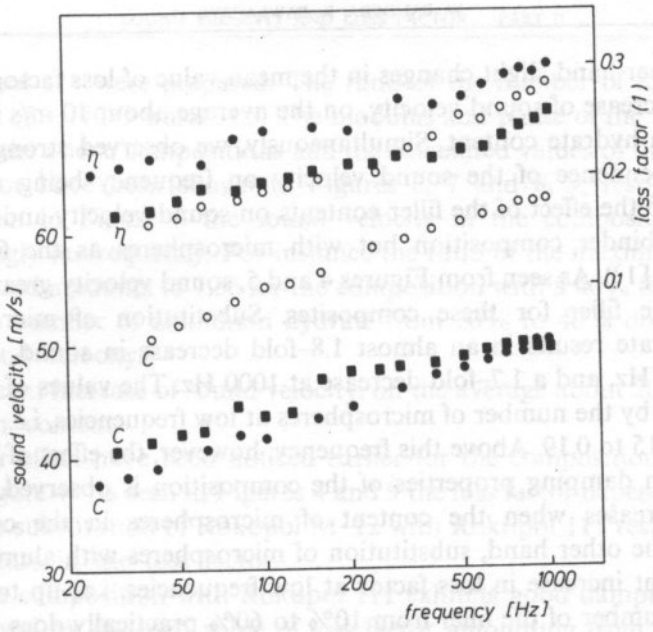

FIG. 4. Sound velocity and loss factor for the compositions with different content of aluminum hydrate. Further legend as for Fig. 2

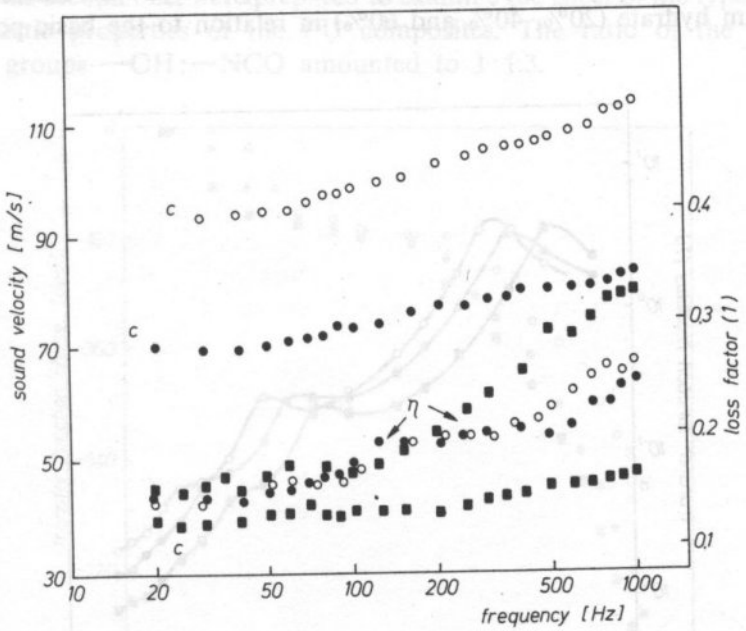

FIG. 5. Effect of microsphere contents on the sound velocity and the loss factor for the compositions with Rokopol M–12. Molar ratio —OH/—NCO = 1:1.3 ■■ 10%, ●● 30%, ○○ 60% microsphere content (after [1])

On the other hand slight changes in the mean value of loss factor are observed. A significant increase of sound velocity, on the average about 10 m/s is observed for 60% aluminum hydrate content. Simultaneously, we observed strong dispersion of sound, the dependence of the sound velocity on frequency being almost linear.

In Figure 5 the effect of the filler contents on sound velocity and loss factor for the same PU binder composition but with microspheres as the filling agent is presented (after [1]). As seen from Figures 4 and 5, sound velocity greatly depends on the type of the filler for these composites. Substitution of microspheres with aluminum hydrate results in an almost 1.8–fold decrease in sound velocity at the frequency of 25 Hz, and a 1.7–fold decrease at 1000 Hz. The values of the loss factor are not affected by the number of microspheres at low frequencies, i.e., up to 200 Hz, varying from 0.15 to 0.19. Above this frequency, however, the effect of the number of microspheres on damping properties of the composition is observed. The value of loss factor decreases when the content of microspheres in the composition is increased. On the other hand, substitution of microspheres with aluminum hydrate results in a slight increase in loss factor at low frequencies, i.e., up to 300 Hz. The change of the number of the filler from 10% to 60% practically does not cause any influences of loss factor, however, a slight increase of the loss factor for the composition with 30% content of the filler is observed.

In the next step of investigation, three PU compositions with different contents of aluminum hydrate (20%, 40% and 60%) in relation to the basic polyurethane

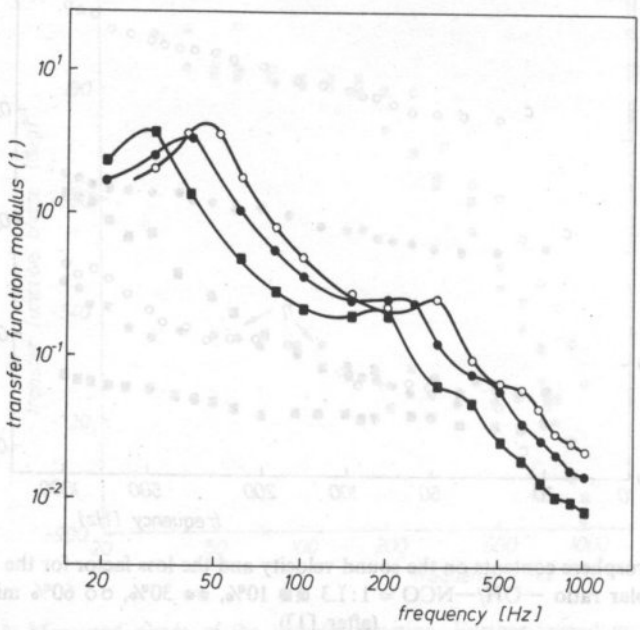

FIG. 6. Measured modulus of the transfer function plotted against frequency for the compositions with Rokopol 111. Molar ratio—OH/—NCO = 1:1.5 ■■ 20%, ●● 40%, ○○ 60% aluminum hydrate content

binder Rokopol 111 were prepared. The ratio of the number of functional groups —OH to that of —NCO was 1:1.5. The modulus and phase of the transfer function measured for the above compositions and the calculated values of the sound velocity and loss factor have been shown in Figures 6, 7 and 8, 9, respectively.

As is seen in Figure 8 the sound velocity in the composition investigated depends strongly on frequency. For instance the ratio of the maximum to minimum velocity of sound amounts to 1.56 for the composition with a 40% filler content. The change of the number of aluminum hydrate from 20% to 40% does not have any effect on sound velocity.

A significant increase of sound velocity, on the average about 20 m/s is observed for 60% filler content.

A similar effect have been noticed earlier for the compositions with Rokopol M–12 (see Figure 4). As seen in Figures 4 and 9 the loss factor depends on the type of Rokopol. The substitution of Rokopol M–12 with Rokopol 111 results in an almost 1.5–fold increase in the loss factor.

Thus, the composition with Rokopol 111 exhibits good damping properties. It has been proved by the high value of loss factor amounting from 0.3 to 0.4 in the investigated frequency range. In the last step of our investigations two compositions with Rokopol 111 and microspheres as the filling agent in the first and aluminum hydrate in the second one, were prepared to examine the effect of the type of the filler on viscoelastic properties of the PU composites. The ratio of the number of functional groups —OH:—NCO amounted to 1:1.3.

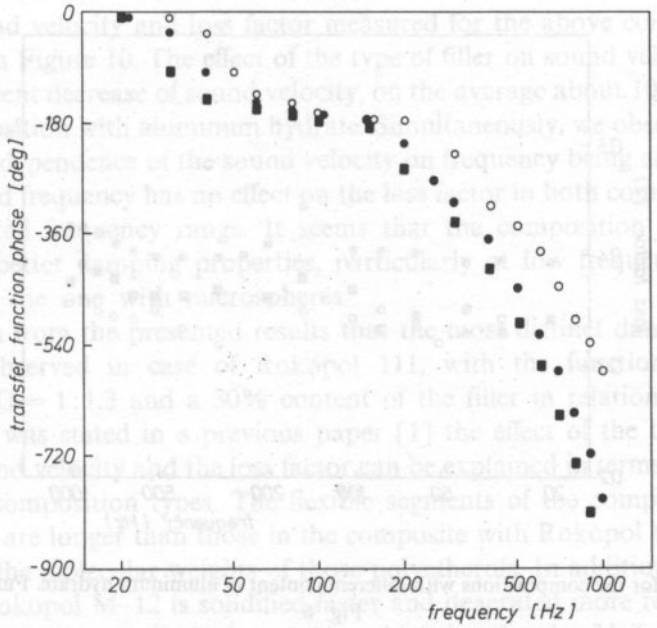

FIG. 7. Measured phase of the transfer function. Further legend as for Fig. 6

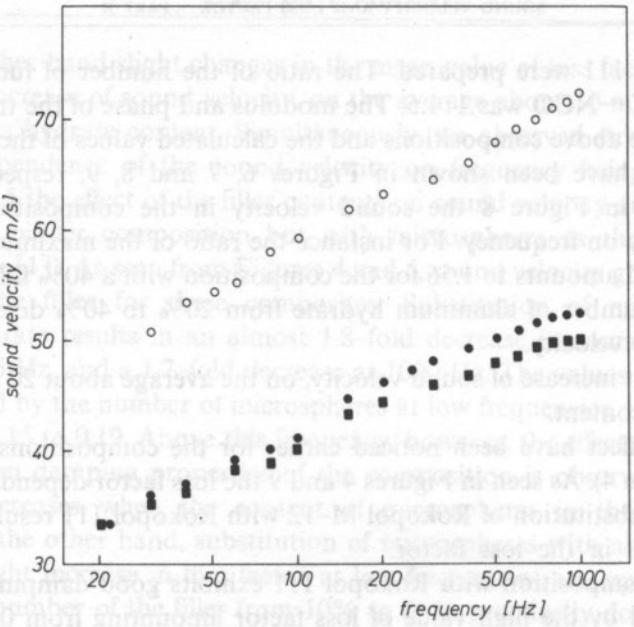

FIG. 8. Sound velocity for the compositions with different content of aluminum hydrate. Further legend as for Fig. 6

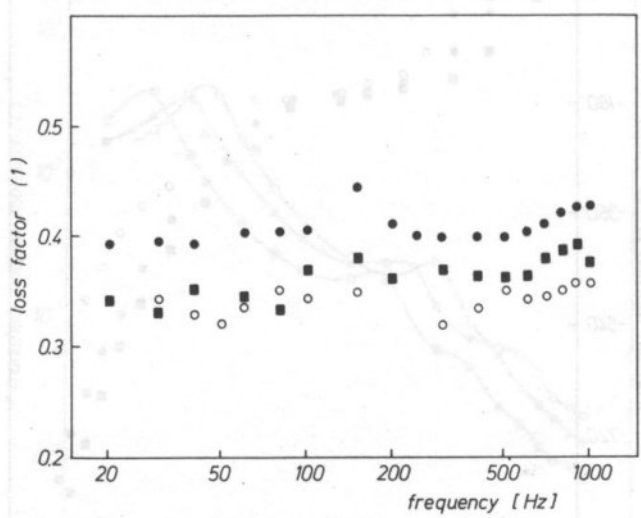

FIG. 9. Loss factor for the compositions with different content of aluminum hydrate. Further legend as for Fig. 6

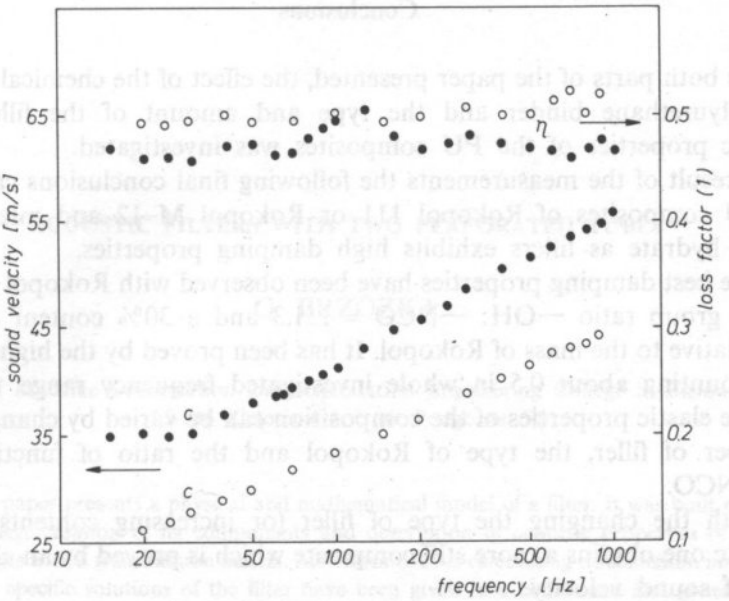

FIG. 10. Effect of the type of filler on the sound velocity and loss factor for the compositions with Rokopol 111 and a 30% filler content. ●● microspheres, ○○ aluminum hydrate. Molar ratio —OH/—NCO = 1:1.3

The sound velocity and loss factor measured for the above compositions have been shown in Figure 10. The effect of the type of filler on sound velocity is evident.

A significent decrease of sound velocity, on the average about 10 m/s is observed for the composition with aluminum hydrate. Simultaneously, we observed dispersion of sound, the dependence of the sound velocity on frequency being almost linear. On the other hand frequency has no effect on the loss factor in both compositions within the investigated frequency range. It seems that the composition with aluminum hydrate has better damping properties, particularly at low frequencies, i.e., up to 100 Hz then the one with microspheres.

It is seen from the presented results that the most distinct damping properties have been observed in case of Rokopol 111, with the functional group ratio —OH/—NCO = 1:1.3 and a 30% content of the filler in relation to the mass of Rokopol. As was stated in a previous paper [1] the effect of the type of Rokopol upon the sound velocity and the loss factor can be explained in terms of the structure of the both composition types. The flexible segments of the composite containing Rokopol 111 are longer than those in the composite with Rokopol M–12 due to the difference in the molecular weights of those polyetherols. In addition, the composite containing Rokopol M–12 is solidified faster and deaerated more readily compared with the compositions with Rokopol 111 which is related with lower viscosity of Rokopol M–12, affecting in turn, the damping properties of the composition.

Conclusions

In the both parts of the paper presented, the effect of the chemical composition of the polyurethane binder and the type and amount of the filler upon the viscoelastic properties of the PU composites was investigated.

As a result of the measurements the following final conclusions can be drawn.

1. PU composites of Rokopol 111 or Rokopol M–12 and microspheres or aluminum hydrate as fillers exhibits high damping properties.

2. The best damping properties have been observed with Rokopol 111, with the functional group ratio —OH: —NCO = 1:1.3 and a 30% content of aluminum hydrate relative to the mass of Rokopol. It has been proved by the high value of loss factor amounting about 0.5 in whole investigated frequency range.

3. The elastic properties of the composition can be varied by changing the type and number of filler, the type of Rokopol and the ratio of functional groups —OH:—NCO.

4. With the changing the type of filler (or increasing contents of filler) in a composite one obtains a more stiff composite which is proved by an almost double increase of sound velocity.

5. It seems that the investigated PU composites could be used as vibroisolating material in constructions of various types.

References

[1] W. BANDERA, K. PAWLACZYK, *Sound velocity and loss factor of polyurethane composites – part I*, Archives of Acoustics, **16** 34, (1991).

[2] W. BANDERA, K. PAWLACZYK, *Właściwości lepkosprężyste poliuretanowej pianki syntaktycznej*, Archiwum Nauki o Materiałach, **11**, 3–4, 243 (1990).

[3] W. BANDERA, K. PAWLACZYK, *Damping properties of polyurethane composites*, Proc. of the Inter-Noise Conference, Gothenburg, Sweden 1990, vol. 2, pp. 1363–1366.

[4] I. L. BUCHANAN, *Numerical solution for the dynamic moduli of a viscoelastic bar*, Journal of Acoustical Society of America, **81** (6), 1775, (1987).

[5] T. PRITZ, *Transfer function method for investigating the complex modulus of acoustic materials: rod-like specimen*, Journal of Sound and Vibration, **81** (3), 359 (1982).

[6] T. PRITZ, *Transfer function method for investigating the complex modulus of acoustic materials: spring like specimen*, Journal of Sound and Vibration, **72** (3), 317 (1980).

ARCHIVES OF ACOUSTICS
16, 3–4 461–474, (1991)

ACOUSTIC FILTERS WITH TWO PERFORATED TUBES

G. BRZÓZKA

Institute of Machine Construction and Exploitation Engineering College in Zielona Góra
(65-246 Zielona Góra, ul. Podgórna 50)

This paper presents a physical and mathematical model of a filter. It was built on the basis of segmentation of its components and description of acoustic properties of these components with a transmission matrix. Also formulae for calculating transmission matrices for many specific solutions of the filter have been given in a convenient and generalized form. The presented model is limited to: the conditions of propagation of a harmonic plane acoustic wave, small dimensions of the holes in the perforation and laminar flow through these holes.

1. Introduction

Previously [3] a physical and mathematical model of an acoustic filter with one perforated tube was presented. Also cases of two parallel perforated tubes in a tube with rigid walls are encountered in practice applications.

Here we will outline the physical model and present a complete mathematical model, which can be a basis for an algorithm and computer programme for the last case.

The general conception of determining a mathematical model was given by SULLIVAN [5, 6]. It was developed by MUNJAL [4], who presented generalized forms of several equations. Yet, mathematical models given in the mentioned paper are too general and it is not possible to elaborate an algorithm for digital calculations on their basis. It took the author of this paper a considerable amount of time to determine detailed mathematical models when he was preparing such a programme. Therefore, the author considered it worth sharing the results of his work in order to save the time of readers who intended to create their own calculation programmes.

2. Outline of physical model

The physical model and accepted notations are presented in Fig. 1. As in the case of one perforated tube [3], this model is based on the assumption that the conditions of propagation of a plane wave are fulfilled in all wave-guides created by the tubes.

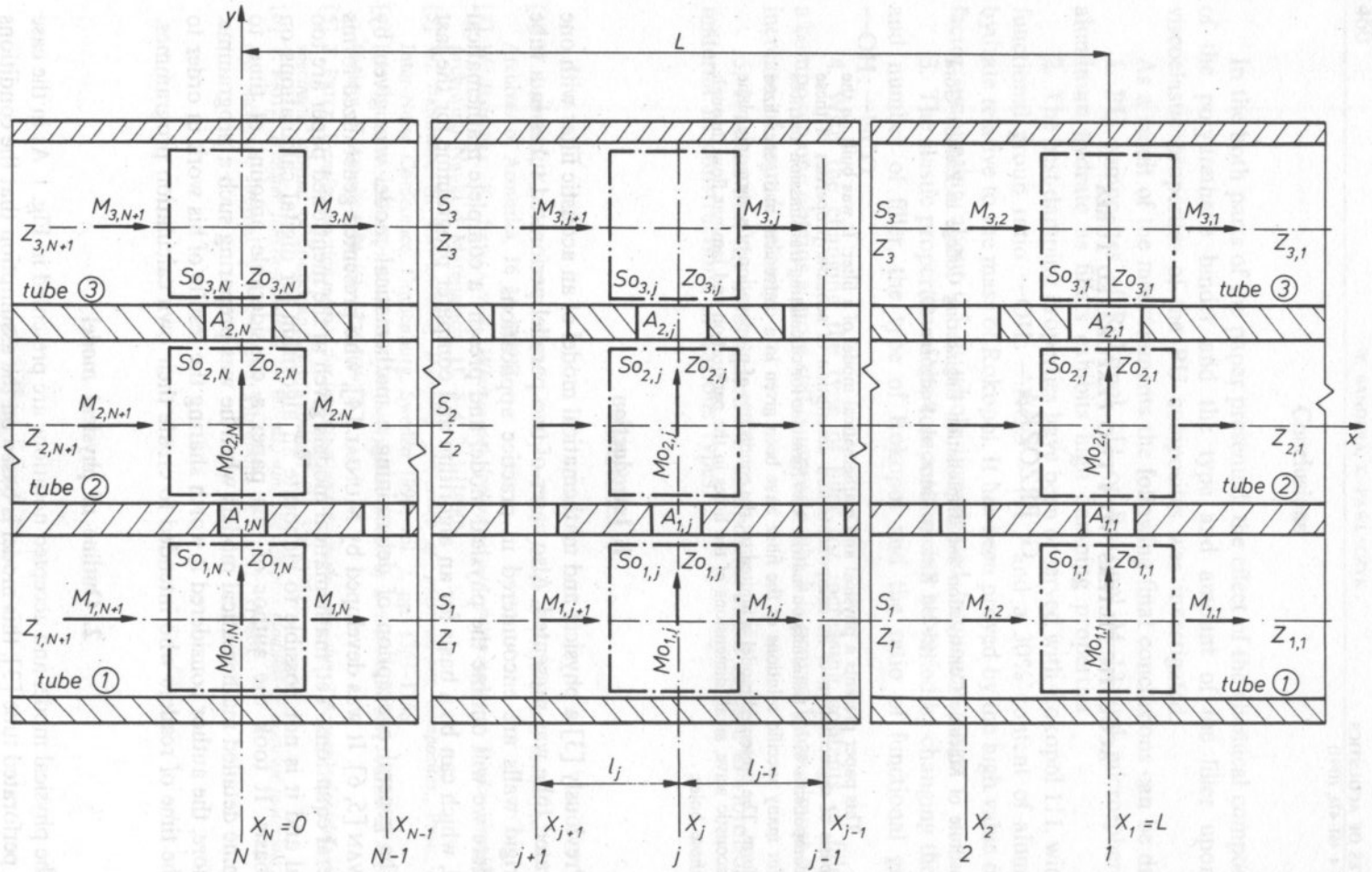

FIG. 1. Physical model and acoustic filter with two perforated tubes

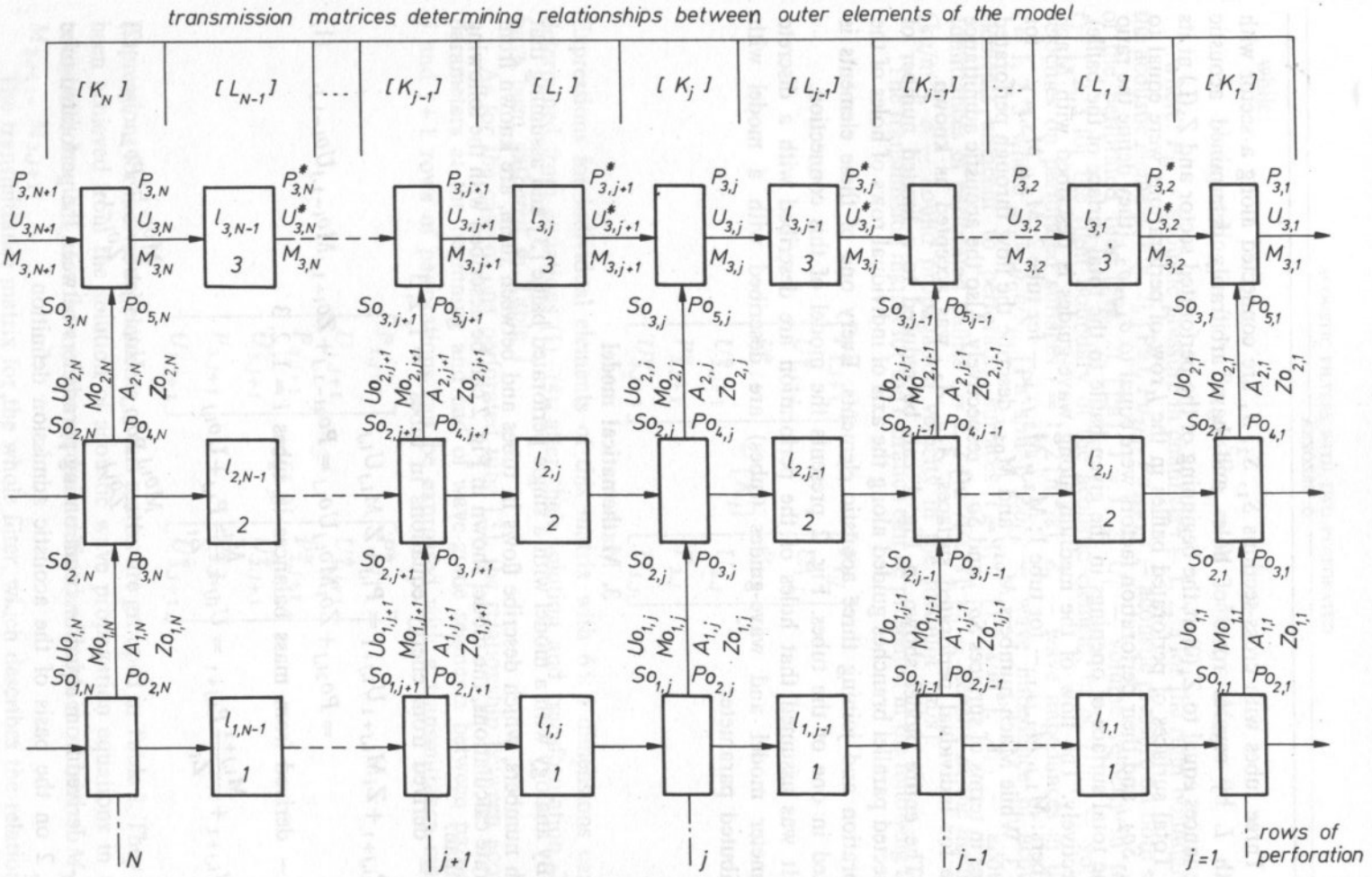

FIG. 2. Diagram of an analogue system of a filter with two perforated tubes

Three tubes with cross-sections S_1, S_2, S_3 are connected along a sector with length L by several rows of holes and have arbitrarily determined acoustic impedances equal to $Z_k(0)$ at the beginning of the perforated sector and $Z_k(L)$ at its end. Total surfaces of perforated baffles in the j row of perforations were equal to $So_{1,j}$, $So_{2,j}$ and their perforation factors were equal to $\sigma_{1,j}$, $\sigma_{2,j}$ (they define the ratio of the total surface of openings in the given baffle to the total surface of the baffle), respectively. The flow of the medium along wave-guides is described with Mach numbers: $M_{1,j}$, $M_{1,j+1}$ – for tube 1; $M_{2,j}$, $M_{2,j+1}$ – for tube 2; $M_{3,j}$, $M_{3,j+1}$ – for tube 3. While Mach numbers $M_{01,j}$ and $M_{02,j}$ describe the flow through perforated baffles in terms of surfaces $So_{1,j}$ and $So_{2,j}$, respectively. Also the acoustic admittance value for individual perforated surfaces. $A_{1,j}$, $A_{2,j}$ was accepted as known.

The entire model shown in Fig. 1 can be reduced to a limited number of connected parallel branches guided along the axis of individual rows of holes of the perforation and joining three acoustic elements. Every one of these elements is located in one of the tubes. Fig. 2 presents the model of this connection.

It was assumed that holes of the perforation are described with a discrete parameter model and wave-guides (tubes) are described with a model with distributed parameter.

3. Mathematical model

By analogy with a model with a single perforated baffle [3] and assuming that Mach numbers, which describe flows in tubes and between them, are known from separate calculations, the model shown in Fig. 2 can be described with the following formulae:

– derived from energy equations in tubes $i = 1, 2, 3$

$$P_{i,j+1}+Z_iM_{i,j+1}U_{i,j+1} = P_{i,j}+Z_iM_{i,j}U_{i,j}$$
$$= Po_{2i,j}+Zo_iMo_{i,j}Uo_{i,j} = Po_{2i-1,j}+Zo_{i-1,j}Mo_{i-1,j}Uo_{i-1,j}, \quad (1)$$

– derived from mass balances in tubes $i = 1, 2, 3$

$$U_{i,j+1}+\frac{M_{i,j+1}}{Z_i}P_{i,j+1} = U_{i,j}+\frac{M_{i,j}}{Z_i}P_{i,j}+Uo_{i,j}$$
$$+\frac{Mo_{i,j}}{Zo_{i,j}}Po_{2i,j}-Uo_{i-1,j}+\frac{Mo_{i-1,j}}{Zo_{i-1,j}}Po_{2i-1,j}, \quad (2)$$

– derived from equations confronting parameters between the perforated tube $i = 1, 2$ on the basis of the acoustic admission definition

$$Po_{2i+1,j} = Po_{2i,j}+\frac{Uo_{i,j}}{A_{i,j}}, \quad (3)$$

while:

$$Uo_{0,j} = Uo_{3,j} = 0; \quad Po_{1,j} = Po_{6,j} = 0; \quad Mo_{0,j} = M_{3,j} = 0. \tag{4}$$

where: P_{ij} – acoustic pressure in channels $i = 1, 2, 3$ for the right boundary of the acoustic element (Fig. 2), [Pa], $Po_{2i,j}$, $Po_{2i+1,j}$ – acoustic pressure on both sides of the perforated tube (Fig. 2), [Pa]; $i = 1, 2$, U_i – volume velocity in tubes $i = 1, 2, 3$ for the right boundary of the acoustic element, m^3/s, $Uo_{i,j}$ – volume velocities on perforated surfaces $i = 1, 2$ [m^3/s], Z_i – wave impedances in tubes $i = 1, 2, 3$ where $Z_i = \varrho_0 c/S_i$, [Pa·s/m^3], $Zo_{i,j}$ – wave impedance of acoustic elements adjacent to perforated surfaces $i = 1, 2$ [Pa·s/m^3], $A_{i,j}$ – acoustic admittances of perforated baffles $i = 1, 2$ [m^3/Pa·s], ϱ_0 – density of the medium, [kg/m^3], c – sound propagation velocity in the medium [m/s].

The transmission matrix for the i–branch can be presented in the following form

$$\begin{bmatrix} P^*_{1,j+1} \\ U^*_{1,j+1} \\ P^*_{2,j+1} \\ U^*_{2,j+1} \\ P^*_{3,j+1} \\ U^*_{3,j+1} \end{bmatrix} = [K_j] \begin{bmatrix} P_{1,j} \\ U_{1,j} \\ P_{2,j} \\ U_{2,j} \\ P_{3,j} \\ U_{3,j} \end{bmatrix}. \tag{5}$$

Expressions for individual elements of this matrix with 6×6 dimensions can be determined from equations (1)–(4), after their solution and transformation. They have been gathered in Table 1.

As for the case of one perforated tube [3], the relationship between acoustic parameters at the beginning and end of wave-guide segments between particular j and $j+1$ rows of perforations can be exprossed with a transmittance matrix

$$\begin{bmatrix} P_{1,j+1} \\ U_{1,j+1} \\ P_{2,j+1} \\ U_{2,j+1} \\ P_{3,j+1} \\ U_{3,j+1} \end{bmatrix} = [L_j] \begin{bmatrix} P^*_{1,j+1} \\ U^*_{1,j+1} \\ P^*_{2,j+1} \\ U^*_{2,j+1} \\ P^*_{3,j+1} \\ U^*_{3,j+1} \end{bmatrix}. \tag{6}$$

Expressions for individual elements of this matrix are grouped in Table 2. They have been achieved from the solution of acoustic wave propagation equations in three tubes with length $l_{i,j}$ for flow of the medium defined with Mach numbers: $M_{1,j+1}$, $M_{2,j+1}$, $M_{3,j+1}$.

The transmittance matrix for the whole filter, which describes the relationship between acoustic parameters in the last N-row and first row of perforations ($j = 1$),

Table 1. Formulae for elements of the transmission matrix $[K_j]$

K_{kl}	Calculation formula	K_{kl}	Calculation formula
K_{11}	$1-B_3G_1/E_1$	K_{21}	G_1/E_1
K_{12}	$B_1-B_3[1-B_1(B_2-G_1)]/E_1$	K_{22}	$[1-B_1(B_2-G_1)]/E_1$
K_{13}	B_3G_1/E_1	K_{23}	$-G_1/E_1$
K_{14}	$B_3C_1G_1/E_1$	K_{24}	$-C_1G_1/E_1$
K_{15}	0	K_{25}	0
K_{16}	0	K_{26}	0
K_{31}	C_3G_1/E_2	K_{41}	$-G_1/E_2$
K_{32}	$B_1C_2G_1/E_2$	K_{42}	$-B_1G_1/E_2$
K_{33}	$1-C_3G_3/E_2$	K_{43}	G_3/E_2
K_{34}	$C_1-C_3[1-C_1(C_2-G_3)/E_2$	K_{44}	$[1-C_1(C_2-G_3)]/E_2$
K_{35}	C_3G_2/E_2	K_{45}	$-G_2/E_2$
K_{36}	$C_3D_1G_2/E_2$	K_{46}	$-D_1G_2/E_2$
K_{51}	0	K_{61}	0
K_{52}	0	K_{62}	0
K_{53}	D_3G_2/E_3	K_{63}	$-G_2/E_3$
K_{54}	$C_1D_3G_2/E_3$	K_{64}	$-C_1G_2/E_3$
K_{55}	$1-D_3G_2/E_3$	K_{65}	G_2/E_3
K_{56}	$D_1-D_3[1-D_1(D_2-G_2)]/E_3$	K_{66}	$[1-D_1(D_2-G_2)]/E_3$

$B_1 = Z_1M_{1,j}$ $\quad B_2 = M_{1,j}/Z_1$ $\quad B_3 = Z_1M_{1,j+1}$ $\quad B_4 = M_{1,j+1}/Z_1$

$C_1 = Z_2M_{2,j}$ $\quad C_2 = M_{2,j}/Z_2$ $\quad C_3 = Z_2M_{2,j+1}$ $\quad C_4 = M_{2,j+1}/Z_2$

$D_1 = Z_3M_{3,j}$ $\quad D_2 = M_{3,j}/Z_3$ $\quad D_3 = Z_3M_{3,j+1}$ $\quad D_4 = M_{3,j+1}/Z_3$

$E_1 = 1-M_{1,j+1}^2$; $\quad E_2 = 1-M_{2,j+1}^2$; $\quad E_3 = 1-M_{3,j+1}^2$;

$G_1 = A_{1,j}(1-Mo_{1,j}^2)$ $\quad G_2 = A_{2,j}(1-Mo_{2,j}^2)$ $\quad G_3 = G_1+G_2$

can be formally noted as

$$\begin{bmatrix} P_{1,N} \\ U_{1,N} \\ P_{2,N} \\ U_{2,N} \\ P_{3,N} \\ U_{3,N} \end{bmatrix} = [T] \begin{bmatrix} P_{1,1} \\ U_{1,1} \\ P_{2,1} \\ U_{2,1} \\ P_{3,1} \\ U_{3,1} \end{bmatrix}. \tag{7}$$

Taking advantage of the properties of a catenary matrix, the transmission matrix of the whole filter $[T]$ can be determined from successive multiplications of the transmission matrices $[K_j]$ and $[L_j]$

$$T = \prod_{k=1}^{N} [K_k][L_k], \tag{8}$$

where

$$L_N \equiv [I] \tag{9}$$

Table 2. Formulae for elements of the transmission matrix L_j

L_{kl}	Calculation formula	L_{kl}	Calculation formula
L_{11}	$F_1(\cos\alpha_1 + iM_{1,j+1}\sin\alpha_1)$	L_{21}	$i(F_1\sin\alpha_1)/Z_1$
L_{12}	$iF_1Z_1(1-M_{1,j+1}^2)\sin\alpha_1$	L_{22}	$F_1(\cos\alpha_1 - iM_{1,j+1}\sin\alpha_1)$
L_{13}	0	L_{23}	0
L_{14}	0	L_{24}	0
L_{15}	0	L_{25}	0
L_{16}	0	L_{26}	0
L_{31}	0	L_{41}	0
L_{32}	0	L_{42}	0
L_{33}	$F_2(\cos\alpha_2 + iM_{2,j+1}\sin\alpha_2)$	L_{43}	$i(F_2\sin\alpha_2)/Z_2$
L_{34}	$iF_2Z_2(1-M_{2,j+1}^2)\sin\alpha_2$	L_{44}	$F_2(\cos\alpha_2 - iM_{2,j+1}\sin\alpha_2)$
L_{35}	0	L_{45}	0
L_{36}	0	L_{46}	0
L_{51}	0	L_{61}	0
L_{52}	0	L_{62}	0
L_{53}	0	L_{63}	0
L_{54}	0	L_{64}	0
L_{55}	$F_3(\cos\alpha_3 + iM_{3,j+1}\sin\alpha_3)$	L_{65}	$i(F_3\sin\alpha_3)/Z_3$
L_{56}	$iF_3Z_3(1-M_{3,j+1})\sin\alpha_3$	L_{66}	$F_3(\cos\alpha_3 - iM_{3,j+1}\sin\alpha_3)$

where: α_m – phase shift, [rad]; $\alpha_m = \dfrac{Klm,j}{1-M_{n,j+1}^2}$; m – number of tube ($m = 1, 2, 3$),

k – wave number $[m^{-1}]$; $k = \omega/c$; $= 2\pi f$,

ω – angular velocity (pulsation), [rad/s]; f – frequency [Hz],

$l_{m,j}$ – length of wave-guides between rows of perforations, [m],

Z_m – wave impedance, [Pa·s/m^3] for tube m ($m = 1, 2, 3$),

$M_{m,j+1}$ – Mach number behind j-row of perforations (Figs. 1 and 2) in tube m,

F_m – auxiliary function $F_m = \cos(M_{m,j+1}\alpha_m - i\sin M_{m,j+1}\alpha_m) = e^{-i}M_{m,j+1}\alpha_m$.

$[I]$ – identity matrix.

The method of calculating the acoustic admittance of the perforated baffle is presented in Section 4.

4. Transmission matrices for particular solutions of the filter

The fundamental variants of solutions of filters two perforated tubes are presented in Table 3. Models under consideration have part of the tubes shut with rigid acoustically impermeable baffles with only one inlet tube and one outlet tube. The impedance of segments from the baffle to the nearest row of perforations can be determined in closed channels. Formulae for calculating this impedance are given in Table 3.

Table 3. Fundamental variants of acoustic have propagation in a three-tube model

direction of sound propagation		diagram of model	example of solution	notation and remarks
longitudinal		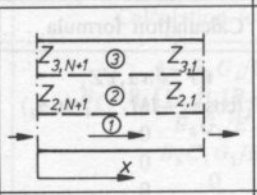	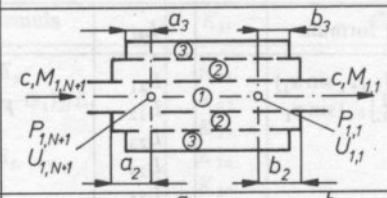	1a $Z_{2,1}=-iZ_2\,ctg\,(kb_2)$ $Z_{3,1}=-iZ_3\,ctg\,(kb_3)$ $Z_{2,N+1}=iZ_2\,ctg\,(ka_2)$ $Z_{3,N+1}=iZ_3\,ctg\,(ka_3)$
		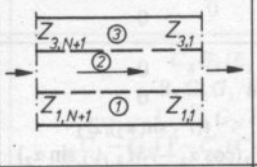	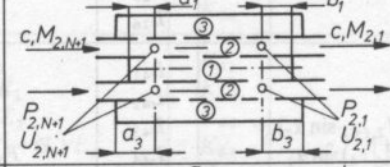	1b $Z_{1,1}=-iZ_1\,ctg\,(kb_1)$ $Z_{3,1}=-iZ_3\,ctg\,(kb_3)$ $Z_{1,N+1}=iZ_1\,ctg\,(ka_1)$ $Z_{3,N+1}=iZ_3\,ctg\,(ka_3)$
transverse		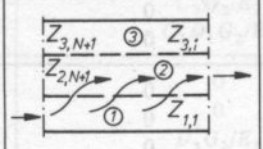	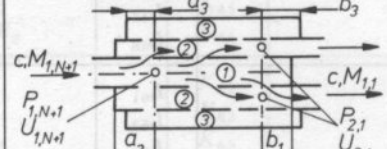	2a $Z_{1,1}=-iZ_1\,ctg\,(kb_1)$ $Z_{3,1}=-iZ_3\,ctg\,(kb_3)$ $Z_{2,N+1}=iZ_2\,ctg\,(ka_2)$ $Z_{3,N+1}=iZ_3\,ctg\,(ka_3)$
		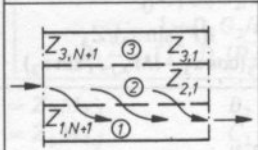	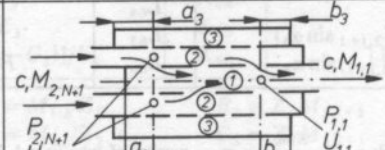	2b $Z_{2,1}=-iZ_2\,ctg\,(kb_2)$ $Z_{3,1}=-iZ_3\,ctg\,(kb_3)$ $Z_{1,N+1}=iZ_1\,ctg\,(ka_1)$ $Z_{3,N+1}=iZ_3\,ctg\,(ka_3)$
		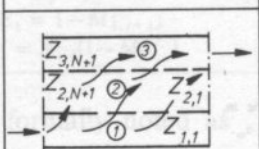	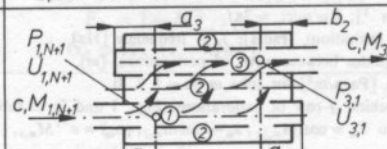	2c $Z_{1,1}=-iZ_1\,ctg\,(kb_1)$ $Z_{2,1}=-iZ_2\,ctg\,(kb_2)$ $Z_{2,N+1}=iZ_2\,ctg\,(ka_2)$ $Z_{3,N+1}=iZ_3\,ctg\,(ka_3)$
reversible		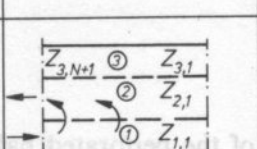	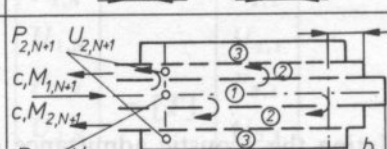	3a $Z_{1,1}=-iZ_1\,ctg\,(kb_1)$ $Z_{2,1}=-iZ_2\,ctg\,(kb_2)$ $Z_{3,1}=-iZ_3\,ctg\,(kb_3)$ $Z_{3,N+1}=iZ_3\,ctg\,(ka_3)$
		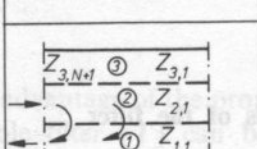	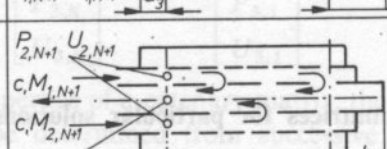	3b as for 3a
		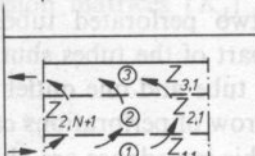		3c $Z_{1,1}=-iZ_1\,ctg\,(kb_1)$ $Z_{2,1}=-iZ_2\,ctg\,(kb_2)$ $Z_{3,1}=-iZ_3\,ctg\,(kb_3)$ $Z_{2,N+1}=iZ_2\,ctg\,(ka_2)$

As in the case of a muffler with one perforated tube [3], the relationship between acoustic parameters of an input and output acoustic wave may be interesting for mentioned above systems. The relationship can be noted in the form of a four-element transmission matrix [T]. The flow of the medium, determined by Mach numbers, has the same direction as sound propagation in models under consideration. If the flow of the medium is oppositely directed to the direction of sound propagation, then negative values for Mach numbers have to be accepted in calculations.

The method of deriving formulae for elements of the transmission matrix [T'] has been presented in detail in paper [3]. While in Tables 4 and 5 we have formulae for individual cases presented in Table 3.

Table 4. Formulae for elements of the transmission matrix [T'] for a case of longitudinal and transverse sound propagation

	Notation and description of specific solution	Values of indices				
		i	m	j	k	n
1a	Propagation along a single perforated baffle	1	1	3	2	2
1b	Propagation along a double perforated baffle	2	2	3	1	1
2a	Transverse propagation to the adjacent tube with double perforated baffle	1	2	3	2	1
2b	Transverse propagation to the adjacent tube with single perforated baffle	2	1	3	1	2
2c	Transverse propagation to the opposite tube	1	3	2	3	1

Formulae for elements of transmission matrix [T']

$$T'_{11} = T_{(2i-1)(2m-1)} + a_{(2i-1)}(AH-CF) + b_{(2i-1)}(CE-AG)/M$$
$$T'_{12} = T_{(2i-1)(2m)} + a_{(2i-1)}(BH-DF) + b_{(2i-1)}(DE-BG)/M$$
$$T'_{21} = T_{(2i)(2m-1)} + a_{(2i)}(AH-CF) + b_{(2i)}(CE-AG)/M$$
$$T'_{22} = T_{(2i)(2m)} + a_{(2i)}(BH-DF) + b_{(2i)}(DE-BG)/M$$

where: T_{xy} – transmission matrix between the $N+1$ and 1 row of perforations, with dimensions (6×6)

$$a_x = T_{x(2j-1)} Z_{j,1} + T_{x(2j)}$$
$$A = T_{(2k-1)(2m-1)} - Z_{k,N+1}\, T_{(2k)(2m-1)}$$
$$C = T_{(2j-1)(2m-1)} - Z_{j,N+1}\, T_{(2j)(2m-1)}$$
$$E = Z_{k,N+1}\, a_{(2k)} - a_{(2k-1)}$$
$$G = Z_{j,N+1}\, a_{(2j)} - a_{(2j-1)}$$

$$b_x = T_{x(2n-1)} Z_{n,1} + T_{x(2n)}$$
$$B = T_{(2k-1)(2m)} - Z_{k,N+1}\, T_{(2k)(2m)}$$
$$D = T_{(2j-1)(2m)} - Z_{j,N+1}\, T_{(2j)(2m)}$$
$$F = Z_{k,N+1}\, b_{(2k)} - b_{(2k-1)}$$
$$H = Z_{j,N+1}\, b_{(2j)} - b_{(2j-1)}$$

$$M = EH - FG \qquad M \neq 0$$

i – index of inlet tube; m – index of outlet tube;
j – tube closed at both ends; $x = 1, 2, \ldots, 6$;
$k = 1, 2, 3$ where $k \neq i$ and $k \neq j$; $n = 1, 2, 3$ where $n \neq j$ and $n \neq m$.

Table 5. Formulae for elements of the transmission matrix [T'] for a case of reversible sound propagation

	Notation and description of specific solution	Values of indices		
		i	m	j
3a	Propagation reversible to adjacent tube with double perforated baffle	1	2	3
3b	Propagation reversible to adjacent tube with single perforated baffle	2	1	3
3a	Propagation reversible to opposite tube	1	3	2

Formulae for elements of transmission matrix T'

$$T'_{11} = B_{(2i-1)}E_{(2m)} - A_{(2i-1)}F_{(2m)} \qquad T'_{12} = A_{(2i-1)}F_{(2m-1)} - B_{(2i-1)}E_{(2m-1)}$$
$$T'_{21} = B_{(2i)}E_{(2m)} - A_{(2i)}F_{(2m)} \qquad T'_{22} = A_{(2i)}F_{(2m-1)} - B_{(2i)}F_{(2m-1)}$$

where

$$A_x = a_x + C_x(a_{(2j-1)} - Z_{j,N+1}\,a_{(2j)})/M \qquad x = 1, 2, \ldots, 6$$
$$B_x = b_x + C_x(b_{(2j-1)} - Z_{j,N+1}\,b_{(2j)})/M$$
$$M = Z_{j,N+1}\,C_{(2j)} - C_{(2j-1)} \qquad M \neq 0$$
$$a_x = T_{x1}\,Z_{1,1} + T_{x2} \qquad b_x = T_{x3}\,Z_{2,1} + T_{x4}$$
$$C_x = T_{x5}\,Z_{3,1} + T_{x6}$$
$$E_x = A_x/W \qquad F_x = B_x/W$$
$$W = A_{(2m)}B_{(2m-1)} - A_{(2m-1)}B_{(2m)}$$

T_{xy} – transmission matrix between the $N+1$ and 1 row of perforations, with dimensions (6×6),
i – index of inlet tube; m – index of outlet tube,
$j = 1, 2, 3$ where $j \neq i$ oraz $j \neq m$

5. Admittance of a perforated surface

It is most convenient to determine the admittance of a perforated baffle on the basis of impedance measurements, as it was done by SULLIVAN [6] or MUNJAL [4]. The conversion formula for the j–row of perforations is as follows

$$A_{i,j} = \frac{1}{Z_{i,j}} = \frac{\sigma_{i,j}}{Zo_{i,j}} \frac{\theta_{i,j} - i\chi_{i,j}}{\theta_{i,j} + \chi_{i,j}} \tag{10}$$

where: $A_{i,j}$ – acoustic admittance of perforated baffles, [m^3/Pa·s], $Z_{i,j}$ – acoustic impedance of perforated baffles walls of perforated tubes $i = 1, 2$, [Pa·s/m^3], $\sigma_{i,j}$ – factor for the i–tube and j–row of perforations, $\theta_{i,j}$ – specific acoustic resistance of perforations, $\chi_{i,j}$ – specific acoustic reactance of perforations.

When empirical data is not available, then approximate formulae described in

previous papers by the author [1, 3] can be applied

$$\theta_{i,j} = \frac{4\sqrt{\pi f \nu}}{C}\left[\frac{h}{d}+(1-\sigma_{i,j})\right]+2.57\frac{Mo_{i,j}}{\sigma_{i,j}}$$
$$\chi_{i,j} = \frac{2\pi}{C} f h_{ef_{i,j}} \tag{11}$$

where: f – frequency of acoustic vibrations, [Hz], ν – kinematic viscosity of the medium, [m^2/s]; it is recommended to increase this coefficient by 114% [7] in order to include the effect of losses due to heat exchange between concentrated and rarefied places in the medium, b – graduation of holes of perforation, [m], d – diameter of holes of the perforation, [m], h – thickness of perforated baffle tube, [m], $h_{ef_{i,j}}$ – effective thickness of j–row of holes of the perforation in the i–tube (including the share of the mass of the medium adjoining the hole), [m]

$$h_{ef} = h+0.85\left(1-\frac{d}{2b}\right)d. \tag{12}$$

Expressions presented above (11) are valid in the range of laminar flow of the medium through the holes of the perforation, i.e. when the following condition is fulfilled

$$R_e = \frac{\overline{V}_0 \cdot d}{\nu} < 10^3 \tag{13}$$

where: $\overline{V}_0$ – average flow velocity in holes of perforation, [m/s], or in a case of low flow velocities through holes of the perforation ($\overline{V}_0 < 0.5$ m/s) for a limited frequency range

$$f < 0.06c/d \tag{14}$$

6. Generalization of the model

The previously considered physical model assumed that individual rows of perforations in both tubes overlap perfectly. However, this model is a specific and rather rare case among actual technological solutions. In general we have to do with mixed connections, where beside the connection described by the model, also a connection between two out of three considered tubes can occur in individual rows of perforations.

The mathematical model of a transmission matrix K_j for these cases can be described with the same formulae, which have been presented in Table 1, when additional substitutions are applied:

– for a connection between tube 1 and 2 only

$$M_{2,j} = 0 \quad \text{and} \quad A_{2,j} = 0 \tag{15}$$

Table 6. Formulae for elements of the transmission matrix K_j for a case of a connection of tube 1 and 2, only, through openings of the perforation

K_{Kl}	Calculation formula	K_{Kl}	Calculation formula
K_{11}	$1-B_3G_1/E_1$	K_{21}	G_1/E_1
K_{12}	$B_1-B_3[1-B_1B_2-G_1)]/E_1$	K_{22}	$[1-B_1(B_2-G_1)]/E_1$
K_{13}	B_3G_1/E_1	K_{23}	$-G_1/E_1$
K_{14}	$B_3C_1G_1/E_1$	K_{24}	$-C_1G_1/E_1$
K_{15}	0	K_{25}	0
K_{16}	0	K_{26}	0
K_{31}	C_3G_1/E_2	K_{41}	$-G_1/E_2$
K_{32}	$B_1C_3G_1/E_2$	K_{42}	$-B_1G_1/E_2$
K_{33}	$1-C_3G_1/E_2$	K_{43}	G_1/E_2
K_{34}	$C_1-C_3[1-C_1(C_2-G_1)/E_2$	K_{44}	$[1-C_1(C_2-G_1)/E_2$
K_{35}	0	K_{45}	0
K_{36}	0	K_{46}	0
K_{51}	0	K_{61}	0
K_{52}	0	K_{62}	0
K_{53}	0	K_{63}	0
K_{54}	0	K_{64}	0
K_{55}	1	K_{65}	0
K_{56}	0	K_{66}	1

Constants B_i, C_i, D_i, E_i, G_i $i = 1, 2, \ldots$ – calculated according to formulae as in Table 1, when substitutions are introduced
$A_{2,j} = 0$ and $Mo_{2,j} = 0 \rightarrow G_3 = G_1$

– for a connection between tube 2 and 3, only

$$M_{1,j} = 0 \quad \text{and} \quad A_{2,j} = 0 \tag{16}$$

when these substitutions are applies, formulae are converted into the form presented in Tables 6 and 7.

Contents of the tables indicate that relations in force between parameters of neighbouring and connected in a given j–row of perforations two tubes are identical with parameters obtained for a model, in which only propagation in two tubes connected by one perforated baffle was considered [3]. While the multiplication by an identity matrix is performed in the case of the third tube (not connected with the other two tubes in the given j–row). This means that acoustic parameters in this particle remain unchanged and that this is in accordance with the accepted physical model.

Table 7. Formulae for elements of the transmission matrix K_j for a case of a connection of tube 2 and 3, only, through openings of the perforation

K_{KI}	Calculation formula	K_{KI}	Calculation formula
K_{11}	1	K_{21}	0
K_{12}	0	K_{22}	1
K_{13}	0	K_{23}	0
K_{14}	0	K_{24}	0
K_{15}	0	K_{25}	0
K_{16}	0	K_{26}	0
K_{31}	0	K_{41}	0
K_{32}	0	K_{42}	0
K_{33}	$1-C_3G$	K_{43}	G_2/E_2
K_{34}	$C_1-C_3[1-C_1(C_2-G_2)]/E_2$	K_{44}	$[1-C_1(C_2-G_2)]/E_2$
K_{35}	C_3G_2/E_2	K_{45}	$-G_2/E_2$
K_{36}	$C_3D_1G_2/E_2$	K_{46}	$-D_1G_2/E_2$
K_{51}	0	K_{61}	0
K_{52}	0	K_{62}	0
K_{53}	D_3G_2/E_3	K_{63}	$-G_2/E_2$
K_{54}	$C_1D_3G_2/E_3$	K_{64}	$-C_2G_2/E_2$
K_{55}	$1-D_3G_2/E_3$	K_{65}	G_2/E_3
K_{56}	$D_1-D_3[1-D_1(D_2-G_2)]/E_3$	K_{66}	$[1-D_1(D_2-G_2)]/E_3$

Constants B_i, C_i, D_i, E_i, G_i $i = 1, 2, \ldots$ – calculated according to formulae as in Table 1, when substitutions are introduced
$A_{1,j} = 0$ and $Mo_{1,j} = 0 \rightarrow G_3 = G_2$

7. Conclusions

This paper presents an analytical model of a filter with two perforated tubes. A segmentation principle for reproducible segments of tubes, analogical to that accepted in a previously presented model [3] for one perforated tube was accepted here. In [3] properties of individual segments were described with a transmission matrix with the application of a discrete parameter to describe properties of acoustic particles related with openings of the perforation, and a model with distributed parameters to describe the propagation of an acoustic wave along sections of tubes between individual rows of perforations.

The presented above description of acoustic properties of discussed filters is very convenient for further computer processing, because transmission matrices related to the filters individual elements are catemary matrices for the filter configuration under consideration. Hence the transmission matrix for the whole filter can be easily achieved by multiplying the transmission matrix for succesive components. Values of

generally applied attenuation measures transmission loss TL and insertion loss IL can be equally easily determined on the basis of the transmission matrix, if only the impedance of the sound source and its outlet from the tube of the muffler or installation is determined [3].

Simple substitutions make it possible to use the presented mathematical model for such cases, where there is no connection between tubes on both perforated surfaces in a single row of perforations at the same time. This simplifies the analytical programme.

The author has included a large number of possible particular solutions of filters in the mathematical model. They include fundamental combinations of closures of parts of tubes, applied in Table 3. Yet, it was possible to formulate a generalized mathematical model for elements of the transmission matrix $[T']$ with the use of not many calculation formulae. This also influenced the simplicity of the programme and calculation time.

The shortcoming of the presented model is that its application is limited to: small dimensions of holes of the perforation discrete parameter model, low flow velocities (laminar flow range) and bottom frequency range (conservation of propagation conditions of a plane wave and a harmonic acoustic wave).

References

[1] G. BRZÓZKA, J. DEGÓRSKI, H. KACZMAREK, *On calculations of acoustic filters with a perforated tube* (in Polish), Proc. XXXI Open Seminar on Acoustics OSA–84, Warszawa 1984, pp. 102–106.

[2] G. BRZÓZKA, T. WIŚNIEWSKI, *On certain properties of mufflers with perforated tubes* (in Polish), Proc. Conf. KONES'85, Poznań-Błażejewko, 1985, pp. 38–43.

[3] G. BRZÓZKA, *Acoustic filters with a perforated tube* (in Polish) Arch. Akustyki **22**, 4, 329–351 (1987), and in English Arch. Acoustics **12**, 3 and 4 (1987).

[4] M. L. MUNJAL, K. N. RAO, A. D. SAHASRABUDHE, *Aeroacoustical analysis of perforated muffler components*, J. of Sound and Vibration **114**, 2, 173–188 (1987).

[5] J. W. SULLIVAN, *A method for modeling perforated tube muffler components, I. Theory*, JASA, 66, 772–778 (1979).

[6] J. W. SULLIVAN, *A method for modeling perforated tube muffler components, II. Applications*, JASA 66, 779–788 (1979).

[7] Z. ŻYSZKOWSKI, Foundations of electroacoustics (in Polish) WNT, Warszawa 1984.

Received December 29, 1989

ARCHIVES OF ACOUSTICS
16, 3–4, 475–487 (1991)

ALGORITHMS FOR CONNECTED WORD RECOGNITION – A GLOBAL APPROACH

S. GROCHOLEWSKI

Institute of Computing Science Technical University of Poznań
(60-965 Poznań, ul. Piotrowo 3a)

In this paper, which is basically a review, three approaches to the problem of recognizing word connected speech are presented. They all use the dynamic programming technique to solve the optimization problem which occurs in matching an unknown utterance against an artificially synthesized sequence of word templates. They are compared with regard to the computation time and the memory requirement.

1. Introduction

In connected word recognition the spoken input is a sequence of words from a limited vocabulary, often uttered without pauses in-between, and the recognition is based on matching isolated word reference templates. The general idea of a global approach consists in comparing artificially synthesized connected reference patterns with an unknown utterance. For a 100-word vocabulary and the maximum of 5 words in an utterance, this approach involves 10^{10} comparisons. Such an unacceptably great number of calculations can be efficiently reduced by the dynamic programming (DP) technique successfully used in isolated word recognition systems [4], [11].

In this paper, three algorithms using the DP technique are presented, concerning three approaches characteristic of the first significant works undertaken in Japan (algorithm I), the USA (algorithm II) and the USSR (algorithm III). The comparisons will be made in terms of both computation and storage requirements.

Let us introduce the basic terms used in the description of these algorithms. Let X signify a sequence of I vectors describing an unknown utterance to be recognized. Let the vocabulary comprise N templates: $W(1), \ldots, W(N)$, and let the n-th template be described by the sequence of $J(n)$ elements vectors.

Let:

– $d(i, j, n)$ signify the local distance between the i-th element of an utterance and the j-th element of the n-th template;

– $D(i, j, n)$ signify the accumulated distance to the point determined by the following coordinates: the i-th element of an utterance and the j-th element of the n-th template from the beginning of the uterance.

2. Algorithm I (Two-Level DP-Matching Algorithm [10])

Let $C(l, m)$ be a partial pattern as the part of the utterance X which begins with the l-th element and ends with the m-th one. At the first level of the algorithm (word level), for all the combinations (l, m) such that $1 \leqslant l < m \leqslant I$ considering all the templates $W(n)$, where $n = 1 \div N$, it is necessary to find:

$$D^*(l, m) = \min_n D\big(C(l, m), W(n)\big) = \min_n D(l, m, n) \tag{1}$$

$$N^*(l, m) = \operatorname{argmin}_n D\big(C(l, m), W(n)\big) = \operatorname{argmin}_n D(l, m, n) \tag{2}$$

where $D^*(l, m)$ – distance between the partial pattern $C(l, m)$ of the utterance X and the nearest template, $N^*(l, m)$ – the nearest template for the $C(l, m)$.

The operator "$\operatorname{argmin}_n D(\ )$" means to find the optimum argument n which minimizes $D(\ )$.

In practice, for every l, conceived of as the beginning of some word, and for the length of its template equal to $J(n)$, the range of m can be determined as in the inequality (3) below:

$$l + J(n) - r \leqslant m \leqslant l + J(n) + r. \tag{3}$$

This is possible assuming that the length of the word differs from the length of its template by the value of r.

The range of m can be determined as demonstrated in Fig. 1a. For every l, with respect to the inequality (3), only $2r+1$ pairs $\{D^*(i, m), N^*(l, m)\}$ should be designated. The conditions expressed in the inequality (3) also cause the limitations of maximum l: $l_{\max} = I - J(n) + r$ (cf. Fig. 1b).

Figure 2 presents the set of all possible pairs (l, m) for a simple example, where $I = 9$, $r = 1$, $J(n) = 3$ for all n. These pairs are represented by the lines connecting the respective points l, m.

After all $N^*(l, m)$ and $D^*(l, m)$ for every pair (l, m) have been found, it is necessary to find, at the second level, such a combination K^* of pairs $\{(l_1 m_1), \ldots, (l_k, m_k), \ldots, (l_{K^*}, m_{K^*})\}$, where

$$l_1 = 1, \quad l_k = m_{k-1} + 1, \quad m_{K^*} = I, \tag{4}$$

for which the sum of distances $D^*(l_k, m_k)$, $k = 1 \div K^*$ henceforth designated by $T_{K^*}(I)$, will be minimum.

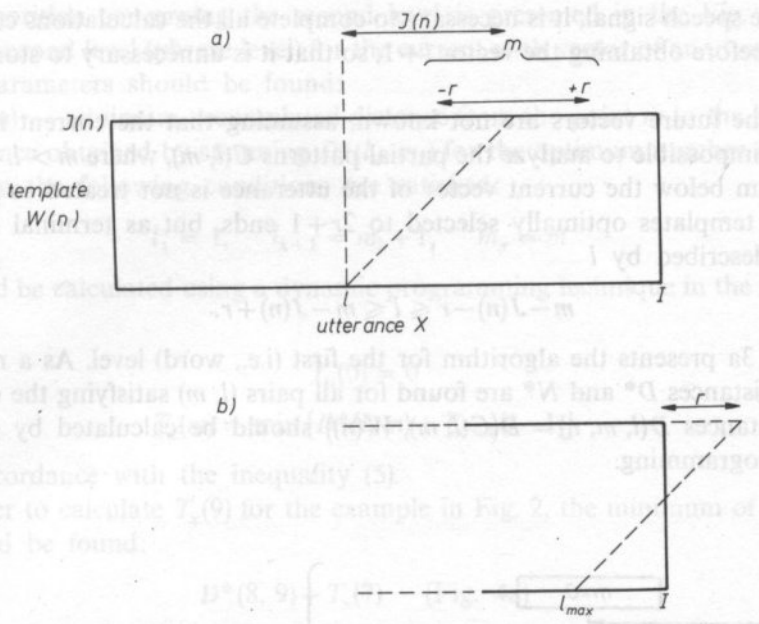

FIG. 1. Illustration of the way in which the range of m can be determined

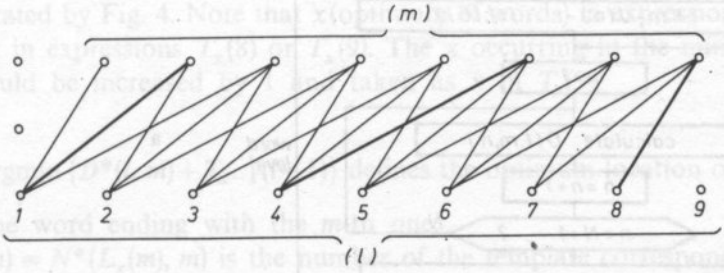

FIG. 2. The set of all possible pairs (l, m) for a simple example, where $I = 9$, $r = 1$, $J(n) = 3$

In Fig. 2 the thick lines present an example of a combination of the 3 pairs $\{(1, 3), (4, 7), (8, 9)\}$ satisfying the conditions (4). Let $K\max$ be the maximum expected number of words in utterance. The optimum number of words is defined as

$$K^* = \underset{K}{\operatorname{argmin}} \{T_K(I)\}, \qquad \text{where } K = 1 \div K_{\max}.$$

On the basis of both the optimum combination K^* of the pairs (l_k, m_k), where $k = 1 \div K^*$, and (2), the sequence of words in this utterance can be easily determined.

Now let us describe such an algorithm which can be useful in a speech recognition system working in real time. This means that after obtaining the i-th

vector of the speech signal, it is necessary to complete all the calculations concerning this vector before obtaining the vector $i+1$, so that it is unnecessary to store the i-th one.

Since the future vectors are not known, assuming that the current is the l-th vector, it is impossible to analyze the partial patterns $C(l, m)$, where $m > l$. Hence, in the algorithm below the current vector of the utterance is not treated as initial for a group of templates optimally selected to $2r+1$ ends, but as terminal for $2r+1$ beginning described by l

$$m-J(n)-r \leqslant l \leqslant m-J(n)+r. \tag{5}$$

Figure 3a presents the algorithm for the first (i.e., word) level. As a result, the minimum distances D^* and N^* are found for all pairs (l, m) satisfying the condition (5). The distances $D(l, m, n) = D(C(l, m), W(n))$ should be calculated by means of dynamic programming.

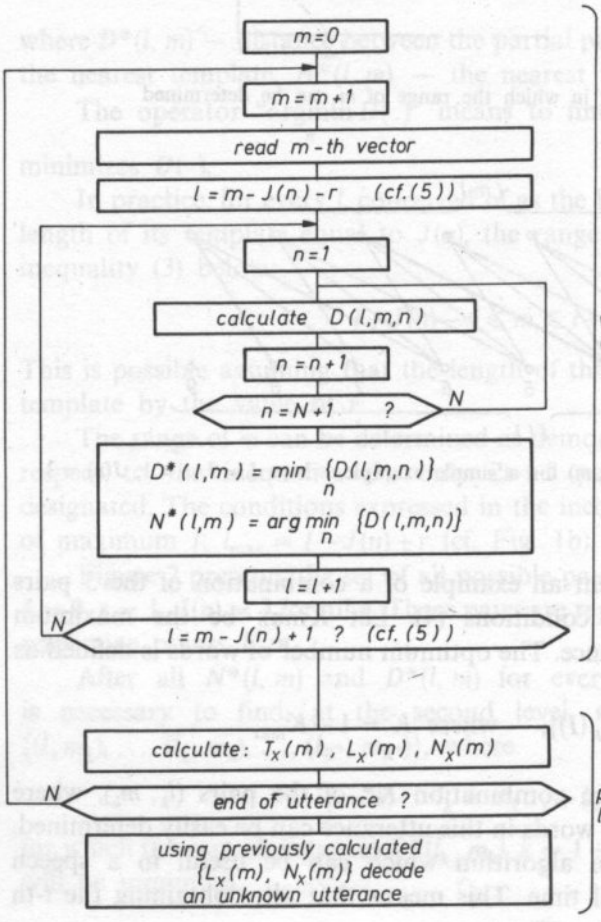

FIG. 3. Description of algorithm *I* for a real time recognition system

The algorithm concerning the second level is presented in the Fig. 3b.

At the second level (phrase level) for the current m-th vector of an utterance, the following parameters should be found:

– $T_x(m)$ – minimum accumulated distance from the point m to the beginning of an utterance obtained by summing $D^*(l_k, m_k)$ for the optimum number of x pairs (l_k, m_k) when the following conditions are satisfied:

$$l_1 = 1, \quad l_{k+1} = m_k + 1, \quad m_x = m. \tag{6}$$

$T_x(m)$ should be calculated using a dynamic programming technique in the following way:

$$T_0(0) = 0$$
$$T_x(m) = \min \{D^*(l, m) + T_{x-1}(l-1)\} \tag{7}$$

for l in accordance with the inequality (5).

In order to calculate $T_x(9)$ for the example in Fig. 2, the minimum of the three sums should be found:

$$D^*(8, 9) + T_x(7) \quad \text{(Fig. 4a)} \tag{8}$$

$$D^*(7, 9) + T_x(6) \quad \text{(Fig. 4b)} \tag{9}$$

$$D^*(6, 9) + T_x(5) \quad \text{(Fig. 4c)} \tag{10}$$

This is illustrated by Fig. 4. Note that x(optimum of words) in expression $T_x(7)$ can differ from x in expressions $T_x(8)$ or $T_x(9)$. The x occurring in the minimum sum (8)–(10) should be increased by 1 and taken as x in $T_x(9)$.

– $L_x(m) = \underset{l}{\operatorname{argmin}} \{D^*(l, m) + T_{x-1}(l-1)\}$ defines the optimum location of the initial vector for the word ending with the m-th one. (11)

– $N_x(m) = N^*(L_x(m), m)$ is the number of the template corresponding to the partial pattern $C(L_x(m), m)$ calculated according to Eq. (2) at the first level.

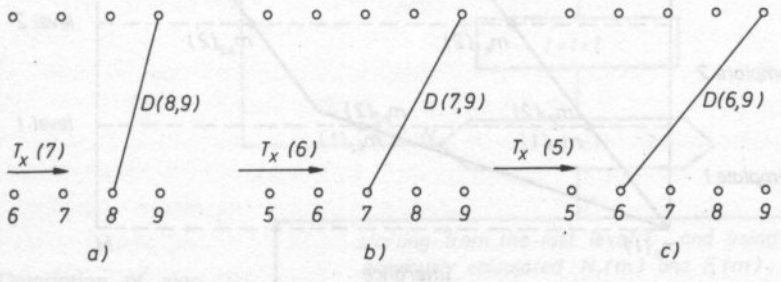

FIG. 4. Three ways of calculating $T_x(9)$ for the example in Fig. 2

The decision about the recognition of the whole utterance is generated on the basis of the pairs $\{N_x(m), L_x(m)\}$ for $m = 1 \div I$ in the manner shown in Fig. 5. The last column in Fig. 5 indicates that the last word is the word $N_{K^*}(I)$, the penultimate one ends for $m = L_x(I) - 1$ and that this is the word $N_x(L_x(I) - 1)$, etc.

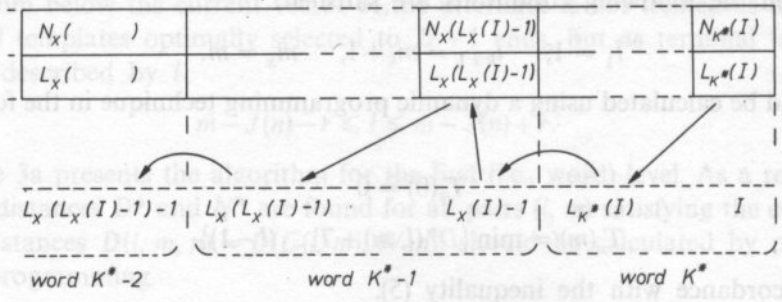

FIG. 5. The manner of decoding of an unknown utterance

3. Algorithm II (Level Building DTW Algorithm [6, 2, 8]

Let us assume that the utterance is a sequence of L words. On the basis of L and the duration (I) of the utterance, it is possible to determine the range of the expected location of the beginning $(m_{p1}(l), m_{p2}(l))$ and the location of the end $(m_{k1}(l), m_{k2}(l))$ of the l-th word. The manner in which they can be determined has been illustrated in Fig. 6 for the case when $L = 4$. The horizontal lines separating the templates define the so-called levels, henceforth they are designated by the letter l; the l-th level concerns

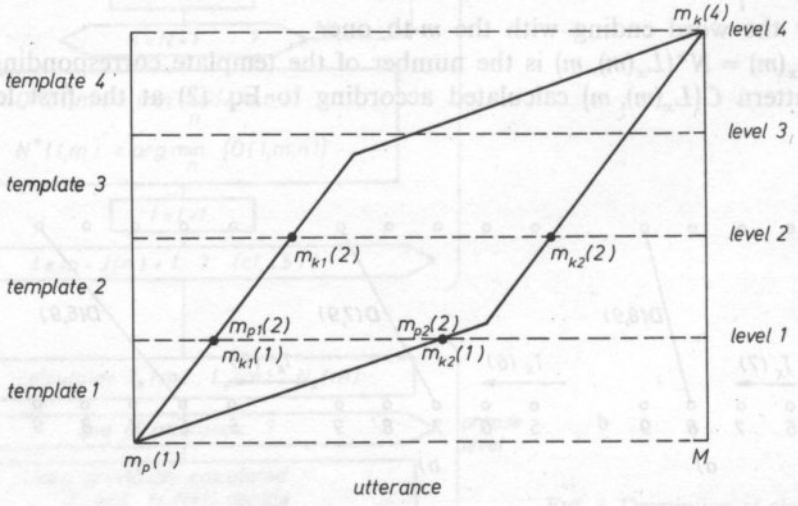

FIG. 6. The presumed beginnings of the successive words in an unkown utterance

the end of the l-th template. The solid lines limit the area for the warping function. The intersections of the lines indicate the possible location of both the end of the previous word and the possible location of the beginning of the subsequent one.

Figure 7 presents the procedure for the recognition of an utterance consisting of L words. This procedure is exemplified in Fig. 8. It has been assumed that the utterance is composed of L words belonging to the following vocabulary $\{A, B, C, D, E, F\}$.

At each level, a pair of $N_l(m)$ for for m satisfying

$$m_{k1}(l) \leqslant m \leqslant m_{k2}(l) \tag{13}$$

has been found. The description of, for instance, a point at the level $l = 3$ of the type $F/4$ means that the optimum warping function passes through the previous level at the point $m = 4$, and that the part of the utterance corresponding to the 3-rd word is the least distant from the template F.

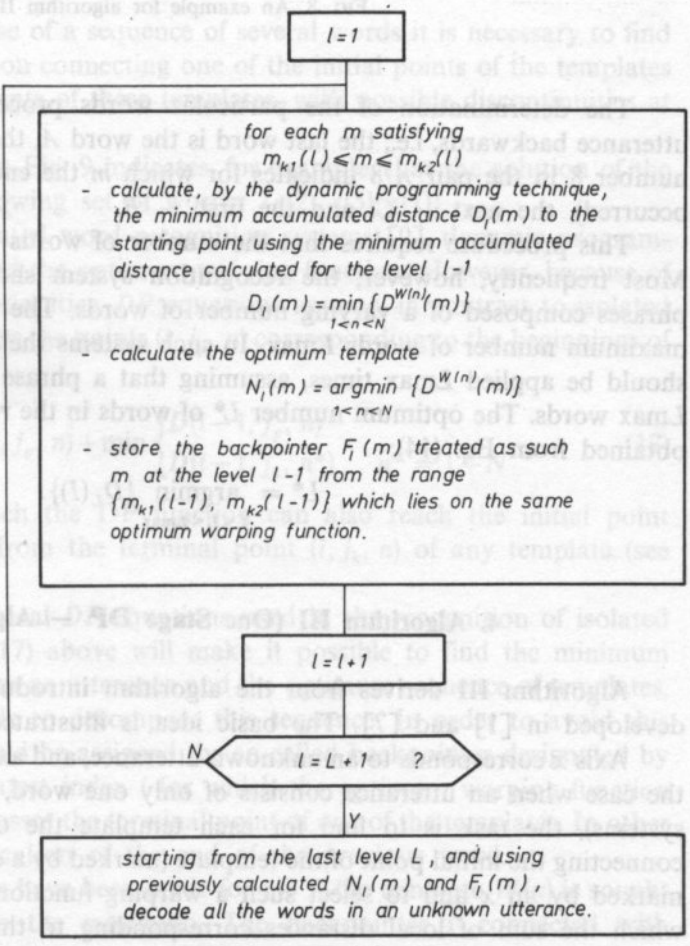

FIG. 7. Description of algorithm II

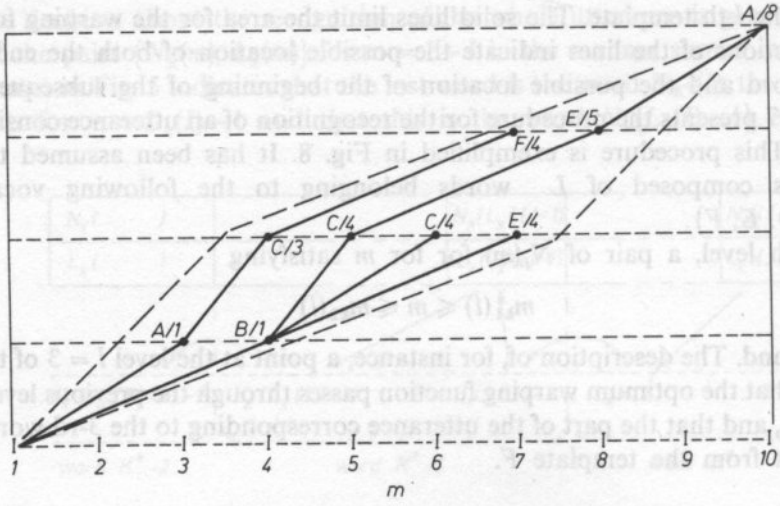

FIG. 8. An example for algorithm II

The determination of the particular words proceeds from the end of the utterance backwards, i.e., the last word is the word *A*, the penultimate one is *E* (the number 8 in the pair *A*/8 indicates for which *m* the end of the penultimate word occurred), the next – *C*, and the first – *B*.

This procedure requires that the number of words in an utterance be known. Most frequently, however, the recognition system should be able to recognize phrases composed of a varying number of words. The only limitation can be the maximum number of words *L*max. In such systems the procedure described above should be applied *L*max times, assuming that a phrase may consist of 1, 2, ... to *L*max words. The optimum number L^* of words in the recognized utterance can be obtained from Eq. (14):

$$L^* = \underset{1<L<L\max}{\operatorname{argmin}} \{D_L(I)\}. \tag{14}$$

4. Algorithm III (One Stage DP – Algorithm [7])

Algorithm III derives from the algorithm introduced by VINTSUK [12] and developed in [1] and [7]. The basic idea is illustrated in Fig. 9.

Axis *x* corresponds to an unknown utterance, and axis *y* to a set of templates. In the case when an utterance consists of only one word, (isolated word recognition systems), the task is to find for each template the optimum warping function connecting the initial point of the template (marked by a circle) with is terminal point marked by an *x* and to select such a warping function (i.e., such a template) for which the sum of local distances corresponding to this function is minimum.

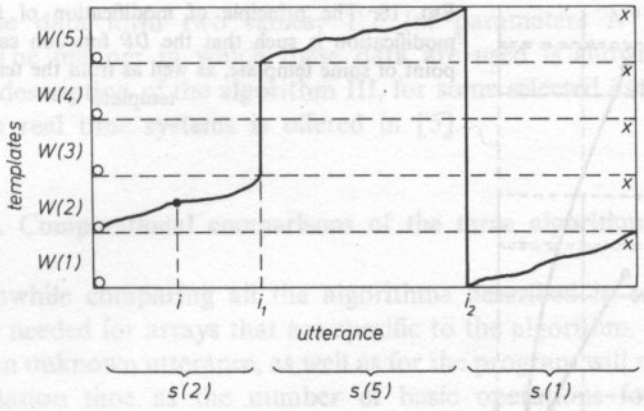

FIG. 9. An example of the optimal warping function for the sequence $\{s(2), s(5), s(1)\}$; $s(n)$ signifies the part of an unknown utterance corresponding to the n-th template

In the more difficult case of a sequence of several words it is necessary to find the optimum warping function connecting one of the initial points of the templates with one of the terminal points of these templates, with possible discontinuities at their boundaries.

The warping function in Fig. 9 indicates, for example, that the solution of the recognition task is the following set of words: $\{s(2), s(5), s(1)\}$.

Similarly as in the isolated word recognition systems [9], dynamic programming can also be used to find the optimum warping function. However, because of the above-mentioned discontinuities, *DP* equations assume, in contrast to isolated words [9], a modified form for the points (i, j_p, n) corresponding to the beginnings of the templates:

$$D(i, j_p, n) = d(i, j_p, n) + \min \begin{cases} D(i-1, j_p, n) \\ D(i-1, j_k, n^*) \end{cases} \qquad n^* = 1 \div N \tag{17}$$

The modification is such the DP function can also reach the initial point (i, j_p, n) of some template, from the terminal point (i, j_k, n) of any template (see Figs. 9 and 10).

The application of classical *DP* equations used in the recognition of isolated words modified as in Eq. (17) above will make it possible to find the minimum accumulated distance between an utterance and the optimum sequence of templates, but will not make it possible to decompose this sequence. In order to avoid this difficulty, each $D(i, j, n)$ should be assigned the so-called backpointer designated by i'. It is defined as such greatest index i for which the optimum warping function reaching the point (i, j, n) crosses the terminal point of one of the templates. In other words, it determines the location of the end of the previous word.

After all the calculations have been made for $i = I$, the template $W(n)$ is sought for which $D(I, j_k, n)$ attains the minimum. The backpointer i' connected with

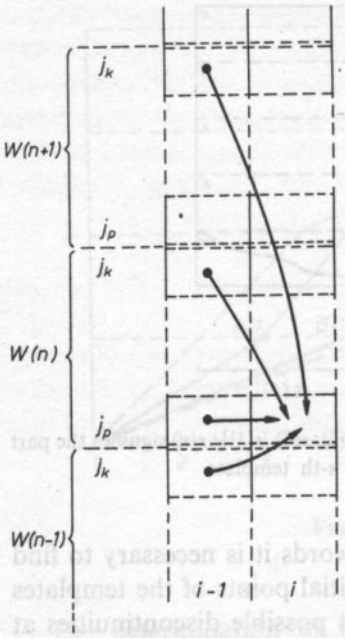

FIG. 10. The principle of modification of *DP* equations: the modification is such that the *DP* function can reach the initial point of some template, as well as from the terminal point of any template

$D(I, j_k, n)$ indicates the end of the previous word. The parameter n for which $D(i', j_k, n) = \min$ identifies this word. By repeating this procedure until $i = 1$, we can find the optimum sequence of words.

From the practical point of view, in order to simplify the above procedure, it is recommended to store for each i the following two data: parameter n, for which $D(i, j_k, n) = \min$, i.e., N^*, and the backpointer i^* connected with the minimum

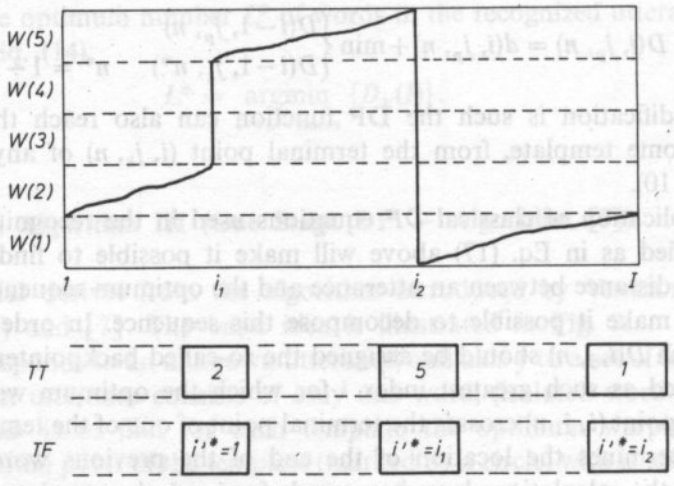

FIG. 11. The manner in which the data in the tables *TT* and *TF* (algorithm III) are used

$D(i, j_k, n)$. These data form two tables: TT (of parameters N^*) and TF (of backpointers). The manner in which these data are used is shown in Fig. 11.

A detailed description of the algorithm III, for some selected data, which could be employed in real time systems is offered in [5].

5. Computational comparisons of the three algorithms

It is worthwhile comparing all the algorithms described in terms of:

– storage needed for arrays that are specific to the algorithm. Storage for the templates and an unknown utterance, as well as for the program will not be included,

– computation time as the number of basic operations for the dynamic programming technique, i.e., calculations of $D(i, j)$ together with $d(i, j)$.

Algorithm I:

– storage

At the first level for each m it is necessary to calculate and store $(2r+1)$ values of $D^*(l, m)$ and $N^*(l, m)$. Thus the first level requires $2I(2r+1)$ memory locations. For calculating $(2r+1)$ pairs of $\{D^*(l, m), N^*(l, m)\}$ for a given m, only a very small number $2r+1$ of memory locations is sufficient. Nevertheless for real time systems, when the calculations at the two levels are performed simultaneously, and after the $(2r+1)$ pairs of $(D^*(m), N^*(m))$ have been determined for a given m, it is necessary to calculate $T_x(m)$, x, $N_x(m)$ additionally. From amongst these data only $(2r+1)$ pairs of $\{T_x(m), x\}$ and all I pairs of $\{L_x(m), N_x(m)\}$ should be stored.

The above considerations indicate that the theoretically minimum number of memory locations for a real time system amounts to $3(2r+1)+2I$. It is worth mentioning, what is also important for the two other algorithms, that the application of only a minimum number of memory locations can decrease the speed of the program.

– computation time

At the first level, for each l, where $l = 1 \div I$, and for each template $W(n)$, where $n = 1 \div N$, the calculation of $D(i, j)$ must be repeated $(2r+1)J_{av}$ times, where J_{av} is an average template length. Hence the number of these calculations equals $INJ_{av}(2r+1)$.

At the phrase level, I dynamic programming equations should be solved, which makes the total number of calculations of $D(i, j)$ at both levels equal to

$$I(NJ_{av}(2r+1)+1) \approx INJ_{av}(2r+1).$$

Algorithm II:

– storage

It theoretically requires minimum $J\max$ memory locations for $D_l(m)$ calculations and $3IL\max$ locations for storing $D_l(m)$, $N_l(m)$, $F_l(m)$

– computation time

In [6] and [7] various algorithms are compared by means of a number of local

distance ($d(i, j)$) calculations. The computations time for algorithm II is given in the quoted works as the number of $d(i, j)$ calculations, i.e., $N L J_{av} I/3$.

Algorithm III

– storage

Algorithm III requires:

– $2NJ_{av}$ memory locations for given i for $D(i, j, n)$ and $i'(i, j, n)$,

– $2I$ memory locations to store N^* and i'^* for every i; hence the total requirement is $2I + J_{av}N$,

– computation time.

The number of DP equations is $NJ_{av}I$.

In order to compare all the described algorithms in terms of storage and computation time, let us consider an example of a recognition system with the following parameters:

– the number of templates $N = 64$,

– the maximum length of an unknown utterance $I = 256$ as the number of vectors describing the speech signal; for a 20 ms frame, this gives ca 5 sec. of speech,

– $r = 8$,

– the average number of vectors in a template equals 32,

– the maximum number of words in a phrase $L_{\max} = 5$.

The storage and computation time requirements for the above example are shown in Fig. 12. It should be emphasized at this point that the quantity of the memory locations required is so small that it does not pose a problem for modern digital technology. It therefore seems that the critical parameter in real time recognition systems will be the computation time. With regard to this, algorithm III seems to be most suitable.

	algorithm I	algorithm II	algorithm III
storage	566	3872	4608
computation time	8.912.896	873.813	524.286

FIG. 12. The comparison of the three algorithms for an example given in the text

8. Conclusions

In this paper three approaches to the problem of connected word recognition are presented. They all use the dynamic programming technique to solve the optimization problem which occurs while comparing an unknown utterance with an artificially synthesized sequence of word templates.

Although algorithm III seems to be most appropriate with regard to the most critical parameter, i.e., computation time, and therefore was implemented in special

purpose chips [3], it is worthwhile mentioning that algorithm I has been used in the first commercial connected word recognition system DP-100 [11].

An experimental system based on algorithm III, worked out and tested by the author, will be presented in [5].

References

[1] J. Bridle, M. Brown, R. Chamberlain, *An Algorithm for Connected Word Recognition*, Proc. ICASSP 1982, pp. 899–902.

[2] Ch. Gagnoulet, M. Couvrat, *SERAPHINE – A Connected Words Speech Recognition System*, Proc. ICASSP 1982, pp. 887–890.

[3] S. Glinski et al., *The Graph Search Machine (GSM): A VLSI Architecture for Connected Speech Recognition and Other Applications*, Proc. of the IEE, 75, 9, pp. 1172–1184 (1987).

[4] S. Grocholewski, *Dynamic Programming in Automatic Speech Recognition*, (in Polish) Elektrotechnika (AGH), 4, 1, pp. 106–126 (1985).

[5] S. Grocholewski, *The Method for Connected Word Recognition*, in preparation for Archives of Acoustics.

[6] C. S. Myers, L. R. Rabiner, *A Level Building Dynamic Time Warping Algorithm for Connected Word Recognition*, IEEE Trans. ASSP, 29, 2, pp. 284–297 (1987).

[7] H. Ney, *The Use of a One-Stage Dynamic Programming Algorithm for Connected Word Recognition*, IEEE Trans. ASSP, 32, 2, pp. 263–271 (1984).

[8] L. R. Rabiner, J. G. Wilpon, F. K. Soong, *High Performance Connected Digit Recognition Using Hidden Markov Models*, Proc. ICASSP 1988, pp. 119–122.

[9] H. Sakoe, S. Chiba, *Dynamic Programming Algorithm Optimization for Spoken Word Recognition*, IEEE Trans. ASSP, 26, 2, pp. 43–49 (1978).

[10] H. Sakoe, *Two-Level DP-Matching – A Dynamic Programming Based Pattern Matching Algorithm for Connected Word Recognition*, IEEE Trans. ASSP, 27, 6, pp. 588–595 (1979).

[11] S. Tsuruta, H. Sakoe, S. Chiba, *DP-100 Connected Speech Recognition System*, presented at INTELCOM 1979.

[12] Т. К. Винцук, *Поэлементное распознавание непрерывной речи составленной из слов заданного словаря*, Кибернетика, 7, 2, pp. 133–143 (1971).

Received January 10, 1990

ARCHIVES OF ACOUSTICS
16, 3–4 489–500 (1991)

AUDIBILITY OF CHANGES IN SPECTRAL STRUCTURE OF SAW-TOOTH STIMULI

H. HARAJDA AND W. MIKIEL

Department of Acoustics, Institute of Physics, Pedagogical University
(65-069 Zielona Góra, Plac Słowiański 6)
Institute of Fundamental Technological Research, Polish Academy of Sciences
(00-049 Warszawa, Świętokrzyska 21)

This paper presents the experiments which provided an answer to the question: what structural changes in the saw-tooth stimuli are likely to affect changes in the colour perception? The sound material of the experiments consisted of signals with structural features which can be found in the signals of natural string instruments. The signals were assumed to be characteristic of the following constant quantities:
– harmonic structure composed of successive component tones,
– triple time structure: attack-steady state-decay,
– gradually decreasing tendency in the level of the spectrum envelope. In the experiments the ATARI computer system was utilized. The groups of observers consisted of 5 subjects well-educated in music and acoustics who went through a special pre-test training. The research findings on the dependence of changes in auditory sensation on the changes in the structure of the saw-tooth stimuli being compared indicate that this relationship assumed a simple form when the variables were either the number of component tones or the decreasing tendency in the level of spectrum envelope.

1. Introduction

Since Helmholtz [10] advanced the problem of the dependence of an aural sensation of sound on the structure of a given signal, a number of suggestions have been put forward to solve this problem including the concept of a tone colour unit the "chrome" [2]. Nevertheless, the problem remains an open one. As the study of the structure complexity of signals produced on musical instruments becomes more precise, the need to define the most important distinguishing features of the structure and the need to move from descriptions of a qualitative relationship between "changes in structure" and "changes in sensation" to quantitative descriptions stands out more clearly [9, 13, 14, 15].

As our knowledge of dynamic spectral structures and the minute structure of natural instrumental and vocal stimuli is still insufficient, it becomes necessary to orient our experiments to stimuli which are structurally less complicated.

For several years experiments on the audibility of structural changes in signals have been carried out using computer techniques. During the last decade, a series of experiments has been regularly carried out by means of profile analysis [4, 6, 7, 8]. The main emphasis has been placed on short multitone complex stimuli modelled following the behaviour of the background of uniform amplitude and the central component of ca. 1000 Hz, distinctive for its amplitude level. A variety of changes have been introduced into this model: changes in the central tone level and the background level, in the number and density of component tones on the frequency scale [4, 5, 7], changes in the frequency and phase [6]. The dependence of change detection on the number of trials [11] has been investigated. The thresholds of difference detection in the spectrum envelope have been determined and, simultaneously, both the background and the central component have been modified [1]. The sound material of the experiments has comprised signals with flat and rippled spectrum envelopes of the background [12], [8].

The spectrum envelope of the natural sounds of string instruments is characteristic of the general decreasing tendency whereas the authors of the above papers of reference assume that the amplitude level is equal for all components.

2. Aim and method

The basic aim of the present experiments is to provide an answer to the question: what structural changes in the saw-tooth stimuli are likely to affect changes in the tone colour sensations?

The sound material of the experiments consisted of signals with the structural features which can be found in the signals of natural string instruments. The signals were assumed to be characteristic of the following constant qualities:

– harmonic structure composed of successive component tones (16 tones in the case of standards);
– a constant spectrum envelope slope;
– signals of 100 ms duration;
– triple time structure; attack-steady state-decay;
– time of increase up the amplitude level of to its steady value in: 50 ms;
– formation time of required frequency; 15 ms;
– signal decay of 50 ms duration.

Altered signals differed from standard ones in one of the following characteristics:

– number of harmonic tones
– value of the spectrum envelope slope.

In the experiments the ATARI computer equipment was used. The stimuli were

tones generated by the POKEY computer system and the only controlled parameter was the tone intensity level. To design the test material, a modified set of SOFTSYNTH programes was used The SOFTWARE SYNTHESIZER, Ch. Nieber, Berlin 1985.

The method was as follows. The analogue image of a stimuli was transformed into a graphic one to set a pattern for the headphone membrane control. Fifteen aural detection tests of three types: N–tests, Tn–tests and R–tests were designed for the experiment. Each test comprised from 10 to 30 tasks to solve by a group of listeners (50 per cent of them were tasks of "standard-standard" type and 50 percent – of "standard-alteration" type).

The time paradigm for all the test tasks is shown in Table 1.

The experiment was carried out in an audiometric booth and the stimuli were presented to the listeners over TDH–49 headphones. The intensity level of signals was varied over 65 ± 3 dB.

The group consisted of 5 subjects well-educated in music and acoustics who went through a special pre-test training session. The task assigned to the subjects was to determine whether the stimuli were the same or different in terms of their tone colour qualities. The listeners were given response sheets on which they marked "+" for "I can hear a difference", "−" for "I can't hear a difference" and "x" for "I can't make a clear statement".

N–tests

At this stage of experiments there were three tests with altered stimuli different in the number of tone components. In the tasks of the "standard-standard" type the stimuli comprised 16 successive harmonic tones whereas in the "standard-alteration" tasks the second stimulus contained from 1 to 15 successive tones. The slope of the amplitude the envelope was − 3 dB. The fundamental frequencies were 196 Hz, 392 Hz and 659.3 Hz. Each set comprised 30 tasks to perform.

Tn–tests

Two sets of six tests were designed for the use in this experiment. The test stimuli consisted of 16 component tones and the fundamental frequencies were 196 Hz, 392 Hz and 659.3 Hz. In the first set, standard stimuli were characterized by the slope of the spectrum envelope of − 3 dB/oct (W.I). In altered stimuli the slopes were of −0.5, −1.0, −1.5, −2.0, −2.5 and − 3.5 dB/oct. Each test contained 14 tasks to perform (7 of the "standard-standard" type and 7 of the "standard-alteration" type).

In the second set the slope of the spectrum envelope for standard stimuli was − 5 dB/oct and in the case of altered stimuli: −1.0, −2.0, −3.0, −4.0 or 6.0 dB/oct

(WII). Each test contained 10 tasks to perform (5 of the "standard-standard" type and 5 of the "standard-alteration" type).

R–tests

The test material was composed of stimuli of fundamental frequencies 196 Hz (g), 293.7 Hz (d^1), 392 Hz (g^1) and 440 (a^1).

Seven tests were designed for this experiment, each of them comprising 16 tasks to perform (8 of "standard-standard" type and 8 of "standard-alteration" type). In the altered stimuli, amplitudes of the maxima located on one of the harmonics (from one of order 3 to 12) were varied, assuming thus different values. The maxima were also set at other places. Changes of the level of maximum piaced on tones 3 and ranged from −0.83 to −2.41 dB, on tones from 5 to 8 ranged from −0.36 to −5.11 dB, on tone 9 from −1.85 to −5.11 dB, on tone 10 from −2.41 to 5.11 dB, on tones 11 and 12 from −3.01 to −5.11 dB (Fig. 4).

Independently of the baseline experiment, the subjects performed 58 individual tasks of the "standard-alteration" type. In altered stimuli, the following variations of the maximum level were introduced:

tone 3 – −0.36 dB and −3.01 dB
tone 4 – ranging from 0.36 to 1.32 dB, and −3.65 dB
tone 9 – ranging from 0.36 to −2.41 dB
tones from 12 to 16 – ranging from −0.36 to −5.11 dB.

This procedure broadened the limits within which the differences between the maximum level and the component tone level in the standard signal were contained from 1.49 dB to 11.64 dB.

In such a distribution of the maximum level variations differences between the maximum level and the amplitude level of the preceding tone were contained within the limits of 0.01 to 2.64 dB when the maximum was located on tone 3, and ranged from 6.31 to 11.14 dB when the maximum was located on tone 16.

To sum up, the differences between the maximum level and the amplitude level of a given component tone in the standard signal ranged from 2.09 dB to 11.64 dB.

Results

N–tests

Totally, 2700 raw data were obtained from the subjects in this type of tests (2.312 correct and 372 incorrect detections, one percent of incorrect detections were false alarms. There were also 112 responses of ambiguity ("I can't make a clear statement").

Table 1. N-tests results

Number of eliminated harmonic tones Δ on	Number of responses N			Percentage of responses: [%]		
	+	−	X	+	−	X
15	88	2	0	98	2	0
14	90	0	0	100	0	0
13	90	0	0	100	0	0
12	89	1	0	99	1	0
11	88	2	0	98	2	0
10	85	5	0	95	5	0
9	74	16	0	82	12	0
8	74	16	0	82	12	0
7	69	21	0	77	23	0
6	62	28	0	69	31	0
5	66	24	0	74	26	0
4	47	52	0	43	48	0
3	34	54	2	38	60	2
2	17	70	3	19	78	3
1	7	79	4	8	83	0
0	1330	17	3	99	1	0
Σ	2312	376	12	86	13	1

Table 1 shows the analysis of the data obtained as dependent on the number of higher successive component tones which have been eliminated, i.e., as dependent on the difference in the number of component tones between standard and altered signals being compared.

Indications of "I can't hear a difference" occurred in cases of slight structural changes (from 1 to 3 component tones).

Table 2 shows the distribution of correct (O.K.) responses in percentage as dependent on the stimulus pitch. Three segments can be seen:

– when the differences are of 10 to 15 tones, a very satisfactory level of agreement (over 95 percent) has been achieved; these changes are clearly audible;

– when the difference is in 5 to 9 component tones, the number of correct directions is from 70 to 95 percentage; changes within this limit are also audible;

– when 1 to 4 tones have been eliminated, the number of correct responses is considerably lower; these changes are very difficult to detect or almost impossible to discriminate.

The results for the highest pitches of the investigated stimuli are definitely lower as compared with the other signals to detect.

Table 2. R-tests results

Harmonic H	Sound	Intensity level of maximum [dB]																					
		−5.11			−4.35			−3.65			−3.01			−2.41			−1.85			−1.32			−0.83			−0.36		
		Number of responses																									
		+	−	×	+	−	×	+	−	×	+	−	×	+	−	×	+	−	×	+	−	×	+	−	×	+	−	×
5	g	8	20	2	0	30	0	0	30	0	13	3	14	10	8	12	20	1	9	26	1	3	30	0	0	30	0	0
	d^1	0	30	0	30	0	0	27	3	0	18	1	11	26	0	4	22	1	7	29	0	1	20	1	9	27	0	3
	g^1	1	28	1	16	14	0	15	10	5	20	4	6	22	2	6	28	0	2	28	0	2	27	0	3	25	0	5
	a^1	16	14	0	28	2	0	28	0	2	27	0	3	28	0	2	25	0	1	30	0	0	30	0	0	30	0	0
6	g	0	30	0	0	30	0	12	16	2	6	18	6	10	8	12	18	0	12	24	1	5	28	0	2	30	0	0
	d^1	6	14	10	12	10	8	25	4	1	30	0	0	30	0	0	26	1	3	30	0	0	30	0	0	30	0	0
	g^1	10	10	10	20	6	4	21	7	2	10	12	8	20	2	8	28	0	2	30	0	0	27	0	3	30	0	0
	a^1	20	10	0	25	5	0	30	0	0	30	0	0	30	0	0	28	0	2	30	0	0	28	0	2	30	0	0
7	g	7	18	5	11	14	5	21	7	2	20	7	3	19	6	5	22	2	6	22	2	6	24	0	6	30	0	0
	d^1	7	20	3	28	0	2	26	0	4	20	3	7	18	5	7	22	3	5	22	1	7	23	0	7	30	0	0
	g^1	20	5	5	14	8	8	12	8	10	22	3	5	28	0	2	23	2	5	22	1	7	25	0	5	30	0	0
	a^1	22	5	3	24	4	2	29	0	1	26	0	4	29	0	1	25	2	3	26	0	4	27	0	3	30	0	0

Tn–tests

In these tests, 1.620 raw data were obtained (1.134 correct and 291 incorrect detections). In the number of incorrect responses there were 16 false alarms. In 15 cases the subjects reported that they could not make a clear statement.

The distribution of correct (O.K.) responses as regards the stimulus pitch is shown in Fig. 3.

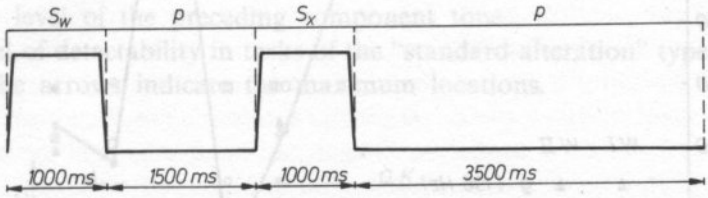

FIG. 1. Time paradigm of test task. S_w – standard signal, S_x – changed signal, p – interval between signals, P – interval for response

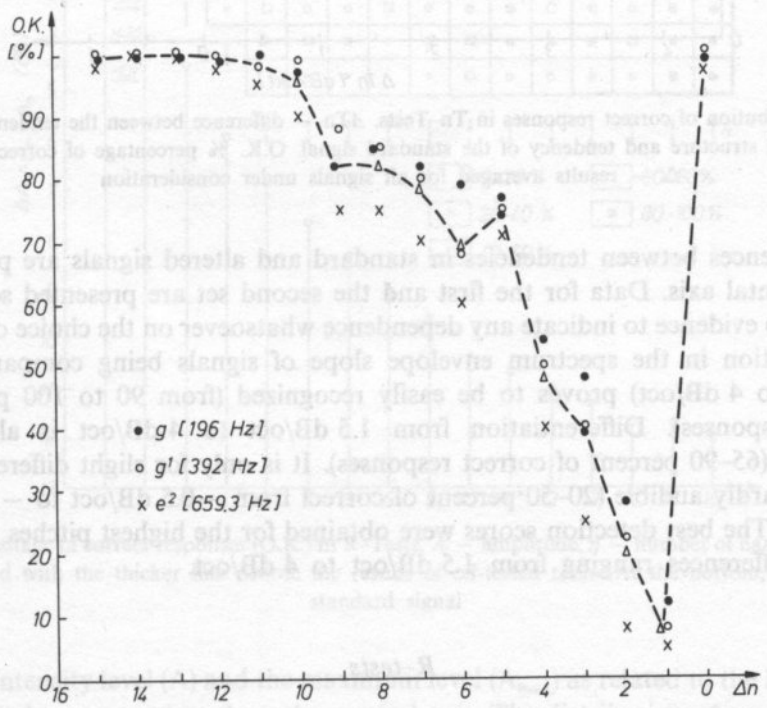

FIG. 2. Distribution of correct responses in N–Tests. Δn – loss in the number of harmonic tones. O.K. [%] – percentage of correct responses, Δ – results averaged for all signals under consideration. Measuring point calculated out on 90 responses

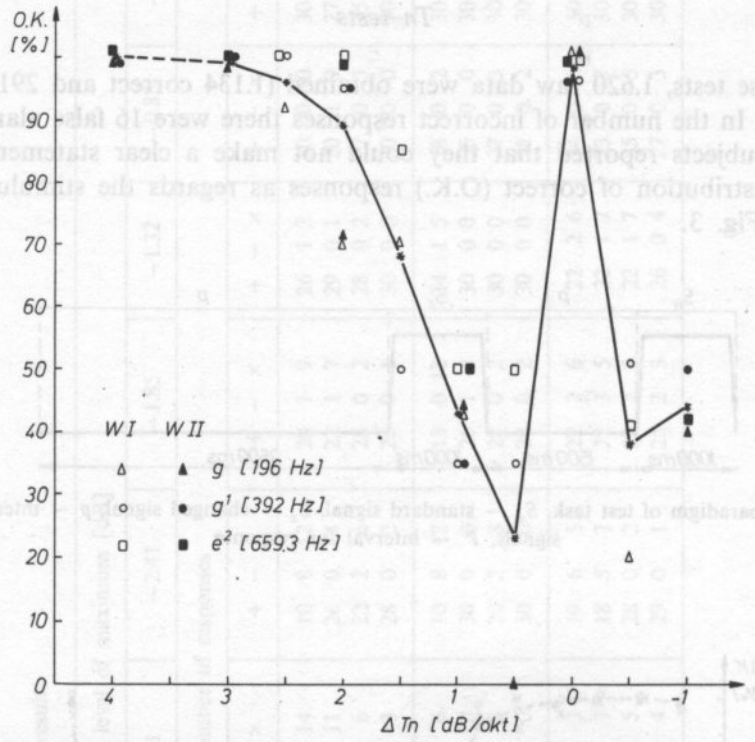

FIG. 3. Distribution of correct responses in Tn–Tests. ΔTn – difference between the tendency of signal with changed structure and tendency of the standard signal. O.K. % percentage of correct responses. △ – results averaged for all signals under consideration

Differences between tendencies in standard and altered signals are plotted on the horizontal axis. Data for the first and the second set are presented separately. There is no evidence to indicate any dependence whatsoever on the choice of pattern. Differentiation in the spectrum envelope slope of signals being compared (from 3 dB/oct to 4 dB/oct) proves to be easily recognized (from 90 to 100 percent of correct responses). Differentiation from 1.5 dB/oct to 4 dB/oct is also easily detectable (65–90 percent of correct responses). It is only for slight differences that they are hardly audible (20–50 percent of correct from −0.5 dB/oct to −1 dB/oct) responses. The best detection scores were obtained for the highest pitches of signals and for differences ranging from 1.5 dB/oct to 4 dB/oct.

R–tests

A total of 9.720 responses was obtained from the subjects for this type of tests and 1.044 responses from solving 58 individual test tasks, 73 percent of correct answers were obtained for both the test and individual tasks. Eighteen percent of

them were incorrect, including 2.2 percent of false alarms. In 11 cases, the listeners reported that they were incapable of making a clear statement.

We can further consider the obtained data on the following grounds:

— we can assume that the intensity level of the fundamental tone is a constant level of reference;

— we can analyse differences in the maximum level with respect to a given level of the component tone in the standard stimulus;

— we can try to find out to what extent the level of a given maximum exceeds the intensity level of the preceding component tone.

The level of detectability in tasks of the "standard-alteration" type is presented in Fig. 4. The arrows indicate the maximum locations.

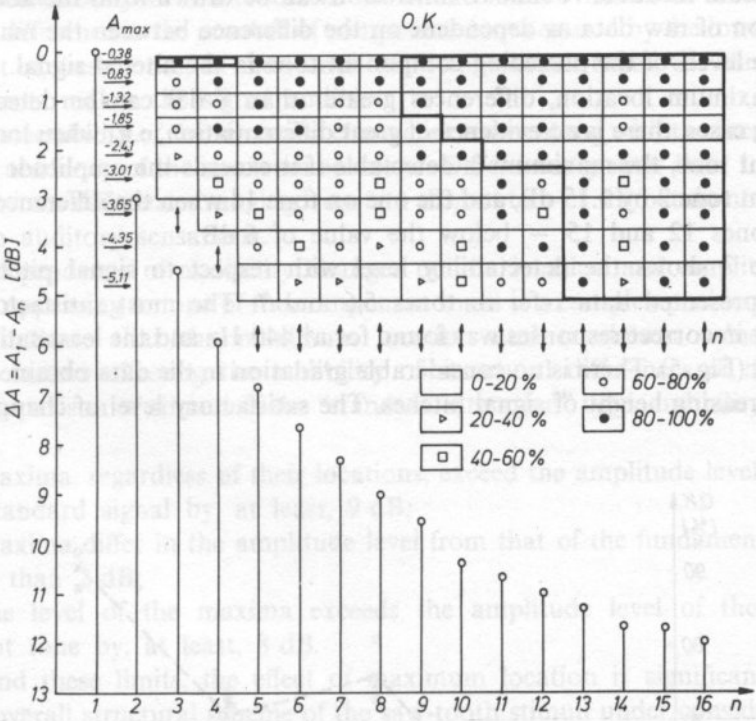

FIG. 4. Percentage of correct responses (O.K.) in R–Tests. A — amplitude, n — number of harmonic tones. Fields circled with the thicker line denote the results of off-tested tasks. At the bottom, spectrum of standard signal

The intensity level (A) and the maximum level (A_{max}) as related to the level of the fundamental tone are plotted on the vertical axis. The distribution of correct (O.K.) responses within the whole range of the alteration field points to a dependence of auditory sensation detectability on both the range of alteration and the maximum location. Overall structural changes comprising a maximum higher than the

fundamental tone by − 2 dB regardless of its location, are easily detected (60 to 100 percent of correct responses).

From the analysis of data distribution as dependent on the difference between the maximum and amplitude levels of a given component tone in the standard stimulus it follows that the differences from 9 dB are satisfactorily detected regardless of the maximum location within the spectrum. In the case of smaller differences there is no evidence of a regular relationship between the maximum level and the percentage of detectable sound differences in signals being compared. For instance, it can be easily calculated from the data in Fig. 4 that the maximum located on tone 7 is audible only if its level exceeds the amplitude level of a given component tone in the standard by 3.15 dB, the maximum on tone 8 − by 5.84 dB, and the maximum on tone 9 − by 4.65 dB. And this point to the dependence of auditory sensation on the maximum location. A similar conclusion can be drawn from the analysis of the distribution of raw data as dependent on the difference between the maximum and amplitude levels of the preceding component tone in the altered signal. Irrespective of the maximum location, differences greater than 8 dB can be detected. In the remaining cases, there is no evidence of great differentiation, e.g., when located on the component tone, the maximum is detectable if it exceeds the amplitude level of the component tone 2 by 1.15 dB, and the one on tone 14 when the difference is 8.59 dB, but on tones 12 and 15 − below the value of 6 dB.

Table 2 shows the detectability level with respect to signal pitches.

The presented data refer to tones 5,6 and 7. The most satisfactory level of agreement in correct responses was found for a^1 440 Hz and the least satisfactory for g (196 Hz) (Fig. 5). There is no considerable gradation in the data obtained as related to the increasing height of signal pitches. The satisfactory level of change detection

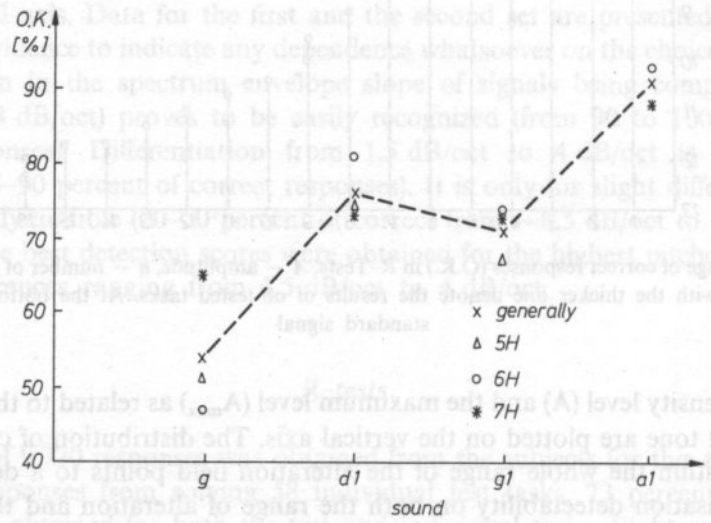

FIG. 5. Distribution of correct responses (O.K.) − in R–Tests. 5H, 6H, 7H − number of harmonic tones

for a^1 and, simultaneously, the low level of detectability of the same changes for g^1 is certainly due to the fact that a^1, a tuning fork sound, is particularly familiar to all those who are professionally concerned with music.

Conclusions

The research findings on the dependence of changes in auditory sensations on the changes in the structure of the saw-tooth stimuli being compared indicate that this relationship assumes a simple form when the variables are either the number of component tones or the decreasing tendency in the level of the spectrum envelope.

The detectability of differences in the sound stimuli increases along with the increasing difference in the number of component tones caused by the lowering of the upper limit of these tones. In the stimuli of 16 component tones, the elimination of 5 components makes the signal audible.

The detectability of the sensation change increases along with the increase in the decreasing tendency of the spectrum envelope. Differences greater than 1 dB/oct are audible whereas differences ranging from +1 dB/oct to − 1 dB/oct do not affect any changes in auditory sensations.

The dependence of audibility changes on the location and amplitude of the maximum appearing on one of the component tones is a complex problem. The data obtained indicate that the maximum location and maximum value are very important factors affecting the audibility of structural differences of this type.

In comparison of stimuli of the "standard-alteration" type, audibility is secured when:

– maxima, regardless of their locations, exceed the amplitude level of a given tone in standard signal by, at least, 9 dB;

– maxima differ in the amplitude level from that of the fundamental tone by not more than 2 dB;

– the level of the maxima exceeds the amplitude level of the preceding component tone by, at least, 8 dB.

Beyond these limits, the effect of maximum location is significant.

The overall structural scheme of the saw-tooth stimuli under consideration can be treated, according to the model known as "profile analysis" [4, 8], as a set of elements forming the background with a signal (i.e., a change in amplitude forming a maximum) set against that background. The experiment data indicate then that the ratio of signal amplitude and the background is not the only factor which (when the background is not altered) results in aural sensation occurrence. The low audibility level of signals located on overtones 4 and 8 (octave positions) suggests the hypothesis that one of the decisive factors in this respect is likely to be the interval function of the component tone forming a signal. This problem is, however, beyond the purpose and scope of this paper. The factors which affect the ability of change

discrimination when the amplitude location is changed in the signals with a decrease in the spectrum envelope have not yet been fully explored and therefore further experiments are called for to clarify the problem.

References

[1] L. R. BENSTEIN, D. M. GREEN, *Detection of simple and complex changes of spectral shape*, J. Acoust. Soc. Am, **82** (5), 1587–1592, (1987).

[2] F. DACOS, *Étude fondamentale du violon*, Proc. X Jub. Seminarium Otw. z Akustyki, Poznań, 65–75 (1967).

[3] DE RE ATARI, Software Development Support Group, COMPTON, USA, 1981.

[4] D. M. GREEN, G. KIDD, Jr, *Further Studies of auditory profile analysis*, J. Acoustic. Soc. Am. 73 (4) 1260–1265, (183).

[5] D. M. GREEN, G. KIDD, JR., M. C. PICARDI, *Successive versus simultaneous comparison in auditory intensity discrimination*, J. Acoust. Soc. Am. 73(2), 639–643, (1983).

[6] D. M. GREEN, Ch. R. MASON, *Auditory profile analysis: Frequency, phase, and Weber's Law*, J. Acoust. Soc. Am. 77 (3), 1155–1161, (1985).

[7] D. M. GREEN, Ch. R. MASON, G. KIDD, JR., *Profile analysis: Critical bands and duration*, J. Acoust. Soc. Am. 75 (4), 1183–1167, (1984).

[8] D. M. GREEN, Z. A. ONSAN, T. G. FORREST, *Frequency effects in profile analysis and detecting complex spectral changes*, J. Acoust. Soc. Am. 81 (3), 692–699, (1987).

[9] H. HARAJDA, *Projet de classification du timbre du violon*, Bulletin de la Soc. des Amis des Sciences de Poznań, 35–41, (1967).

[10] H. HELMHOLTZ, *Sensations of Tone*, A. J. Ellis, London (1985).

[11] G. KIDD, JR., Ch. R. MASON, *Evidence for sensory-trace comparison in spectral shape discrimination*, J. Acoust. Soc. Am. 84 (1), 144–149, (1988).

[12] G. KIDD, JR., Ch. R. MASON, D. M. GREEN, *Auditory profile analysis of irregular sound spectra*, J. Acoust. Soc. Am. 79 (4), 1045–1053, (1986).

[13] KOENG-MO SUNG, *String instrument tone synthesis using nonlinear distortion technique*, International Symposium on Musical Acoustics, Mittenwald, Abstracts, 135 (1989).

[14] M. KWIEK, *Resonant factors in sound colour* (in Polish), Polski Rocznik Muzykologiczny, 2, 1–8 (1963).

[15] M. A. MÜLLER, M. SCHLESKE, *Is Scientific Research useful for Violin Makers*, International Symposium on Music Acoustic, Mittenwald, Astracts, 151 1989.

This work was supported by the Central Research Project CPBP 0203/7.10 – 1989

Received November 13, 1989

ARCHIVES OF ACOUSTICS
16, 3–4, 501–511 (1991)

USE OF ANTHROPOMORPHIC COMPRESSED BREAST PHANTOMS FOR COMPARING ULTRASOUND BREAST IMAGERS

E. KELLY-FRY

Indiana University School of Medicine Indianapolis, Indiana, USA

E. L. MADSEN, G. R. FRANK

University of Wisconsin, Madison, Wisconsin, USA

Two anthropomorphic breast phantoms were used to compare state-of the art ultrasound imagers. The phantoms mimic refractive effects at fat to nonfat boundaries, and include simulated and pathological structures like fibroadenomas, cysts, calcifications and malignant tumors. Images of those structures obtained by means of various ultrasound systems are compared and discussed. In conclusion, the authors recommend use anthropomorphic breast phantoms which simulate the acoustic characteristics of normal and pathological breast tissues to test ultrasound mammography systems prior to their routine use on patients.

Two anthropomorphic breast phantoms representing the compressed breast – and already reported in the literature [1] were used to compare state-of-the-art ultrasound imagers. The phantoms mimic the breast regarding attenuation and refractive effects at fat to nonfat boundaries. This includes bulk ultrasonic properties and geometric factors.

Diagrams of the contents of the first phantom (phantom I) are shown in Fig. 1. Three different views are shown. In Fig. 1 a is a view from the top. The phantom is 24 by 10 cm, as viewed, and includes 19 simulated spherical masses and one large fat-mimicking sphere. Of most importance in the present paper are six sets of 3 identical tissue-mimicking masses labeled *A B C E F* and *G*. For example, row *A* consists of 3 identical 6.3 mm diameter very highly attenuating spheres. These differ in their depth in the simulated glandular region. These three are also depicted in the side view shown in Fig. 1b. Their differences in depth are illustrated. Row *B* consists of 6.3 mm diameter low scatter masses representing fibroadenomas. Row *C* contains 6.3 mm diameter simulated cysts, Row *E*, 9.5 mm diameter cysts, Row *F*,

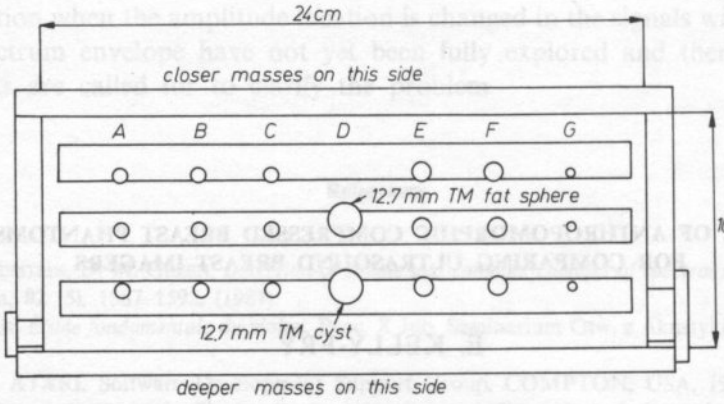

FIG. 1a. Diagram of phantom I viewed through the scanning window. Rows *A*, *B*, *C*, *E*, *F* and *G* each contain three identical spherical simulated lesions suspended in the tissue-mimicking *TM* glandular region. Row *D* contains two 12.7 mm diameter spherical objects, the upper one, a *TM* fat sphere and the lower one a *TM* cyst

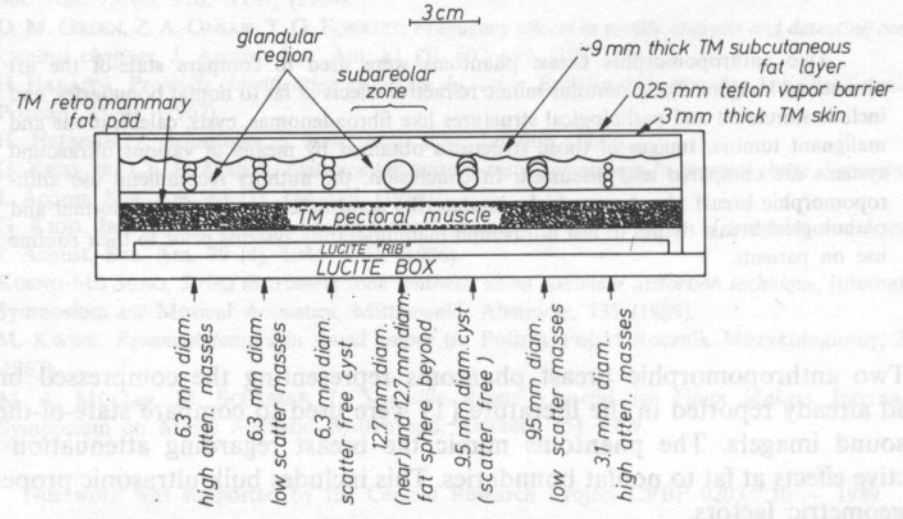

FIG. 1b. Side view diagram of phantom I showing the various layers of *TM* material and the different depths of the simulated lesions. An end view of the 1 mm diameter stacked agar rods simulating pectoral muscle bundles is shown. Also note the undulating interface between the *TM* subcutaneous fat layer and the glandular region

9.5 mm low scatter masses. Row *G* contains 3 mm diameter high attenuation masses composed of the same material as those in Row *A*. Notice the realistic irregularly shaped interface between the subcutaneous fat and the glandular region. Also of importance, regarding realistic beam distortions, is the fact that 25% of the

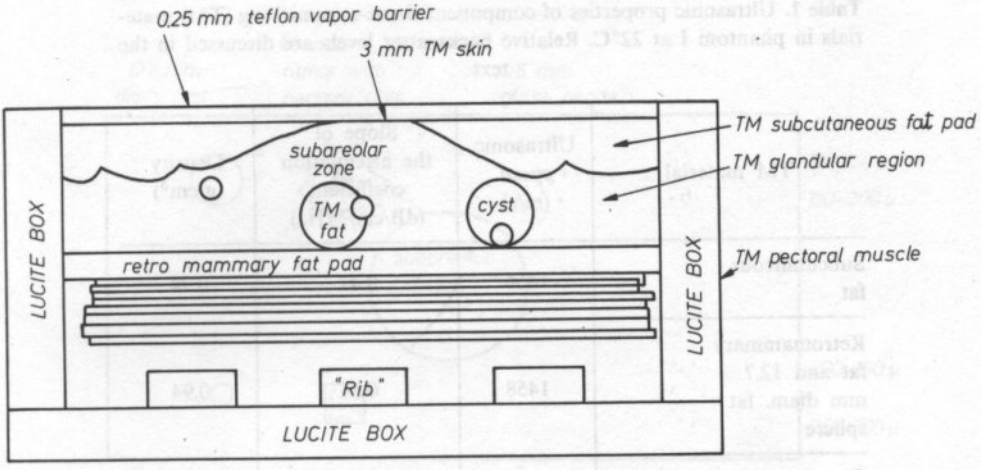

FIG. 1c. End view diagram of phantom I again showing the different depths of the lesions in the identical sets of three

glandular region is composed of randomly positioned fat spheres having diameters between 3 and 6 mm. In Fig. 1c is shown an end view of the phantom with the increasing depth of sets of three masses shown more plainly.

In Table 1 are shown ultrasonic properties of the contents of the phantom. Of importance is the much lower ultrasonic speed in the simulated fat, 1456 m/s, compared to that in the other simulated tissues. The fat also has a lower density, 0.94 gm/cm^3, compared to 1.03. Notice also the low attenuation in the cysts, 0.1 dB/cm/MHz, and the very high value of 8.7 dB/cm at 3 MHz for the highly attenuating spheres.

Fig. 2a and 2b depict phantom II, which is simpler in some ways than phantom I. Relatively large calcifications are represented with 4 one-half mm diameter glass beads. Smaller calcifications are represented with 5 sets of calcium hydroxyapatite particles varying from 100 through 300 microns in diameter. One set of 250 to 300 micron diameter particles are embedded in the glandular parenchyma, and another such set is embedded in an approximately 1 cubic cm volume having a backscatter level 6 dB below that of the surrounding glandular parenchyma. Notice also the simulated malignant tumor with a highly attenuating necrotic corea. A 4 mm diameter low scatter simulated fibroadenoma is also present. Another difference between this phantom and phantom I is that there are no fat spheres distributed in the glandular region.

The remaining figures emphasize the importance of breast phantoms in determining whether a specific imaging system can identify small masses located in **deep** regions of the breast and whether that system is also capable of definitively imaging the wall characteristics and internal structures of breast masses.

In Fig. 3a is an image obtained with the Siemens sonoline SL-1; that in Fig. 3b with the Aloka 620. All three of the three mm diameter highly attenuation masses in

Table 1. Ultrasonic properties of component tissue-mimmicking (TM) materials in phantom I at 22°C. Relative backscatter levels are discussed in the text

TM material	Ultrasonic speed (m/s)	Slope of the attenuation coefficient (dB/cm/MHz)	Density (g/cm^3)
Subcutaneous fat	1456	0.47	0.94
Retromammary fat and 12.7 mm diam. fat sphere	1458	0.54	0.94
Glandular parenchyma	1569	0.34	1.03
Fat spheres composing 25% of glandular region	1445	0.3	0.92
Cysts	1568	0.1	1.02
Low scatter lesions ("fibroadenomas")	1564	0.34	1.03
High attenuation lesions	1508	8.7 at 3 MHz	1.05
Pectoral muscle	1540	0.4	1.08
Skin	1570	0.6	1.05

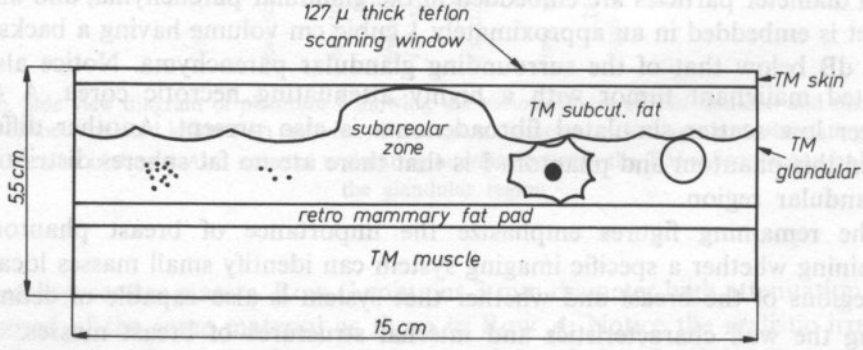

FIG. 2a. Side view diagram of the contents of phantom I including calcifications and a simulated malignancy with a necrotic core. The 8 cm × 15 cm scanning window is perpendicular to the figure.

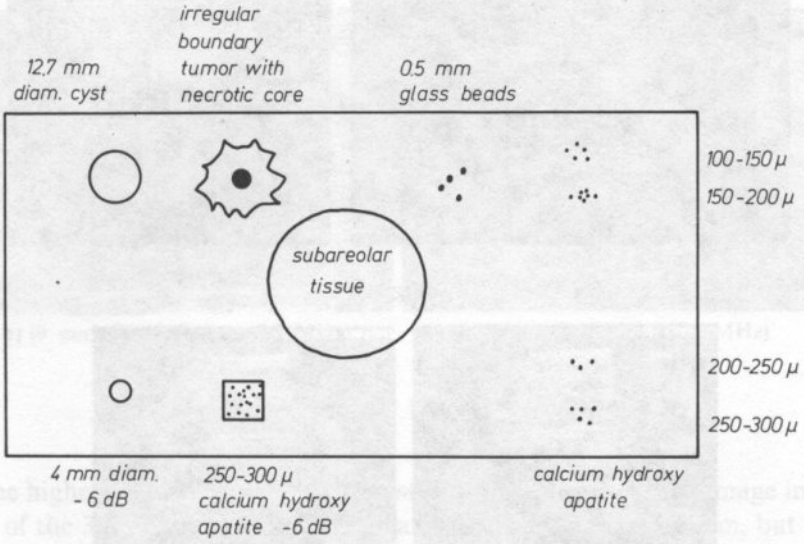

FIG. 2b. Diagrammatic view of anthropomorphic compressed breast phantom II from the scanning window side. Various objects are embedded in the *TM* glandular parenchyma. Six sets of simulated calcification are shown, five of which are Calcium hydroxyapatite, which is the inorganic component of bone. The leftmost set of calcifications are randomly suspended in a 0.5 cm^3 volume of *TM* abnormal tissue having a − 6 dB scatter level relative to the *TM* glandular parenchyma. Also shown is a realistic simulated tumor with an irregular boundary and a highly attenuating necrotic core. The vital part of the tumor is at − 6 dB scatter level relative to the glandular parenchyma except for two small "chips" of higher scatter material present to produce an irregular internal texture

phantom I are distinctly visible in Fig. 3a. In Fig. 3b, the mass closest to the surface is visible, and that located mid-region is also imaged. A significant finding was that the deepest mass could not be adequately imaged with this 7.5 MHz system.

Figures 4a and 4b show images of the 3 mm high attenuation mass closest to the phantom surface. That in Fig. 4a was obtained with the 6 MHz, linear array Phillips system and that in Fig. 4b with the 5 MHz linear array Acuson system. Note that

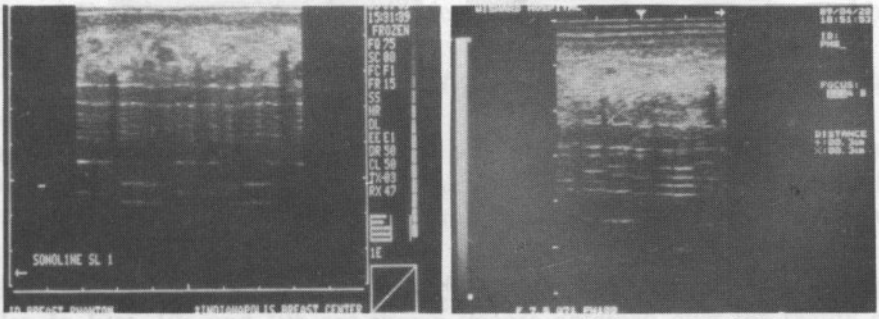

a) (Siemens − 7.5 MHz) b) (Aloka − 7.5 MHz)

Fig. 3. Images of 3 mm masses in Phantom I

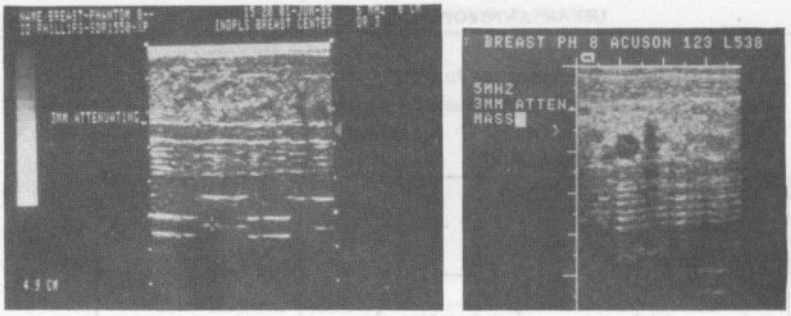

a) b)

Fig. 4

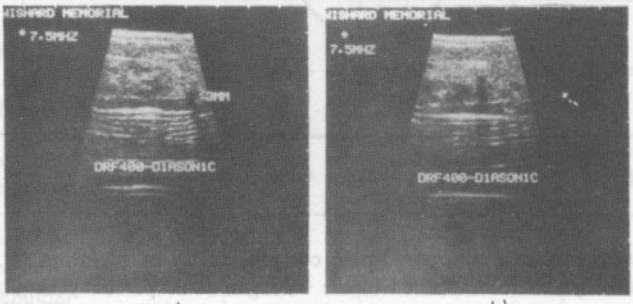

a) b)

Fig. 5

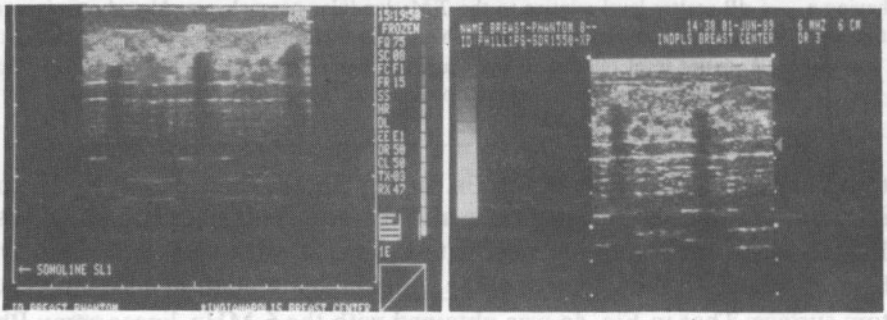

a) b)

Fig. 6

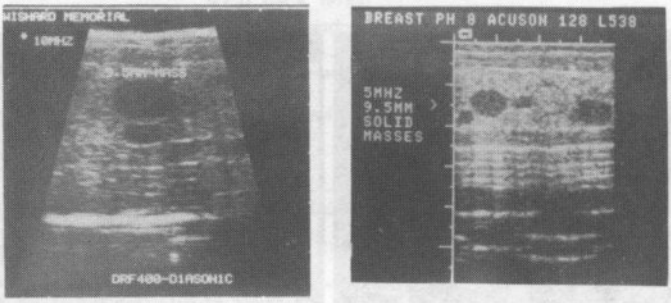

a) Fig. 7 b)

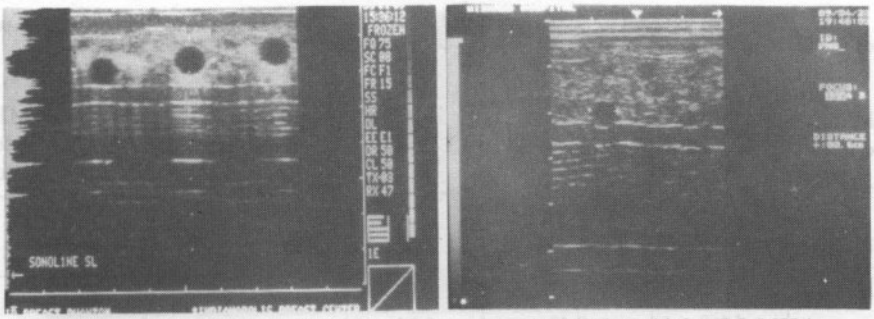

a) (9 mm Cysts-Siemens 7.5 MHz) b) (6 mm Cyst-Aloka 7.5 MHz)

Fig. 8

FIG. 3–8. Images of cystic structures in phantom I

despite the higher frequency, the 3 mm mass is poorly shown on the image in Fig. 4a. All three of the 3 mm masses could be located with the 5 MHz system, but only the most shallow one could be detected with the 6 MHz system, that is, the 6 MHz system could not locate either the mid-depth or deepest mass.

It was found that the Diasonics 7.5 MHz sector scanner was capable of imaging all three of these 3 mm masses. The deepest and most shallow are shown in Figs. 5a and 5b.

All of the tested systems could detect the 6 mm highly attenuating masses irrespective of the depth of their location. The Siemens 7.5 MHz linear array system provided the image in Fig. 6a, and the Phillips 6 MHz linear array system provided the image shown in Fig. 6b. Note the difference in resolution of wall structures in these two images.

Figures 7a and 7b are of interest because they compare images of the same solid mass by a 10 MHz sector scanner (Fig. 7a) and a 5 MHz linear array scanner (Fig. 7b). As you can see, in this case, the **lower** frequency system provided an image which is far superior to that of the higher frequency system.

All of the tested systems were capable of imaging all cysts shown in Phantom I. Figure 8a shows three 9.5 mm cysts imaged by the Siemens 7.5 MHz linear array system, and Fig. 8b shows an image of a deeply located 6 mm cyst as imaged by the 7.5 MHz linear array Aloka system.

The remaining figures show images of phantom II in the regions of simulated microcalcifications.

Images of the 1/2 mm glass beads are shown in Figs. 9a and 9b. The image in Fig. 9a was obtained with the 5 MHz Acuson system, that in Fig. 9b with the 5.0 MHz Aloka system. All of the systems tested were capable of imaging the highly reflective glass beads.

However, none could image the 100–300 micron calcium hydroxy apatite particles. In Figs. 10a and 10b are shown images obtained over the region of the 250–300 micron particles suspended in the 1 cm^3 low scatter tissue-mimicking

Table 2. Ultrasonic properties of TM materials in phantom II at 22°C: c ≡ ultrasonic speed; α/f ≡ slope of the attenuation coefficient with frequency; ϱ ≡ density; η ≡ backscatter coefficient

TM material	c (m/s)	α/f (dB/cm/MHz)	ϱ gm/ml	η (sr^{-1} cm^{-1})	η at 5 MHz relative to glandular (dB)
TM glandular	1561	0.36	1.04	$4.4X10^{-3}$ *	0
Subcutaneous fat	1458	0.43	0.94		−12
Retromammary fat	1458	0.40	0.94		−11
Tumor around necrotic core	1554	0.70	1.07		−6
Low scatter lesion with calcifications	1556	0.56	1.06		−6
Muscle	1559	0.55	1.05		+6
low scatter 4 mm mass	1561	0.33	1.04		−6
cyst	1560	0.12	1.02		--

* **in vivo** breast glandular tissue at 5 MHz: $\eta \sim 6X10^{-3}$ sr^{-1} cm^{-1} (DAVROS et al., 1986)

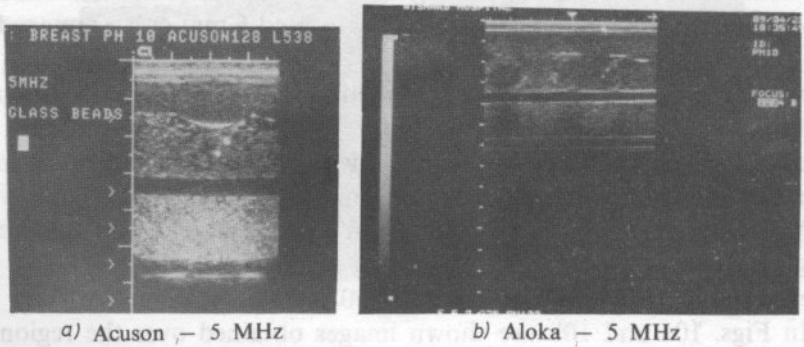

a) Acuson — 5 MHz b) Aloka — 5 MHz

Fig. 9. Images of 5 mm glass beads in phantom II

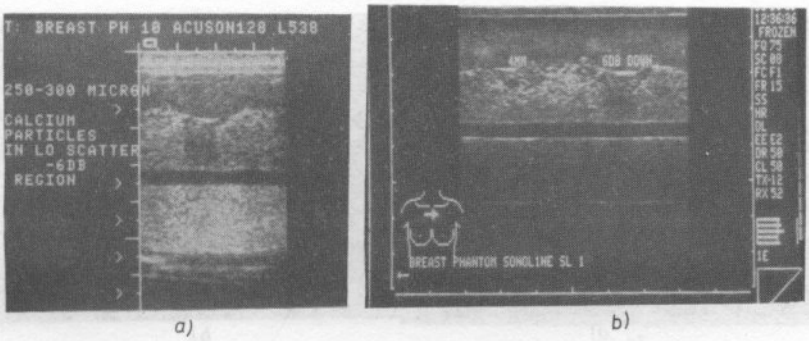

Fig. 10. Failure to image 100–300 micron particles in low-scatter region of Phantom II

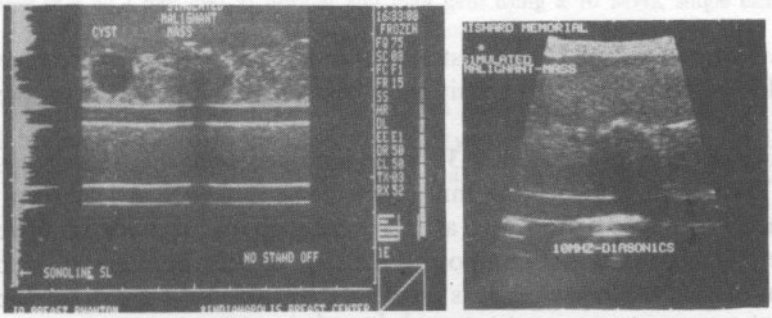

Fig. 11. Images of cept and simulated malignant mass at 7.5 MHz (a) and of same malignant at 10 MHz (b). Phantom II

region. Note in both images that the low-scatter – 6dB tissue mimicking region is recognizable, but no highly reflective particles are imaged within this region. In Fig. 10b, the 4 mm, low-scatter mass is also imaged. This small mass could be detected by all of the systems, but in some cases, it was not apparent whether this was a solid or cystic mass.

The simulated malignant mass was imaged by all of the real-time systems, but accurate delineation of its wall and internal structure was highly dependent on design of the ultrasound unit. Figure 11a shows an image of the malignant mass, and associated cyst, obtained with the 7.5 MHz Siemens system. Figure 11b shows this same mass as imaged with the Diasonics 10 MHz sector transducer. Both of these images include the region of the necrotic core. As you can see, the necrotic core is sharply imaged in Fig. 11a but is barely visible in Fig. 11b.

The images in Figs. 12a and 12b are still controversial regarding their meaning. They were made using an Aloka 7.5 MHz linear array and show a large cyst in a real breast. The cystic nature was verified by needle aspiration. In Fig. 12a the cyst is essentially echo free. In Fig. 12b, however – at a higher gain – artifactual echoes in the cyst are seen and a misdiagnosis of a solid mass could be made. Notice that the echoes have an irregular boundary. Presumably reverberations involving

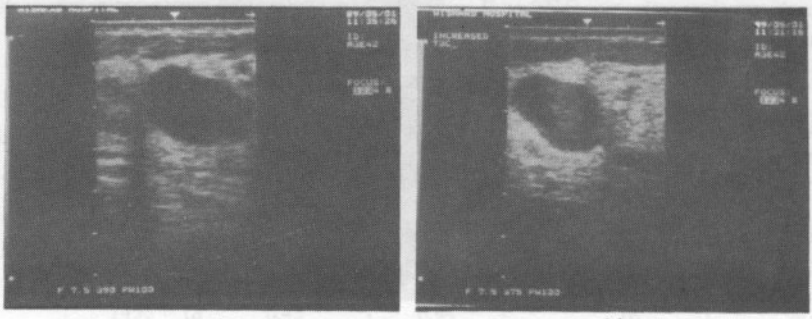

a) b)

FIG. 12. Images of a large cyst in a real breast

strong scatterers proximal to the cyst are involved, but perhaps these reverberations are added to strong laterially positioned scatterers to give rise to the irregular boundary.

The images in Figs. 13a and 13b were obtained with the Acuson system using phantom II. In Fig. 13a the 12.7 mm diameter simulated cyst is shown essentially free of echos. In Fig. 13b, however, at increased gain, discrete echoes have appeared within the cyst. The material composing the cyst is clear pure gelatin and therefore no internal echoes are expected. It is possible that these echoes are sidelobe artifacts related to the strong scatterers in the simulated glandular parenchyma lateral to the cyst. However, we have not yet ruled out the possibility that some imputities giving rise to echoes actually exist in the cyst.

Some evidence that the side-lobe explanation is the true one is offered in the images in Figs. 14a and 14b, obtained with a 10 MHz single element focused system. The cyst is imaged on the left in Fig. 14a at intermediate gain and in Fig. 14b at high gain. The cyst is echo free in both cases.

In summary, based on the variability of the systems tested with respect to their capability of detecting small deeply located masses and their ability to provide adequate image data on the structural characteristics of masses, the following recommendation is made.

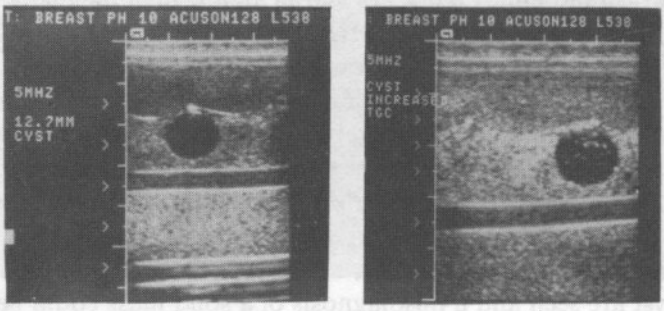

a) b)

Fig. 13. Images of a 12.7 mm cept at normal and high gain using a 5 MHz real-time system (Phantom II)

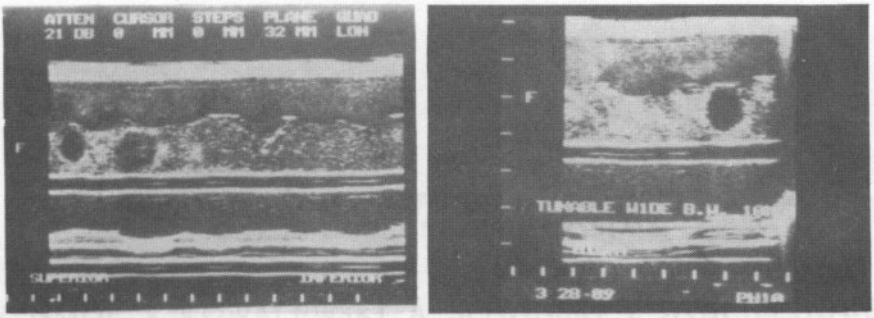

a) b)

Fig. 14. Images of a 12.7 mm cyst at normal and high gain using a 10 MHz, single element focused transducer. (Phantom II)

Anthropomorphic breast phantoms which simulate the acoustic characteristics of normal breast tissues and that of various type of benign and malignant breast masses should be used to test ultrasound mammography systems prior to their routine use on patients.

Acknowledgement

This work was supported in part by NIH grant RO1CA25634. Figures 1 and 2 and Tables 1 and 2 have been reproduced from Ref. [1] with permission of the publishers of Ultrasound in Med. and Biol.

References

[1] E. L. Madsen, E. Kelly-Fry, G. R. Frank, *Anthropomorphic phantoms for assessing systems used in ultrasound imaging of the compressed breast*, Ultrasound in Med. and Biol. **14**, Sup. 1, 183–201 (1988).

Received December 7, 1990

ARCHIVES OF ACOUSTICS
16, 3–4, 513–530 (1991)

INVESTIGATION OF LIGHT DIFFRACTION ON AN ULTRASONIC WAVE IN LIQUID NEMATIC CRYSTALS

M. KOSMOL, S. KOWALEWSKI, A. ŚLIWIŃSKI, I. WOJCIECHOWSKA

Institute of Experimental Physics, University of Gdańsk
(80-952 Gdańsk ul. Wita Stwosza 57)

During the investigation of laser polarized light diffraction on a pulse ultrasonic wave a fine structure in diffraction orders was observed in a cell filled with a nematic liquid crystalline medium (N—4 hexyloxybenzyliden, merck 4, merck 5 or a mixture of liquid W5 crystals). The fine structure is visible only after exceeding of the threshold intensities of the ultrasonic wave introduced into the nematic first ordered by the external magnetic field (B = 0.8 T) for polarized light in the polarization plane of the ordinary ray. This effect is connected with the reorientation of the location of the molecule axis caused by the ultrasonic wave. Basing on the interference images (obtained by orthoscopic method) average values of torsion angles of the optical molecule axis were calculated in the volume of the sample.

1. Introduction

The following works [1, 2, 3, 4] were devoted to the investigations of acoustic–optical effects in anisotropic liquid media. In this paper we present the investigation results of the changes of molecule orientation of a nematic liquid crystal with planar texture caused by an ultrasonic wave. The information concerning the order of the molecules of the liquid crystalline medium was based on the interpretation of the diffraction images of the light interacting with the acoustic field introduced into the liquid–crystalline sample. Light diffraction by an ultrasonic wave first investigated by DEBYE and SEARS [5] as well as by LUCAS and BIQUARD [6] has been described by many authors. Later on the problem of light diffraction on an ultrasonic wave was dealt with in a number of papers and monographs e.g. [9, 10, 11, 12] though the diffraction of Bragg's type and Raman–Nath's type in isotropic media was treated separately. In 1974 Tshirikov and Parigin presented a theoretical paper combining both cases of light diffraction by one mathematical description [13]. The

The work has been carried out under CPBP 02.03 project coordinated by the Polish Academy of Sciences.

interaction of light with an acoustic wave is particularly interesting in anisotropic media. The optical birefringes of these media can change the polarization state of both the light and acoustic wave passing through the medium and thus it can effect the final diffraction pattern. In liquid–crystalline media the acoustic wave can change the molecule arrangement. The orientating effect of the ultrasonic wave of liquid crystal molecules was first stated by KESSLER and SAWYER [14] who had observed a dynamic light scattering in an originally non-oriented PAA sample (para-azoksyanizol). The orientation effect of the ultrasonic wave in a monocrystalline layer of the nematics was also described by MAILER and LINKS [15] et al. [16, 17, 18]. The changes of orientation arrangement of the liquid–crystalline molecules in the volume of the sample caused by the acoustic wave changes the light diffraction image after passing through the sample. This effect was the subject of papers [19] and [3]. Liquid crystals are media in which molecules have anisotropic dielectric properties (that is also optical ones) [20, 21] and show a defined degree of a far range orientation order. The molecule axes are placed, parallely to each other in the volume of the sample. In such a mezophase molecules have translational degrees of freedom, unlike those of a solid. The acoustic wave introduced into the sample interrupts the state of mutual arrangement which can evoke progressive movements of the media of the masses of molecule groups v.s. the neighbor groups in the range of the acoustic field. Such movements cause the formation of local streamings of laminar or turbulent character: the dynamics of these processes is described by hydrodynamics equations completed by the law of energy and mass conservation [22, 23, 24, 25] taking into account the anisotropic visco-elastic constants. Below a general description on the light and ultrasonics interaction is presented as a guide to the experiments which following results qualitatively have confirmed the description.

2. Description of light and ultrasonics interaction in liquid crystals

The Fig. 1 presents the experimental geometry for perpendicular interaction between linearly polarized light beam and the ultrasonic one in the liquid crystal sample. In the case of nematic sample with a planar texture (Fig. 1) located in the range of the light beam passing along the optical axis z of a liquid crystal we do not observe the effect of double refraction because the angle between the optical axis (director) and the direction of the polarization plane $\phi(z) = 0$. On the introduction of the ultrasonic wave into the sample the orientations of the axes of the liquid crystal molecules change under the influence of the acoustic field and birefringence occur. The angle between the polarization plane and the direction of the directors $\phi(z) \neq 0$ and is dependent on the parameters of the acoustic field [19, 29]. Let us denote the refractive index of the ordinary beam as n_0 and the refractive index of the extraordinary as n_θ beam only the second one will be changed and for that variation n_θ one has:

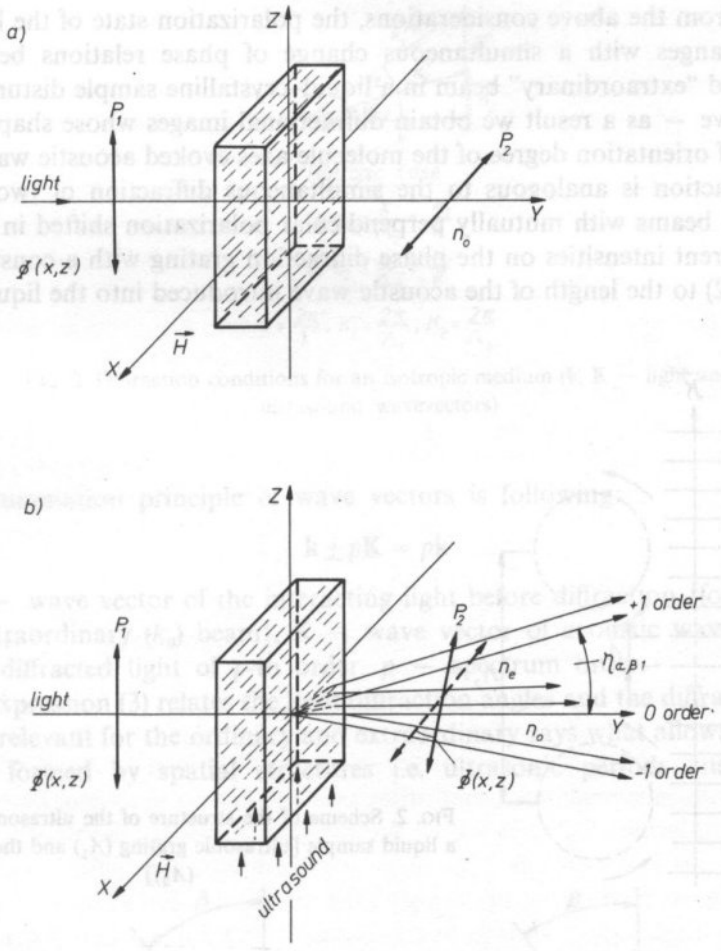

FIG. 1. Geometry and coordinate system for perpendicular iteraction lineary polarized light beam (a) and the ultrasonic one in the liquid crystal sample (b)

$$n_\theta(z, f_{a,k}) = \frac{n_0 n_\theta}{(n_0^2 \cos\phi(z, f_{ak}) + n_e^2 \sin\phi(z, f_{ak}))^{1/2}} \tag{1}$$

where: f_{ak} – characterizes the influence of an acoustic field (intensity, frequency, field distribution etc.).

The phase shift between the ordinary and extraordinary beams will be:

$$\delta(z) = \frac{2\pi d(f_{ak}) < \Delta n(z, f_{ak})}{\lambda} \tag{2}$$

where: d – thickness of the traversed way, λ – wavelength of light, $\Delta n = n_0 - n_\theta$, $\langle \ldots \rangle$ – sign of averaging process along the thickness of the layer.

As seen from the above considerations, the polarization state of the light beam undergoes changes with a simultaneous change of phase relations between the "ordinary" and "extraordinary" beam in a liquid–crystalline sample disturbed by an ultrasonic wave – as a result we obtain diffractional images whose shapes depend on the state of orientation degree of the molecule axes evoked acoustic wave. In this case the diffraction is analogous to the simultaneous diffraction of two (Fig. 1b) coherent light beams with mutually perpendicular polarization shifted in the phase and with different intensities on the phase diffraction grating with a constant equal (see also Fig. 2) to the length of the acoustic wave introduced into the liquid crystal.

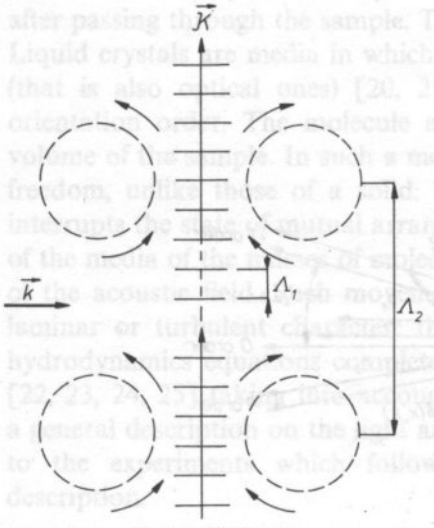

FIG. 2. Scheme of the structure of the ultrasonic field into a liquid sample [ultrasonic grating (Λ_1) and the vortex one (Λ_2)]

That picture is different, however, when the ultrasonic beam has great intensity i.e. when its radiation pressure causes a streaming of the liquid. After achieving a threshold of intensity the laminar streaming becomes a turbulent one and characteristic vortecess occur. According to MIYANA and SHEN [27] in the case of the turbulent reorientation rotation of liquid crystal molecules caused by the acoustic field formed vortecess [22, 23, 25, 26] which represent an additional spatially periodic deformation creating an additional diffractional grating with the constant (Λ_2) equal to the distance between the spatial structures (vortecess). The situation depends on the visco-elastic properties of the liquid crystal molecules their orientation and the parameters of the acoustic field (f_{ak}). Schematically such a model is presented in Fig. 2 [29]. The overlapping of these two diffraction gratings should manifest itself by the appearance of additional orders in the diffraction pattern (fine structure). As an example, Fig. 3 presents the expected diffraction conditions for an isotropic medium, and Fig. 4 – analogous diffraction conditions for a birefringent refraction medium (as liquid crystal).

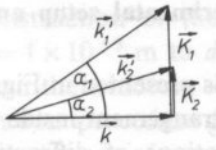

isotropic case

$$tg\,\alpha_1 = \frac{\lambda}{\Lambda_1} = \frac{K_1}{k}$$

$$tg\,\alpha_2 = \frac{\lambda}{\Lambda_2} = \frac{K_2}{k}$$

$$k = \frac{2\pi}{\lambda},\ K_1 = \frac{2\pi}{\Lambda_1},\ K_2 = \frac{2\pi}{\Lambda_2}$$

FIG. 3. Diffraction conditions for an isotropic medium ($\mathbf{k}$, $\mathbf{K}$ – light and ultrasound wavevectors)

The summation principle of wave vectors is following:

$$\mathbf{k} \pm p\mathbf{K} = p\mathbf{k}' \tag{3}$$

where: $\mathbf{k}$ – wave vector of the interacting light before diffraction {for an ordinary (k_0) or extraordinary (k_θ) beam}, $\mathbf{K}$ – wave vector of acoustic wave, $\mathbf{k}'$ – wave vector of diffracted light of p-th order, p – spectrum order.

The expression (3) relates the light diffraction angles and the diffraction gratings constants relevant for the ordinary and extraordinary rays what allows to find those constants formed by spatial structures i.e. ultrasonic periods and distance of vortecess.

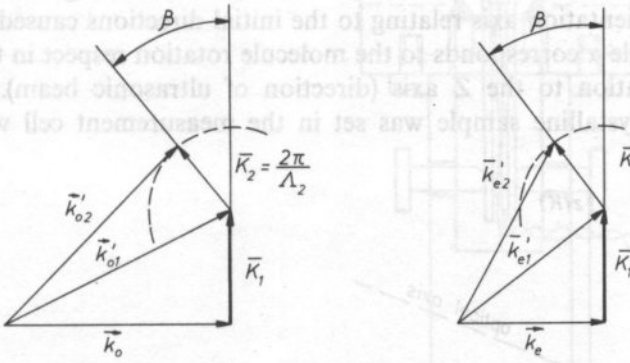

$$k_o = \frac{2\pi}{\Lambda_o} \qquad k_e = \frac{2\pi}{\Lambda_o} \qquad K_1 = \frac{2\pi}{\Lambda_1} \qquad K_2 = \frac{2\pi}{\Lambda_2}$$

$$k_{01}' = \frac{2\pi}{\lambda_{01}'} \qquad k_{e1}' = \frac{2\pi}{\lambda_{e1}'} \qquad k_{02}' = \frac{2\pi}{\lambda_{02}'} \qquad k_{e2}' = \frac{2\pi}{\lambda_{e2}}$$

FIG. 4. Diffraction conditions for anisotropic medium ($\mathbf{k}_0$, $\mathbf{k}_\theta$ – light wavevectors, $\mathbf{K}_1$ – ultrasonic wavevectors, $\mathbf{K}_2 = \frac{2\pi}{\Lambda_2}$, Λ_2 – distance between vortecess

3. Experimental setup and procedure.

The measurement system is presented in Fig. 5. The system can be used both for an investigation of molecule arrangement inside the sample by classical orthoscopic optical methods and investigations of diffraction images formed by the spatial structures of the investigated sample.

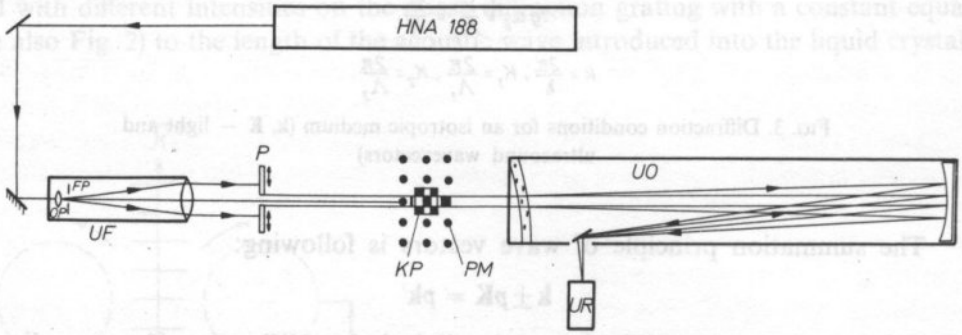

FIG. 5. Scheme of the experimental setup. HNA – He-Ne laser, UF–light beam formed system, OM–microscope objective, FP–spatial cell, PM–perpendicular magnetic field, UO–optical receiver, UR–record system

In the system the natural anisotropy of the medium can be modified using the external ordering magnetic field, and other external factors changing density, stress, streaming of molecule etc. by exposing the medium to an ultrasonic wave (see Fig. 1.b). The measure of the modification may be variation of the angles α and β (Fig. 6) of the molecule orientation axis relating to the initial directions caused by magnetic field only. The angle α corresponds to the molecule rotation respect in the plane XY and β to the rotation to the Z axis (direction of ultrasonic beam).

The liquid–crystalline sample was set in the measurement cell with precisely

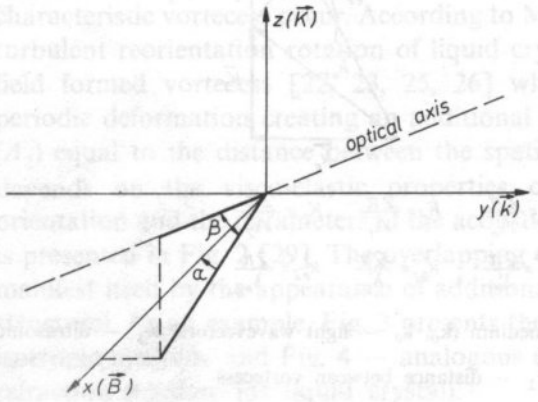

FIG. 6. Orientation liquid crystal molecule in the sample

parallel windows (Fig. 7). The construction of the cell enabled to adjust their distances within the limits from $d = 1 \times 10^{-3}$ m to $d = 10 \times 10^{-3}$ m with accuracy $\pm 0.1 \times 10^{-3}$ m. The distance between the windows – the sample thickness – was found in the interferometric calibration procedure filling the cell with additional isotropic liquid within the temperature range of nematic phase of the liquid crystal being examined. In the cell the temperature was kept within the limits of phase transitions with the accuracy to 0.01 deg by means of a thermoregulator.

The measurements were made on samples with thicknesses $d = 1 \times 10^{-3}$, 2×10^{-3} and 7×10^{-3} m for planar texture obtained by means of the external magnetic field induction $B = 0.8$T. Two transducers – quarz (9.70 MHz) or PZT ceramic (6.72 MHz) were used to form the longitudinal ultrasonic wave perpendicular to the initial axes of the liquid crystalline molecules (Fig. 1). In order to avoid thermal instabilities caused by a continuous ultrasonic wave, pulse supply was used with pulse duration 50 μs with repetition $10^4 s^{-1}$.

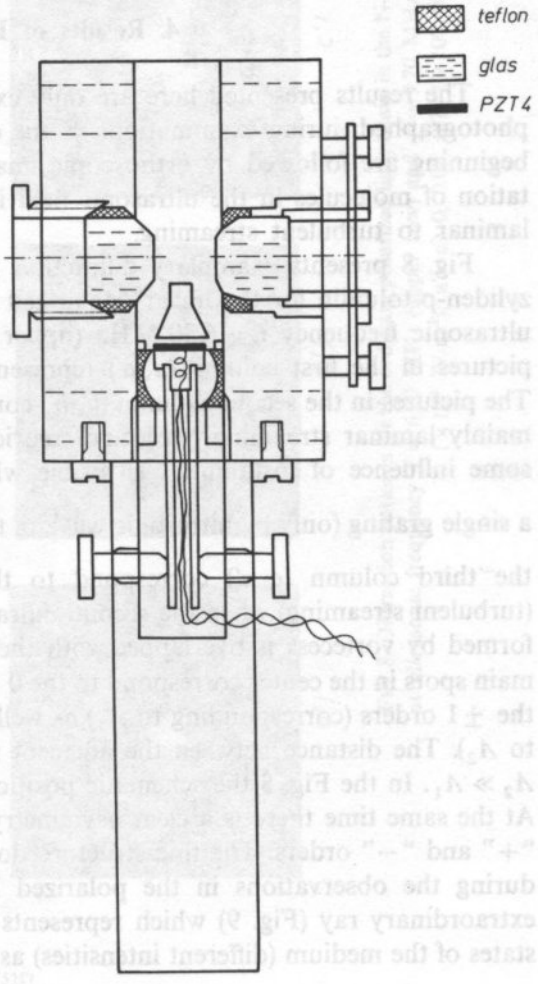

FIG. 7. Scheme of the experimental cell

The diffraction images were registered separately for the polarized light in the polarization plane of the "ordinary" and "extraordinary" ray. The observation of the diffraction images was carried out for liquid–crystalline samples: N–4hexyloxybenzyliden -p- toluidin, merck 4, merck 5 and W5 mixture for the ultrasonic wave with ultrasonic intensity from 0.0 to 1.0×10^4 W/m^2.

The intensity of the ultrasonic wave was estimated basing on the analysis of the equivalent circuit of the pistonlike radiating piezo-electric vibrator with regard to the shape of the applied energy concentrator and the sample thickness [28].

In order to find correlation between the observed diffraction effects and changes of the molecule arrangement of a nematics (which corresponds to the changes of the direction of the sample optical axis), orthoscopic investigations of the sample were made in parallel to diffraction investigations.

4. Results of Experiments

The results presented here are only examples of many pictures observed and photographed during examinations. Some characteristic diffraction patterns at the beginning are followed by orthoscopic images which enabled to determine orientation of molecules in the ultrasonic field including the threshold of passage from laminar to turbulent streaming.

Fig. 8 presents examplary diffraction patterns obtained for N-4hexyloxybenzyliden-p-toluidin for the lineary polarized light parallely to the ordinary beam at ultrasonic frequency $f = 6.70$ MHz (upper row) and 9.70 MHz (lower row). The pictures in the first column (a, a') represents the initial state without ultrasonics. The pictures in the second column (b, b') correspond to the state below the treshold; mainly laminar streaming, molecules reoriented of an angle ϕ occur; beside that some influence of instabilities is visible when diffraction of light takes place on a single grating (only by ultrasonic wave of the wave length $\Lambda_1 = \frac{c}{f}$). The pictures in the third column (c, c') correspond to the state above the intensity treshold (turbulent streaming) when the second diffraction grating (of the constant equal Λ_2) formed by vortecess is overlapped with the ultrasonic grating. In the patterns the main spots in the center correspond to the 0 – order of diffraction and the side spots the ± 1 orders (corresponding to Λ_1) as well as fine structure orders (corresponding to Λ_2). The distance between the adjacent fine structure fringes are small because $\Lambda_2 \gg \Lambda_1$. In the Fig. 8 the schematic positions of diffraction orders are drawn, too. At the same time there is a clear asymmetry (Fig. 8c) between the fine structure in "+" and "−" orders. The fine structure does not manifest itself in the ± 1 orders during the observations in the polarized light in the polarization plane of the extraordinary ray (Fig. 9) which represents patterns for the same frequencies and states of the medium (different intensities) as in Fig. 8 obtained for diffraction of the

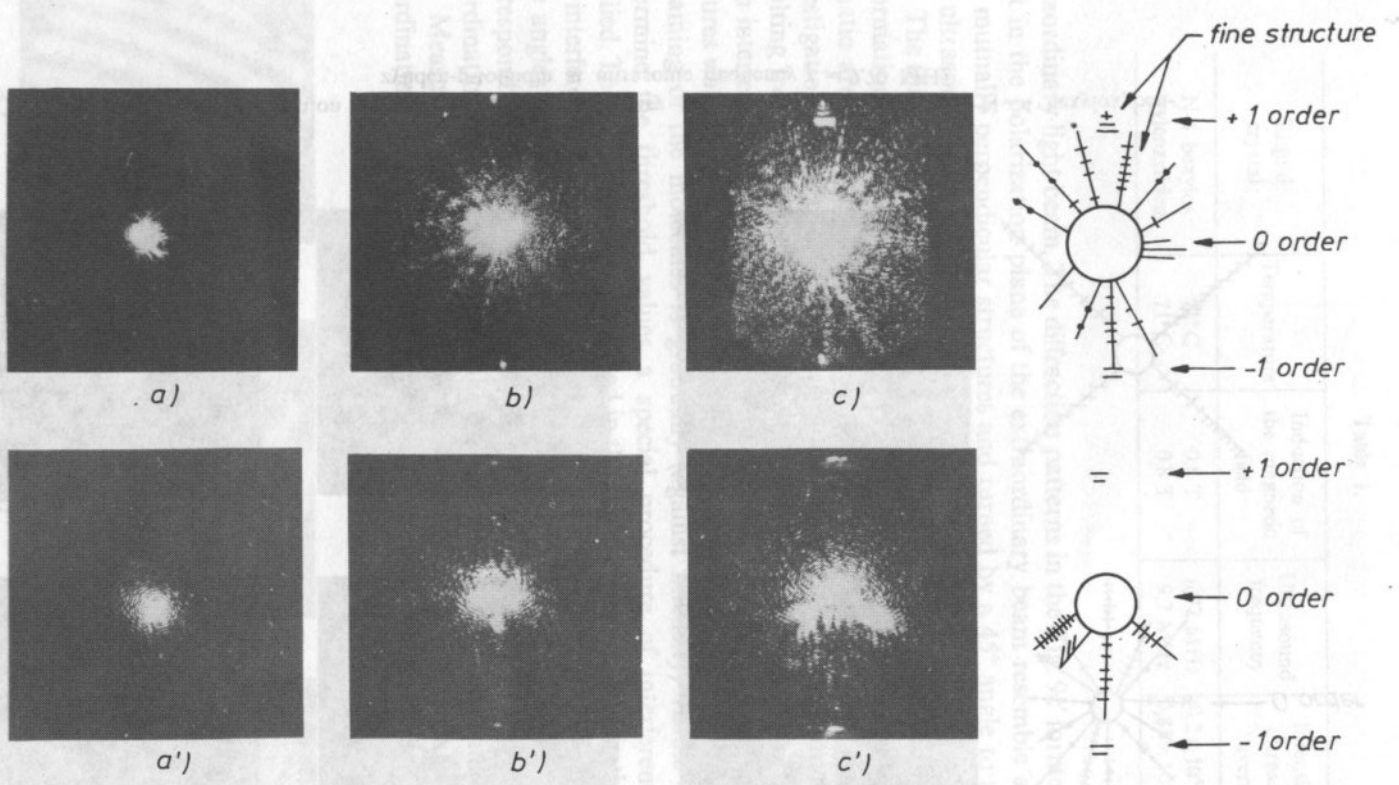

FIG. 8. Diffraction patterns for the ordinary polarized light beam in the N-4hexyloxybenzyliden-p-toluidin at ultrasonic frequency $f = 6.70$ MHz (upper row) and $f = 9.70$ MHz (lower row). a–c) 0, 0.02, 0.20 ($\times 10^4$ W/m^2); a′–c′) 0, 0.08, 0.74 ($\times 10^4$ W/m^2)

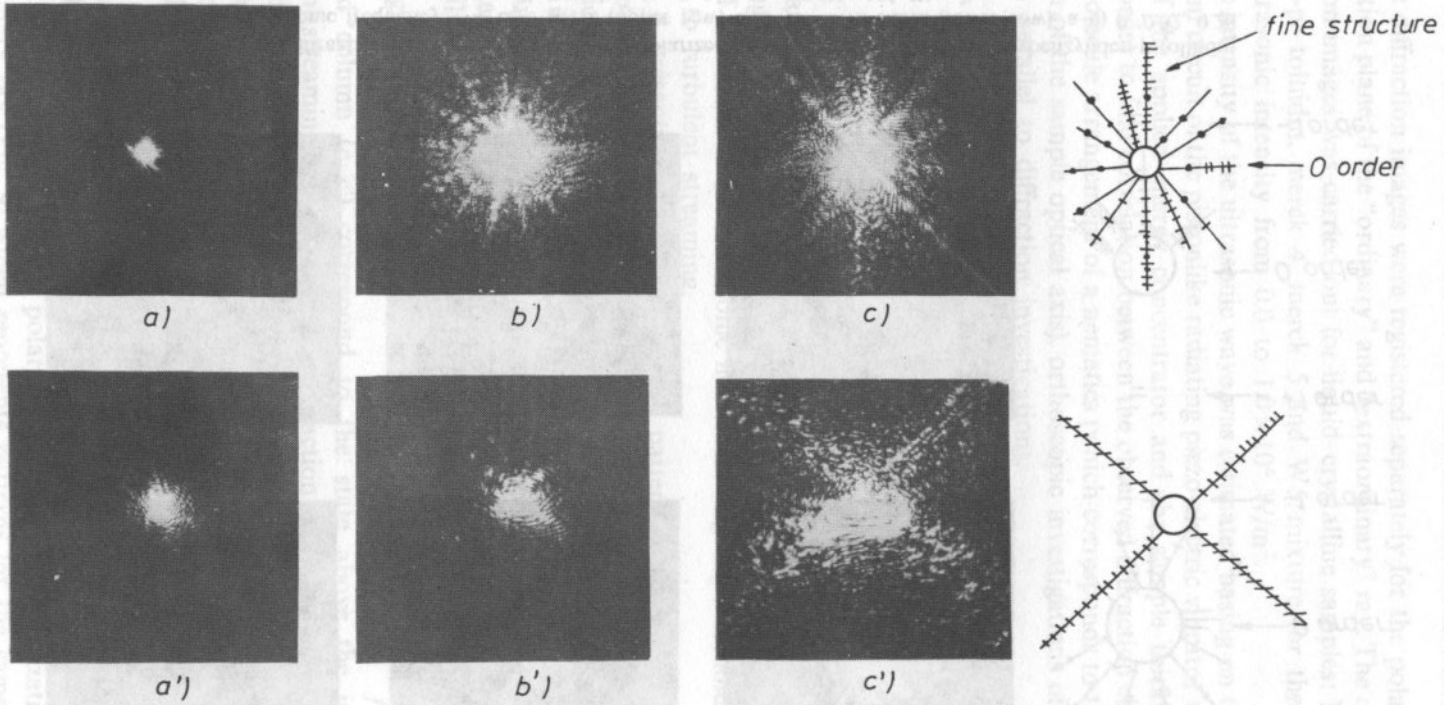

FIG. 9. Diffraction patterns for the extraordinary polarized light beam in the N−4 hexyloxybenzyliden-p-toluidin at ultrasonic frequency $f = 9.70$ MHz

Table 1.

Liquid crystal	Temperature	Induction of the magnetic field	Ultrasound frequency	Intensity of ultrasound average
N-4 hexylo--xylenzyliden	71°C 71°C	0,8 T 0,8 T	6,72 MHz 9,7 MHz	$0{,}2 \times 10^4$ W/m^2 $0{,}85 \times 10^4$ W/m^2

extraordinary light beam. The diffraction patterns in the Fig. 9c′ formed for polarized light in the polarization plane of the extraordinary beam resemble a diffraction on two mutually perpendicular structures and turned by a 45° angle to the direction of the ultrasonic wave [31].

The threshold values of the ultrasonic wave intensities at which one can observe a formation of the fine structure in the diffraction patterns of the investigated nematic are listed in the Table 1. The values where determined on the base of investigations in the orthoscopic system which enabled observing interference images resulting from the ordinary and extraordinary beams interaction. The examples of such interference fringes are shown in Fig. 10 (6.7 MHz) and Fig. 11 (9.7 MHz). The pictures were taken for different ultrasonic intensities. The influence of the turbulent streaming of the molecules is gradually (against intensity) visible (b. and c.). To determine the threshold values a special procedure of interference fringes was applied. The angles β and α presented in the Fig. 6 can be related to the inclination of the interference frings and the variation of the distance between them, respectively. The angles can be determined for different places of the interference image which correspond to local positions of the light beam cross-section in the sample. The coordinations of those positions taken for calculations are presented in the Fig. 12.

Measuring the inclinations of the interference fringes corresponding to the coordination net the local changes of the direction of the optical axis for the average

FIG. 10. Interference patterns for the N-4 hexyloxybenzyliden-p-toluidin at ultrasonic frequency $f = 6.70$ MHz, a) 0.18×10^4 W/m^2, b) 0.51×10^4 W/m^2, c) 0.74×10^4 W/m^2

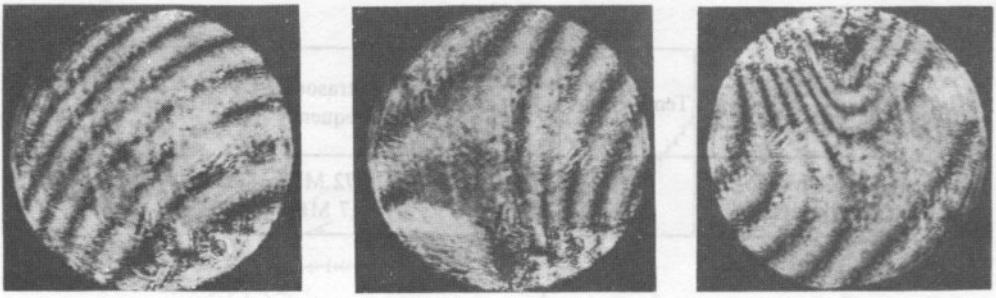

FIG. 11. Interference patterns for the N-4 hexyloxybenzyliden-p-toluidin at ultrasonic frequency $f = 9.70$ MHz. a') 0.16×10^4 W/m^2, b') 0.46×10^4 W/m^2, c') 0.72×10^4 W/m^2

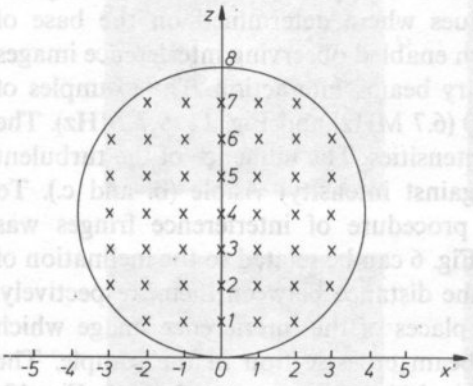

FIG. 12. Coordinat system for the liquid beam cross-section

thickness of the sample ($\Delta\beta$) were found in the function of ultrasonic wave intensity for chosen places of the sample (Fig. 13a-13d). The Fig. 13a presents the dependence for positions determined by $x = -2 = \text{const}$ and for three values of z (2, 4, 6), Fig. 13b for $x = -1 = \text{const}$, Fig. 13c for $x = \text{const}$ and Fig. 13d for $x = +1 = \text{const}$ and for the same z (2, 4, 6).

The Fig. 14 and 15 shows the variations of the direction of the optical axis in the function of the ultrasonic intensity for the observation points starting from the axis of the ultrasonic wave beam ($x = 0$, Fig. 12) for the left and the right ($x = 1$) sides of the axis for the case of frequency 6.72 MHz. The Fig. 15 shows the situation for the case of frequency 9.70 MHz for $z = 2$ against x coordinate for six different intensities. Similar dependence for the frequency 6.72 MHz and three intensities is given in the Fig. 16. In this case an interacting inversion of the optical axis at a distance from the ultrasonic beam axis is evidently manifested. It must be related to the change of the direction of the molecule streaming on the opposite one at the given place of the

cross-section of the sample. Such local change of the direction may confirm appearing of a vortex in the area and the inversion corresponds the passage through a izocline layer between two local streamings of opposite directions. A remarkable difference in the character of the local rotation of the optical axis of the nematic molecules with frequencies 9.70 and 6.72 MHz was observed. For frequency 9.70 MHz the rotation of the optical axis occurs only in one direction ($\Delta\beta > 0$) and

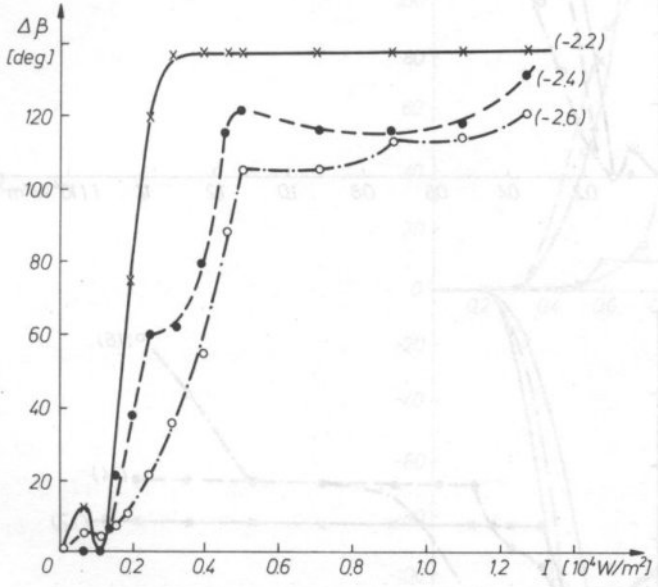

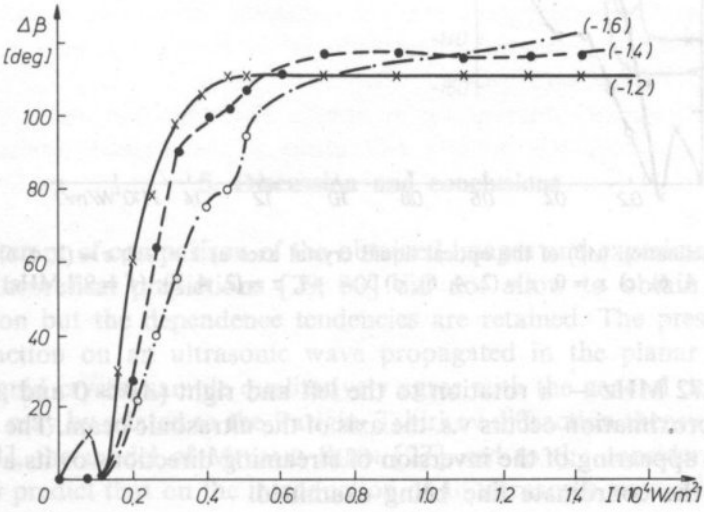

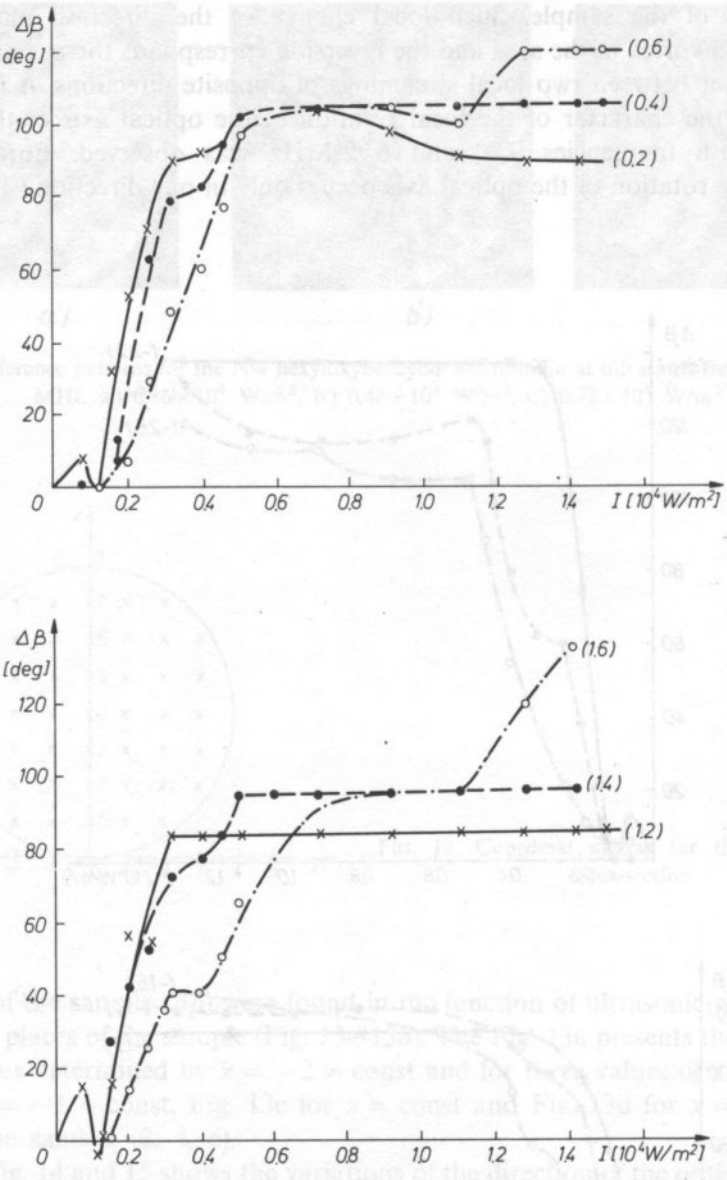

FIG. 13. Average inclination ($\Delta\beta$) of the optical liquid crystal axes a) $x = -2$, $z = (2, 4, 6)$ b) $x = -1$, $z = (2, 4, 6)$, c) $x = 0$, $z = (2, 4, 6)$, d) $x = +1$, $z = (2, 4, 6)$; ($f = 9.7$ MHz)

for frequency 6.72 MHz – a rotation to the left and right ($\Delta\beta > 0$ and $\Delta\beta < 0$) in symmetrical approximation occurs v.s. the axis of the ultrasonic beam. The difference is related to the appearing of the inversion of streaming directions or its absence on the way along the coordinate line being examined.

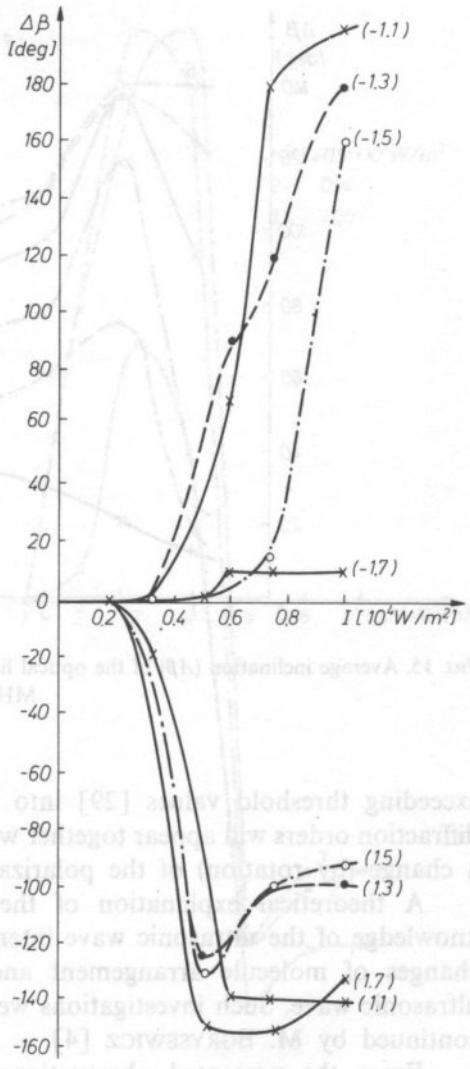

FIG. 14. Average inclination ($\Delta\beta$) of the optical liquid crystal axes for the fixed coordinats x, y ($f = 6.72$ MHz)

5. Discussion and conclusions

An attempt of comparison of the obtained images and experimental dependences with theoretical predictions [29, 30] did not allow to obtain a quantitative confirmation but the dependence tendencies are retained. The presented result of light diffraction on an ultrasonic wave propagated in the planar texture of the nematic liquid crystal sample qualitatively agree with the general description given above and may by related to the Parigin–Tshirkov diffraction theory for anisotropic bodies [13], the model of MIYANO–SHEN [27] and to the considerations given in [29]. They predict that on the introduction of an ultrasonic wave with the intensity

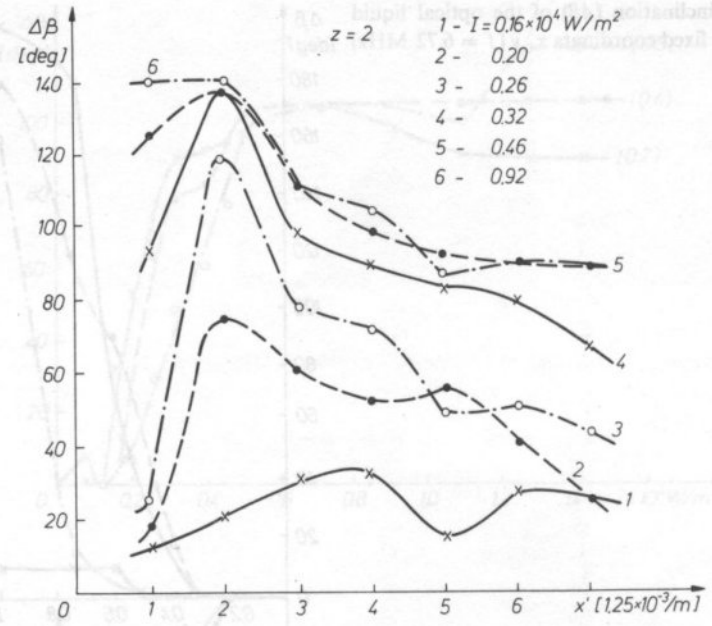

FIG. 15. Average inclination ($\Delta\beta$) of the optical liquid crystals axes in the x coordinat function ($f = 9.7$ MHz, $z = 2$)

exceeding threshold values [29] into the medium, changes of light intensity in diffraction orders will appear together with a change of ultrasonic wave intensity and a change (by rotation) of the polarization plane.

A theoretical explanation of the observed phenomena requires a precise knowledge of the ultrasonic wave interaction in a nematic sample, first of all, the changes of molecule arrangement and the molecule movement evoked by an ultrasonic wave. Such investigations were initiated by NAGAI and PETERS [17] and continued by M. BORYSEWICZ [4].

From the presented observations it results that the fine structure of the diffraction spectrum obtained in light and ultrasonic interaction appears at the moment of diversion from the laminar to turbulent streaming caused by acoustic radiation pressure.

References

[1] J. JÓZEFOWSKA, M. KOSMOL, A. ŚLIWIŃSKI, J. de Phys. **33**, 6, 239 (1972).
[2] M. KOSMOL, Acta Phys. Polon., A50, 375 (1976).
[3] M. WITKOWSKA-BORYSEWICZ, *Badania efektów akustooptycznych w ciekłych kryształach nematycznych*, Gdańsk 1980.

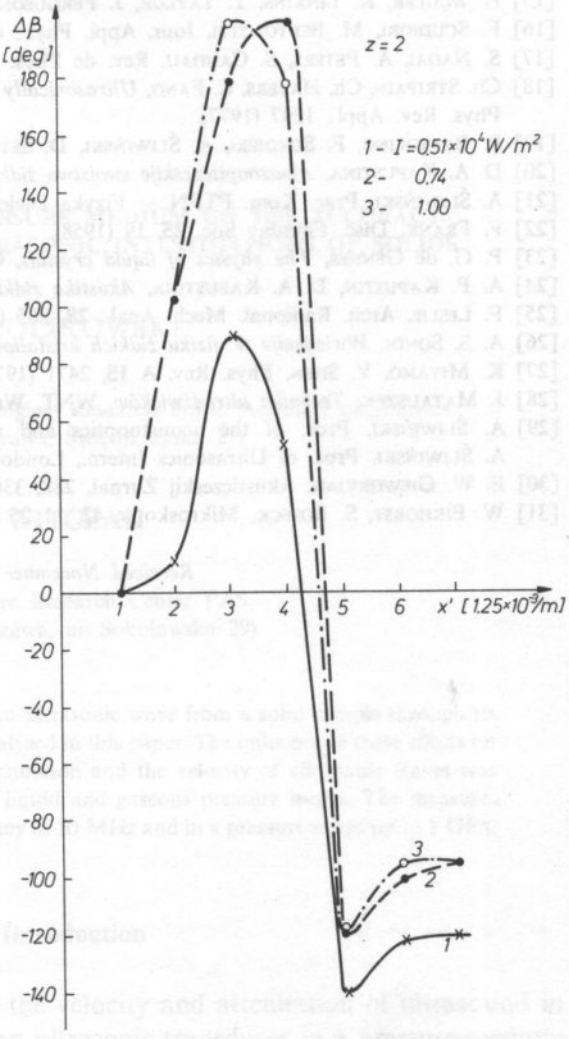

FIG. 16. Average inclination ($\Delta\beta$) of the optical liquid crystal axes in the x coordinat function (f = 6.72 MHz, z = 2)

[4] M. WITKOWSKA-BORYSEWICZ, A. ŚLIWIŃSKI, J. de Physique **44**, 411–430 (1983).
[5] P. DEBYE, F. W. SEARS, Nat. Ac. Sci. U.S. **18**, 409 (1932).
[6] R. LUCAS, P. BIQUARD, J. Phys. Radium **3**, 464 (1932).
[7] L. BERGMAN, *Der Ultraschall*, Stuttgart, Hirzel 1954.
[8] M. BERRY, *The diffraction of light by ultrasound*, London and N.Y. 1966.
[9] R. W. DIXON, IEEE J. Quant. Electron. QE-3, 85 (1967).
[10] D. F. NELSON, *Electric, optic and acoustic interaction in dielectrics*, J. Wiley and Sons, New York 1979.
[11] D. F. NELSON, M. LAX, Phys. Rev. Lett., **24**, 379 (1970).
[12] R. W. DAMON, W. T. MALONEY, D. H. MC MAHON, *Physical acoustics*, [Ed.] W. P. Mason, Ac. Press, N. Y.–London 1970 vol. 7, 273.
[13] V. N. PARIGIN, L. E. CHIRKOV, Sov. J. Quant. Electron., **5**, 180 (1975).
[14] L. KESSLER, S. SAWYER, Appl. Phys. Lett., **17**, 440 (1970).

[15] H. MAILER, K. LINKINS, T. TAYLOR, J. FERGUSON, Appl. Phys. Lett., **18**, 105 (1971).
[16] F. SCUDIORI, M. BERTOLOTTI, Jour. Appl. Phys., **47**, 3781 (1976).
[17] S. NAGAI, A. PETERS, S. CANDAU, Rev. de Phys. Appl., **12**, 21 (1977).
[18] Ch. STRIPAIN, Ch. HAYERS, C. FANG, *Ultrasonically induced optical effect in a nematic liquid crystal*, Phys. Rev. Appl., 1297 (1977).
[19] R. BARTOLINO, F. SOVDIERI, A. ŚLIWIŃSKI, D. SETTE, J. Appl. Phys., **46**, 1928 (1975).
[20] D. A. KAPUSTINA, *Akustoopticzeskije swojstwa żidkich kristałłow i ich primenenije*, Moskwa 1979.
[21] A. ŚLIWIŃSKI, Prac. Kom. PTPN – Fizyka Dielektryków i Radiospektroskopia **11**, 151 (1979).
[22] F. FRANK, Disc. Faraday Soc. **25**, 19 (1958).
[23] P. G. de GENNES, *The physics of liquid crystals*, Clarendon Press Oxford 1974.
[24] A. P. KAPUSTIN, D. A. KAPUSTINA, *Akustika żidkich kristałłow*, Nauka, Moskwa 1986.
[25] F. LESLIE, Arch. Radional. Mech. Anal., **28**, 265 (1968).
[26] A. S. SONIN, *Wwiedenije w fiziku żidkich kristałłow*, Nauka, Moskwa 1983.
[27] K. MIYAMO, V. SHEN, Phys. Rev. A **15**, 2471 (1977).
[28] J. MATAUSZEK, *Technika ultradźwięków*, WNT, Warszawa 1961.
[29] A. ŚLIWIŃSKI, Proc. of the acoustooptics and application, Gdańsk – Wieżyca 1983, 225. A. ŚLIWIŃSKI, Proc. of Ultrasonics Intern., London 1987.
[30] E. W. GIEWORKIAN, Akusticzeskij Żurnał, 288, 336 (1982).
[31] W. EIKHORST, S. BOSECK, Mikroskopie **42**, 11 25 (1985).

Received November 28, 1989

ARCHIVES OF ACOUSTICS
16, 3-4, 531-545 (1991)

THE INFLUENCE OF A PRESSURE MEDIUM ON THE ACCURACY OF MEASUREMENTS IN ULTRASONIC INVESTIGATIONS OF SOLIDS

J. KRÓLIKOWSKI

Institute of Fundamental Technological Research Polish Academy of Sciences
(00-049 Warszawa, Świętokrzyska 21)

Z. WITCZAK

High Pressure Research Center PAS
(01-142 Warszawa, ul. Sokołowska 29)

The effects related to leaking of an ultrasonic wave from a solid sample through its end faces to a pressure medium were analysed in this paper. The influence of these effects on the results of measurements of the attenuation and the velocity of ultrasonic waves was experimentally investigated for several liquid and gaseous pressure media. The measurements were performed at a wave frequency of 10 MHz and in a pressure range up to 1 GPa.

1. Introduction

The pulse method of measuring the velocity and attenuation of ultrasound in a solid sample placed together with an ultrasonic transducer in a pressure medium has been applied by many investigators. The results of such measurements are influenced by pressure fluctuations of the acoustic properties of the medium, a layer coupling the transducer with the sample and the transducer itself. The geometry of the measuring system also changes during the experiment. The thicknesses of the sample, the transducer and the bound layer are reduced. The analysis of the effect of hydrostatic pressure on an ultrasonic transducer has already been presented in the literature [1]. Owing to this analysis, the influence of pressure phenomena related to the latter on the accuracy of measurements can be assessed. An increase of hydrostatic pressure increases the resonance frequency of an ultrasonic transducer. This results from the reduction in the thickness of the transducer and from the increase of the velocity of ultrasound propagating in it. The relative increment of the resonance frequency per unit of the hydrostatic pressure increment for a quartz X-cut

transducer was equal 1.46×10^{-5} MPa^{-1}. VARIUKHIN et al. [2] has investigated experimentally several pressure media in order to obtain the maximal value of the reflection coefficient of an ultrasonic wave from the sample-pressure medium interface. Their differential measurements performed on samples of various lengths revealed that a change in the attenuation of ultrasound in the material of the sample due to the increase in hydrostatic pressure may be tens of times weaker than the change due to leaking of ultrasound into the pressure medium. Also the changes in the phase of the wave reflected from the sample-ultrasonic transducer interface was taken into account in accurate measurements of the velocity of ultrasonic waves [1]. However, the above observations applied only to the case of an ultrasonic transducer having one free surface, i.e. radiating only in one direction, to the sample. The value of the correction of the measured travel time of the wave due to the above mentioned effect can approach one half of its period. This means that the lower the wave frequency is, the greater can be the error made in the measurement of the time of travel of an ultrasonic signal through the sample. Since the acoustic impedance of the pressure medium changes together with hydrostatic pressure, the conditions of leaking of the wave through the end faces of the sample into the pressure medium also have to change. The aim of this paper is to analyse the influence of the pressure medium and the layer of coupling material on the results of measurements of the attenuation coefficient and the velocity of ultrasonic waves.

2. Theoretical

Let us consider a measurement system consisting of an ultrasonic transducer of thickness b and acoustic impedance Z_T, attached to a solid sample having flat and parallel end faces by means of a layer of a bonding material of thickness a, and acoustic impedance Z_B. The material of the sample is isotropic of acoustic impedance Z_s. A free surface of the sample and a free surface of the ultrasonic transducer adjoin the pressure medium of acoustic impedance Z_M. The case is illustrated in Fig. 1.

The method which is most frequently applied for measuring the travel time of the ultrasonic wave through the sample has been proposed by Papadakis [3]. It is based on the choice of a release frequency of an oscilloscope presenting successive echoes reflected from the back side of the sample, so that the time between a pair of echoes chosen for measurements is equal to the period of pulses releasing the time base of the oscilloscope. In such a case a superposition of ultrasonic pulses occurs on the oscilloscope screen. For two following echoes the travel time T, registered in the experiment, can be expressed as a sum of three components:

$$T = \delta + n/f - \varphi/2\pi f \tag{1}$$

where δ is the actual travel time of the wave, n – an integer expressing the possibility of an error in the time measurement by the multiple of the wave period, φ – the sum

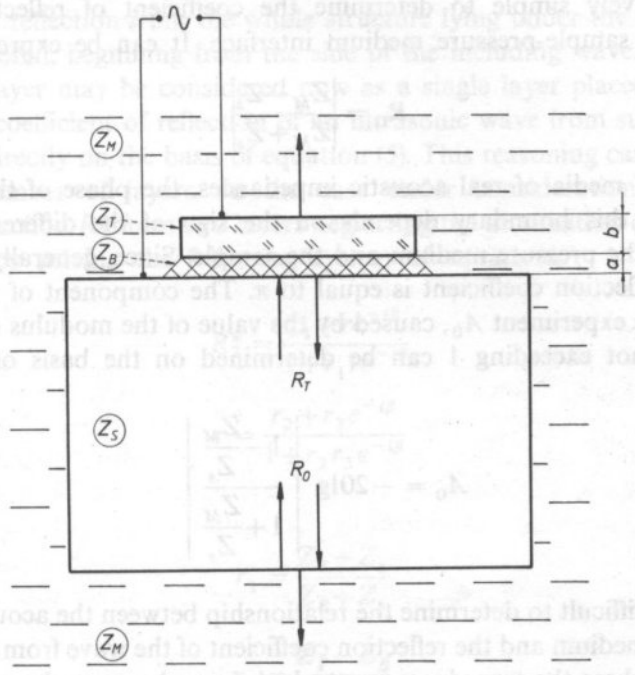

FIG. 1. Geometry of acoustical system. Z_s – acoustic impedance of sample, Z_B – acoustical impedance of bond, Z_T – acoustic impedance of transducer, Z_M – acoustic impedance of pressure medium, a – bond thickness, b – transducer thickness

of reduced (without π) phases of the coefficients of reflection on both sides of the sample, and f is the frequency of the wave. With this method the travel time of ultrasound through the sample can be measured with the accuracy better than 0.1 ns.

The attenuation of ultrasound A, measured on the path equal to the double length of the sample can be expressed in decibels as follows:

$$A = -20\lg(R_0 R_T e^{-2\gamma l}) \tag{2}$$

where l is the length of the sample, γ – the coefficient of attenuation of the wave in the material of the sample, and R_0, R_T – the moduli of the reflection coefficient of the wave from both end faces of the sample, on the side of the pressure medium and the side of the transducer, respectively.

The above mentioned relationships do not take into account the diffraction effects which occur when the wave propagates through the sample [3÷5].

Both coefficients of reflection are responsible for the leakage of ultrasound from the sample to the pressure medium, hence increasing the registered attenuation. As the pressure can influence the value of these coefficients, it is not possible to assess and investigate in direct observation the effect produced by hydrostatic pressure only on the sample subjected to it. Because of this, it is important to know the effect of parameters R_0 and R_T on the quantities observed in experiments.

It is relatively simple to determine the coefficient of reflection R_0 of the wave from the sample-pressure medium interface. It can be expressed as follows

$$R_0 = \left| \frac{Z_M - Z_s}{Z_M + Z_s} \right| \tag{3}$$

In cases of media of real acoustic impedances, the phase of the coefficient of reflection from this boundary depends on the sign of the difference of acoustic impedances of the pressure medium and the sample. Since, generally, $Z_M < Z_s$, the phase of the reflection coefficient is equal to π. The component of the attenuation registered in the experiment A_0, caused by the value of the modulus of the reflection coefficient R_0 not exceeding 1 can be determined on the basis of relation:

$$A_0 = -20\lg \left| \frac{1 - \frac{Z_M}{Z_s}}{1 + \frac{Z_M}{Z_s}} \right| \tag{4}$$

It is more difficult to determine the relationship between the acoustic impedance of the pressure medium and the reflection coefficient of the wave from the second face of the sample, where the transducer is attached. In such a case the wave is reflected from the parallel layers places between two elastic halfspaces. This problem may be solved with the method well-known from the literature, developed mainly for the needs of optics [6]. It requires, however, an inconvenient calculation multiplication of matrices, solution of a system of equations. Ready formulae can be found too, (e.g. [7]). Applying the known dependence of the reflection coefficient of an ultrasonic wave from a single layer of impedance Z_2 and of thickness x, placed between two elastic half-spaces of acoustic impedances Z_1 and Z_3 [8] we obtain

$$R^* = \frac{r_{12} + r_{23} e^{-i2xk}}{1 - r_{21} r_{23} e^{-i2xk}} \tag{5}$$

where

$$r_{ij} = \frac{Z_j - Z_i}{Z_j + Z_i} \tag{6}$$

and k is the wave number in the layer.

Generally, the effects due to the attenuation in the layer and the halfspaces surrounding it can be taken into consideration by applying the complex forms of the wave impedances of media and the wave number. Considering a system of two parallel layers between elastic halfspaces, as it is shown in Fig. 1, it is possible to express the reflection coefficient of the wave from these layers by an expression similar to the one obtained for a single layer. The reflection coefficient from the first layer-second layer interface (denoted by symbol r_{23} in eq. (5)) must be replaced with

the coefficient of reflection from the whole structure lying under the first layer. The layers are numbered, beginning from the side of the including wave. The structure under the first layer may be considered now as a single layer placed between two halfspaces. The coefficient of reflection of an ultrasonic wave from such a layer can be determined directly on the basis of equation (5). This reasoning can be applied to an arbitrary number of layers. In the case under consideration, the pressure coefficient of reflection R_T^* from two layers neglecting the attenuation of the wave can be determined by solving the following system of equations:

$$R_T^* = \frac{r_1 + re^{-i\vartheta}}{1 + r_1 re^{-i\vartheta}} \tag{7}$$

$$r = \frac{r_2 + r_3 e^{-i\beta}}{1 + r_2 r_3 e^{-i\beta}} \tag{8}$$

where

$$r_1 = \frac{Z_B - Z_s}{Z_B + Z_s} \tag{9}$$

$$r_2 = \frac{Z_T - Z_B}{Z_T + Z_B} \tag{10}$$

$$r_3 = \frac{Z_M - Z_T}{Z_M + Z_T} \tag{11}$$

$$\vartheta = 2ak_B \tag{12}$$

$$\beta = 2bk_T \tag{13}$$

while k_B and k_T denote wave numbers in the coupling layer and in the transducer, respectively. The solution of the above equations results in the following expressions for the modulus R_T and the phase Φ of the reflection coefficient that was searched for:

$$R_T = \left[1 - \frac{1 - r_1^2 r_2^2 r_3^2 - r_1^2(1-r_3^2) - r_2^2(1-r_1^2) - r_3^2(1-r_2^2)}{1 + r_2^2 r_3^2 + r_1^2 r_2^2 + r_1^2 r_3^2 + 2r_2[r_1(1+r_3^2)\cos(\vartheta) + r_3(1+r_1^2)\cos(\beta)]}\right.$$
$$\left. \frac{}{+ 2r_1 r_3[\cos(\vartheta+\beta) + r_2^2\cos(\vartheta-\beta)]}\right]^{1/2} \tag{14}$$

$$\operatorname{tg}(\Phi) = \left[(r_1^2 - 1)\frac{r_2(1+r_3^2)\sin(\vartheta) + r_3[\sin(\vartheta+\beta) + r_2^2\sin(\vartheta-\beta)]}{r_1(1+r_2^2)(1+r_3^2) + 4r_1 r_2 r_3\cos(\beta) + r_2(1+r_1^2)(1+r_3^2)\cos(\vartheta) + }\right.$$
$$\left. \frac{}{r_3(1+r_1^2)[\cos(\vartheta+\beta) + r_2^2\cos(\vartheta-\beta)]}\right]. \tag{15}$$

When the transducer works at its resonance frequency which is the most frequent case, expressions (14) and (15) are simplified because in this case:

$$\cos\beta = 1 \tag{16}$$

$$\sin(\beta) = 0 \tag{17}$$

This leads to the relation:

$$R_T = \left[1 - \frac{1 - r_1^2 r_2^2 r_3^2 - r_1^2(1-r_3^2) - r_2^2(1-r_1^2) - r_3^2(1-r_2^2)}{1 + r_1^2 r_2^2 + r_1^2 r_3^2 + r_2^2 r_3^2 + 2r_2 r_3(1+r_1^2) + 2r_1(r_2+r_3)(1+r_2 r_3)\cos(\vartheta)}\right]^{1/2} \tag{18}$$

$$\operatorname{tg}(\Phi) = \left[\frac{(1+r_2 r_3)(r_2+r_3)(r_1^2-1)\sin(\vartheta)}{r_1(r_2^2+1)(r_3^2+1) + 4r_1 r_2 r_3 + (r_2+r_3)(1+r_1^2)(1+r_2 r_3)\cos(\vartheta)}\right]. \tag{19}$$

If the real part of the reflection coefficient R_T^* is negative, then $\varphi = \operatorname{arctg}(\Phi)$.

The modulus of the reflection coefficient influences the registered value of the attenuation of ultrasound in the investigated material. In the case of measurements applying two successive echoes, the attenuation measured on a path equal to the double length of the sample is increased by term A_T, which can be expressed by

$$A_T = -20\lg(R_T). \tag{20}$$

This parameter versus the ratio of the impedance of the pressure medium to the impedance of investigated sample is presented in Fig. 2. The dependence is determined for several values of the parameter ϑ. This parameter characterizes elastic properties of the coupling layer, as well as its thickness, because it defines the ratio of the thickness of the layer to the length of the wave propagating in it. After suitable transformations it can be proved that for $\vartheta = 0$ the coefficient A_T in terms of the impedance of the pressure medium is identical to the one obtained from formula (4), which describes the relationship between the attenuation component A_0 in the relative value of the pressure medium acoustic impedance. In this case the moduli of coefficients of reflection remain equal to each other in spite of the fact that one side of the sample adjoins the transducer, while the other side directly adjoins the pressure medium. This effect occurs, because the transducer (considered here as a parallel layer) is transparent for the wave at its resonance frequency, provided we neglect attenuation of the ultrasonic wave in the material of the transducer. For greater values of the parameter ϑ the A_T dependence on Z_M/Z_s practically coincides with this dependence for $\vartheta = 0$ and small values of Z_M/Z_s. When the ratio Z_M/Z_s is increased, the curves become divergent and the greater is the value of the parameter ϑ, the earlier this occurs.

The character of this dependence is somehow different for even greater values of the parameter ϑ. In this case a rapid increase of the attenuation accompanying an increase of impedance of the pressure medium for small Z_M/Z_s is observed, and then, after the maximum is exceeded, a decrease to zero for greater values of Z_M/Z_s occurs. A high ϑ can correspond to a thicker coupling layer. The analysis of expression (18)

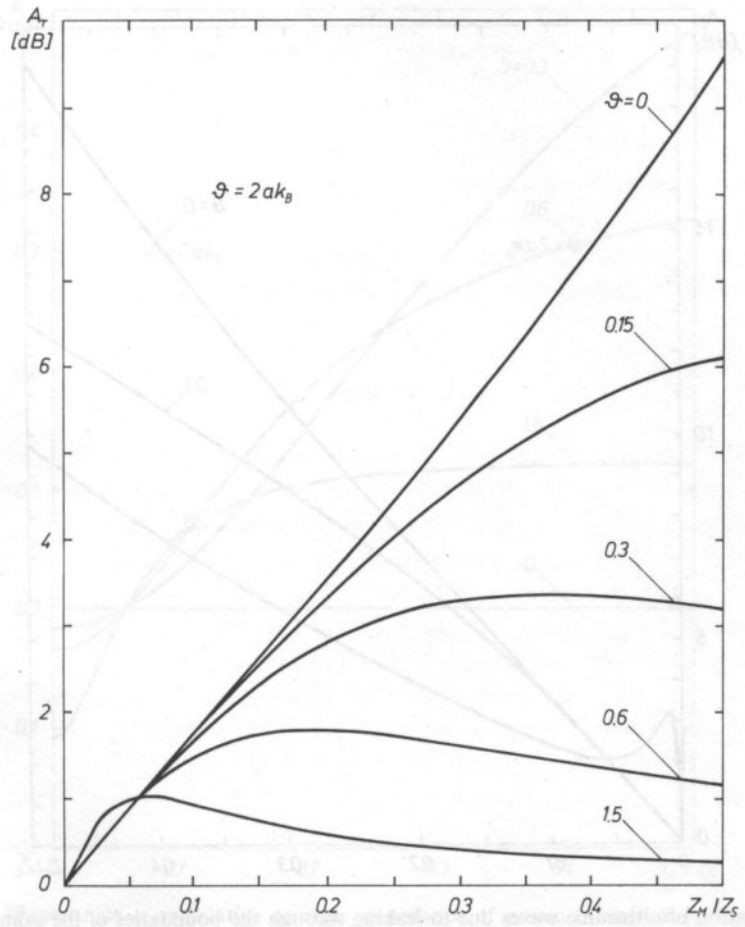

FIG. 2. Attenuation of ultrasonic waves due to leaking through the sample-transducer boundary vs relative acoustic impedance of pressure medium $A_T = 20\lg(R_T)$

results in a conclusion that when the impedance of the pressure medium is equal to the acoustic impedance of the coupling layer $Z_M = Z_B$, then the value of the attenuation component A_T is independent of the value of the ϑ parameter and, hence, of the thickness of the coupling layer. It is equal to $A_T = -201\ \mathrm{g}|r_1|$. Figure 3 illustrates the total effect of the reflection coefficient at both sides of the sample. It presents the attenuation component A_E, due to leaking of ultrasound into the pressure medium, which is a sum of parameters A_0 and A_T.

$$A_E = A_0 + A_T \tag{21}$$

in terms of the ratio of the impedance of the pressure medium to the impedance of the sample. It can be seen in this figure that the parameter ϑ, which characterizes the coupling layer, has a considerable influence on this dependence. As for A_T in Fig. 2,

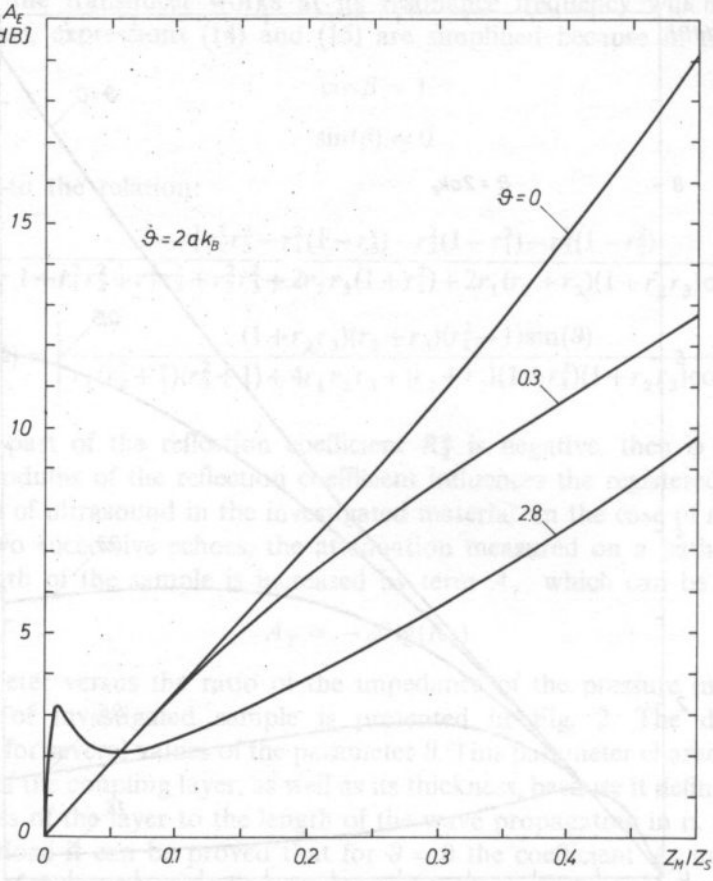

FIG. 3. Attenuation of ultrasonic waves due to leaking through the boundaries of the sample vs relative acoustic impedance of pressure medium $A_E = 20\lg(R_0 R_T)$

the attenuation component A_E is monotonic for small values of the parameter ϑ. A_E increases when the impedance of the pressure medium is increased, whereas for higher values of the parameter ϑ a very rapid increase of the attenuation of ultrasound due to its leaking to pressure medium is observed. In this case the curve reaches a maximum, then its values decrease and futher on then increase monotonically for higher values of the argument Z_M/Z_s when the curve asymptotically approaches the value of component A_0.

The influence of an increase of the acoustic impedance of the pressure medium on the phase of the reflected wave is shown in Fig. 4. It can be seen that if the transducer is placed directly on the sample, the phase of the reflected wave does not depend on the impedance of the pressure medium. In all other cases the phase increases when the parameter Z_M/Z_s increases. For $Z_M = 0$ the parameter φ assumes

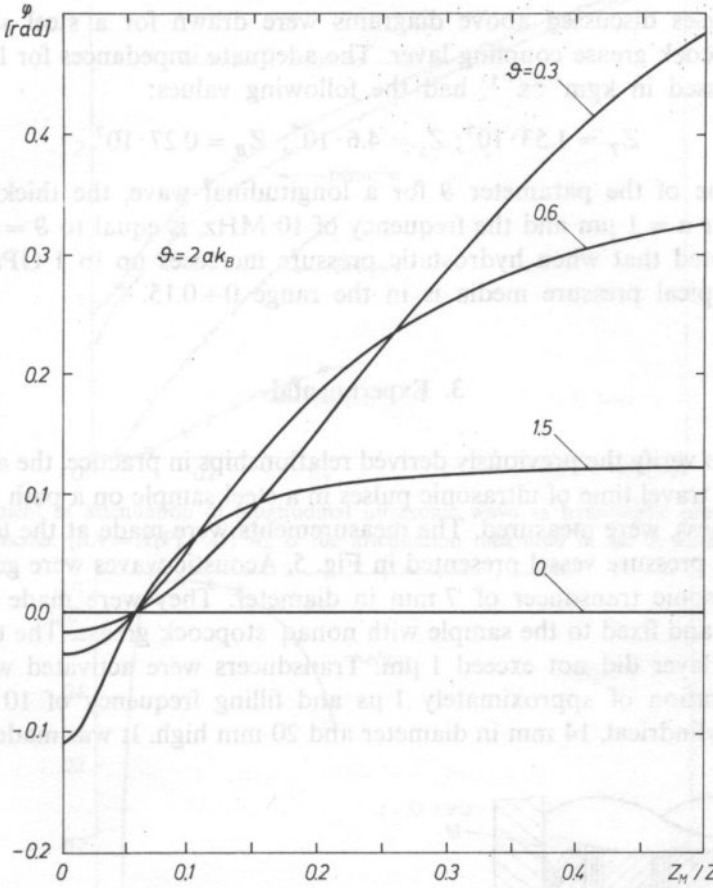

FIG. 4. Phase angle φ vs relative acoustic impedance of pressure medium ($\Phi = \varphi + \pi$)

the following value

$$\varphi = \operatorname{arctg} \frac{(1-r_1^2)\sin(\vartheta)}{2r_1-(1+r_1^2)\cos(\vartheta)}. \tag{22}$$

Hence, if $\cos(\vartheta) = 2r_1/(1+r_1^2)$, then $|\varphi| = \pi/2$. For small Z_M/Z_s values the higher is the value of the coefficient ϑ, the greater becomes the rate of these changes. When $Z_M = Z_B$, the phase of the reflected wave does not depend on the thickness of the coupling layer, which was the case for A_T and A_E, while for the sample exceeding Z_B/Z_s for very small values of ϑ, the phase changes are very small. For greater values they rapidly increase, achieve maximum and then decrease. When is equal to about $\pi/2$, the phase for increasing values of the impedance of the pressure medium practically remains unchanged. Because of the periodical character of described functions, definitions concerning the parameter ϑ refer to the first period only.

In all cases discussed above diagrams were drawn for a steel sample with a nonaq stopcock grease coupling layer. The adequate impedances for longitudinal waves, expressed in $kgm^{-2}s^{-1}$, had the following values:

$$Z_T = 1.53 \cdot 10^7;\ Z_s = 4.6 \cdot 10^7;\ Z_B = 0.27 \cdot 10^7$$

The value of the parameter ϑ for a longitudinal wave, the thickness of the coupling layer a = 1 μm and the frequency of 10 MHz, is equal to $\vartheta = 0.06$ rad. It should be noted that when hydrostatic pressure increases up to 1 GPa, the ratio Z_M/Z_s for typical pressure media is in the range $0 \div 0.15$.

3. Experimental

In order to verify the previously derived relationships in practice, the attenuation, as well as the travel time of ultrasonic pulses in a steel sample on a path equal to its double thickness, were measured. The measurements were made at the temperature of 300 K in a pressure vessel presented in Fig. 5. Acoustic waves were generated by circular ultrasonic transducer of 7 mm in diameter. They were made of *X*– and *Y*–cut quartz and fixed to the sample with nonaq stopcock grease. The thickness of the coupling layer did not exceed 1 μm. Transducers were activated with electric pulses of duration of approximately 1 μs and filling frequency of 10 MHz. The sample was cylindrical, 14 mm in diameter and 20 mm high. It was made of bearing

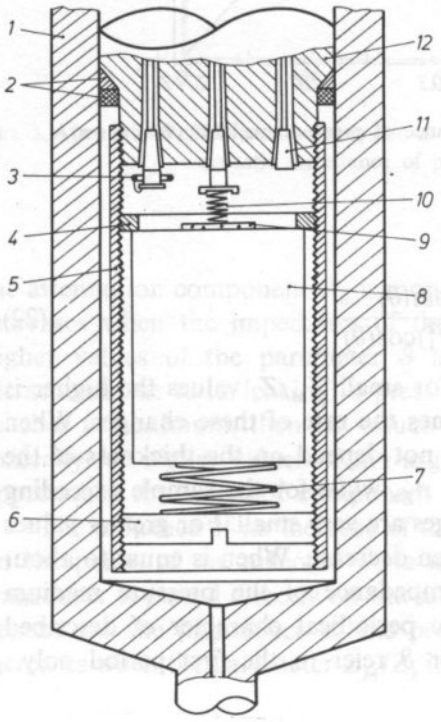

FIG. 5. Equipment used for ultrasonic investigation of solids under high hydrostatic pressure [9], *1* – pressure vessel, *2* – sealing, *3* – manganin gauge, *4* – screw ring, *5* – sample holder, *6* – screw, *7* – spring, *8* – sample, *9* – transducer, *10* – R. F. lead spring, *11* – electrical fit through, *12* – plug

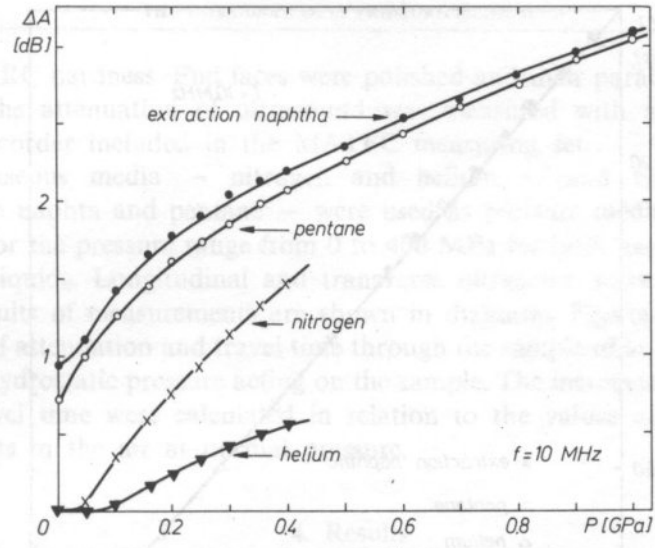

FIG. 6. Increment of attenuation of longitudinal ultrasonic wave vs hydrostatic pressure for various pressure media. $(\Delta A = A(P) - A_0)$ A_0 is the attenuation measured in air at ambient pressure

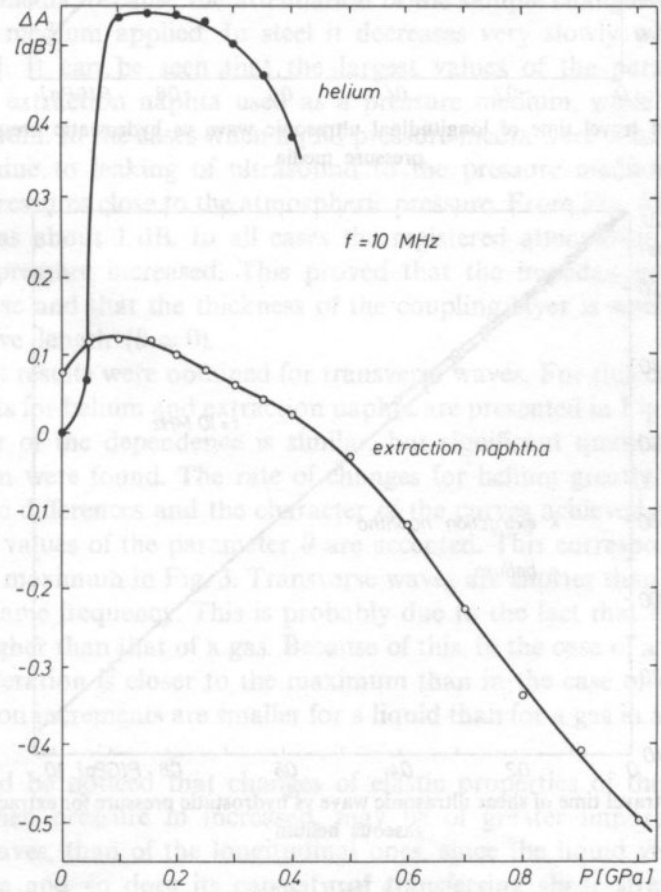

FIG. 7. Increment of attenuation of shear ultrasonic wave vs hydrostatic pressure for extraction naphta and gaseous helium

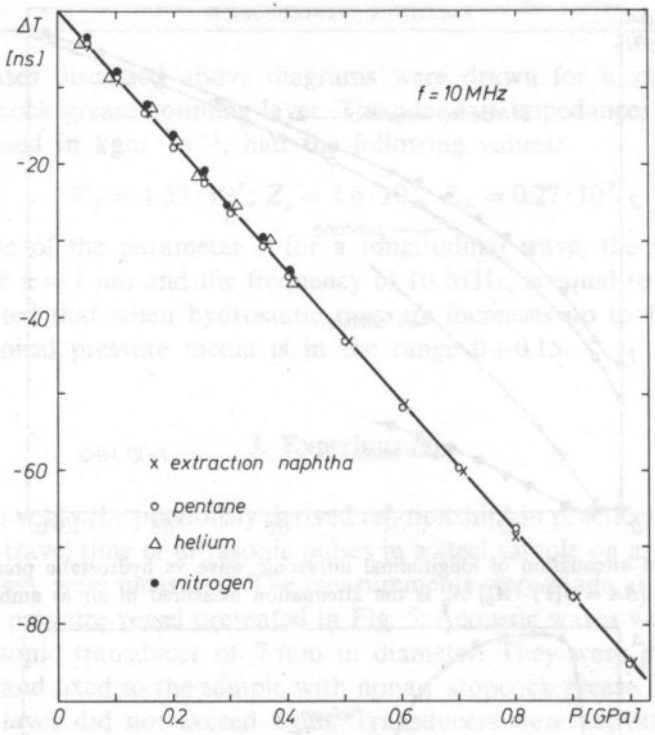

FIG. 8. Increment of travel time of longitudinal ultrasonic wave vs hydrostatic pressure for various pressure media

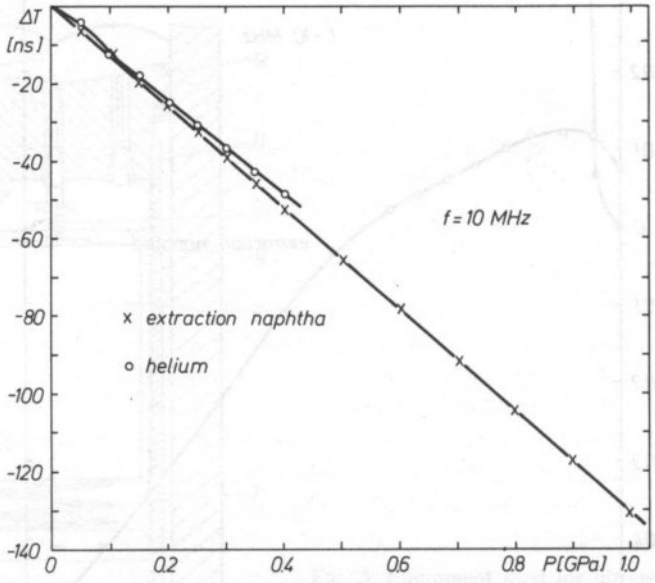

FIG. 9. Increment of travel time of shear ultrasonic wave vs hydrostatic pressure for extraction naphta and gaseous helium

steel of 62 HRC hardness. End faces were polished and their parallelism was better than 30″. The attenuation of ultrasound was measured with an automatic attenuation recorder included in the MATEC measuring set.

Two gaseous media – nitrogen and helium – and two liquid media – extraction naphta and pentane – were used as pressure media. Measurements were made for the pressure range from 0 to 400 MPa for both gases and from 0 to 1 GPa for liquids. Longitudinal and transverse ultrasonic wave were applied.

The results of measurements are shown in diagrams Figs. 6–9. They present increments of attenuation and travel time through the sample of an ultrasonic signal in terms of hydrostatic pressure acting on the sample. The increments of attenuation and the travel time were calculated in relation to the values achieved from the measurements in the air at normal pressure.

4. Results

All differences observed in Fig. 6 result from the difference of the attenuation of the pressure media, because the attenuation of the sample changes independently of the pressure medium applied. In steel it decreases very slowly when the pressure increases [2]. It can be seen that the largest values of the parameter ΔA were achieved for extraction naphta used as a pressure medium, while the lowest were found for helium. In the cases when liquid pressure media were used, an increment of attenuation due to leaking of ultrasound to the pressure medium, was observed already for pressures close to the atmospheric pressure. From Fig. 6 it results that the increment was about 1 dB. In all cases the registered attenuation increased when hydrostatic pressure increased. This proved that the impedances of the pressure media increase and that the thickness of the coupling layer is small in comparison with the wave length ($\vartheta \approx 0$).

Different results were obtained for transverse waves. For this case the results of measurements for helium and extraction naphta are presented in Fig. 7. In both cases the character of the dependence is similar, but significant quantitative differences between them were found. The rate of changes for helium greatly exceeds that for liquids. These differences and the character of the curves achieved can be explained when higher values of the parameter ϑ are accepted. This corresponds to the curve with a single maximum in Fig. 3. Transverse waves are shorter than the longitudinal ones of the same frequency. This is probably due to the fact that the impedance of a liquid is higher than that of a gas. Because of this, in the case of a liquid, the point under consideration is closer to the maximum than in the case of a gas. Therefore, the attenuation increments are smaller for a liquid than for a gas in a similar range of pressures.

It should be noticed that changes of elastic properties of the coupling layer, occurring when pressure in increased, may be of greater importance in case of transverse waves, than of the longitudinal ones, since the liquid viscosity increases with pressure and so does its capacity of transferring shear stresses.

The results of measurements of a pulse travel time through the sample are presented in Figs. 8 and 9. The travel time of ultrasonic pulses through the sample decreases when hydrostatic pressure increases. According to the expression (1), this is due to the changes of the velocity of ultrasonic waves, the length of the sample and the conditions of reflection of ultrasound at both faces of the sample in terms of pressure. As it can be seen in Fig. 8, all results for pentane, extraction naphta and both gases in the case of longitudinal waves are very similar. The maximal difference between them is equal to only 2 ns. From among the factors considered only the component resulting from the change of the phase of the ultrasonic waves, when they are reflected from the sample-ultrasonic transducer interface, can be the source of these differences, for the phases of reflected waves depend on the acoustic impedance of the pressure medium at a given pressure. As it was mentioned previously, the maximal correction to the time measurements due to this mechanism can be equal to a half period. This is 0.05 μs for the frequency of 10 MHz. In Fig. 4 it can be seen that the changes in the pressure medium impedance weakly influence the phase of the waves reflected from both faces of the sample for small values of the parameter ϑ. Hence, the same concerns the results of time measurements. The comparison of the results for transverse waves, shown in Fig. 9, indicates a qualitative compatibility with the results of theoretical calculations presented in Fig. 4. Due to the fact that the impedance of a liquid exceeds the impedance of a gas at a fixed value of pressure, the phase change of the wave reflected from the sample-ultrasonic transducer interface is greater for the liquid than for the gas at the same pressure. It also increases when the value of the parameter ϑ increases. This results from Eq. (1) showing that changes of the travel time are quicker for a pressure medium of higher acoustic impedance. The changes are quicker in the case of a liquid than that of a gas, as can be seen in Fig. 9.

5. Conclusions

– In investigations of longitudinal wave attenuation helium was found to be the least disturbing medium. In this case the registered increments of attenuation per unit of hydrostatic pressure increment were the smallest. The highest values of attenuation were registered for extraction naphta as a pressure medium.

– The influence of the pressure medium on the results of measurements of ultrasound velocity in megahertz frequency range seems to be very small and may be neglected in many cases (long samples, thin coupling layer, high frequency).

– The measurements made with the application of transverse waves (attenuation, in particular) seem to be more sensitive to impedance changes of the pressure medium. It is mainly the result of the higher value of the parameter ϑ in the case than in the case of longitudinal waves of the same frequency.

– The phase of the wave reflected from the sample-transducer interface is independent of the impedance of the pressure medium when the latter is equal to the acoustic impedance of the coupling material. Then the attenuation component due

to leaking of the wave to the pressure medium is independent of the thickness of the coupling layer in this case. Therefore, the same liquid should be used as a pressure medium and the coupling material in accurate ultrasonic measurements.

References

[1] H. J. McSkimin, P. Andreatch, *Analysis of the pulse superposition method for measuring ultrasonic wave velocities as a function of temperature and pressure*, JASA 5, 609–615, (1962)

[2] Б. Х. Варюхин, О. Н. Дацко, Н. П. Пилипенко, *Методика измерения затухания ультразвука в металлах под гидростатическим давлением*, Физика и техника высоких давлений, **6**, 85–87, (1981).

[3] E. P. Papadakis, *Ultrasonic phase velocity by the pulse-echo-overlap method incorporating diffraction phase correction*, JASA 42, 5, 1045–1051, (1967)

[4] A. S. Khimunin, *Numerical calculation of the diffraction corrections for the precise measurement of ultrasound absorption*, Acoustica **27**, 4, 173–181 (1972)

[5] S. Mackiewicz, *Diffraction correction for the measurement of ultrasound absorption in solids*, Proceedings of the XXXV Open Seminar on Acoustics, 124–129, Białowieża, (1988)

[6] P. G. Jespers, F. van de Wiele, M. H. White, *Solid state imaging*, Noordhof, Leyden (1976)

[7] Л. М. Бреховских, *Волны в слоистых средах*, Изд. АНСССР, Москва, (1957).

[8] B. A. Auld, *Acoustic fields and waves in solids*, John Willey and Sons Inc, (1973)

[9] J. Królikowski, J. Szczepek, Z. Witczak, *Ultrasonic investigation of contact between solids under high hydrostatic pressure*, Ultrasonics **27**, 45–49, (1989)

Received October 20, 1989

ARCHIVES OF ACOUSTICS
16, 3–4, 547–557 (1991)

ACOUSTICAL ADAPTATION OF THE THESSALONIKI MUSIC-THEATRE

G. PAPANIKOLAOU

Aristotle University of Thessaloniki, Thessaloniki, Greece

Acoustical adaptation design for a musical theatre situated in a residential building at Thessaloniki downtown is described. Peculiar details of the completed adaptation are discussed and some conclusions derived, stressing the importance of a high sound insulation level as a factor of the good acoustical quality of concert halls.

1. Introduction

Adaptations of existing buildings to new requirements due to altered building destination, cause very often troublesome problems. They are especially difficult in the domain of acoustical adaptations, when a high quality concert-hall or theatre-hall is foreseen as an adaptation aim.

The problems are of various kinds and of different degrees of difficulty depending on adaptation design assumptions and on their conditions of realization. Thus, no general solution is available and every case has to be studied, designed, and realized on its own way. The character of designers' tasks is, however, restricted to a few specific areas of concepts. They may be mentioned, grouped in the following way.

A. The correction of the hall shape, the positioning of the stage and the distribution of audience; the geometrical study of sound reflections to secure uniform sound distribution.

B. The acoustical design of the interior; placement of sound absorbing and of sound reflecting materials and diffusing elements; correction of frequency characteristics.

C. The design of sound systems; recording, reinforcement, monitoring, pageing, reverberation, etc.

D. The design of improved sound insulation, in order to suppress extraneous noise penetrating the hall, and to prevent radiation of sounds out of the hall adjacent dwellings.

As problems concerning solutions of tasks quoted in items A, B, and C are

rather often described in acoustical literature, so appropriate concepts are commonly known. On the contrary, those encountered in item D are very seldom described. Moreover, as they belong to building acoustics rather than to room acoustics domain so they are, as a rule, presented separately. However, those problems are often to be solved by sound-engineers or by acoustical consultants working on room acoustics designs.

Thus, a presentation of design considerations and of the results obtained in the course of adaptation undertaken at the new music-theatre in Thessaloniki, may turn out to be a useful hint for designers of similar projects, and may be of interest as practical example for acousticians and sound-engineers. The more so, because the most essential task of the design consisted of sound insulating constructions separating acoustically the hall interior and the outer part of the building.

2. Object data

A part of the building constructed in the fifties, situated in the busy district of Thessaloniki eastern downtown, at the crossing of Vasilissas Olgas and M. Botsari streets, occupied earlier by a cinema, has been destinated to be converted into a music-theatre, named REX. The building adaptation design was consigned to an outstanding architect Nikos Gortsios, while the present author was charged with the acoustical design of the object. The adaptation enterprise began to be realized in January 1989. Designs had to be ready for implementation immediately. All decisions had to be undertaken without any delay because of urgent deadlines for their execution. The whole adaptation work has been completed within 64 days.

Two sectional views of the object are shown in Fig. 1. It should be explained that four floors of the building situated above the depicted part, lodge numerous residential flats. Such situation demands very high transmission loss of sound penetrating through separating barriers, walls and floors of the hall, into the residential part of the building.

On the other hand, the sound insulation requirements imposed by the level of traffic noise prevailing nearby, are also very difficult to be fulfilled.

3. Traffic noise conditions

Measurements of the traffic noise levels have been recently carried on for the Thessaloniki downtown [4]. A map section is shown in Fig. 2, where the theatre site is marked encircled with dashed line. Numbers along streets denote traffic intensities. The measured equivalent level for Vasilissas Olgas street in the theatre neighborhood $L_{eq} = 78$ dB(A), i.e. the highest level of traffic noise observed in the whole downtown area. Unmeasured were, however, ground vibrations caused by the traffic.

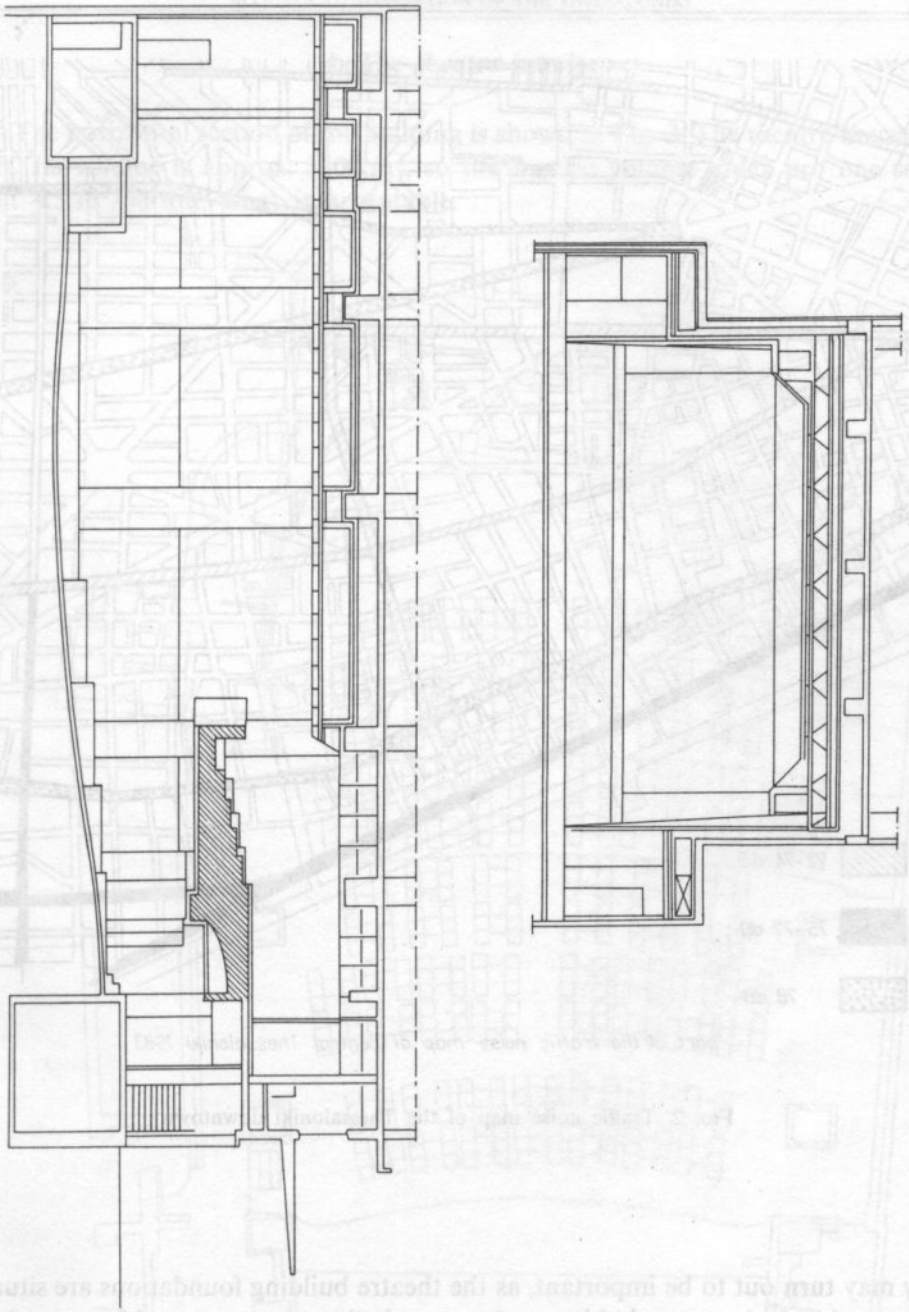

FIG. 1. Cross sections of the theatre hall

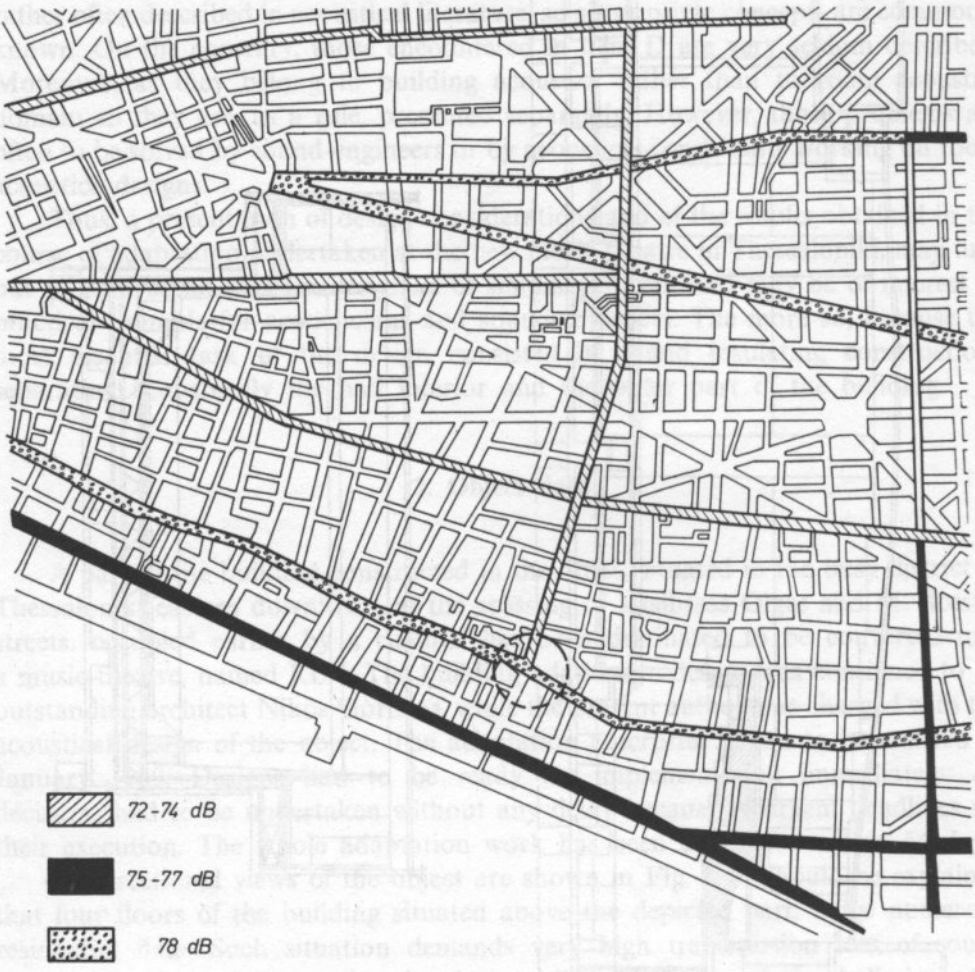

FIG. 2. Traffic noise map of the Thessaloniki downtown

They may turn out to be important, as the theatre building foundations are situated near an old rivulet, now hidden underground, then on an unstable ground.

Thus, conditions for a design of appropriate insulation against the mentioned level of noise and vibrations were severe. Moreover, a constant tendency to augmentation of the traffic noise in the city will aggravate the conditions soon. Then, the design must take it into account.

4. The theatre interior

The horizontal section of the building is shown in Fig. 3. The theatre houses 850 seats. Its volume is approx. 3800 m^3, so the specific volume index pro one seat is aboit 4.5 m^3/person, what is acceptable.

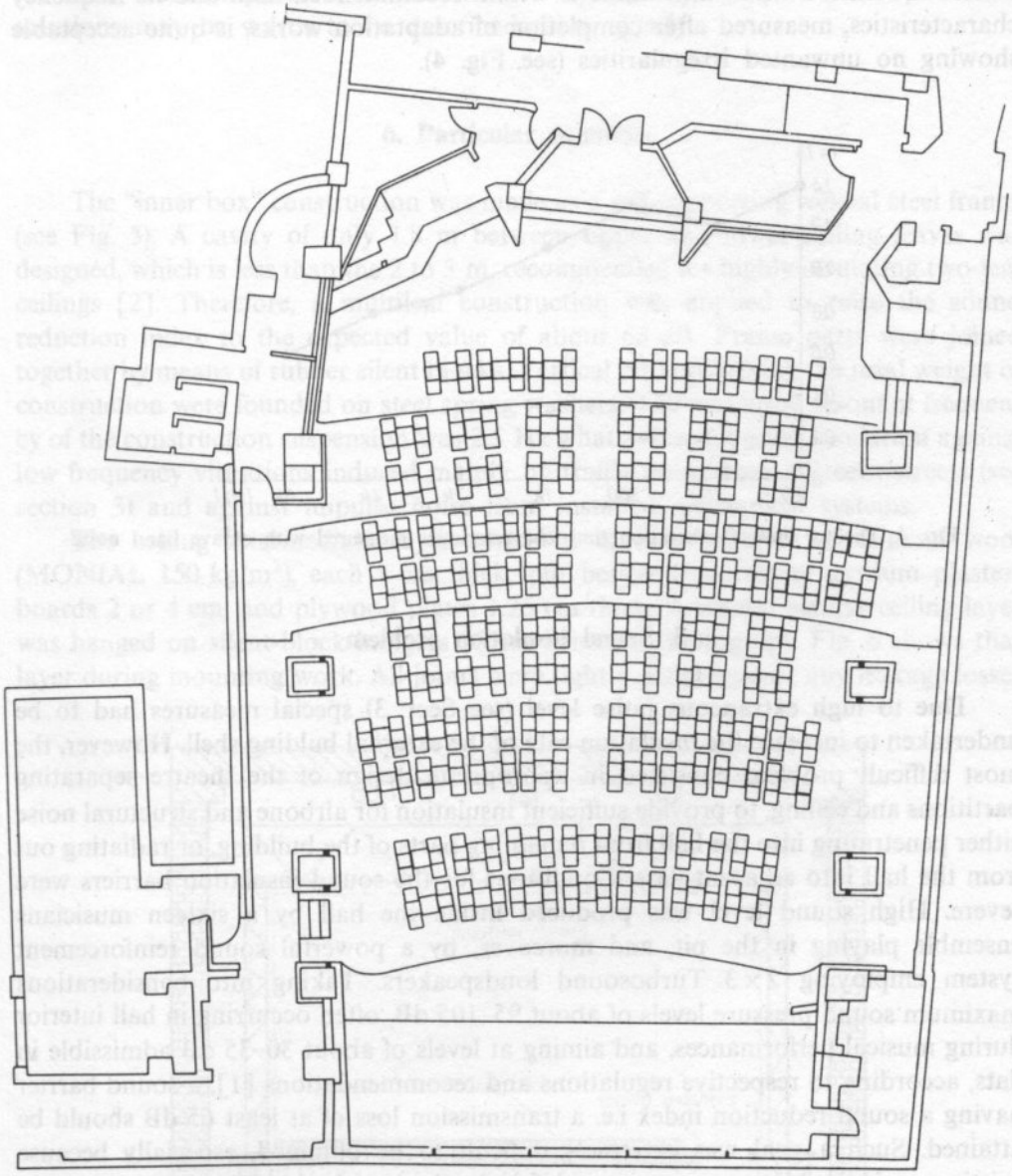

FIG. 3. Ground floor plan of the theatre hall

The shape of the interior has been redesigned so as to obtain good visibility towards the stage from all seats, however their distribution depends mainly on the presence of side pillars designed to support an inner shell of the ceiling and partitions. Due to such unusual interior construction some problems of sound distribution arise, yet generally the listening conditions in all seats are favourable. The reverberation mean-time value is within recommended data and its frequency characteristics, measured after completion of adaptation works, is quite acceptable showing no unwanted irregularities (see Fig. 4).

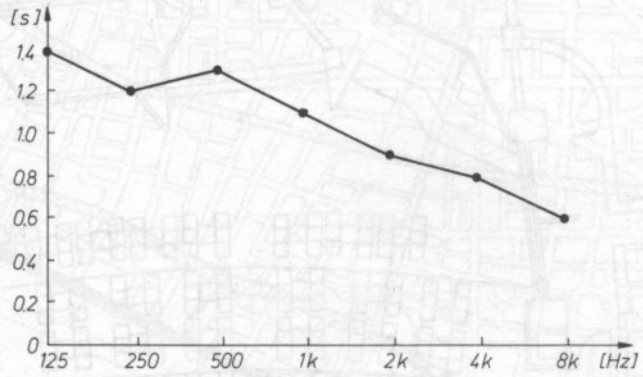

FIG. 4. Theatre hall reverberation time characteristics measured with octave band noise

5. Sound insulation problem

Due to high extraneous noise level (see Sect. 3) special measures had to be undertaken to increase the insulation rate of the external bulding shell. However, the most difficult problem consisted in appropriate design of the theatre separating partitions and ceiling, to provide sufficient insulation for airbone and structural noise either penetrating into the hall from remaining parts of the building, or radiating out from the hall into adjacent flats. Conditions for the sound insulation barriers were severe. High sound level was produced inside the hall by a sixteen musicians ensemble playing in the pit, and moreover, by a powerful sound reinforcement system employing 2×3 Turbosound loudspeakers. Taking into considerations maximum sound pressure levels of about 95–105 dB, often occurring in hall interior during musical performances, and aiming at levels of about 30–35 dB admissible in flats, according to respective regulations and recommendations [1], a sound barrier having a sound reduction index i.e. a transmission loss of at least 65 dB should be attained. Such a goal was extremely difficult to be obtained, especially because existing main building structures and facades had to be preserved.

A general concept of the design depended on the application of a "box within box" construction. The existing building structure was taken as an outer box, while

the inner one was to be build. A very thick intermediate insulating layer was to be put between. Besides of high insulation introduced by the material selected for intermediate layer, it should be mounted as tight as possible in order to reduce eventual leakage of sound through holes and cracks [1].

As the above presented concept turned out to be an efficient tool for resolving the most difficult problem of the entire adaptation project, so some particular solutions may be worth to be described more closely.

6. Particular solutions

The "inner box" construction was made as a self-supporting welded steel frame, (see Fig. 5). A cavity of only 1.8 m between upper and lower ceiling leaves was designed, which is less than the 2 to 3 m, recommended for highly insulating two-leaf ceilings [2]. Therefore, a multileaf construction was applied to raise the sound reduction index to the expected value of about 65 dB. Frame parts were joined together by means of rubber silent blocks. Vertical pillars carrying the total weight of construction were founded on steel spring washers. The measured resonant frequency of the construction suspension was 2.5 Hz what assured a good insulation against low frequency vibrations induced mainly by traffic noise from adjacent streets (see section 3) and against impulse noise from installed mechanical systems.

The ceiling intermediate layer consisted of three courses of mineral wool (MONIAL 150 kg/m^3), each 8 cm thick, put between courses of gypsum plasterboards 2 or 4 cm, and plywood plates 1.25 cm thick. A second similar ceiling layer was hanged on silent-block-hangers 35 cm beneath. Photograph Fig. 6 shows that layer during mounting work. All joints were tightly glued against any leakage losses

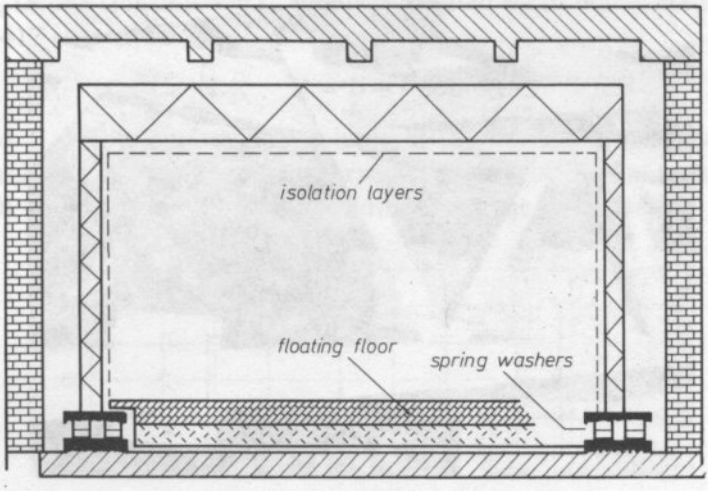

FIG. 5. "Box within box" construction-self supporting steel frame with steel spring washers

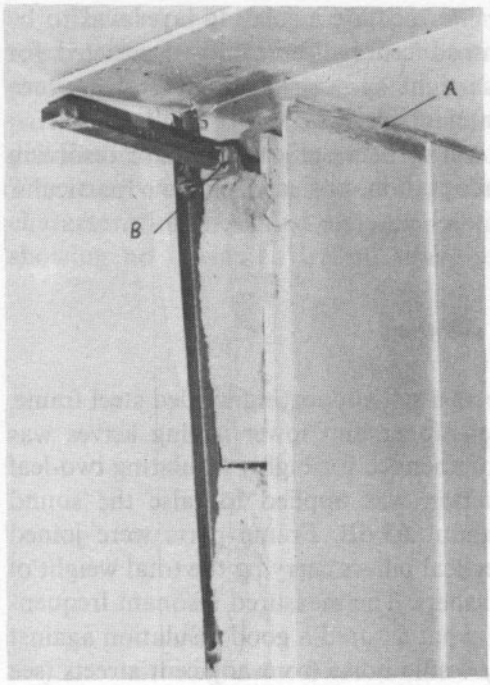

FIG. 6. Mounting of the mineral wool insulating layer

of insulation. The total thickness of the inner ceiling, including a 35 cm spacing from the outer one, was 120 cm. Side partitions of similar construction were spaced only 15 cm from outer walls. Another view of mounting work showing part of steel frame construction and spaced supporting battens and trusses in is shown in Fig. 7.

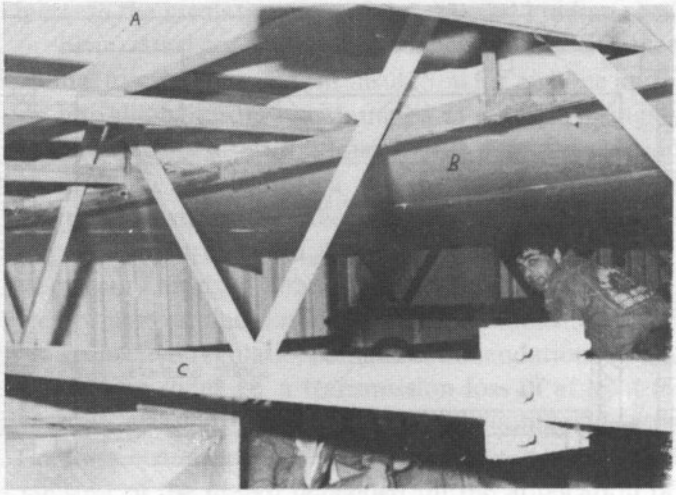

FIG. 7. View of the insulating layers glueing work

7. Obtained results

Several test were made in order to check the efficiency of the implemented solutions.

The first test consisted of noise level measurements made in residential flats situated directly above the theatre ceiling. A block diagram of the measuring equipment is shown in Fig. 8. During a performance when the sound level on stage

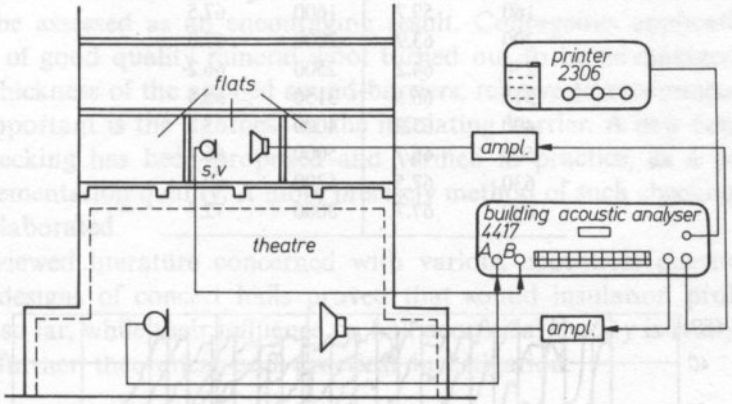

FIG. 8. Block diagram of the instrumentation used for transmission loss measurements of the ceiling

was at about 100 dB, the weighted noise level measured in flats reached from 28 dB (A) to 38 dB(A), depending on frequency band. Detailed results plotted as normalized level difference vs. midfrequency of tierce-bands are shown in Fig. 9, while same results obtained from a printer are listed in Table 1. The normalized level difference R, i.e. the transmission loss, was calculated by Building Acoustic Analyzer B and K 4417, the equations (after ISO 140):

$$D = L_1 - L_2; \quad R = D + 10\log(6{,}15ST/V)\text{dB}$$

where S and V denote surface and volume of the flat room, in square and cubic metres respectively, while T means reverberation time of the flat room, in seconds (see Fig. 10) also measured by the Building Acoustic Analyzer.

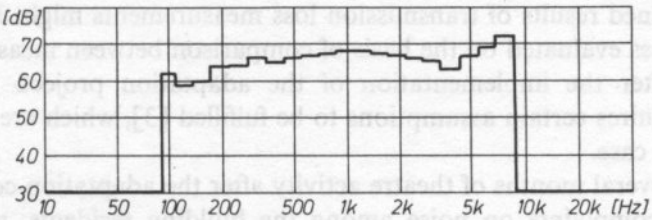

FIG. 9. Measurements results – transmission characteristics

Table 1. Measurements results – table of transmission loss values

00:00:45
NRM. LEVEL DIFF.
V = 36 S = 11,5

HZ CODES	DB	HZ CODES	DB
100	62.2	1000	68.0
125	58.5	1250	68.2
160	59.7	1600	67.5
200	63.9	2000	67.0
250	64.2	2500	66.2
315	66.5	3150	65.5
400	65.2	4000	63.2
500	66.7	5000	66.7
630	67.5	6300	69.5
800	67.7	8000	72.2

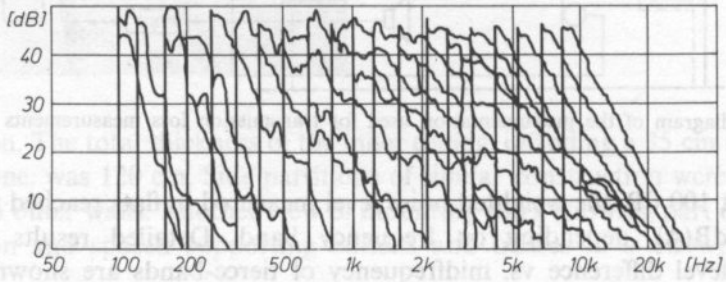

FIG. 10. Decay curves measured in a flat above theatre ceiling

Beside of transmission loss measurements a tightness test was executed. Ventilation system was used to check the tightness of the mounted sound barriers. All doors were shut and door slits were sealed up with glue-tapes. After the blow-in system was switched in, while the exhaust system was switched out, the static pressure rose quickly to 0.5 at above the normal level, thus showing very good tightness of the implemented sound-barriers.

The obtained results of transmission loss measurements might be compared to an insertion loss evaluated on the basis of comparison between measurements made before and after the implementation of the adaptation project. However, such evaluation requires certain assumptions to be fulfilled [3], which are not satisfied in the presented case.

During several months of theatre activity after the adaptation completion there were neither complaints on noise among the building residents, nor any critical remarks of performers or of audience on unwanted sound inside the hall.

8. Conclusions

A brief description of an acoustical adaptation design was given. The presented information seems to be sufficient to derive conclusions useful for acoustical designers dealing with similar problems, which may be relatively often met in practice.

The concept of "box within box" insulating construction gained a successful application example, applied to an existing building, not a newly built one. The attained degree of insulation expressed by the more than 65 dB sound reduction index may be assessed as an encouraging result. Courageous application of very thick layers of good quality mineral wool turned out to be advantageous, despite small total thickness of the applied sound-barriers, relative to recommended values.

Very important is the tightness of the insulating barrier. A new concept of the tightness checking has been proposed and verified in practice, as a proof of the barrier implementation quality. A more precisely method of such checking should be of course, elaborated.

The reviewed literature concerned with various acoustical questions met in adaptation designs of concert halls proved that sound insulation problems were disregarded so far, while their influence on hall acoustical quality is really important and worth further theoretical and practical investigation.

References

[1] D. J. Croome, *Noise, buildings and people*, Pergamon Press, Oxford 1977

[2] C. Gilford, *Acoustics for radio and televisions studios*, IEEE Monograph, Peregrinus London 1972

[3] G. Papanikolaou, A. Trochidis, *Design of a test facility for transmission loss measurement*, Applied Acoustics, 18, 315–323 (1985)

[4] S. Vougias, G. Papanikolaou, *Traffic noise and atmospheric pollution in Thessaloniki*, 1984.

Received October 10, 1990

ARCHIVES OF ACOUSTICS
16, 3–4 559–569 (1991)

A RELAXATION MODEL OF PHONON GAS INTERACTION WITH AN EXTERNAL FIELD

S. PIEKARSKI

Institute of Fundamental Technological Research Polish Academy of Sciences
(00-049 Warszawa, ul. Świętokrzyska 21)

In the paper, a kinetic model of interactiona of optical and acoustical phonons is discussed, basing on four life-times. Equations of non-diffusive transfer of heat perturbations, induced by an external field acting upon an assembly of optical phonons, are derived form the proposed model.

1. Introduction

In phenomenological description of heat conduction, the Fourier law of heat conduction is usually applied. According to this law, heat flux is a linear function of temperature gradient. Processes of heat transfer may be also described by microscopic models, deduced from solid state physics. They lead, in the case of dielectrics, to description of heat transfer in terms of mutual interactions of elementary excitations, called phonons [1, 2]. In this paper, we limit ourselves to discussion of a model in which dynamics of a phonon gas is described by the kinetic Boltzmann-Peierls equation [2]. As it is known, the Fourier law of heat conduction may be deduced from kinetic equations for phonons if the relevant modification of Chapman-Enskog method is applied. This derivation is based on the search of such solutions of phonon kinetic equations which may be expressed in the form of asymptotic expansions in terms of temperature gradients [2]. The scope of applications of the Chapman-Enskog method is, however, limited to those states of the system only which differ insignificantly from local thermodynamical equilibrium. For states significantly different from local thermodynamical equlibrium, conditions required by Chapman-Enskog method are not satisfied and heat transfer due to phonon interactions may not be approximated by the Fourier law of heat conduction. Conditions in which the state of phonons assembly is far from local thermodynamical equilibrium may correspond to situation in a dielectric treated, for instance, by laser radiation. Strickly speaking, description of heat transfer in such

conditions requires solving kinetic equation. In the limits of approximations stated further and based on a relaxation model of phonon interactions, it is possible to deduce equations of heat transfer in the form of a closed system of differential equations. In the paper, we consider a dielectric in which optical, as well as acoustic, vibration modes exist. For simplicity we limit ourselves to the case when only one branch of each type of vibrations exists. For such a system, the kinetic Boltzmann-Peierls description reduces to a set of two coupled kinetic equations for one-point distribution functions for optical and acoustic phonons.

We assume that energy is transmitted from outside directly to the assembly of optical phonons and then, as a result of mutual phonon interactions, transformed into phonon excitations in the acoustic branch. We also assume that the dominating contribution to energy transport processes comes from the assembly of acoustic phonons. It is known, from solid state physics, that interactions of phonons, ocurring under the influence of electromagnetic radiation, depend on radiation frequency. These effects may be taken into account by assuming that collision integrals in phonon kinetic equations depend on history of external fields. From the processes of phonons interactions, we can separate processes of mutual energy exchange between optical and acoustical phonons assemblies, relaxation processes in optical phonons gas and relaxation process in acoustical phonons gas. The description of these processes by four life-times is introduced, and conformance of the model to the second principle of thermodynamics is shown. Next, basing on moment equations, a set of field equations is educed, which couples energy densities of optical and acoustic phonons with heat flux of acoustic phonons. In the limits of the proposed model, influence of external field reduces to apparition of a time-dependent source in energy balance for optical phonons. From the relations obtained, a set of two equations which connect densities of optical and acoustic phonons, follows.

The microscopic model of transport phenomena, used in this paper, is based on description of phonon interactions in a rigid dielectric. Hence, it does not give the possibility of discussion of effects of coupling thermal and deformation fields. Discussion of such effects, based on microscopic description of phonon assembly and deformation field interaction, will be the subject of a separate paper.

2. Relaxation model of phonon heat transfer

Let us consider a microscopic model of heat transfer in a dielectric, based on the following system of coupled kinetic equations for optical and acoustic phonons

$$\begin{aligned} &\frac{\partial}{\partial t} f_0(\mathbf{x}, \mathbf{k}, t) + \frac{\partial \omega_0(\mathbf{k})}{\partial k_i} \frac{\partial f_0(\mathbf{x}, \mathbf{k}, t)}{\partial x_i} = J_0\big(f_0(\mathbf{x}, \mathbf{k}, t), f_a(\mathbf{x}, \mathbf{k}, t), E_s(t)\big) \\ &\frac{\partial}{\partial t} f_a(\mathbf{x}, \mathbf{k}, t) + \frac{\partial \omega_a(\mathbf{k})}{\partial k_i} \frac{\partial f_a(\mathbf{x}, \mathbf{k}, t)}{\partial x_i} = J_a\big(f_0(\mathbf{x}, \mathbf{k}, t), f_a(\mathbf{x}, \mathbf{k}, t), E_s(t)\big) \end{aligned} \tag{2.1}$$

where $\mathbf{x}$ is a space variable, $\mathbf{k}$ is a phonon wave vector, t mean time, $f_0(\mathbf{x}, \mathbf{k}, t)$ is a distribution function of optical phonons, $f_a(\mathbf{x}, \mathbf{k}, t)$ is a distribution function of acoustic phonons; $\omega_0(\mathbf{k})$ and $\omega_a(\mathbf{k})$ are dispersion curves for optical and acoustic phonons, respectively; $J_0(f_0(\mathbf{x}, \mathbf{k}, t), f_a(\mathbf{x}, \mathbf{k}, t), E_s(t))$ is the collision integral in the kinetic equation for optical phonons, $J_a(f_0(\mathbf{x}, \mathbf{k}, t), f_a(\mathbf{x}, \mathbf{k}, t), E_s(t))$ is the collision integral in the kinetic equation for acoustic phonons; $E_s(t) = E(t-s)$, $s \geqslant 0$ describes history of an external field acting upon the whole system; x_i and k_i are cartesian coordinates of vectors $\mathbf{x}$ and $\mathbf{k}$. In the above model, it is assumed for simplicity that there exists only one branch for each type of phonon excitations.

From solid state physics, it is known that functions $\hbar\omega_0(k)$ and $\hbar\omega_a(k)$ have a meaning of energy of a single phonon from the corresponding branch ($2\pi\hbar$ is the Planck constant) [2]. After multiplying Eqs. $(2.1)_1$ and $(2.1)_2$ by $\hbar\omega_0(\mathbf{k})$ and $\hbar\omega_a(\mathbf{k})$, respectively, integrating equations obtained with respect to $\mathbf{k}$ and changing the order of integration and differentiation, we obtain energy balance equations for optical and acoustical phonons

$$\begin{aligned} &\frac{\partial}{\partial t}\varepsilon_0(\mathbf{x}, t) + \operatorname{div}\mathbf{q}_0(\mathbf{x}, t) = P_0(\mathbf{x}, t) \\ &\frac{\partial}{\partial t}\varepsilon_a(\mathbf{x}, t) + \operatorname{div}\mathbf{q}_a(\mathbf{x}, t) = P_a(\mathbf{x}, t) \end{aligned} \tag{2.2}$$

where

$$\begin{aligned} \varepsilon_0(\mathbf{x}, t) &= \int \hbar\omega_0(\mathbf{k}) f_0(\mathbf{x}, \mathbf{k}, t) \frac{d^3\mathbf{k}}{(2\pi)^3} \\ \mathbf{q}_0(\mathbf{x}, t) &= \int [\hbar\omega_0(\mathbf{k}) \nabla_{\mathbf{k}} \omega_0(\mathbf{k})] f_0(\mathbf{x}, \mathbf{k}, t) \frac{d^3\mathbf{k}}{(2\pi)^3} \\ P_0(\mathbf{x}, t) &= \int \hbar\omega_0(\mathbf{k}) J_0(f_0(\mathbf{x}, \mathbf{k}, t), f_a(\mathbf{x}, \mathbf{k}, t), E_s(t)) \frac{d^3\mathbf{k}}{(2\pi)^3} \end{aligned} \tag{2.3}$$

are energy density of optical phonons, heat flux carried by the gas of optical phonons, and a source in the energy balance for optical phonons, while

$$\begin{aligned} \varepsilon_a(\mathbf{x}, t) &= \int \hbar\omega_a(\mathbf{k}) f_a(\mathbf{x}, \mathbf{k}, t) \frac{d^3\mathbf{k}}{(2\pi)^3} \\ \mathbf{q}_a(\mathbf{x}, t) &= \int [\hbar\omega_a(\mathbf{k}) \nabla_{\mathbf{k}} \omega_a(\mathbf{k})] f_a(\mathbf{x}, \mathbf{k}, t) \frac{d^3\mathbf{k}}{(2\pi)^3} \\ P_a(\mathbf{x}, t) &= \int \hbar\omega_a(\mathbf{k}) J_a(f_0(\mathbf{x}, \mathbf{k}, t), f_a(\mathbf{x}, \mathbf{k}, t), E_s(t)) \frac{d^3\mathbf{k}}{(2\pi)^3} \end{aligned} \tag{2.4}$$

are energy density of acoustic phonons, heat flux carried by the gas of acoustic phonons and source in the energy balance for acoustic phonons.

In Eqs. (2.3), (2.4) we make use of the convention of normalization of phonon distribution functions which in usually applied in solid state physics [2]. Symbols $\nabla_{\mathbf{k}}$ and div mean gradient in respect to $\mathbf{k}$ and space divergence, respectively.

Adding the two balance equations $(2.2)_1$ and $(2.2)_2$ gives the balance equation for the total energy.

$$\frac{\partial}{\partial t}\varepsilon + \operatorname{div}\mathbf{q} = P \tag{2.5}$$

where

$$\begin{aligned} \varepsilon &= \varepsilon_0 + \varepsilon_a \\ \mathbf{q} &= \mathbf{q}_0 + \mathbf{q}_a \\ P &= P_0 + P_a \end{aligned} \tag{2.6}$$

are total energy density, total energy flux and a source component, respectively.

Let us assume that collision integrals in Eqs. $(2.1)_1$, $(2.1)_2$ have the form of the following sums

$$\begin{aligned} J_0(f_0(\mathbf{x}, \mathbf{k}, t), f_a(\mathbf{x}, \mathbf{k}, t), E_s(t)) &= J_{0,E}(f_0(\mathbf{x}, \mathbf{k}, t), E_s(t)) \\ &+ J_{0,R}(f_0(\mathbf{x}, \mathbf{k}, t)) + J_{0,I}(f_0(\mathbf{x}, \mathbf{k}, t), f_a(\mathbf{x}, \mathbf{k}, t)) \end{aligned} \tag{2.7}$$

$$J_a(f_0(\mathbf{x}, \mathbf{k}, t), f_a(\mathbf{x}, \mathbf{k}, t), E_s(t)) = J_{a,R}(f_a(\mathbf{x}, \mathbf{k}, t)) + J_{a,I}(f_0(\mathbf{x}, \mathbf{k}, t), f_a(\mathbf{x}, \mathbf{k}, t)).$$

The component $J_{0,E}(f_0(\mathbf{x}, \mathbf{k}, t), E_s(t)$ of the collision integral $(2.7)_1$ describes processes in which an external field transmits energy to the assembly of acoustic phonons. We assume that these processes may depend on the form of optical phonon distribution $f_0(\mathbf{x}, \mathbf{k}, t)$.

Expressions $J_{0,I}(f_0(\mathbf{x}, \mathbf{k}, t), f_a(\mathbf{x}, \mathbf{k}, t))$ and $J_{a,I}(f_0(\mathbf{x}, \mathbf{k}, t), f_a(\mathbf{x}, \mathbf{k}, t))$ describe processes of mutual energy exchange between the assemblies of optical and acoustic phonons. The principle of conservation of energy requires that the sum of contributions of these processes to the total energy source is equal to zero

$$\begin{aligned} &\int \hbar\omega_0(\mathbf{k}) J_{0,I}(f_0(\mathbf{x}, \mathbf{k}, t), f_a(\mathbf{x}, \mathbf{k}, t)) \frac{d^3\mathbf{k}}{(2\pi)^3} \\ &+ \int \hbar\omega_a(\mathbf{k}) J_{a,I}(f_0(\mathbf{x}, \mathbf{k}, t), f_0(\mathbf{x}, \mathbf{k}, t)) \frac{d^3\mathbf{k}}{(2\pi)^3} = 0. \end{aligned} \tag{2.8}$$

Expression $J_{0,R}(f_0(\mathbf{x}, \mathbf{k}, t))$ describes relaxation processes in the optical phonons assembly; i.e. processes in which acoustic phonons do not participate, and which describe the tendency of optical phonons assembly towards thermodynamical equilibrium if only processes of mutual transmutations of optical and acoustic phonons are eliminated and if $J_{0,E}(f_0(\mathbf{x}, \mathbf{k}, t), E_s(t))$ equals zero.

It follows, from the principle of conservation of energy, that the energy source related to relaxation processes described by $J_{0,R}(f_0(\mathbf{x}, \mathbf{k}, t))$ must be to equal zero

$$\int \hbar\omega_0(\mathbf{k}) J_{0,R}(f_0(\mathbf{x}, \mathbf{k}, t)) \frac{d^3\mathbf{k}}{(2\pi)^3} = 0. \tag{2.9}$$

Expression $J_{a,R}(f_0(\mathbf{x}, \mathbf{k}, t))$ describes relaxation processes in the acoustic phonons assembly and, like $J_{0,R}(f_0(\mathbf{x}, \mathbf{k}, t))$, satisfies the identity corresponding to energy conservation

$$\int \hbar\omega_0(\mathbf{k}) J_{a,R}(f_a(\mathbf{x}, \mathbf{k}, t)) \frac{d^3\mathbf{k}}{(2\pi)^3} = 0 \tag{2.10}$$

According to the general rules of constructing relaxational models for multiple "competing" dissipation processes, we substitute the components of collision integrals separated above by their relaxation equivalents, in which processes of mutual phonon transmutations are approximately described by life-times dependent, in general, on the wave vector $\mathbf{k}$ [3].

The relaxation model of the $J_{0R}(f_0(\mathbf{x}, \mathbf{k}, t))$ component of the collision integral $(2.7)_1$ is described by

$$C_{0,R}(f_0(\mathbf{x}, \mathbf{k}, t)) = -(\tau_{0,R}(\mathbf{k}))^{-1}(f_0(\mathbf{x}, \mathbf{k}, t) - \Phi_{0,R}(\alpha(\mathbf{x}, t))) \tag{2.11}$$

where $\tau_{0,R}(\mathbf{k})$ is a life-time, modelling dissipation processes described by $J_{0,R}(f_0(\mathbf{x}, \mathbf{k}, t))$; function $\alpha(\mathbf{x}, t)$ is given as the solution of the following identity

$$\int \frac{\hbar\omega_0(\mathbf{k})}{\tau_{0,R}(\mathbf{k})} \left[f_0(\mathbf{x}, \mathbf{k}, t) - \frac{1}{e^{\alpha(\mathbf{x},t)\hbar\omega_0(\mathbf{k})} - 1} \right] \frac{d^3\mathbf{k}}{(2\pi)^3} = 0 \tag{2.12}$$

while

$$\Phi_{0,R}(\alpha(\mathbf{x}, t)) = \frac{1}{e^{\alpha(\mathbf{x},t)\hbar\omega_0(\mathbf{k})} - 1} \tag{2.13}$$

(Because the life-time is positive, it follows that the above definition of $\alpha(\mathbf{x}, t)$ is unambiguous).

It can is seen that the expression (2.11), defined in such a way, satisfies condition of conservation of energy. Similarly, dissipation processes described by $J_{a,R}(f_a(\mathbf{x}, \mathbf{k}, t))$, which are responsible for relaxation to thermodynamical equilibrium of the acoustical phonons assembly, are modelled by the life-time $\tau_{a,R}(\mathbf{k})$ dependent on the wave vector. The relevant contribution to the collision integral has the form

$$C_{a,R}(f_a(\mathbf{x}, \mathbf{k}, t)) = -(\tau_{a,R}(\mathbf{k}))^{-1}(f_a(\mathbf{x}, \mathbf{k}, t) - \Phi_{a,R}(\beta(\mathbf{x}, t))) \tag{2.14}$$

where

$$\Phi_{a,R}(\beta(\mathbf{x}, t)) = \frac{1}{e^{\beta(\mathbf{x},t)\hbar\omega_a(\mathbf{k})} - 1} \tag{2.15}$$

and the condition of energy conservation

$$\int \frac{\hbar\omega_a(\mathbf{k})}{\tau_{a,R}(\mathbf{k})} \left(f_a(\mathbf{x}, \mathbf{k}, t) - \Phi_{a,R}(\beta(\mathbf{x}, t))\right) \frac{d^3\mathbf{k}}{(2\pi)^3} = 0 \tag{2.16}$$

determines the value of $\beta(\mathbf{x}, t)$ which appears in (2.14) and (2.15) as a parameter.

Expressions $J_{0,I}(f_0(\mathbf{x}, \mathbf{k}, t), f_a(\mathbf{x}, \mathbf{k}, t))$ and $J_{a,I}(f_0(\mathbf{x}, \mathbf{k}, t), f_a(\mathbf{x}, \mathbf{k}, t))$, describing mutual transmutation processes of optical and acoustic phonons, are approximated by

$$\begin{aligned} C_{0,I}(f_0(\mathbf{x}, \mathbf{k}, t), f_a(\mathbf{x}, \mathbf{k}, t)) &= -(\tau_{0,I}(\mathbf{k}))^{-1}(f_0(\mathbf{x}, \mathbf{k}, t) - \Phi_{0,I}(\gamma(\mathbf{x}, t))) \\ C_{a,I}(f_0(\mathbf{x}, \mathbf{k}, t), f_a(\mathbf{x}, \mathbf{k}, t)) &= -(\tau_{a,I}(\mathbf{k}))^{-1}(f_a(\mathbf{x}, \mathbf{k}, t) - \Phi_{a,I}(\gamma(\mathbf{x}, t))), \end{aligned} \tag{2.17}$$

respectively, where

$$\begin{aligned} \Phi_{0,I}(\gamma(\mathbf{x}, t)) &= \frac{1}{e^{\gamma(\mathbf{x},t)\hbar\omega_0(\mathbf{k})} - 1} \\ \Phi_{a,I}(\gamma(\mathbf{x}, t)) &= \frac{1}{e^{\gamma(\mathbf{x},t)\hbar\omega_a(\mathbf{k})} - 1} \end{aligned} \tag{2.18}$$

while the condition of energy conservation in energy transfer processes between the optical and acoustic phonons assemblies takes the form of equality

$$\begin{aligned} 0 = &\int \frac{\hbar\omega_0(\mathbf{k})}{\tau_{0,I}(\mathbf{k})} \left(f_0(\mathbf{x}, \mathbf{k}, t) - \Phi_{0,I}(\gamma(\mathbf{x}, t))\right) \frac{d^3\mathbf{k}}{(2\pi)^3} \\ &+ \int \frac{\hbar\omega_a(\mathbf{k})}{\tau_{a,I}(\mathbf{k})} \left(f_a(\mathbf{x}, \mathbf{k}, t) - \Phi_{a,I}(\gamma(\mathbf{x}, t))\right) \frac{d^3\mathbf{k}}{(2\pi)^3}. \end{aligned} \tag{2.19}$$

This equality determines the value of $\gamma(\mathbf{x}, t)$. It is easily verified that, for any pair of distribution functions $f_0(\mathbf{x}, \mathbf{k}, t)$ and $f_a(\mathbf{x}, \mathbf{k}, t)$, the quantity $\gamma(\mathbf{x}, t)$ is determined unambigously.

Hence, the proposed system of kinetic equations takes the form

$$\begin{aligned} &\frac{\partial}{\partial t} f_0(\mathbf{x}, \mathbf{k}, t) + \frac{\partial\omega_0(\mathbf{k})}{\partial k_i} \frac{\partial f_0(\mathbf{x}, \mathbf{k}, t)}{\partial x_i} = -(\tau_{0,R}(\mathbf{k}))^{-1}(f_0(\mathbf{x}, \mathbf{k}, t) - \Phi_{0,R}(\alpha(\mathbf{x}, t))) \\ &\quad -(\tau_{0,I}(\mathbf{k}))^{-1}(f_0(\mathbf{x}, \mathbf{k}, t) - \Phi_{0,I}(\gamma(\mathbf{x}, t))) + J_{0,E}(f_0(\mathbf{x}, \mathbf{k}, t), E_s(t)) \\ &\frac{\partial}{\partial t} f_a(\mathbf{x}, \mathbf{k}, t) + \frac{\partial\omega_a(\mathbf{k})}{\partial k_i} \frac{\partial f_a(\mathbf{x}, \mathbf{k}, t)}{\partial x_i} = -(\tau_{a,R}(\mathbf{k}))^{-1}(f_a(\mathbf{x}, \mathbf{k}, t) - \Phi_{a,R}(\beta(\mathbf{x}, t))) \\ &\quad -(\tau_{a,I}(\mathbf{k}))^{-1}(f_a(\mathbf{x}, \mathbf{k}, t) - \Phi_{a,I}(\gamma(\mathbf{x}, t))). \end{aligned} \tag{2.20}$$

The functions $\Phi_{0,R}$, $\Phi_{0,I}$, $\Phi_{a,I}$, $\Phi_{a,R}$ are given by the formulae (2.13), (2.18) and (2.15), while their arguments, functions $\alpha(\mathbf{x}, t)$, $\gamma(\mathbf{x}, t)$ and $\beta(\mathbf{x}, t)$, are defined as the solutions of Eqs. (2.12), (2.19) and (2.16).

The functions $\Phi_{0,R}$, $\Phi_{0,I}$, $\Phi_{a,I}$, $\Phi_{a,R}$ have the form of local equilibrium Planck distributions in which the inverse of product of temperature and the Boltzmann constant is identified with the functions $\alpha(\mathbf{x}, t)$, $\gamma(\mathbf{x}, t)$ and $\beta(\mathbf{x}, t)$, respectively.

Hence, $\alpha(\mathbf{x}, t)$ may be assigned such a temperature field which determines the local equilibrium state to which the distribution of optical phonons tends if all the interaction, but optical phonon relaxation processes, are "turned off". The functions $\beta(\mathbf{x}, t)$ and $\gamma(\mathbf{x}, t)$ may be interpreted in a similar way.

3. Entropy balance

We will show that the proposed system of kinetic equations (2.20) conforms to thermodynamics in the sense that its solutions satisfy entropy balance. In the entropy balance, the source term is a sum of two components; the first, always non-negative, describes dissipation processes inside the assembly while the second describes an entropy source due to the influence of external field. The entropy source related to external field depends only on processes described by the component $J_{0,E}(f_0(\mathbf{x}, \mathbf{k}, t), E_s(t))$ of the collision integral. The term is non-negative if the source of optical phonons described by $J_{0,E}(f_0(\mathbf{x}, \mathbf{k}, t), E_s(t))$ is non-negative for any values of the wave vector, i.e., if interaction with the external field does not diminish the number of optical phonons, independently of their spectrum range.

It is known from solid state physics that entropy densities of optical and acoustic phonons are given, respectively, by the formulae

$$\begin{aligned} S_0(\mathbf{x}, t) &= \int \{(f_0+1)\ln(f_0+1) - f_0 \ln f_0\} \frac{d^3\mathbf{k}}{(2\pi)^3} \\ S_a(\mathbf{x}, t) &= \int \{(f_a+1)\ln(f_a+1) - f_a \ln f_a\} \frac{d^3\mathbf{k}}{(2\pi)^3}. \end{aligned} \tag{3.1}$$

(From now on, to simplify the notation, arguments on which phonon distribution functions depend will not be written explicitly.) Total entropy density S is a sum of expressions $(3.1)_1$ and $(3.1)_2$

$$S(\mathbf{x}, t) = S_0(\mathbf{x}, t) + S_a(\mathbf{x}, t). \tag{3.2}$$

It can be seen, on differentiating (3.2) with respect to time and using Eq. (2.20), that the total entropy balance of the assembly being considered has the form

$$\frac{\partial}{\partial t} S(\mathbf{x}, t) + \operatorname{div} \mathbf{S} = P_S \tag{3.3}$$

where

$$\mathbf{S}(\mathbf{x}, t) = \int \{(f_0+1)\ln(f_0+1) - f_0 \ln f_0\} \nabla_{\mathbf{k}} \omega_0(\mathbf{k}) \frac{d^3\mathbf{k}}{(2\pi)^3} + \int \{(f_a+1)\ln(f_a+1) - f_a \ln f_a\} \nabla_{\mathbf{k}} \omega_a(\mathbf{k}) \frac{d^3\mathbf{k}}{(2\pi)^3} \tag{3.4}$$

is the total entropy flux, and

$$P_S(\mathbf{x}, t) = \int \left(\ln \frac{f_0+1}{f_0}\right) C_{0,R}(f_0) \frac{d^3\mathbf{k}}{(2\pi)^3} + \int \left(\ln \frac{f_a+1}{f_a}\right) C_{a,R}(f_a) \frac{d^3\mathbf{k}}{(2\pi)^3}$$
$$+ \int \left(\ln \frac{f_0+1}{f_0}\right) C_{0,I}(f_0, f_a) \frac{d^3\mathbf{k}}{(2\pi)^3} + \int \left(\ln \frac{f_a+1}{f_a}\right) C_{a,I}(f_0, f_a) \frac{d^3\mathbf{k}}{(2\pi)^3}$$
$$+ \int \left(\ln \frac{f_0+1}{f_0}\right) J_{0,E}(f_0, E_s(t)) \frac{d^3\mathbf{k}}{(2\pi)^3} \tag{3.5}$$

is the source of entropy. To investigate signs of components appearing in (3.5), we use the well-known identity stating that, for any positive numbers y, z, the following inequality holds [2]

$$(y-z)\ln \frac{y}{z} \geqslant 0. \tag{3.6}$$

On substituting $y = (f_0)^{-1}(f_0+1)$, $z = (\Phi_{0,I})^{-1}(\Phi_{a,I}+1)$ and $y = (f_a)^{-1}(f_a+1)$, $z = (\Phi_{a,I})^{-1}(\Phi_{a,I}+1)$ we obtain, after multiplied by $\Phi_{a,I} f_0$ and $\Phi_{a,I} f_a$, respectively,

$$(\Phi_{0,I} - f_0)\ln \frac{(f_0+1)\Phi_{0,I}}{f_0(\Phi_{0,I}+1)} \geqslant 0$$
$$(\Phi_{a,I} - f_a)\ln \frac{(f_a+1)\Phi_{a,I}}{f_a(\Phi_{a,I}+1)} \geqslant 0. \tag{3.7}$$

After multiplying the inequalities $(3.7)_1$ by $(2\pi)^{-3}(\tau_{0,I}(\mathbf{k}))^{-1}$ and $(3.7)_2$ by $(2\pi)^{-3}(\tau_{a,I}(\mathbf{k}))^{-1}$, adding the results, integrating the sum in respect to $\mathbf{k}$, and taking into account (2.19) we arrive at the inequality

$$-\int (f_0 - \Phi_{0,I})\ln \frac{f_0+1}{f_0} \frac{d^3\mathbf{k}}{(2\pi)^3} - \int (f_a - \Phi_{a,I})\ln \frac{f_a+1}{f_a} \frac{d^3\mathbf{k}}{(2\pi)^3} =$$
$$= \int \left(\ln \frac{f_0+1}{f_0}\right) C_{0,I}(f_0, f_a) \frac{d^3\mathbf{k}}{(2\pi)^3} + \int \left(\ln \frac{f_a+1}{f_a}\right) C_{a,I}(f_0, f_a) \frac{d^3\mathbf{k}}{(2\pi)^3} \geqslant 0. \tag{3.8}$$

From (3.8) it follows that the sum of the third and fourth components of (3.5) is non-negative. It testifies that, in the scope of the model assumed, processes of mutual transmutations of optical and acoustic phonons give a non-negative contribution to the entropy source. In a similar way, it can be is demonstrated that the contributions

from the first two components on the right side of (3.5) are non-negative, as well. The last component of the sum (3.5) describes the entropy source due to external interaction upon the systems. As we mentioned, if the external interaction, independently of spectrum range of optical phonons, increases the number of excitations then their contribution to the total entropy source is also non-negative.

4. Education of field equations

In order to derive the system of field equations describing heat transport processes, we additionally assume that the life-times $\tau_{0,I}(\mathbf{k})$, $\tau_{a,I}(\mathbf{k})$, $\tau_{0,R}(\mathbf{k})$ and $\tau_{a,R}(\mathbf{k})$ do not depend on the wave vector, and that dispersion curve of acoustic phonons is described by the formula

$$\omega_a(\mathbf{k}) = c|\mathbf{k}| \tag{4.1}$$

where c is interpreted as the velocity of sound [2]. On multiplying Eq. $(2.20)_1$ by $(2\pi)^{-3}\hbar\omega_0(\mathbf{k})$ and integrating it with respect to $\mathbf{k}$, we obtain an equation for energy balance of acoustic phonons

$$\frac{\partial}{\partial t}\varepsilon_0 + \operatorname{div}\mathbf{q}_0 = -(\tau_{0,I})^{-1}(\varepsilon_0 - \varepsilon_0(\gamma)) + P_E \tag{4.2}$$

where ε_0 and $\mathbf{q}_0$ are described by the formulae $(2.3)_{1,2}$ while

$$P_E = \int \hbar\omega_0(\mathbf{k}) J_{0,E}(f_0, E_s)\frac{d^3\mathbf{k}}{(2\pi)^3}. \tag{4.3}$$

Next, after multiplying $(2.20)_2$ consecutively by $(2\pi)^{-3}\hbar\omega_a(\mathbf{k})$ and $(2\pi)^{-3}\hbar\omega_a(\mathbf{k})\nabla_{\mathbf{k}}\omega_a(\mathbf{k})$, integrating with respect to $\mathbf{k}$ and substituting (4.1), we obtain equations for energy balance and heat flux of acoustic phonons

$$\begin{aligned}
\frac{\partial}{\partial t}\varepsilon_a + \operatorname{div}\mathbf{q}_a &= -(\tau_{a,I})^{-1}(\varepsilon_a - \varepsilon_a(\gamma)) \\
\frac{\partial}{\partial t}\mathbf{q}_a + \operatorname{div}\mathbf{Q}_a &= -\mathbf{q}_a[(\tau_{a,R})^{-1} + (\tau_{a,I})^{-1}]
\end{aligned} \tag{4.4}$$

where

$$\mathbf{Q}_a = \int \hbar\omega_a(\mathbf{k})[\nabla_{\mathbf{k}}\omega_a(\mathbf{k})]\otimes[\nabla_{\mathbf{k}}\omega_a(\mathbf{k})] f_a \frac{d^3\mathbf{k}}{(2\pi)^3} = \hbar c^3 \int \frac{\mathbf{k}}{|\mathbf{k}|}\otimes\mathbf{k} f_a \frac{d^3\mathbf{k}}{(2\pi)^3}$$

$$\varepsilon_0(\gamma(\mathbf{x}, t)) = \int \hbar\omega_0(\mathbf{k})\frac{1}{e^{\gamma(\mathbf{x},t)\hbar\omega_0(\mathbf{k})} - 1}\frac{d^3\mathbf{k}}{(2\pi)^3} \tag{4.5}$$

$$\varepsilon_a(\gamma(\mathbf{x}, t)) = \hbar c \int |\mathbf{k}|\frac{1}{e^{\gamma(\mathbf{x},t)\hbar c|\mathbf{k}|} - 1}\frac{d^3\mathbf{k}}{(2\pi)^3}$$

while, as it follows from (2.19), the value of $\gamma(\mathbf{x}, t)$ is related to energy densities of optical and acoustic phonons by the formula

$$\tau_{a,I}(\varepsilon_0(\mathbf{x}, t)))-\varepsilon_0(\gamma(\mathbf{x}, t)) = \tau_{0,I}(\varepsilon_a(\mathbf{x}, t)-\varepsilon_a((\gamma(\gamma(x, t))) \tag{4.6}$$

(It can be easily verified that, for any pair of non-negative values ε_0, ε_a, the formula (4.6) determines unambigously the value of γ).

To obtain a closed set of equations from the relations deduced above, we assume that the heat flux transferred by optical phonons is negligibly small as compared with the heat flux transferred by acoustic phonons, and that the dominating contribution to the change in time of energy density of optical phonons is related to processes described by the source component in Eq. (4.2) (this assumption conforms to estimates known in literature, eg. cf. [4]).

The tensor $\mathbf{Q}_a$, which has a meaning of a heat flux tensor may be uniquely expressed as a sum of a spherical and a traceless tensors

$$\mathbf{Q}_a = \tfrac{1}{3}\hat{I}\cdot \mathrm{Tr}\mathbf{Q}_a + \langle \mathbf{Q}_a \rangle \tag{4.7}$$

where $\hat{I}$ is the unit tensor, Tr means trace operation, and $\langle Q_a \rangle$ is the traceless part of Q_α. We assume that the dominant part of the tensor Q_a is the spherical one and that $\langle Q_a \rangle$ may be neglected we repeat the argumentation used by Peierls [5]. This assumption holds when the dominant part of the distribution function is invariant in respect to rotations of $\mathbf{k}$. In particular, it is true when the distribution function of acoustic phonons has the shape approaching that of local equilibrium Planck distribution.

The above approximations imply a closed set of relations, describing propagation of perturbations in a coupled system of optical and acoustic phonons:

$$\begin{aligned}
&\frac{\partial}{\partial t}\varepsilon_0 = -(\tau_{0,I})^{-1}(\varepsilon_0-\varepsilon_0(\gamma))+P_E \\
&\frac{\partial}{\partial t}\varepsilon_a+\mathrm{div}\mathbf{q}_a = -(\tau_{a,R})^{-1}(\varepsilon_a-\varepsilon_a(\gamma)) \\
&\frac{\partial}{\partial t}\mathbf{q}_a+\mathrm{div}(\hat{I}\cdot\tfrac{1}{3}c^2\varepsilon_a) = -\mathbf{q}_a((\tau_{a,R})^{-1}+(\tau_{a,I})^{-1}) \\
&\tau_{a,I}(\varepsilon_0-\varepsilon_0(\gamma)) = \tau_{0,I}(\varepsilon_a-\varepsilon_a(\gamma))
\end{aligned} \tag{4.8}$$

where $\varepsilon_0(\gamma)$ and $\varepsilon_a(\gamma)$ are determined by the formulae $(4.5)_2$, $(4.5)_3$ and (4.6). In the above description, the function P_E, describing velocity with which an external field transfers energy to the optical phonons, is regarded as given. It is seen that the life-time $\tau_{0,R}$, describing relaxation velocity of optical phonons to an equilibrium state, does not appear in the set (4.8).

Taking divergence of Eq. $(4.8)_3$ gives

$$\frac{\partial}{\partial t}\mathrm{div}\mathbf{q}_a+\frac{c^2}{3}\Delta\varepsilon_a = -\mathrm{div}\mathbf{q}_a((\tau_{a,R})^{-1}+(\tau_{a,I})^{-1}) \tag{4.9}$$

After substituting in (4.9) expressions for $\operatorname{div}\mathbf{q}_a$ and $\frac{\partial}{\partial t}\operatorname{div}\mathbf{q}_a$ determined from $(4.8)_2$ and its time derivative, we obtain a set of two equations, relating space densities of energies of optical and acoustic phonons

$$\begin{cases} -\frac{\partial^2}{\partial t^2}\varepsilon_a + \frac{c^2}{3}\Delta\varepsilon_a = \left((\tau_{a,R})^{-1} + (\tau_{a,I})^{-1}\right)\left[\frac{\partial}{\partial t}\varepsilon_a + (\tau_{a,R})^{-1}(\varepsilon_a - \varepsilon_a(\gamma))\right] \\ \qquad\qquad + (\tau_{a,R})^{-1}\frac{\partial}{\partial t}(\varepsilon_a - \varepsilon_a(\gamma)) \\ \frac{\partial}{\partial t}\varepsilon_0 = -(\tau_{0,I})^{-1}(\varepsilon_0 - \varepsilon_0(\gamma)) + P_E \end{cases} \tag{4.10}$$

Processes of heat transfer, described by (4.10), have a different character than processes described by the Fourier law of heat conductivity. We may notice that in the set (4.10) we can assume different primitive fields which can be easily physically interpreted. Namely, one of the variables may be taken to be the field γ (proportional to the inverse of the (temperature to which the system relaxes locally), while the other one may be the $\varepsilon_a - \varepsilon_a(\gamma)$ (or, equivalently, $\varepsilon_0 - \varepsilon_0(\gamma)$), describing the measure of deviation of the system from local thermodynamical equilibrium.

References

[1] J. A. REISSLAND, *The physics of phonons*, John Wiley, London 1973.

[2] V. L. GURIEWICZ, *Kinietika fononnych sistiem*, Nauka, Moskwa 1980.

[3] C. CERCIGNANI, *Mathematical problems in the kinetic theory of gases in*: Mathematical models and methods in mechanics, Banach Center Publications, vol. 15 PWN, Warszawa 1985.

[4] G. P. SRIVASTAVA, *Acoustic-optical phonon interactions in solids*, in: Phonon scattering in condensed matter. International Conference on Phonon Scattering in Condensed Matter, Brown University 1979, Proceedings Ed. H. J. Maris, Plenum Press, New York 1980.

[5] R. E. PEIERLS, *Quantum theory of solids*, Clarendon Press, Oxford 1955.

Received November 29, 1989

ARCHIVES OF ACOUSTICS
16, 3-4, 571-579 (1991)

ACOUSTIC SCATTERING AFFECTED BY MONOMOLECULAR FILMS SPREAD OVER A WIND-DRIVEN WATER SURFACE

S. J. POGORZELSKI

Environmental Acoustics Laboratory University of Gdańsk
(80-952 Gdańsk, Wita Stwosza 57)

A spectrum of amplitude fluctuations of the ultrasonic signal scattered from a wind-created water surface covered with an oil substance monolayer of well-defined viscoelastic properties was examined under laboratory conditions. The presence of an oil film causes a shift of the peak frequency towards higher frequencies and increases the fall-off on the high-frequency band of the spectrum if compared to clean surface scattering. The effect turned out to be unequivocally related to rheological parameters of the given monolayer film.

1. Introduction

It is well-known that the organic films on the sea surface both natural and artificial are very predominant in coastal zones. The existence of mineral oil spills at sea is becoming a problem of growing concern to our society because of its adverse effects on marine life in coastal and inland waters. Therefore there is a great need for aerial surveillance systems capable of a detecting oil-derivative contaminations under all weather conditions and independent of the time of the day. These slicks strongly affect the surface waves field and thereby influence most air-sea interaction processes, for instance, the momentum and energy transfer from the wind to the wave field, and the gas exchange at the air-sea interface [5], [7], [26].

In modern oceanography studies of this variability are closely connected with the problem of remote sensing techniques of oceanic processes by their manifestation on the wavy surface. For example, the electromagnetic emission in the microwave [2], [3], and visible [9] spectral bands as well as the scattering of electromagnetic waves are influenced by monomolecular surface films [10], [11]. The theoretical background for an acoustic remote sensing method is derived, potentially applicable

This paper was presented in part at the 7th Symposium on Hydroacoustic, Gdańsk-Stawiska 1990, Poland

for determining physicochemical characteristics of surface films. The presented theory makes use of the bond existing between rheological surface film properties, damping, and signatures of wind-excited waves spectra as turned out strictly related to ultrasonic surface scattering spectra of amplitude fluctuations.

The Marangoni effect has been recently identified as being responsible for resonance like type damping of short gravity waves when the wavy surface is covered with viscoelastic films [3], [13]. Short gravity and capillary waves which play a principal role in Marangoni damping are characterized by a particular shape i.e. they have a large slope and a rather small amplitude [24]. The most suitable acoustic system for investigation of scattering on this kind of wavy surfaces consists of a directional transducer irradiating a small area of the studied surface [8], and creating conditions of scattering on so-called high-freequencies (i.e. at large values of Rayleigh parameter). In light of the scattering theory [25], if the wavelength and beam geometry are known, the specularly scattered sound intensity (relative to the plane surface situation) is solely determined by the mean-square surface slope for "rough surfaces" [6, 17].

All systematic changes of the rough surface undulation, for example due to presence of a layer of oil substance, express themselves in corresponding changes in the scattered signal statistics as already shown in laboratory and at-sea experiments by the author [19–22].

In this paper the author reports about the analysis of the amplitude fluctuations spectrum of the ultrasonic signal scattered from a wind-created surface of clean water and its surface covered with a monolayer of well-defined rheological properties. The substances under study stand for a group of commercially available crude oil derivatives having very different physical properties, and which can be found out in natural waters as contaminations. Surface pressures of the spread films were on the order of a few dynes/cm, similarly the natural sea slick took on the same value [4], [5], [9], [14]. The spectra were analysed to characterize the surface pressure, dilational elasticity modulus and structural diffusion parameter values which completely identify the spread film [1], [7]. Another motivation for this experiment was to predict the sensitivity of the amplitude fluctuations spectra to monomolecular surface films. The wind wave tunnel results indicate that the method based on high-frequency surface scattering appears to be a feasible approach in the field of sea surface contamination monitoring. It is pointed out that as a precursor to the at-sea application additional experiments with well-defined artificial films of different chemical structure ought to be performed.

2. Experimental arrangement and method

The wind-wave flume was open-ended, being 0.24 m wide by 0.10 m high and 0.60 m long. It contained tap water to a depth 0.3 m (see Fig. 1). A stream of air is generated using two fans (*1*, *2*) which allows forming the characteristics of the stream,

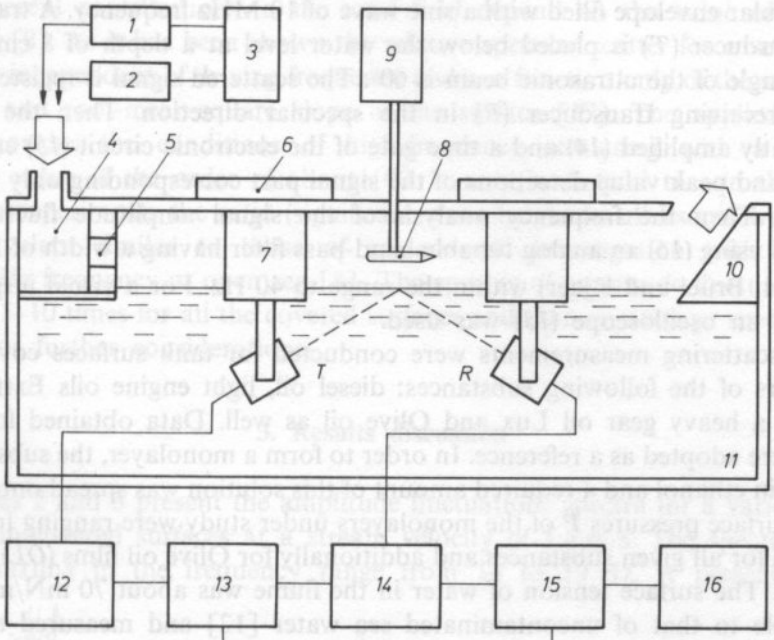

FIG. 1. Block diagram of experimental set-up. For details see text

and introduced it to the tunnel through a nozzle (*4*) equipped with several guide vanes (*5*). A supply system allows smooth adjustment of an air stream velocity up to 15 m/s. The tunnel centreline wind speed V was measured by means of a Prandtl tube (*8*, *9*) at a fetch of 0.3 m and situated directly above the point of ultrasound beam scattering. In this paper we are largely concerned with very low winds for which the flow is aerodynamically smooth, the thickness of the viscous sublayer exceeds the characteristic height of the surface waves for stream velocities below 4 m/s [23]. The opposite bank (*10*) of the channel is inclined at an angle of 40° with respect to the water surface, which significantly reduces the influence of reflected waves. An air stream causes a shear stress at the wavy surface, which results in Stokes drift and unfavourable effect of water accumulation at the end of the linear tunnels of conventional construction [4, 13, 14]. A top-side view of author's tunnel design which consists of special plexiglass shields situated on both sides of the tunnel along its entire length was presented in [19]. Shields screen a part of the surface from action of the air stream and provide the recirculating path between the end and front of the tank. Application of shields also leads to obtain a uniform surface pressure of the spread monolayer over the entire length of the tank surface. Hence, conditions created for generation of wind waves and spreading of oil films are close to natural.

An acoustic part of the experimental set-up consists of a pulse operating ultrasonic transmitter (*12*), which forms series of pulses lasting several microseconds

of rectangular envelope filled with a sine wave of 10 MHz frequency. A transmitting quart transducer (T) is placed below the water level at a depth of 8 cm, and the incident angle of the ultrasonic beam is 60°. The scattered signal is registered by an identical receiving transducer (R) in the specular direction. Then the signal is subsequently amplified (*14*) and a time gate of the electronic circuit (*15*) enables the envelope and peak value detections of the signal part corresponding only to surface scattering. Then the frequency analysis of the signal amplitude fluctuations is performed using (*16*) an analog tunable band-pass filter having a width of 1/3 octave (Type 1621, Brüel and Kjaer) within the range to 40 Hz. For a visual inspection of the signal an oscilloscope (*13*) was used.

The scattering measurements were conducted for tank surfaces covered with monolayers of the following substances: diesel oil, light engine oils Extra 15 and Hipol 15, a heavy gear oil Lux and Olive oil as well. Data obtained for a clean surface were adopted as a reference. In order to form a monolayer, the substance was dissolved in ethanol and a required amount of this solution was spread onto the tank surface. Surface pressures P of the monolayers under study were ranging from 3.4 to 4.7 mN/m for all given substances and additionally for Olive oil films (OL) at 11 and 15 mN/m. The surface tension of water in the flume was about 70 mN/m which is comparable to that of uncontaminated sea water [12] and measured as well as surface pressure of films using a Wilhelmy plate method [1], directly through the window in a roof of the tunnel. Each monolayer of a film-forming oil substance has certain viscoelastic rheological properties characterized by the surface pressure P, which represents a surface tension reduction of a clean water surface due to the film presence, by the dilational elasticity modulus E_0, and finally structural diffusion parameter w_d values. The magnitude of E_0, defined as $E_0 = -d\gamma/d\,(\ln\Gamma)$, [1], where γ – is the surface tension of studied surface and Γ – is the surface concentration of film-forming substance, depends only on a chemical nature and concentration of the material composing the film. The remaining parameter w_d is governed by the kinetics and mechanism of the rearrangement process which takes place within an insoluble oil monolayer during compression/expansion cycles [7]. $1/w_d$ corresponds to a doubled characteristic time of the relaxation phenomenon. In order to determine these parameters additional measurements were carried out in which the dynamical method proposed by LOGLIO et al. [15] was adopted. It has been shown by HÜHNERFUSS et al. [12], [13] that these values of E_0 and w_d obtained under dynamic conditions are much more suitable for describing the wave damping effect of monolayers. These investigations were performed in a Langmuir through with a Wilhelmy plate connected to a wire balance as a surface pressure sensor at the same temperature and surface pressures as encountered on the tunnel surface.

The scattering coefficient of acoustic waves can be defined as the ratio of the received intensity when the acoustic wave is reflected by surface under study to the received intensity when the wave is reflected in the specular direction by a plane surface according to BECKMANN [6]. Generally, the scattered field registered in a specular direction consists of both coherent and incoherent components. Coherent

and incoherent contributions to the total field depend on the value of Rayleigh parameter [8]. As it has been shown the relative specular scatter for a very "rough surface" is independent of driving frequency and is a function only of the experiment geometry and root-mean-square slope of the surface [17]. The applied acoustic system provides the conditions of high-frequency scattering with a Rayleigh parameter value of the order of about 100. It may be helpful to add that in the laboratory experiments the ratio (significant wave height to ultrasonic wavelength) took on values similar to those of an acoustic investigation with waves of 80 –100 kHz frequency at open sea [8]. The spectra of amplitude fluctuation were measured 5–10 times for all the covered surfaces and then an average spectrum was adopted for further considerations.

3. Results discussion

Figures 2 and 3 present the amplitude fluctuations spectra for a variety of the studied film-covered surfaces at a stream velocity of 1.4 m/s. The spectra exhibit distinct maxima in the frequency range from 14 to 19 Hz. A presence of the

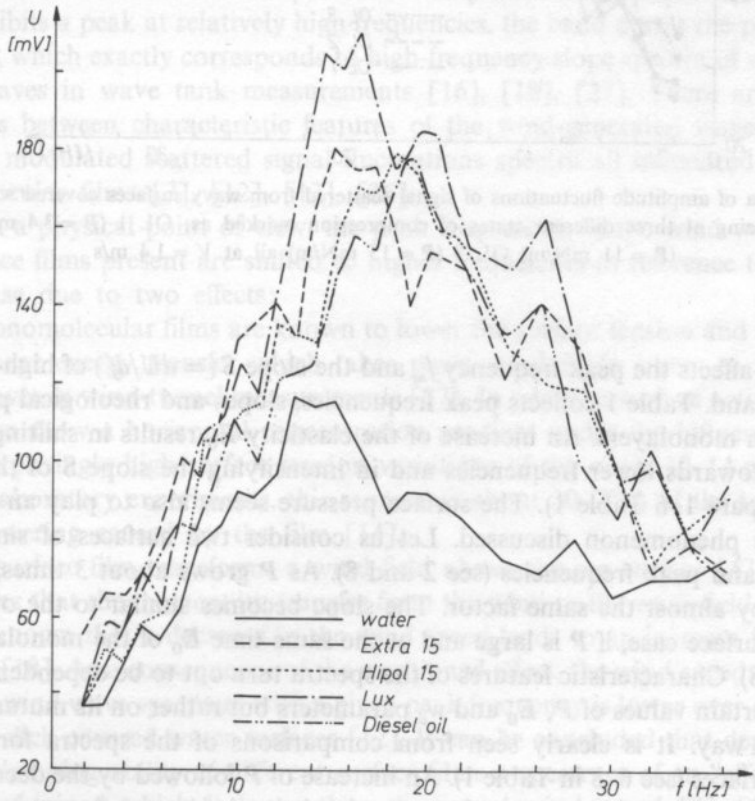

FIG. 2. Spectra of amplitude fluctuations of signal scattered from wavy surfaces covered with monolayers of chosen oil substances at $V = 1.4$ m/s. Clean water surface reference curve ——

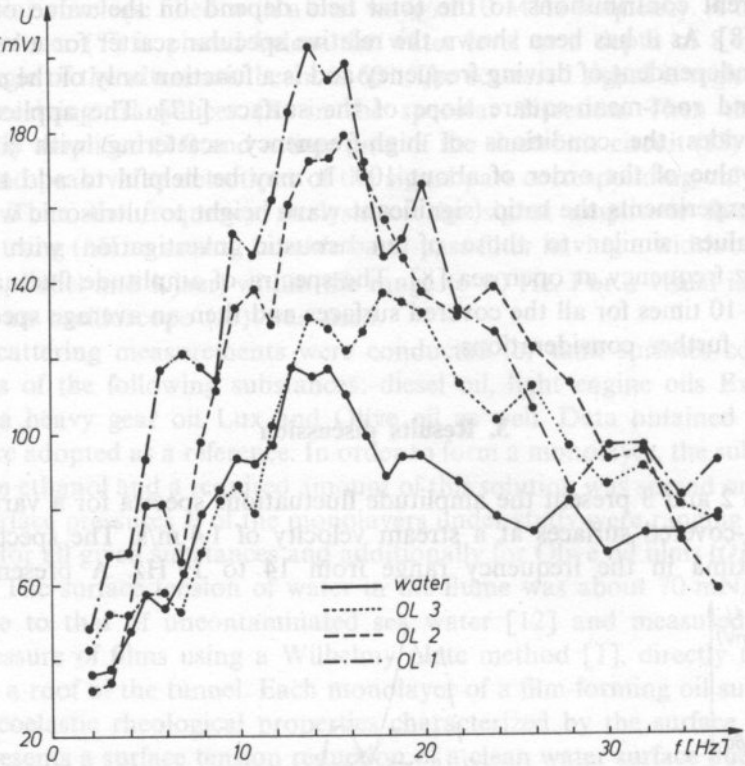

FIG. 3. Spectra of amplitude fluctuations of signal scattered from wavy surfaces covered with Olive oil monolayers being at three different states of compression marked as: OL 1 ($P = 3.4$ mN/m) OL 2 ($P = 11$ mN/m) OL 3 ($P = 15$ mN/m) all at $V = 1.4$ m/s

monolayer affects the peak frequency f_m and the slope $S(= dU/df)$ of high-frequency spectrum band. Table 1 collects peak frequencies, slopes and rheological parameters of the given monolayers. An increase of the elasticity E_0 results in shifting the peak frequency towards lower frequencies and in intensifying the slope S of the spectral band (compare 1–6 Table 1). The surface pressure seems also to play an important role in the phenomenon discussed. Let us consider two surfaces of similar both elasticities and peak frequencies (see 2 and 8). As P grows about 3 times, the slope decreases by almost the same factor. The slope becomes similar to the observed in the clean surface case, if P is large and at the same time E_0 of the monolayer is low (see 1 and 8). Characteristic features of the spectra turn out to be dependent not only on given certain values of P, E_0 and w_d parameters but rather on its mutual ratios in a complex way. It is clearly seen from comparisons of the spectra for Olive oil covered surfaces (see 6–8 in Table 1). An increase of P followed by the decrease of E_0 results in lowering of the mean spectrum level, in shifting of the peak frequency

Tab. 1 Peak frequencies f_m and high-frequency band slopes S of measured spectra versus viscoelastic properties of the spread oil substance monolayers. *SD* – standard deviation

SUBSTANCE	P [mN/m]	E_0 [mN/m]	w_d [10^{-3} rad/s]	f_m [Hz]	S [mV/Hz] (SD)
1 water	–	–	–	14.0	−2.10 (0.17)
2 Diesel oil	4.4	9.8	0.97	18.8	−8.0 (0.56)
3 Hipol 15	4.7	10.0	0.59	18.0	−8.18 (0.49)
4 Extra 15	3.9	13.5	1.02	16.0	−6.67 (0.46)
5 Lux	4.1	14.5	1.08	15.0	−10.0 (0.76)
6 OL 1	3.4	16.0	0.43	14.5	−8.0 (0.42)
7 OL 2	11.0	13.0	"	16.4	−5.31 (0.29)
8 OL 3	15.0	8.0	"	18.2	−2.73 (0.22)

towards higher frequencies, and in a drop of S to the value observed for the clean surface case. One can note that a spectrum of amplitude fluctuations of the scattered signal exhibits a peak at relatively high frequencies, the band above the peak follows an $1/f$ law, which exactly corresponds to high-frequency slope spectra of wind-driven surface waves in wave tank measurements [16], [18], [27]. There are apparent similarities between characteristic features of the wind-generated waves and low-frequency modulated scattered signal fluctuations spectra all influenced by surface monomolecular films [7], [12], [13], [26].

From a physical point of view, the peak frequencies of the wind wave spectra with surface films present are shifted to higher frequencies in reference to the clean surface case due to two effects:

1. Monomolecular films are known to lower the surface tension and thus affects the nonlinear energy transfer which takes place via 5–9 Hz waves to longer and shorter waves in wind-tunnel measurements [27]. In addition surface active films are expected to show a horizontal concentration gradient under the influence of wave action. Surprisingly high surface tension variations of the order 12–14 mN/m were found in laboratory experiments, this represents about 30–70% of the total surface tension lowering caused by the film [14].

2. A surface film transforms a wind field above the sea surface [5], [9], [26]. This implies that the momentum transfer from the wind to the wave field is lowered. It is well known that a decrease in the wind speed leads to an increase in the peak frequency [18]. As a consequence of the mentioned effect, the wind speed required to produce a wind wave spectrum with a given peak frequency is lower over clean water than over slick-covered water surfaces [12]. It can be concluded that depending on the wave damping ability of different surface films a spectrum of an "effective wind speed" is obtained which is lower than the actual wind speed [3], [13].

4. Conclusions

The presence of an oil substance monolayer spread onto a wavy water surface affects the peak frequency and slope of the high-frequency band of the scattered signal amplitude fluctuations spectrum. The effect is unequivocally related to the viscoelastic rheological properties of the film.

Taking together reported apparent similarity between the wind wave spectra and amplitude fluctuations spectra of scattered acoustic signals, if influenced by surface oil derivative films, the observed peak frequency shift might be a measure of the covered surface susceptibility to deformation caused by an air stream.

It is of course too early to deduce the physicochemical surface films characteristics by remote sensing acoustic methods based on the presented results, but the method appears to be a feasible approach. However, it has to be stressed that additional experiments with well-defined artificial sea slicks have to be performed.

Acknowledgements

The author wishes to thank Profs. R. CINI and G. LOGLIO at the University of Florence, Italy and Drs. P. LANGE and H. HÜHNERFUSS at the University of Hamburg, F. R. Germany for stimulating discussions.

This work was carried out in the framework of the research programme CPBP 02.03/II/2.16, coordinated by the Polish Academy of Sciences.

References

[1] A. W. ADAMSON, *Physical Chemistry of Surfaces*, Wiley, New York 1982.

[2] W. ALPERS, H-J. BLUME, W. D. GARRETT, H. HÜHNERFUSS, *The effect of monomolecular surface films on the microwave brightness temperature of the sea surface*, Int. J. Remote Sensing **3**, 457–474 (1982).

[3] W. ALPERS, H. HÜHNERFUSS, *Radar signatures of oil films floating on the sea surface and the Marangoni effect*, J. Geophys. Res. **93**, C4, 3642–3648 (1988).

[4] W. ALPERS, H. HÜHNERFUSS, *The damping of ocean waves by surface films: A new look at an old problem*, J. Geophys. Res. **94**, C5, 6251–6265 (1989).

[5] W. R. BARGER, W. D. GARRETT, E. L. MOLLO-CHRISTENSEN, K. W. RUGGLES, *Effects of an artificial sea slick upon the atmosphere and the ocean*, J. Appl. Meteorol. **9**, 196–400 (1970).

[6] P. BECKMANN, A. SPIZZICHINO, *The Scattering of electromagnetic waves from rough surfaces*, Mc Millan, New York 1963, p. 22–23.

[7] R. CINI, P. P. LOMBARDINI, H. HÜHNERFUSS, *Remote sensing of marine slicks utylizing their influence on wave spectra*, Int. J. Remote Sensing **4**, 101–110 (1983).

[8] C. S. CLAY, H. MEDWIN, *Acoustical Oceanography: Principles and applications*, Wiley, New York 1977.

[9] S. A. ERMAKOV, A. M. ZUJKOVA, A. R. PANCHENKO, S. G. SALASHIN, T. G. TALIPOVA, V. I. TITOV, *Surface film effect on short wind waves*, Dyn. Atoms. Oceans **10**, 31–50 (1986).

[10] B. FISCELLA, P. P. LOMBARDINI, P. TRIVERO, P. PAVESE, R. CINI, *Measurements of the damping effect of a spreading film on wind-excited sea ripples using a two-frequency radar*, Il Nuovo Cimento **8C**, 175–183 (1985).

[11] H. HÜHNERFUSS, W. ALPERS, A. CROSS, W. D. GARRETT, W. C. KELLER, P. A. LANGE, W. J. PLANT, F. SCHLUDE, D. L. SCHULER, *The modification of X and L band radar signals by monomolecular sea slicks*, J. Geophys. Res. **88**, C11, 9817–9822 (1983).

[12] H. HÜHNERFUSS, W. ALPERS, P. A. LANGE, W. WALTER, *Attenuation of wind waves by artificial surface films of different chemical structure*, J. Geophys. Res. Lett. **8**, 1184–1186 (1981).

[13] H. HÜHNERFUSS, W. WALTER, P. LANGE, W. ALPERS, *Attenuation of wind waves by monomolecular sea slicks and the Marangoni effect*, J. Geophys. Res. **92**, C4, 3961–3963 (1987).

[14] P. A. LANGE, H. HÜHNERFUSS, *Horizontal surface tension gradients induced in monolayers by gravity water wave action*, J. Phys. Oceanogr. **14**, 1620–1628 (1984).

[15] G. LOGLIO, U. TESEI, R. CINI, *Viscoelastic dilatation processes of fluid/fluid interfaces: time-domain representation*, Colloid Polymer Sci. **264**, 712–718 (1986).

[16] S. C. LUBARD, J. E. KRIMMEL, L. R. THEBAUD, D. D. EVANS, H. SHEMDIN, *Optical image and laser slope meter intercomparisons of high-frequency waves*, J. Geophys. Res. **85**, 4996–5002 (1980).

[17] H. MEDWIN, *Specular scattering of underwater sound from a wind-driven surface*, J. Acoust. Soc. Am. **41**, 1485–1495 (1967).

[18] H. MITSUYASU, *Measurement of the high-frequency spectrum of ocean surface waves*, J. Phys. Oceanogr. **7**, 882–891 (1977).

[19] S. J. POGORZELSKI, *Statistics of underwater acoustic signals scattered by the rough water surface covered with a layer of oil substances*, Oceanologia **27**, 47–62 (1989).

[20] S. J. POGORZELSKI, *Detection of oil-derivative contamination of water surfaces by statistical analysis of scattered acoustical signals*, J. Acoust. Soc. Am. **85**, 2383–2387 (1989).

[21] S. J. POGORZELSKI, *An investigation of ultrasound scattering from the sea surface influenced by oil pollutants*, *Proc. of* the 6th Symposium on Hydroacoustics, p. 253–260, Gdańsk 1989 (in Polish).

[22] S. J. POGORZELSKI, *Remote sensing of the sea oil pollution by means of high-frequency surface scattering*, Archives of Acoustics **15**, 437–446 (1990).

[23] H. SCHLICHTING, *Boundary-layer theory*, Mc Graw-Hill, New York 1968.

[24] A. H. SCHOOLEY, *Profiles of wind-created water waves in the capillary-gravity transition region*, J. Mar. Res. **16**, 100–108 (1958).

[25] I. TOLSTOY, C. S. CLAY, *Ocean acoustics*, Mc Graw-Hill, New York 1966.

[26] J. WU, *Suppression of oceanic ripples by surfactant-spectral effects deduced from sun-glitter, wave staff and microwave measurements*, J. Phys. Oceanogr. **19**, 238–245 (1989).

[27] H. Y. WU, E. Y. HSU, R. L. STREET, *Experimental study of nonlinear wave-wave interaction and white-cap dissipation of wind-generated waves*, Dyn. Atmos. Oceans **3**, 55–78 (1979).

Received January 12, 1990

ARCHIVES OF ACOUSTICS
16, 3–4, 581–590 (19991)

ACOUSTIC RADIATION OF CIRCULAR PLATE INCLUDING THE ATTENUATION EFFECT AND INFLUENCE OF SURROUNDINGS

W. RDZANEK

Institute of Physics of Pedagogical College
35-310 Rzeszów, ul. Rejtana 16a

This paper presents an analysis of the acoustic power of a thin circular plate, which includes internal dissipation in the plate's material and the influence of the acoustic wave radiated by the plate on it's vibrations. A fully fixed plate was accepted, which vibrates in a rigid and flat acoustic baffle under the influence of a definite external pressure, sinusoidal in terms of time, and radiates into a lossless and homogeneous liquid medium. The factor which forced vibrations was accepted as fixed. The acoustic power was calculated on the basis of the known distribution of vibration velocity into a series of eigenfunctions. The power radiated by the plate was expressed in the form of a strongly convergent series, so the frequency characteristics could be determined. Also the effect of the plate's internal attenuation was estimated, as well as the influence of the acoustic field radiated by the plate on the modification of its vibrations.

1. Introduction

At the present stage of development of experimental and technical acoustics, theoretical investigations should be aimed at the analysis of models representing more closely actual vibrating systems. This means that the analysis of acoustic power radiated by a circular plate should include the effect of attenuation inside the plates material and the influence of the acoustic wave, generated by the plate, on the form of its vibrations.

The problem of acoustic power radiated by a thin circular plate has been given particular attention in the present decade. In paper [3] the author has analysed acoustic power of single axially-symmetric vibration modes of a circular plate for high frequencies. LEVINE and LEPPINGTON [1] have considered this subject in greater detail and included the term defining the oscillating character in the expression for the real component of power. Paper [4] presents acoustic interaction of the field radiated by a circular plate. It also contains an analytical assesment of mutual resistance for high frequencies. The acoustic power of a plate, including the factor

forcing vibrations, but excluding losses and the influence of associated vibrations of the air column, has been considered in paper [5].

From among classical problems of generation and propagation of acoustic waves this paper takes up the problem of acoustic power of a thin circular plate, including the attenuation effect and the influence of the acoustic wave radiated by the plate on its vibrations. The external pressure, displacement and velocity of plates vibrations were expressed with familiar distributions into serieses with respect to a complete system of eigenfunctions. As a result, acoustic power was given in the form of a series with 3 expansion coefficients forming a system of linear algebraic equations. In a wide frequency range expansion coefficients can be calculated with the application of the method of successive approximations, for example.

Results of numerical calculations of the acoustic power, including the effect of internal attenuation and the influence of the acoustic field of the radiating plate on the form of its vibrations, are also presented in graphical form.

2. Assumptions of analysis

A fixed thin circular plate, excited to vibrate by an external pressure $\mathrm{Re}[f(r)\exp(-i\omega t)]$ for $0 \leqslant r \leqslant a$, is placed in a liquid medium with rest density ϱ_0 in a flat and rigid acoustic baffle. The analysis is based on the equation of vibrations (see [2])

$$B_0 \nabla^4 \eta(r, t) + M \frac{\partial^2 \eta(r, t)}{\partial t^2} = f(r, t) - R \frac{\partial}{\partial t}[\nabla^4 \eta(r, t)] - 2p(r, t) \tag{1}$$

where: η is the transverse dislocation of a point on the plates surface, R – loss of plates material, M – plates mass per surface unit, B_0 – plates bending rigidity, $p(r, t)$ – acoustic pressure radiated by plate for $z = +0$. Because accepted processes are sinusoidal with respect to time, we have: $p(r) = ip_0 \omega \varphi(r)$, $v(r) = -i\omega\eta(r)$, and instead of Equation (1) we obtain the following equation of vibrations [1]

$$(\nabla^4 k_p^{-4} - 1) v(r) + 2\varepsilon_1 k_0 \varphi(r) = -\frac{i}{M\omega} f(r) \tag{2}$$

where: $\varphi(r)$ is the amplitude of the acoustic potential, $B = B_0(1 - i\omega R/B_0)$, $\varepsilon_1 = \varrho_0/(Mk_0)$, $k_0 = 2\pi/\lambda$, $k_p^4 = M\omega^2/\beta$.

The velocity of the plates vibrations is presented in the form of a series

$$v(r) = \sum_n c_n v_n(r) \tag{3}$$

where

$$v_n(r) = v_{0n}\left[J_0(\gamma_n r/a) - \frac{J_0(\gamma_n)}{I_0(\gamma_n)} I_0(\gamma_n r/a)\right]$$

for $v_{0n} = [a]\, J_0(\gamma_n)]^{-1}$ presenting the complete, orthonormal system of eigenfunctions of a homogeneous equation $(\nabla^4 k_n^{-4} - 1)\, v_n = 0$, while $\gamma_n = k_n a$ is a solution to the frequency equation $J_0(\gamma_n) I_1(\gamma_n) + J_1(\gamma_n) I_0(\gamma_n)$, $n = 1, 2, \ldots$. (see [2, 3]).

Expansions coefficients c_n are determined from a system of algebraic equations [1]

$$c_n \left(\frac{k_n^4}{k_p^4} - 1 \right) - 2\varepsilon_1 \sum_m i\zeta_{mn} c_m = f_n \tag{5}$$

where

$$f_n = -\frac{i}{M\omega} \int_0^a f(r) v_n(r) r dr \tag{6}$$

while [1, 4]

$$\zeta_{mn} = 4\gamma_m^3 \gamma_n^3 \int_0^\infty \frac{x}{\gamma} \left(\frac{a_m J_0(x) - x/\gamma_m J_1(x)}{x^4 - \gamma_m^4} \right) \left(\frac{a_n J_0(x) - x/\gamma_n J_1(x)}{x^4 - \gamma_n^4} \right) dx \tag{7}$$

is an expression for the normalized mutual impedance of axially-symmetrical modes of the same circular plate in a case of free vibrations. Quantity γ is defined as follows:

$$\gamma = [1 - (x/k_0 a)^2]^{1/2} \quad \text{for } 0 \leqslant x \leqslant k_0 a \text{ and } \gamma = i[(x/k_0 a^2) - 1]^{1/2}$$

for $k_0 a \leqslant x < \infty$ while $a_n = J_1(\gamma_n)/J_0(\gamma_n)$.

3. Calculation of acoustic power

The acoustic power of the vibrating system under consideration is calculated according to definition

$$N = 1/2 \int_\sigma p(r) v^*(r) d\sigma \tag{8}$$

where [3]

$$p(r) = \varrho_0 c k_0^2 \int_0^{\pi/2 - i\infty} J_0(k_0 r \sin\vartheta) \left[\int_0^a v(r_0) J_0(k_0 r_0 \sin\vartheta) r_0 dr_0 \right] \sin\vartheta d\vartheta \tag{9}$$

quantity c is the velocity of wave propagation in a medium with density ϱ_0 and $v(r_0)$ is calculated from formula (3).

The characteristic function of a circular plate for a spherical distribution of velocity of vibrations (3) is defined as follows [4]:

$$W(\vartheta) = \Sigma c_n W_n(\vartheta) \tag{10}$$

where

$$W_n(\vartheta) = \int_0^a v_n(r_0) J_0(k_0 r_0 \sin\vartheta) r_0 dr_0 \tag{10'}$$

is the plates partial characteristic function, i.e. when the plate is excited to vibrate with free vibrations $v_n(r_0)$ for an axially-symmetric mode of vibrations $(0, n)$. After integrating (10') we obtain

$$W_n(\vartheta) = 2a\gamma_n^3 \frac{a_n J_0(x) - x/\gamma_n J_1(x)}{\gamma_n^4 - x^4} \tag{10''}$$

where $x = k_0 a \sin\vartheta$.

The acoustic power (8) is equal to

$$N = \pi\varrho_0 c k_0^2 \sum_n \sum_s c_n c_s^* \int_0^{\pi/2 - i\infty} W_n(\vartheta) W_s^*(\vartheta) \sin\vartheta d\vartheta \tag{11}$$

or finally, after expressions (10'') and (7) are included, we reach

$$N = \varrho_0 c\pi \sum_n \sum_s c_n c_s^* \zeta_{ns}. \tag{11'}$$

This expression is converge convenient for numerical calculations, because the series are very strongly convergent with respect to values of normalized impedances ζ_{ns}. A detailed analysis and methods of calculating quantity ζ_{ns} in specific cases are presented in papers [1, 3] and [4].

It is convenient to use the convenient to use the notion of relative acoustic power N/N_0 in numerical calculations, where N_0 denotes the plates active power for $k_0 \to \infty$. If $k_0 \to \infty$, then $p(r) = \varrho_0 c v(r)$, hence on the basis of formula (8) we have

$$N_0 = \pi\varrho_0 c \int_0^a v^2(r) r dr, \tag{12}$$

and in a case of velocity of vibrations (3)

$$N_0 = \pi\varrho_0 c \sum_n c_n^2. \tag{12'}$$

Also a representation for acoustic power different from expression (11') is possible. Both sides of the system of Equations (5) are multiplied by c_s^* and summed up with respect to index s, and expression (11') is used, then we finally obtain the following formula for the acoustic power of a circular plate

$$N = \frac{i\varrho_0 c\pi}{2\varepsilon_1} \sum_n \left[c_n^* f_n - c_n^2 \left(\frac{k_n^4}{k_p^4} - 1 \right) \right]. \tag{13}$$

In comparison to expression (11') this formula is less convenient for numerical calculations, because the series occuring here is slowly convergent in general.

4. Numerical example

The acoustic power of a circular plate was numerically calculated under the assumption that the amplitude distribution of the external pressure exciting the plate to vibrate has the following (from see [5]):

$$f(r) = \begin{cases} f_0 & \text{for } 0 < r < a_0 \\ 0 & \text{for } a_0 < r < a \end{cases} \tag{14}$$

where $f_0 = \text{const}$. In this case according to definition (6) the n Fourier coefficient f_n is equal to

$$f_n = -i\frac{af_0\varepsilon_0}{M\omega}\frac{J_1(\varepsilon_0\gamma_n)}{\gamma_n J_0(\gamma_n)}\left[1+\frac{J_1(\gamma_n)}{J_1(\varepsilon_0\gamma_n)}\frac{I_1(\varepsilon_0\gamma_n)}{I_1(\gamma_n)}\right] \tag{15}$$

where $\varepsilon_0 = a_0/a$.

If the entire surface of the plate is excited to vibrate by a factor not equal to zero, then for $a_0 = a$ we have

$$f_n = -i\frac{2af_0}{M\omega}\frac{a_n}{\gamma_n}. \tag{15'}$$

The acoustic power was calculated from formula (11') and Fourier coefficients c_n were calculated from the system of equations (5). For a wide frequency range coefficients c_n can be calculated with approximate methods, e.g. method of successive approximations. In the case under consideration it was sufficient to limit calculations to the (2) approximation, and to the first few terms of expansion in formula (5) ($n, s \leqslant 4$).

The notion of relative apparent power was applied in numerical calculations and graphical illustrations, i.e. apparent power $N' = [N_x^2+N_y^2]^{1/2}$ is related to quantity $N_0' = \pi a^2 \varrho_0 c(f_0/M\omega_1)^2$, where $N = N_x - iN_y$. The influence of the interaction of the acoustic field radiated by the plate on the form of its vibration is characterized with the constant $\varepsilon_1' = 2\varrho_0 c/(M\omega_1)$ while $\varepsilon_1 = 0.5\varepsilon_1'\omega_1/\omega$ $\omega_1 = \sqrt{B_0/M}(\gamma_1/\mathrm{a})^2$. The quantity $\varepsilon_2' = \omega_1 R/B_0$, was accepted as the measure of internal attenuation in the plates material. Also parameter $b = k_0 a/(ka)^2$ $= (h/2a)\cdot\sqrt{E/[3\varrho c^2(1-\nu^2)]}$, was introduced. It characterizes the quotient of the plates thickness h to its diameter $2a$, E is the Young's modulus ϱ – density of plate's material, ν – Poisson's ratio. This parameter has a limited top value, because of the analysis of the problem for thin plates and adequate values of material constants.

The numerical example includes several different values of the a_0/a parameter. This makes it possible to estimate the effect of the external pressure, which forces vibrations, on the value of radiated power. Also such a_0/a values were chosen which correspond with the plates volumetric displacements equal to zero. These values are equal to 0.5995, 0.7373, 0.4064, respectively for the second and third resonance frequency.

5. Conclusions

Expressions for acoustic power radiated by a thin circular plate were derived within the performed theoretical analysis.

They included:

1) external pressure forcing the plates vibrations,

2) effects of internal dissipation,

3) the influence of the acoustic wave, radiated by the plate on the form of its vibrations.

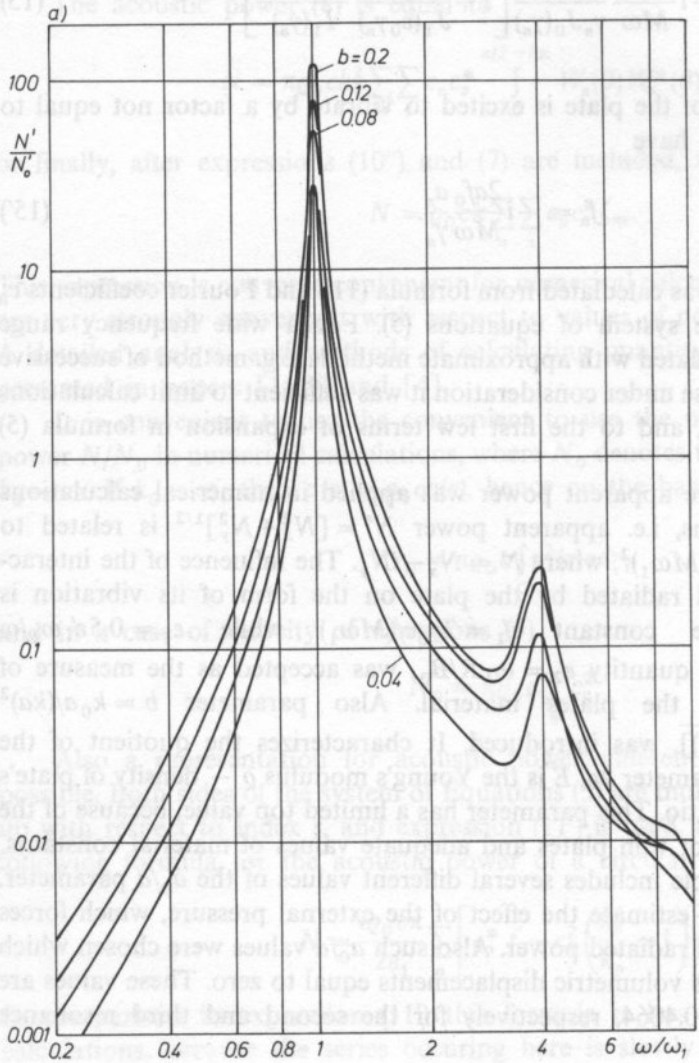

FIG. 1. Relative frequency characteristics of apparent power (a) and power factor (b) of circular plate. For $a_0/a = 1$, $\varepsilon_1' = 0$, $\varepsilon_2' = 0.05$

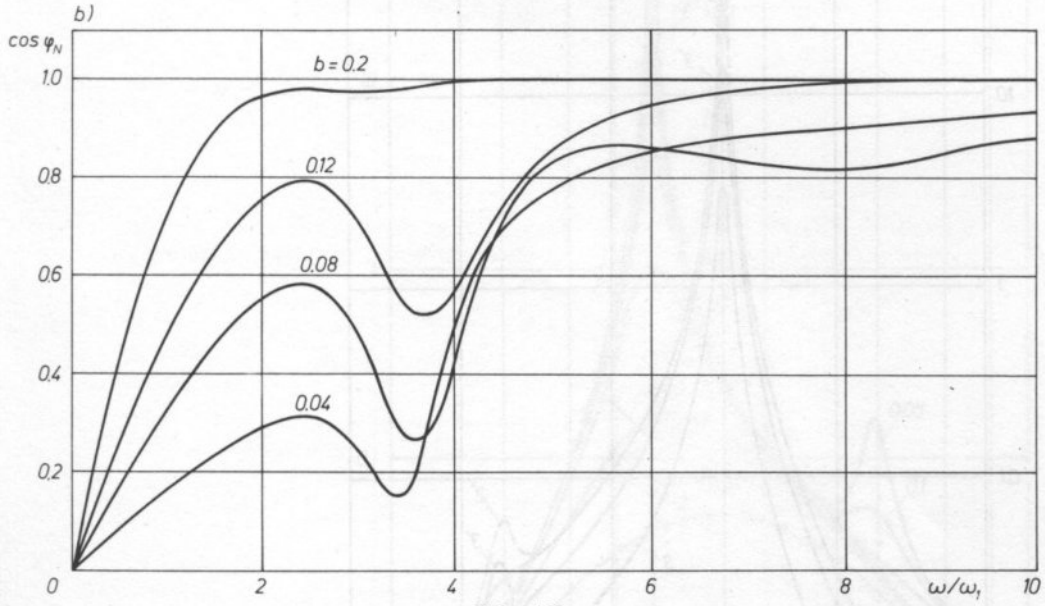

[Fig. 12]

The value of radiated power is significantly depend upon the distribution of the external pressure, which forces the plates vibrations. The analysed example proves that an increase of the central surface excited to vibrate is accompanied by an increase of the value of radiated power (see Figs. 2 a, b).

It was stated that the frequency characteristics of radiated power (Figs. 1 a, b) depends on the plates thickness, its diameter and material constants. An increase of the value of acoustic power accompanies and increase of the quotient $h/2a$ in the range between zero and the second resonance frequency. Frequency bands with radiation efficiency decreasing for a definite value of parameter b are distinctly outlined.

A clear influence of internal attenuation on the radiated acoustic field occurs for bands around resonance frequencies (see Figs. 2 and 3). The influence of attenuation decays for volumetric displacement of the vibrating plate equal to zero (curve 1 in Figs. 2a, b).

Attenuation resulting from the interaction of the acoustic wave radiated by the plate has a minor effect. A narrow band near the first resonance frequency is an exception. Damping of the fluid medium, surrounding the plate, influence the value of the radiated energy of the acoustic field in this band. (see Fig. 4).

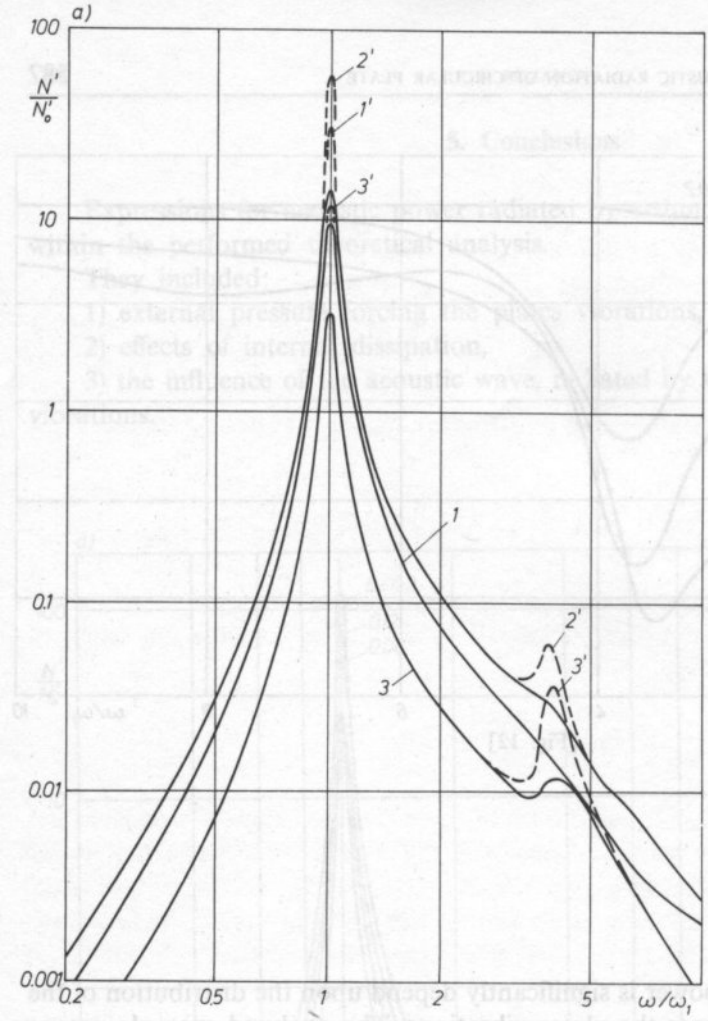

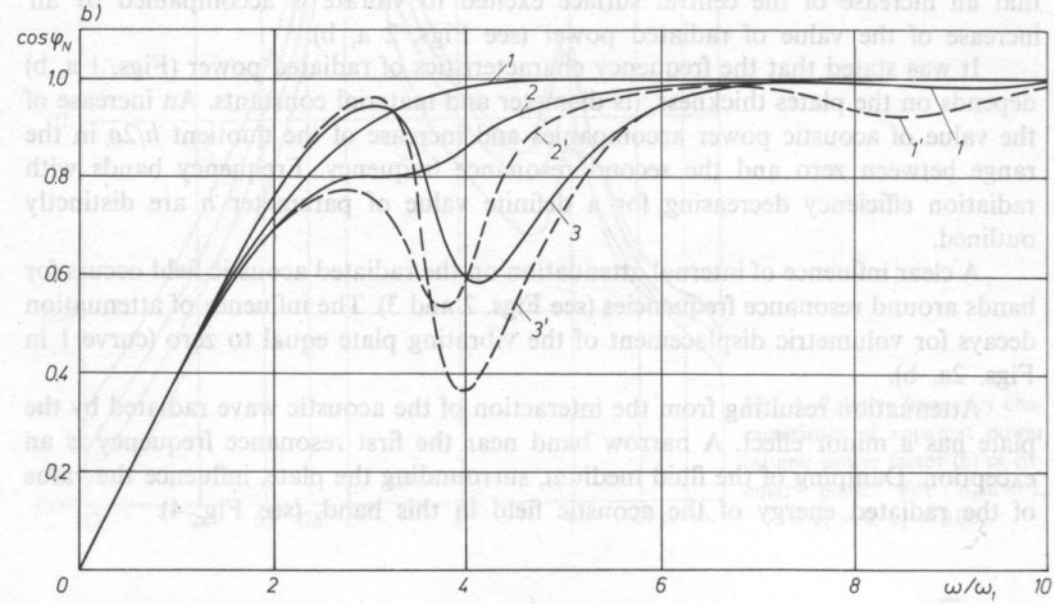

FIG. 2. Relative frequency characteristics of apparent power (a) and power factor (b) of circular plate. For $b = 0.1$; $\varepsilon_1' = 0$ 1 — $a_0/a = 0.5995$; 2 — $a_0/a = 0.7373$; 3 — $a_0/a = 0.4064$ – – – – – – $\varepsilon_2' = 0.05$ —— $\varepsilon_2' = 0.1$

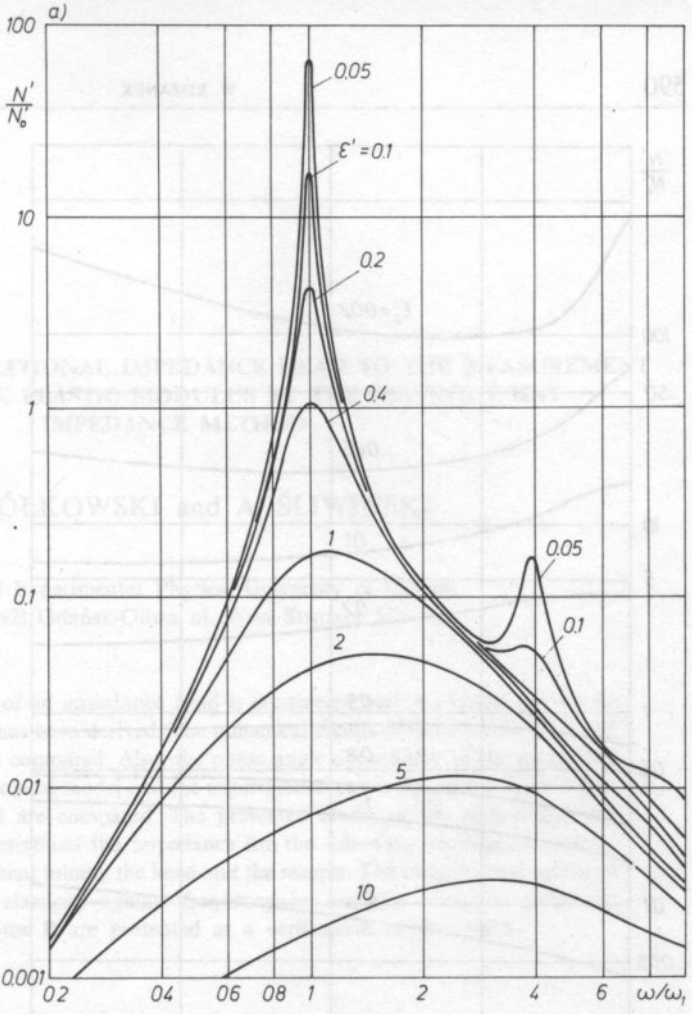

FIG. 3. Relative frequency characteristics of apparent power (*a*) and power factor (*b*) of circular plate. For: $a_0/a = 1$; $b = 0.1$; $\varepsilon_1' = 0$

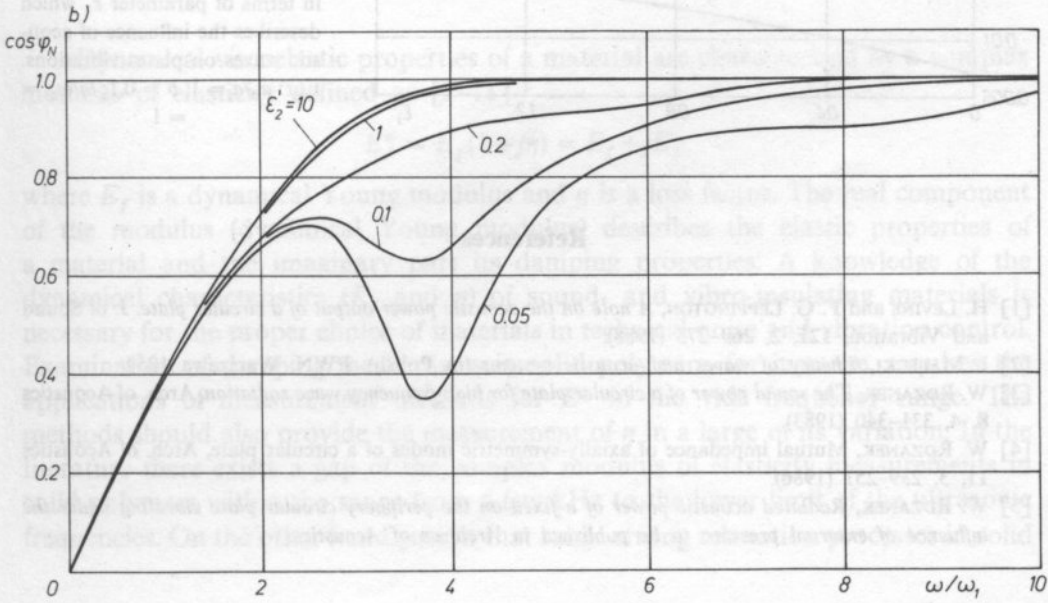

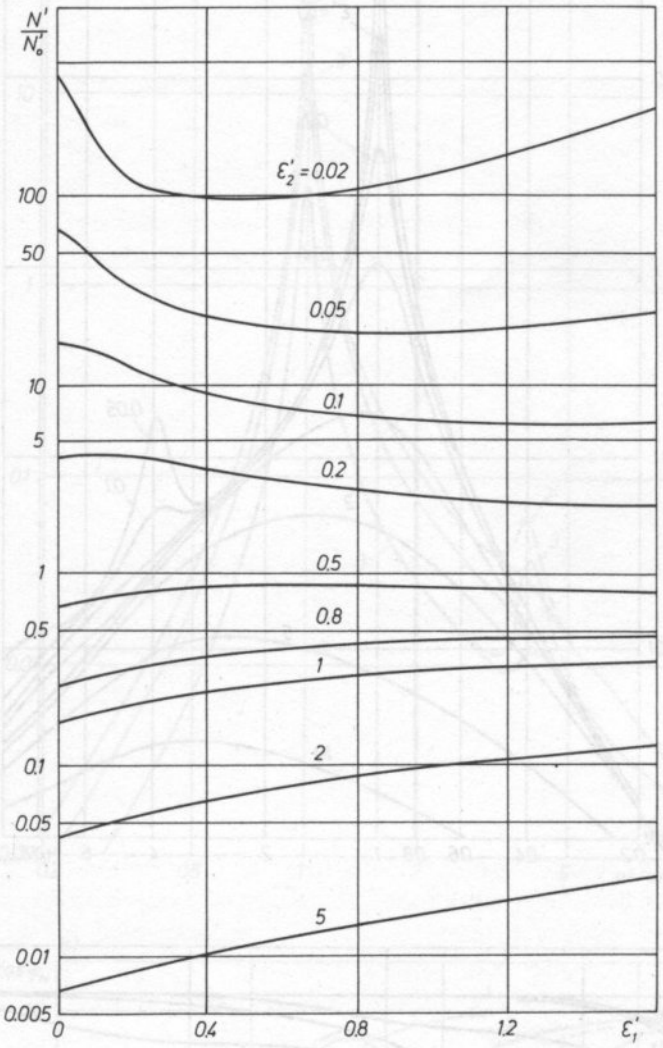

FIG 4. Relative apparent power in terms of parameter ε_1' which describes the influence of acoustic waves on plates vibrations. For: $a_0/a = 1$, $b = 0.1$; $\omega/\omega_1 = 1$

References

[1] H. LEVINE and F. G. LEPPINGTON, *A note on the acoustic power output of a circular plate.* J. of Sound and Vibration, **121**, 2, 269–275 (1988).

[2] I. MALECKI, *Theory of waves and acoustic systems* (in Polish), PWN, Warszawa 1964.

[3] W. RDZANEK, *The sound power of a circular plate for high-frequency wave radiation*, Arch. of Acoustics **8**, 4, 331–340 (1983).

[4] W. RDZANEK, Mutual impedance of axially-symmetric modes of a circular plate, Arch. of Acoustics **11**, 3, 239–251 (1986).

[5] W. RDZANEK, *Radiated acoustic power of a fixed on the periphery circular plate vibrating under the influence of external pressure to be published in Archives of Acoustics.*

ARCHIVES OF ACOUSTICS
16, 3–4, 591–607 (1991)

APPLICATION OF A VIBRATIONAL IMPEDANCE HEAD TO THE MEASUREMENT OF THE COMPLEX ELASTIC MODULUS BY THE DRIVING POINT IMPEDANCE METHOD

W. ZIÓŁKOWSKI and A. ŚLIWIŃSKI

Institute of Experimental Physics, University of Gdańsk
(80-952) Gdańsk-Oliwa ul. Wita Stwosza 57)

A rheological model of an impedance head is considered and the expression for its mechanical impedance Z_H has been derived. The numerical results of the modulus $|Z_H|$ and the experimental data were compared. Also, the phase angle dependence of the measuring head Φ_{num} for a given rheological model and the experimental curve Φ_{exp} of the Brüel-Kjaer type 8001 impedance head are compared. The presented model of the measuring head impedance was used to determine the impedance for the following mechanical system: beam–measuring head–element joining the head and the sample. The experimental results of the complex modulus of elasticity against frequency for samples of a few polymers: plexiglass, PVC and Razotex B are presented as a verification of the model.

1. Introduction

Dynamical viscoelastic properties of a material are characterized by a complex modulus of elasticity defined as [1–11]

$$E_f^* = E_f(1+j\eta) = E_f + jE'_f$$

where E_f is a dynamical Young modulus and η is a loss factor. The real component of the modulus (dynamical Young modulus) describes the elastic properties of a material and the imaginary part its damping properties. A knowledge of the dynamical characteristics (E_f and η) of sound- and vibro-insulating materials is necessary for the proper choice of materials in technical noise and vibration control. Examination of damping mechanisms in solid polymers, for instance, requires the applications of measurement methods for E^* in the vide frequency range. The methods should also provide the measurement of η in a large of its variation. In the literature there exists a gap of the complex modulus of elasticity measurements in solid polymers within the range from a few kHz to the lower limit of the ultrasonic frequencies. On the other hand, just in that range strong relaxation processes in solid

polymers are observed due to the macromolecular structure of a polymer. For this reason, a good and reliable method of the complex modulus of elasticity with the possibility of evaluating exactly the experimental errors seemed to be necessary and useful.

The point impedance of a beam method permits to determine the complex modulus of elasticity in the relatively wide range of frequency, namely between 20–15000 Hz and to obtain η values in the range of 10^{-4}–1.0. Theoretical considerations on the application of the method based on the Bernoulli-Euler beam theory were performed by J. C. SNOWDOWN [3]. His results have been applied in the experimental method for measurements of visco elastic beams using the impedance head [1, 2]. In the paper [2] the influence of the inaccuracy in determining the midpoint position of a beam sample on the measurement of the complex elastic modulus E^* when using the driving sinusoidal force in the point impedance method was discussed in details. Now, the possibilities and limits of the method will be considered. In particular, two problems are important to determine the complex elasticity modulus of the beam, namely, the influence of the mechanical impedance and the phase angle of the measuring head. In the paper the numerical results for $|Z_u|$ and Φ_n as a function of the nondimensional parameter $(na) \sim \sqrt{\omega}$ for large values of the loss factor are presented.

In the theoretical considerations an approximative rheological model of the impedance head was applied and experimentally verified. The impedance head model was implemented in further considerations to determine the mechanical impedance of the total system: the beam sample, the impedance head including the element joining the head and the sample. Consequently, the formulas for the modulus and the phase angle of the impedance of the system were derived. In the experimental part the measuring setup is described and the results are presented together with the error evaluation.

2. Theory and numerical results

The mechanical point impedance of the system: beam sample-impedance head Z_u is the sum of the beam point impedance Z_0 [1, 3] and the head impedance Z_H at the driving point (Fig. 1):

$$Z_u = Z_0 + Z_H \tag{1}$$

The measurement method for small values of the loss factor of viscoelastic beams driving by a sinusoidal force to excite bending vibrational modes was described

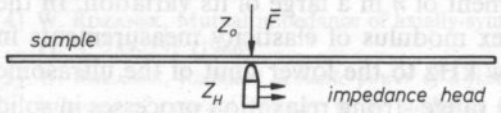

FIG. 1. The system: sample – impedance head

in the papers [1, 2]. The influence of the reactant mass of the support situated above the force transducer of the impedance head on the determination of E^* was discussed. In the case of samples of larger values of the mechanical impedance modulus $|Z_0|$ for the (antyresonance frequencies or for samples having masses much larger than the mass situated above the force transducer of the head), the influence of the reactant mass can be neglected. In the case when the ratio of those masses is significant, the component Z_H becomes comparable to the component Z_0 and neglecting Z_0 leads to great errors in determining the complex modulus of elasticity. The error is the greatest when the measurement takes place for the resonance frequency. For the measurement at the antyresonance frequencies, the error is about 10% when $\left|\frac{Z_H}{Z_u}\right| < 0.1$.

2.1. *The mechanical impedance of the measuring head*

The subject of the theoretical analysis as well as the examinations was the Bruel and Kjaer type 8001 impedance head. In the head the piezoelectric element is joined with a movable support of the mass of 10^{-3} kg. The support is connected elastically with the head casting with a silicon rubber ring. Its influence is not only the kind of the mass; also, its elasticity and viscosity play an important role. When masses of samples are several times greater than the mass of the movable support, the influence of the impedance of the tightening ring on the accuracy of determination of the loss factor η, as will be seen, is essential, particularly when it is measured for resonance frequencies. The producer of the head does not say anything about the influence of that ring on the phase characteristics and as far as the authors know there is nothing to find on the matter in the literature.

The approach which takes into account the additional influence of the impedance of the ring in the total impedance of the head gives reasons for the necessity to enlarge the measuring range of the complex modulus of elasticity in the frequency range, particularly in higher frequencies. In experiments very thin samples (about 10^{-3} m) and narrow (10^{-2} m) are used. The limits of lateral dimensions of a sample result from the assumptions of the Bernoulli-Euler theory for bending waves of a beam [1]. The small mass of samples becomes comparable with the mass of the element above the force transducer and the tightening ring of the head. Therefore, the mechanical impedance of the head must be taken into account when measuring the mechanical impedance of the sample-beam.

The mechanical impedance of the head can be described by the system of rheological elements a spring, a mass and a damper connected by the way presented in Fig. 2.

The ring tightening the impedance head is fixed to the edge of a movable mass M_p situated above the piezoelectric element and can be treated as a dynamic absorber. The mechanical impedance of the ring (dynamic absorber) Z_R can be

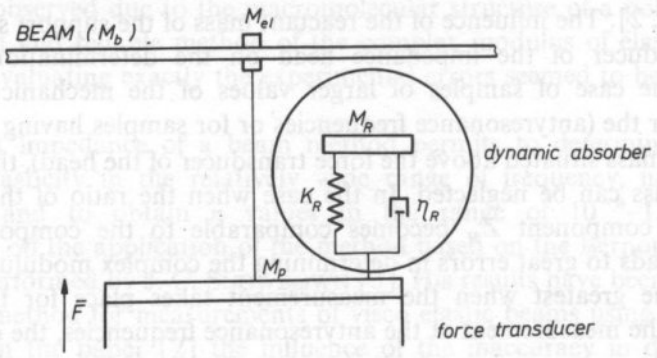

FIG. 2. Mechanical rheological model of the impedance head type 8001, Bruel-Kjaer

written as

$$Z_R = \left[\frac{1}{j\omega M_R} + \frac{1}{\frac{K_R}{j\omega} + \eta_R}\right]^{-1} \tag{2}$$

where M_R is the mass of the silicon ring, K_R is its stiffness, η_R its loss factor.

So, one can write in the first approximation the expression for the complete mechanical impedance of the head Z_H as follows:

$$Z_H = j\omega M_p + Z_R = \frac{(M_p+M_R)K_R - \omega^2 M_R M_p + j\omega\eta_R(M_p+M_R)}{\eta_R + j\omega(M_R - K_R/\omega^2)} = \frac{R_N + jI_N}{R_0 + jI_p} \tag{3}$$

where M_p is the mass above the piezoelectric element. The eventual mechanical coupling between the piezoelement and the casting was not taken into account.

The modulus of the mechanical impedance of the head is equal to

$$|Z_H| = \left[\frac{R_N^2 + I_N^2}{R_D^2 + I_D^2}\right]^{1/2} \tag{4}$$

where

$$R_N = (M_p+M_R)K_R - M_R M_p \omega^2$$

$$I_N = \omega\eta_R(M_p+M_R)$$

$$R_p = \eta_R$$

$$I_p = \omega\left(M_R - \frac{K_R}{\omega^2}\right)$$

For a quantitative evaluation of the influence of the impedance of the ring against the frequency, one can take the value of 1000 Hz up to which the influence is small and above that it becomes more and more significant.

Dividing the numerator and the denominator of the expression by K_R^2 and substituting $k_R \approx 10^7$ N/m and $\eta \approx 40$ kg/s for $f < 1000$ Hz, one obtains for the modulus of the reactant mass

$$Z_H \approx (M_P + M_R)\omega \tag{5}$$

It is seen from Eq. (5) and Fig. 2 that for frequencies less than 1000 Hz the modulus of the mechanical impedance of the head is equal to the modulus of reactance of the system: movable support – tightening ring. By measuring the modulus of the reactance head Z_H in the low frequency, range one can determine the dynamical mass of the ring M_R, namely,

$$|Z_H| = 2\pi f (M_R + M_P) = \frac{U_{RMS}}{CV_{RMS}}, \tag{6}$$

where U_{RMS} is the root mean square voltage on the force transducer. V_{RMS} – the root mean square vibrational velocity, and C is the sensitivity of the transducer.

The dynamical mass M_R was experimentally determined as equal to 1.4×10^{-3} kg.

The stiffness k_R may be calculated from the expression of the antyresonance frequency of the head which can be obtained from Eq. (4) by putting the first derivatives equal to zero, namely $|Z'| = 0$. The antyresonance frequency of the head was measured (Fig. 3a) as $f_a = 1.4 \times 10^4$ Hz. Having Z_H and f_a as well as the values M_R, M_p and η, one can use the formula (4) to calculate $k_R = 2.38 \times 10^7$ N/m.

For further experimental vrification of the assumed theoretical rheological model of the head the numerical calculations of the modulus of the mechanical impedance of the head were performed.

The values assumed above for the viscoelastic elements of the head, namely, k_R, M_R, η and M_p were introduced into Eq. (4). Figure 3 represents the results of the experimental measurement (a) in comparison with the numerical ones (b) of the

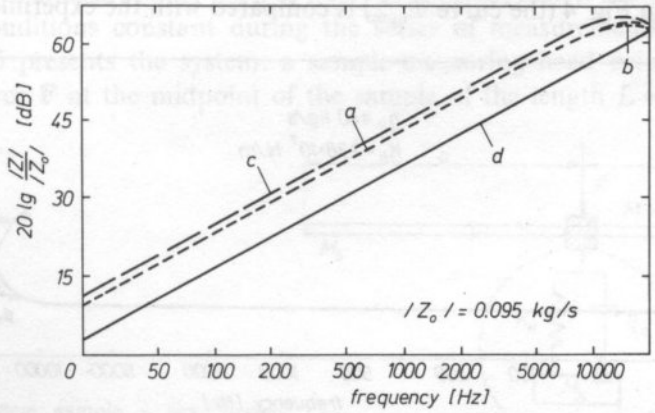

FIG. 3. Mechanical impedance modulus level of the impedance head against frequency

modulus level of the mechanical impedance of the head, as $20 \log \left|\frac{Z_u}{Z_0}\right|$, for different excitation velocities: 0.5; 2.0; 5.0 mm/s.

The experimental curve (a) and the theoretical one (b) are overlapped in the low frequency range. A small difference, about 0.5 dB, occurs at the range of the antyresonance frequency; however, both curves have the same behaviour. It results from Fig. 3 that the impedance of the tightening ring (the curves (a) and (b)) contributes significantly to the total impedance of the head when compared with the curve (d) calculated assuming the ring impedance is neglected.

The curve (c) in Fig. 3 represents the total mechanical impedance of the system: the head – the element which joins the head and the sample.

It results from the theoretical analysis and the experimental examinations that the contribution from the impedance of the measuring head should be taken into account when one determines the visco-elastic parameters from the experimental data of the modulus of the sample impedance.

2.2. *Phase angle of the measuring head*

The influence of the tightening ring appears also as an additional phase shift between the vibrational velocity and the exciting force. The phase angle of the impedance head can be expressed as the ratio of the imaginary part to the real part of the head impedance Z_H.

After corresponding transformation of the formula (3), and according to the definition, one obtains the following expression for the phase angle of the impedance of the head:

$$\Phi = \operatorname{arctg} \frac{I_N R_D - R_N I_D}{R_N R_D + I_N I_D}. \tag{7}$$

The calculated phase angle for the assumed rheological model of the impedance head presented in Fig. 4 (the curve Φ_{num}) is compared with the experimental one (the

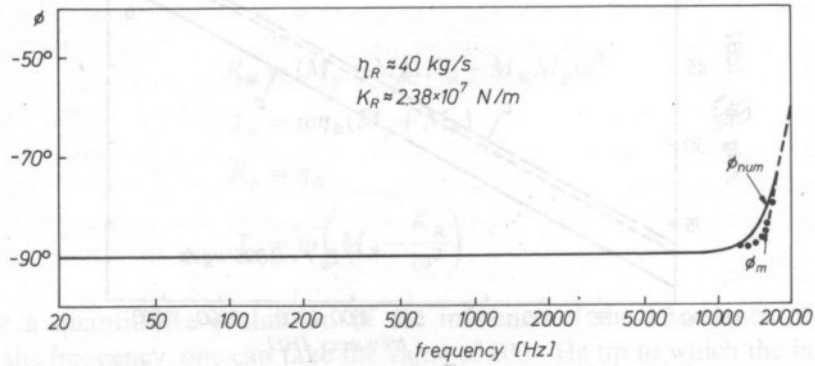

FIG. 4. Phase angle of the measuring impedance head

curve Φ_{pom}). Both curves Φ_{num} and Φ_{pom} overlap each other up to 14 kHz within the experimental error of the phase measured with a phasemeter of the accuracy $\pm 1°$. Above the range of 14 kHz, the divergence of the curves is observed due to the resonance range of the B and K vibrator (type 4809) used and to the resonance of the impedance head.

This is worth mentioning, too, that in the consideration of the impedance head model from which the formulas for mechanical impedance and for the phase angle were derived, the coupling between the casting and the accelerometer as well as the transducer of the force has been neglected. It is also possible that the coupling is responsible for the divergence of both curves in Fig. 4 above 14 kHz.

In materials of great values of η the modulus of the point impedance in the vicinity of resonance and antiresonance frequencies of the beam is a function of diffused extrema. The function $|Z_u(f)|$ in the increase of the frequency has a small dynamic of variations of its value for the consecutive resonance and antiresonance frequencies. So, to determine the loss factor on the basis of experimental data for materials of great internal losses, namely $\eta > 0.1$, it is necessary to measure not only the modulus of the impedance but also the phase Φ between the vibrational velocity and the force in the driving point.

2.3. The point impedance of the system: beam sample – measuring impedance head

Analyzing the application of the point impedance method to the complex modulus of elasticity measurements of solid materials, a beam shape sample was considered, two ends of which were free and driven at its midpoint with the harmonic force to obtain bending vibrations. The choice of such boundary conditions was dictated by the fact that their practical realization is relatively simple. It is easier and more reproducible to fix a sample in those conditions comparing, for instance with cases when two ends are stiffly fixed or freely supported; then it is difficult to keep the boundary conditions constant during the series of measurements.

Figure 5 presents the system: a sample-measuring head being driven by the harmonic force **F** at the midpoint of the sample of the length $L = 2a$. Mechanical

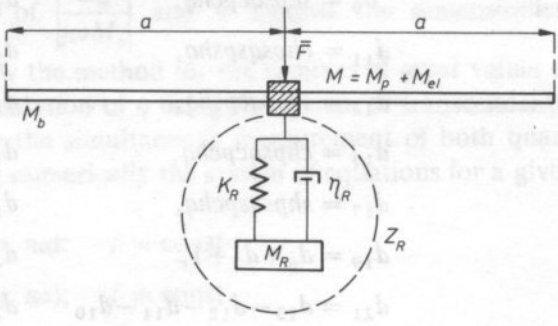

FIG. 5. The system: sample – head driven with the harmonic force to bending vibrations

point impedance of the system: beam-head is the sum of the point impedance of the beam Z_0 and the impedance of the measuring head Z_H:

$$Z_u = Z_0 + Z_H = Z_0 + Z_R + j\omega M \tag{8}$$

where Z_R is the mechanical impedance of the tightening ring, $M = M_p + M_{el} + M_b$, M_p is the mass of the force transducer and M_{el} the mass of the element joining the head with the sample, M_b the mass of the sample.

The expression for the modulus of the normalized point impedance of the total system is as follows:

$$\left|\frac{Z_u}{j\omega M_b}\right| = \left\{\frac{X_N^2 + Y_N^2}{X_D^2 + Y_D^2}\right\}^{1/2} \tag{9}$$

and for the phase angle

$$\Phi_u = \operatorname{arctg} \frac{Y_N X_D - X_N Y_D}{X_N X_D + Y_N Y_D} \tag{10}$$

where

$$X_D = d_{18} d_{24} - d_{19} d_{23},$$

$$Y_D = d_{18} d_{23} + d_{19} d_{24},$$

$$X_N = d_{18} d_{26} + d_{19} d_{25} + d_4 d_{20} + d_5 d_{21},$$

$$Y_N = -d_{18} d_{25} + d_{19} d_{26} + d_4 d_{22} + d_5 d_{20}$$

and

$$d_1 = (M + M_R) k_R, \qquad d_2 = \omega^2 M M_R,$$

$$d_3 = \omega \eta_R (M + M_R), \qquad d_4 = \omega M_l \eta_R,$$

$$d_5 = \omega^2 M_b \left(M_R - \frac{k_R}{\omega^2} \right), \qquad d_6 = chpcqcpchq,$$

$$d_7 = shpsqspshq, \qquad d_8 = chpcqspshq,$$

$$d_9 = shpsqcpchq, \qquad d_{10} = shpcqcpchq,$$

$$d_{11} = chpsqspshq, \qquad d_{12} = chpcqspchq,$$

$$d_{13} = shpsqcpshq, \qquad d_{14} = shpcqspshq,$$

$$d_{15} = chpsqcpchq, \qquad d_{16} = chpcqcpshq,$$

$$d_{17} = shpsqspchq, \qquad d_{18} = d_8 - d_9,$$

$$d_{19} = d_6 + d_7 + 1, \qquad d_{20} = d_{14} - d_{15} - d_{16} - d_{17},$$

$$d_{21} = d_{13} - d_{12} - d_{11} - d_{10}, \qquad d_{22} = d_9 + d_{11} + d_{15} - d_{13},$$

$$d_{23} = pd_5 + qd_4, \qquad d_{24} = pd_4 - qd_5,$$

$$d_{25} = pd_1 - pd_2 - qd_3, \qquad d_{26} = qd_1 - qd_2 + pd_3.$$

The parameters p and q are determined as

$$p = na\left(\frac{E_0}{E_f}\right)^{1/4}\left[\frac{1}{2\sqrt{D}} + \frac{(1+D)^{1/2}}{2\sqrt{2}D}\right]^{1/2},$$

$$q = -na\left(\frac{E_0}{E_f}\right)^{1/4}\left[\frac{1}{2\sqrt{D}} - \frac{(1+D)^{1/2}}{2\sqrt{2}D}\right]^{1/2},$$

where

$$D = (1+\eta^2)^{1/2}.$$

The dynamical Young modulus E_f is given by the formula

$$E_f = \frac{\omega^2 \varrho a^4 A}{(na)^4 I} \tag{11}$$

where ϱ is the density of the material, A is the lateral cross section of the beam sample, I is the momentum of of the lateral cross section, (na) is the dimensionless parameter proportional to $\sqrt{\omega}$, $n = \sqrt{\dfrac{\omega^2 \varrho A}{E_f I}}$ is the wave number and a is the half of the length of the beam.

The Young modulus E_0 is the reference value equal to the dynamical Young modulus for a given reference frequency f_0. Usually, the first antiresonant frequency of the beam is chosen as f_0.

Using the formulas (9)–(11) numerical calculation of the modulus of the point impedance and of the phase angle of the system: beam-head being driven at the midpoint were performed for great values of the loss factor (the formula (10)). For the calculations the following values were taken: $\gamma = \dfrac{M}{M_b} = 0.1$ and $\eta = 0.1$ (Fig. 6a), $\eta = 1.0$ (Fig. 6b) and $\eta = 5.0$ (Fig. 6c).

In the numerical analysis the viscosity η_R and the stiffness k_R of the tightening ring of the head was neglected.

The behaviour of the curves of $\left|\dfrac{Z_m}{j\omega M_b}\right|$ and Φ against the dimensionless parameter $(na) \sim \sqrt{\omega}$ points out how the method for the samples of great values of η should be chosen. The correct calculation of η using the system of transcendental equations is possible by performing the simultaneous measurement of both quantities, namely $|Z_u|$ and Φ and solving numerically the system of equations for a given frequency:

$$\eta = h(\eta, na); \quad f = \text{const}$$

$$\Phi = g(\eta, na); \quad f = \text{const}.$$

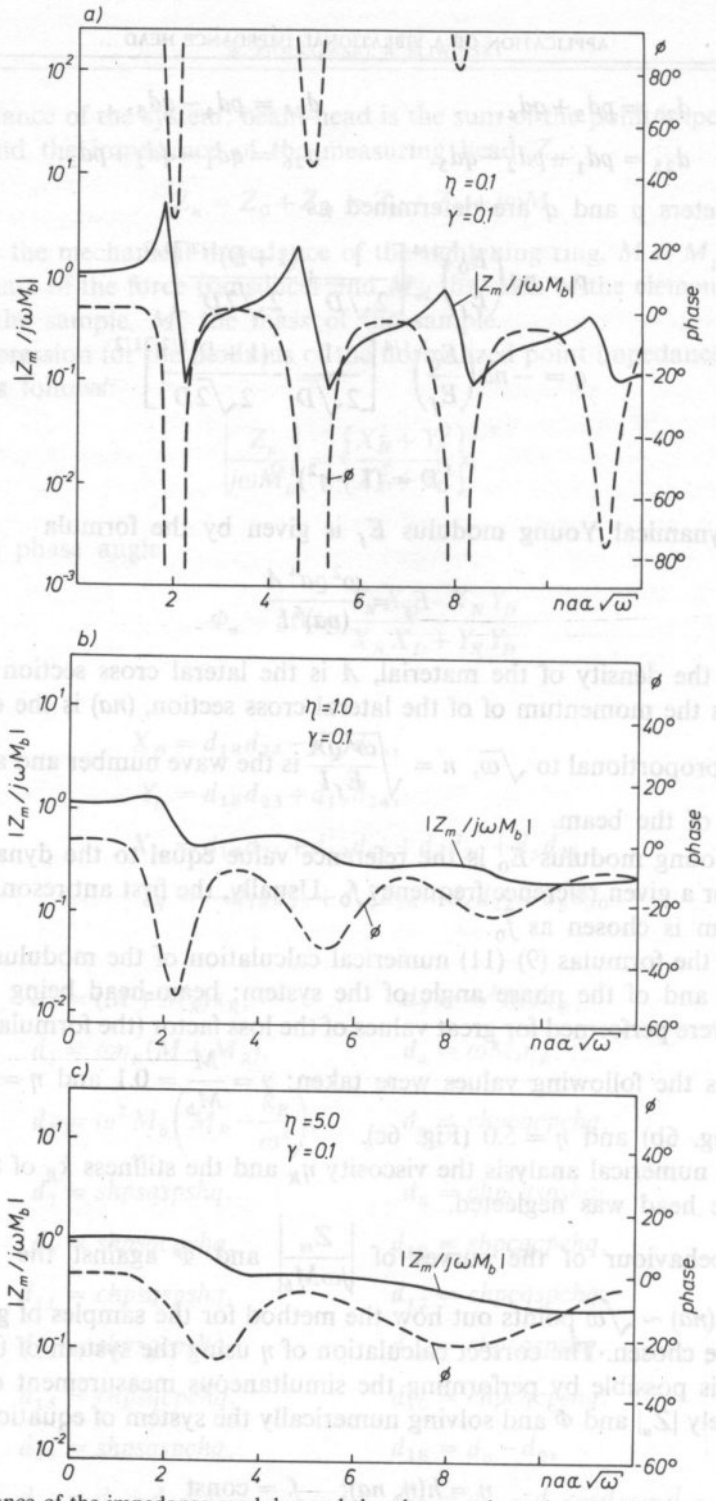

FIG. 6. Dependance of the impedance modulus and the phase angle against the frequency: a) $\eta = 0.1$; b) $\eta = 1.0$; c) $\eta = 5.0$

3. Experimental results

The experimental results presented in this paper are based on the first approximation, i.e., assuming that the mechanical impedance of the measuring head is equal to the reactance of the mass of component elements of the impedance head, namely, to the reactance of the mass situated above the force transducer and the reactance of the mass of the tightening ring (Eqs. (9)–(10)).

Solid polymer methyl-polymethacrilate (plexiglass) was chosen for measurements because the substance was already examined by many authors who applied various measuring methods to determine the complex modulus of elasticity in dependance on frequency and temperature [4–11].

The complex modulus of elasticity was numerically calculated for three following mass ratio:

1) $\gamma = \dfrac{M_{el} + M_p + M_R}{M_b}$

2) $\gamma = \dfrac{M_{el} + M_p}{M_b}$ (the contribution of the ring is neglected)

3) $\gamma = 0$ (the total contribution of the impedance head is neglected, i.e., $|Z_H| = 0$.

The measuring setup is presented in Fig. 7. The samples of plexi glass had three different dimensions (obtained by the consecutive shortening by cutting out (305, 285, 265 x 10.76 x 1.99) x 10^{-3} m^3. All measurements were performed at room temperature.

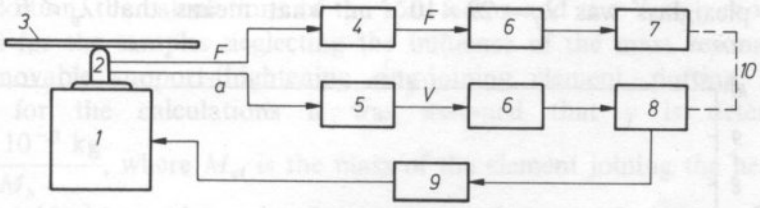

FIG. 7. Measuring arrangement. *1.* vibration exciter Bruel-Kjaer type 4809; *2.* impedance head B-K type 8001; *3.* beam being tested; *4.* preamplifier; *5.* preamplifier and integrator; *6.* frequency analyzer B-K type 2120; *7.* level recorder B-K type 2307; *8.* since generator B-K type 1024; *9.* power amplifier B-K type 2706; *10.* mechanical linkage

The measurements were carried out for three different values of the vibrational velocity applied at the driving point of the sample: $V_{RMS} = (2, 5, 15)$ x 10^{-3} m/s. In the whole frequency range the values of the vibrational velocity were kept constant. The measured values of F_{RMS}, V_{RMS} at given f were used to calculate the modulus of impedance for the system: beam-head mass from the formula $|Z_u(f)| = \dfrac{F_{RMS}}{V_{RMS}}$, at the resonance and antiresonance conditions.

The resulting values of $|Z_u(f)|$ were introduced to the formulas (10) or (11), respectively, and the loss factor and the dynamic Young modulus were calculated for the given resonance frequencies of the whole system: beam-head mass. Finding η from the transcendental equation (9), the dependence of the loss factor on the dimensionless parameter $\eta(na)$ was exploited at the vicinity of the resonance and antiresonance frequencies for the bending vibrations of the total system. The loss factor approaches its maximum value for $(na)_{ext}$ corresponding to the resonance frequency or antiresonance frequency, respectively. At the vicinity of the extremal value na_{ext} the loss factor decreases. Hence the calculation of the loss factor consists in seaeching the maximal value $\eta_{max} = \eta(na)_{rez}$ (or η $(na)_{antirez}$) over a small range of the dimensional parameter na within a narrow vicinity of the resonance or antiresonance frequency (see [1]).

In the case of the determination of η and E_f out of the discrete resonance and antiresonance values one must measure not only the modulus of the point impedance but also the phase angle between the force and the velocity.

The measurement results of η and E_f for the driving velocities $V_{RMS} = (2$ and $15) \times 10^{-3}$ m/s have been overlapped (in the limit of the experimental error) with those ones for $V_{RMS} = 5 \times 10^{-3}$ m/s, therefore only the last ones are presented in this paper.

Anyway, the results for three different values of velocities have shown the linear range of vibrations what was the condition for the validity of the Bernoulli-Euler theory. The maximal vibrational velocity (driving takes place at the loop of wave) at the resonance may be evaluated from the relation $V_{RMS} \ll \lambda_g f/10$.

The wavelength for the highest frequency measured 8000 Hz (the 9-th resonance mode) in plexiglass was $\lambda_g = 29 \times 10^{-3}$ m, what means that $\lambda_g \gtrsim 6$ h and the

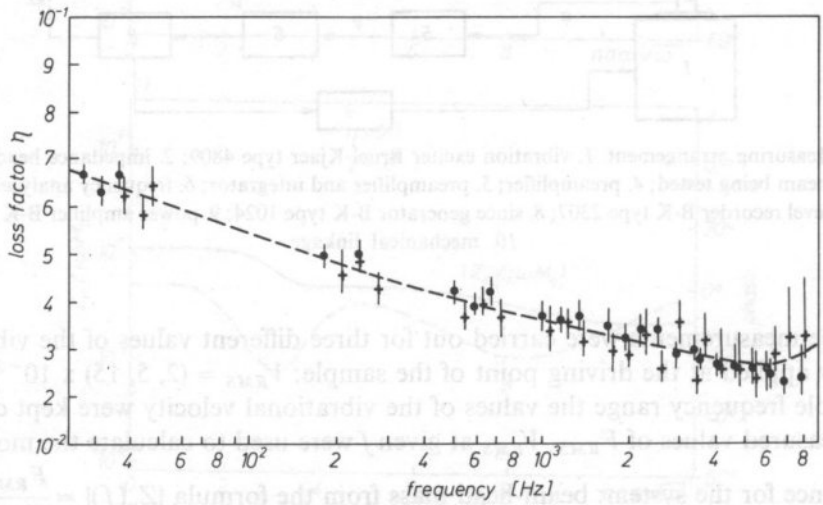

FIG. 8. Dependance of the loss factor η against the frequency for samples of plexiglass •, + – values of the loss factor measured at antiresonances and resonances of the sample, respectively

assumption of the Bernoulli-Euler theory is satisfied. Such evaluation is not possible for the antiresonance frequencies because then driving takes place at the mode of the sample.

Figure 8 represents the dependance of the loss factor in the plexiglass sample against the frequency. The range of experimental errors is shown in the figure, too.

In Fig. 9 the dependance of the dynamical Young modulus is shown against the frequency. Using the formula (11) and taking into account the geometrical dimensions of the sample the antiresonance or resonance frequency and calculated (from the transcendental equation $\eta = h(\eta, na)$) dimensionless parameter na were determined. In some other methods [1, 9, 10] the values of na are taken such as for the pure elastic samples, what leads to the wrong calculations of E_f.

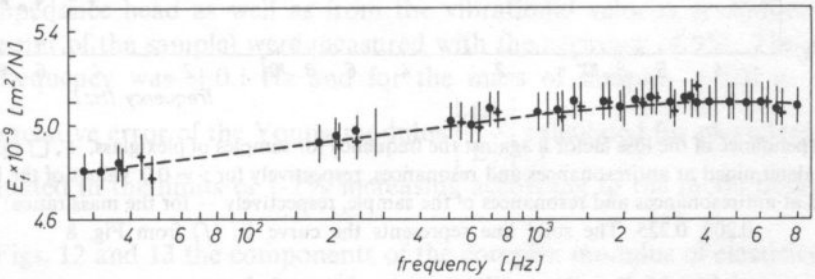

FIG. 9. Dependance of the Young modulus E_f against the frequency for samples of plexiglass, •, + values of the Young modulus measured at antiresonances and resonances of the sample, respectively

In addition, the calculations of the loss factor and the Young modulus were performed for the samples neglecting the influence of the mass resonance of the system: movable support-thightening ring-joining element, putting $\gamma = 0.0$. In addition, for the calculations it was assumed that γ is determined as $\gamma = \dfrac{M_{el} + 10^{-3}\ \text{kg}}{M_b}$, where M_{el} is the mass of the element joining the head and the sample and 10^{-3} kg is the mass of the support above the force transducer in the impedance head of the Bruel and Kjaer type 8001.

Figure 10 illustrating the dependance of the loss factor against the frequency for the plexiglass samples shows the divergence of η values (increasing for the resonance frequencies and decreasing for the antiresonance frequencies) when the frequency increases, for the mass ratios $\gamma = 0.0$; 0.195; 0.209; 0.225.

The agreement of η values measured in the corresponding resonance and antiresonance modes of the sample gives an evidence of correct determination of the loss factor.

The neglecting of the reactant mass of the system: moveable support-tightening ring-joining element (i.e. $\gamma = 0.0$) in calculations of the Young modulus results decreasing of E_f value determined at resonance and antiresonance frequencies of the sample (see Fig. 11).

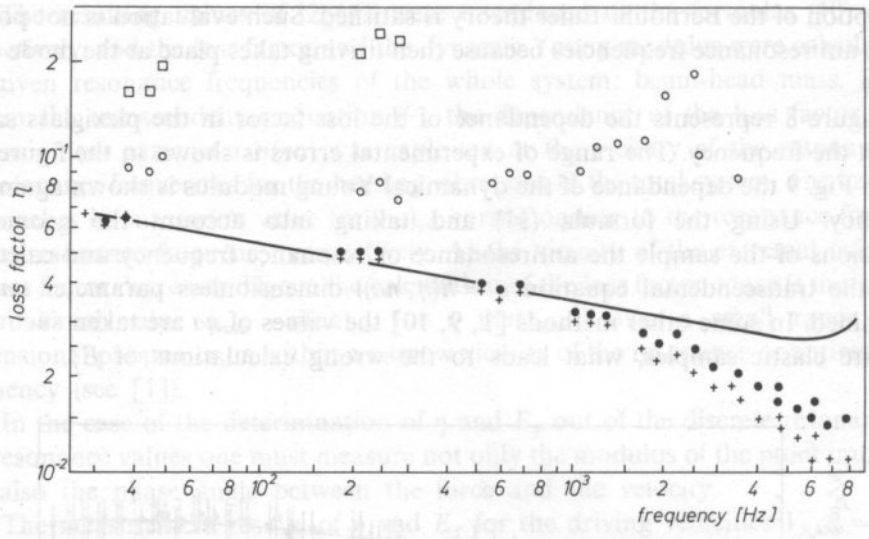

FIG. 10. Dependance of the loss factor η against the frequency for samples of plexiglass, +, □ values of the loss factor determined at antiresonances and resonances, respectively for $\gamma = 0.0$, values of the loss factor determined at antiresonances and resonances of the sample, respectively – for the mass ratios: $\gamma = 0.195$, 0.209, 0.225. The solid line represents the curve E_f (f) from Fig. 8

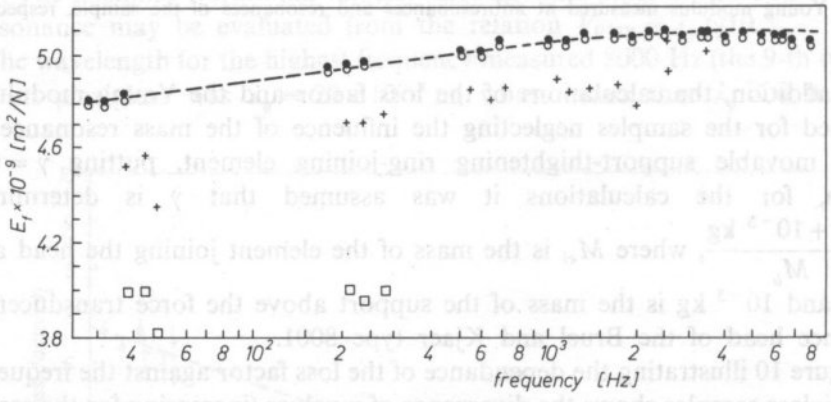

FIG. 11. Dependance of the Young modulus E_f against the frequency for plexiglass samples. +, □ values determined at antiresonances and resonances of the sample, respectively, for $\gamma = 0.0$, •, ○ – at resonances and resonances, respectively, for $\gamma = 0.195$; 0.209; 0.225. The dotted line illustrates the dependance of $E_f(f)$ from Fig. 9

Loss factor η values calculated for corresponding resonances and antiresonances are charged by an additional error due to the inaccuracy in determining the midpoint for driving the sample [2]. The influence of that error on the determination of η in plexiglass samples was neglected for the first 9 resonance and antiresonance

modes of the sample because the error could be minimized by a special selection of samples before the measurements [2].

The relative error of the loss factor

$$\left|\frac{\Delta\eta}{\eta}\right| = \left|\frac{\eta_+ - \eta_-}{\eta}\right|$$

for the most unadvantageous 9-th resonance mode is about 40% and decreases when the number of the mode decreases approaching about 10% for the 1-st mode. For the 9-th antiresonance mode the error is about 30% being, however, less than 10% for the first 6 modes.

For measuring the electric signals proportional to F_{RMS} and V_{RMS}, the Bruel-Kjaer analyzer 2120 was used. The values of voltages from the force transducer of the impedance head as well as from the vibrational velocity transducer (at the driving point of the sample) were measured with the accuracy of 5%. The accuracy for the frequency was ± 0.1 Hz and for the mass of samples ± 0.01 g.

The relative error of the Young modulus $\left|\frac{\Delta E_f}{E_f}\right|$ calculated for plexiglass samples was evaluated in the limits of 1-2% increasing according to the mode number from 1 to 9.

In Figs. 12 and 13 the components of the complex modulus of elasticity against the frequency are presented for softening PCW (polivinilchloride) and Razotex

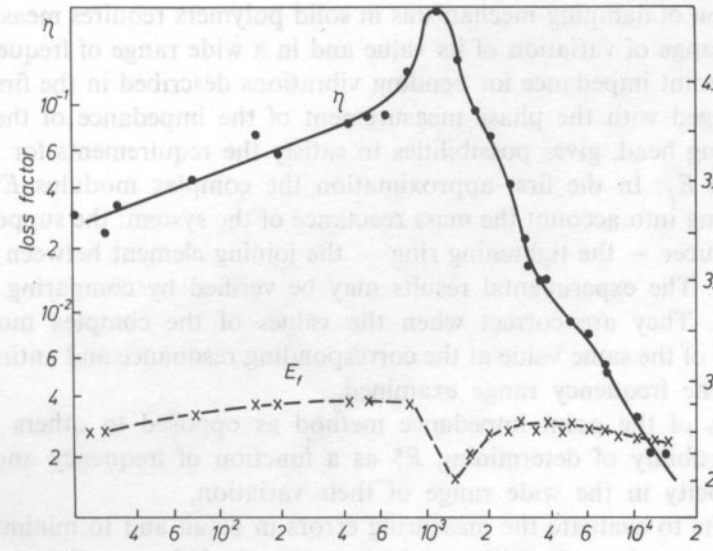

FIG. 12. Components of complex modulus of elasticity against the frequency for PCW

B (fenole epoxy), respectively. For PCW a strong damping for bending waves appears at the vicinity of 1000 Hz. For the maximum the inner structure of the polymer related to the relaxation mechanism is responsible. For the Razotex no relaxation process was observed within the frequency range examined.

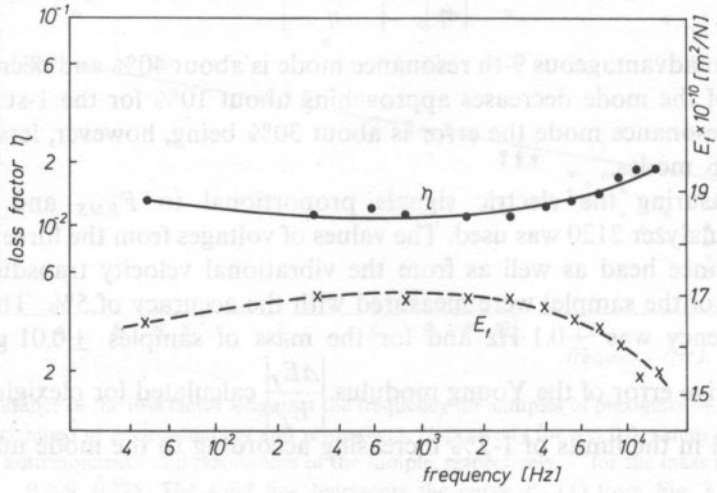

FIG. 13. Values of E_f and η against frequency for Rezotex B

4. Conclusions

Examination of damping mechanisms in solid polymers requires measurements of η in a wide range of variation of its value and in a wide range of frequency. The method of the point impedance for bending vibrations described in the first part of the paper enlarged with the phase measurement of the impedance of the system: sample-measuring head, gives possibilities to satisfy the requirements for measurements of η and E_f. In the first approximation the complex modulus E_f^* can be determined taking into account the mass reactance of the system: the support above the force transducer – the tightening ring – the joining element between the head and the sample. The experimental results may be verified by comparing with the numerical ones. They are correct when the values of the complex modulus of elasticity E_f^* are of the same value at the corresponding resonance and antiresonance frequencies in the frequency range examined.

Advantages of the point impedance method as opposed to others

1. The possibility of determining E_f^* as a function of frequency and driving vibrational velocity in the wide range of their variation,

2. It permits to evaluate the measuring errors in detail and to minimize them, too, as it has been analyzed in this paper in respect to the influence of the impedance of the measuring head on the determination of E_f^* for some viscoelastic materials.

References

[1] W. ZIÓŁKOWSKI, A. ŚLIWIŃSKI, Journal of Sound and Vibration **80**, 2, 209–222 (1982).
[2] W. ZIÓŁKOWSKI, A. ŚLIWIŃSKI, Journal of Sound and Vibration, **97**, 1, 11–21 (1984).
[3] J. C. SNOWDON, *Vibration and shock in damped mechanical system*, New York-London-Sydney: John Wiley and Sons Inc. 1968.
[4] L. CREMER, H. HECKL, *Structure borne sound*. Transl. E. Ungar Berlin-New York 1973.
[5] J. D. FERRY, *Viscoelastic properties of polymer*, New York, Chichester, Bristranc, Toronto, John Wiley and Sons Inc. 1980.
[6] J. M. WARD, *Mechanical properties of solid polymers*, London, New York, Sydney, Toronto, John Wiley and Sons Ltd 1971.
[7] A. V. TOBOLSKY, *Properties and structure of polymers*, New York, John Wiley and Sons Inc. 1960.
[8] R. G. C. ARRIDGE, *Mechanics of polymers*, Clarendon Press, Oxford 1975.
[9] W. ZIÓŁKOWSKI, A. ŚLIWIŃSKI, *Application of the point impedance method to the measurement of the complex elastic modulus in viscoelastic beams*, Proc. of the 33-rd Open Seminar on Acoustics, Rzeszów 1986.
[10] W. ZIÓŁKOWSKI, A. ŚLIWIŃSKI, *The measurement of the complex modulus of elasticity in the visco-elastic beam with the point impedance and with the resonance methods*, Proc. of the 34-th Open Seminar on Acoustics, Wrocław 1987.
[11] A. SCHLAGEL, *Measurements of modulus of elasticity and loss factor for solid materials*, Technical Review Bruel and Kjaer **4**, 1–11 (1957).

Received November 21, 1989